Technische Universität München
TUM School of Engineering and Design

Efficient Multi-Scale Simulation of Deflagration-to-Detonation Transition in Stratified H_2-CO-Air Mixtures

Christoph Johannes Barfuß

Vollständiger Abdruck der von der TUM School of Engineering and Design der Technischen Universität München zur Erlangung des akademischen Grades eines

DOKTORS DER INGENIEURWISSENSCHAFTEN (DR.–ING.)

genehmigten Dissertation.

Vorsitz:
Prof. Dr.-Ing. Florian Holzapfel
Prüfer*innen der Dissertation:
Prof. Dr.-Ing. Thomas Sattelmayer
Prof. Knut Vågsæther, Ph.D.

Die Dissertation wurde am 16.05.2023 bei der Technischen Universität München eingereicht und durch die TUM School of Engineering and Design am 06.09.2023 angenommen.

Vorwort

Die vorliegende Arbeit entstand am Lehrstuhl für Thermodynamik der Technischen Universität München während meiner Tätigkeit als wissenschaftlicher Mitarbeiter. Sie wurde durch das Bundesministerium für Wirtschaft und Energie über die Gesellschaft für Anlagen- und Reaktorsicherheit gefördert.

Zu aller erst möchte ich meinem Doktorvater Prof. Dr.-Ing. Thomas Sattelmayer für das in mich gesetzte Vertrauen danken. Durch die gewährten Freiheiten in der Projektdurchführung konnte ich mich sowohl wissenschaftlich als auch menschlich weiterentwickeln. Prof. Knut Vågsæther danke ich für die freundliche Übernahme des Koreferats und Prof. Dr.-Ing. Florian Holzapfel für die Übernahme des Prüfungsvorsitzes.

Die Lehrstuhlgemeinschaft hat mein Leben sehr bereichert. Egal ob es sich um die thematischen Arbeiten, gemeinsame Feiern oder um das wöchentliche Fußballspielen handelte, die Kollegen und Kolleginnen gaben immer Gas. Ich bin sehr froh über die daraus entstandenen Freundschaften. Allen "Explodierern" des Lehrstuhls danke ich für die vielen fachlichen Diskussionen und Anregungen. Meinem Projektpartner Daniel Heilbronn möchte ich für die vier Jahre Büroehe gesondert danken. Die intensiven inhaltlichen Gespräche haben mich immer weitergebracht und der Spaß ist weder im Alltag noch auf den Konferenzen zu kurz gekommen. Helga Bassett und Sigrid Schulz–Reichwald danke ich für die Unterstützung in sämtlichen organisatorischen Angelegenheiten.

Meinen ehemaligen Studenten danke ich für ihren Beitrag zum Gelingen des Projekts. Besonders möchte ich jedoch die Leistungen von Utkarsh Pathak hervorheben. Durch seinen unermüdlichen Einsatz und seine Programmierkenntnisse gelang die Rechenzeitoptimierung des entwickelten Lösers sowie die Umstrukturierung des Codes. Seine Leistungen waren ein großer Beitrag zum Erfolg der Arbeit.

Daniel Heilbronn, Dr.-Ing. Thomas Hofmeister, Dr. Aly Taleb, Simon Tartsch und Manuel Würth danke ich für das Korrigieren dieser Dissertation. Eure

Anmerkungen haben die inhaltliche und sprachliche Qualität der Arbeit stark verbessert.

Meinen Eltern, Ursula und Jürgen, danke ich für die lebenslange Unterstützung, die mich hierhin gebracht hat. Danke, dass Ihr mir die Möglichkeit gegeben habt mich frei zu entwickeln und diesen Weg zu gehen.

Mein innigster und herzlichster Dank gilt Dir, liebe Eva. Seit vielen Jahren gehen wir gemeinsam durchs Leben und du hast mich auf dem gesamten Werdegang dieser Arbeit durch Höhen und Tiefen begleitet. Deine bedingungslose Unterstützung und Liebe ermöglichte es mir überhaupt erst die Phasen größter Anstrengung durchzustehen. Diese Arbeit ist in erster Linie auch Dein Erfolg. Ich freue mich auf unsere gemeinsame Zukunft.

München, im Mai 2023 Christoph Barfuß

Abstract

Weak ignition of hydrogen-carbon monoxide-air (H_2-CO-air) gas in a confining geometry can lead to flame acceleration. In the worst case, deflagration-to-detonation transition (DDT) takes place, which can lead to the failure of the confining structure due to high structural loads. The present thesis introduces an efficient CFD simulation framework for DDT risk assessment in stratified H_2-CO-air mixtures.

The solver is based on previous developments of H_2-air explosion simulations for small and large-scale accident scenarios. Sub-models and combustion-specific parameters in the turbulent flame speed closure model for deflagrative flame propagation are adjusted to consider the multi-component fuel H_2-CO. The laminar flame speed, the Lewis number and the critical velocity gradients for turbulent quenching are computed during simulation without any limitations by the H_2-CO-air composition. Hence, the framework can be applied to accident scenarios with any initial mixture distribution. A two-step mechanism, which consists of a detonation criterion and a volumetric heat release, models the detonation propagation. A mixture and cell-size-dependent scaling of the volumetric heat release source term is introduced, guaranteeing a cell-size-independent detonation velocity. At the same time, the detonation model's forest-fire mechanism maintains the detonation complex's sharp gradients despite the under-resolved simulation approach.

Separate flame-propagation transport equations are applied for small and large-scale scenarios. A newly introduced load-balancing algorithm for the geometrical Volume-of-Fluid method reduces the computation time noticeably for large-scale deflagration-to-detonation transition simulations.

A validation of H_2-CO-air DDT simulations is conducted with experiments at the small-scale GraVent facility and the large-scale semi-confined A1-vessel. Varying the mixture composition and the obstacle configurations and investigating vertical fuel concentration gradients provides a broad validation basis. Simulated flame velocity profiles agree with the experimental data, especially when a distinct DDT with subsequent stable detonation is present in the ex-

periments. However, slow flames in the semi-confined geometry pose a limit for the modeling strategy. Non-reflecting boundary conditions describe pressure waves exiting the semi-confined geometries through venting surfaces. The ability to handle semi-confined geometries increases the presented CFD framework's applicability compared to the previous code for H_2-air DDT simulations.

The standard approach of explosion risk assessment by empirical criteria lacks generality. The presented CFD-based risk analysis treats the entire process from flame acceleration to DDT and subsequent stable detonation in a continuous simulation. Simulating the flame acceleration, which preconditions the fresh gas via pressure waves accordingly that DDT can occur, incorporates geometrical and reactive dependencies of DDT in the CFD-based risk analysis. The result is a more generally applicable risk assessment strategy for combustion-related accidents with H_2-CO-air mixtures.

Kurzfassung

In vollständig oder teilweise eingeschlossenen Wasserstoff-Kohlenmonoxid-Luft (H_2-CO-Luft) Gasmischungen kann es nach einer schwachen Zündung zur Flammenbeschleunigung kommen. Im schlimmsten Fall führt diese zum Deflagrations-Detonations-Übergang (DDT), der große Drucklasten auf die einschließende Struktur zur Folge hat. Um den DDT Eintritt vorhersagen zu können, stellt diese Arbeit einen effizienten CFD Löser zur Berechnung von schnellen Flammen und DDT in geschichteten H_2-CO-Luftmischungen vor.

Die Verbrennungsmodellierug wird ausgehend von Arbeiten zu H_2-Luftexplosionssimulationen für den Mehrkomponentenbrennstoff H_2-CO angepasst. Ein turbulentes Flammenschließungsmodell beschreibt die Flammenausbreitung im Deflagrationsbereich. Die notwendigen Verbrennungsparameter wie laminare Flammengeschwindigkeit, Lewis-Zahl und kritische Streckungsraten für turbulentes Flammenlöschen stehen dem CFD Löser über effiziente Korrelationen oder Interpolationstabellen für alle Zusammensetzungen des H_2-CO-Luftgemischs zur Verfügung. Die CFD-basierte Risikoanalyse kann dadurch aus rein technischer Sicht auf Unfallszenarien mit beliebigen Gemischzusammensetzungen angewendet werden. Ein Zweischrittmodell bestehend aus Detonationskriterium und volumetrischer Wärmefreisetzung beschreibt die durch Selbstzündung ausgelöste Detonation. Eine Quellltermskalierung in Abhängigkeit von der Zusammensetzung und der Berechnungszellengröße wurde implementiert. Sie garantiert eine zellgrößenunabhängige Ausbreitungsgeschwindigkeit der Detonation. Trotz des unteraufgelösten Berechnungsansatzes erhält der *Forest-Fire* ähnliche Mechanismus des Zweischrittmodels die steilen Gradienten des Detonationskomplexes.

Der vorgestellte CFD Löser setzt unterschiedliche Transportgleichungen für die Flammenausbreitung in klein- bzw. großskaligen Geometrien ein. Die Implementierung eines *load-balancing* Algorithmus für das in großskaligen Geometrien verwendete Flammenverfolgungskonzept, die geometrische Volume-of-Fluid Methode, reduziert die Berechnungszeit von großskaligen

DDT Simulationen deutlich.

Die DDT Simulationen in H_2-CO-Luftgemischen wurden mit experimentellen Daten des kleinskaligen GraVent Explosionskanals und des großskaligen, teilweise offenen Explosionskanals im A1-Behälter validiert. Die Validierung besitzt durch die Variation der Gemischzusammensetzung und der Hinderniskonfiguration sowie durch die Untersuchung von vertikalen Brennstoffungleichverteilungen eine breite Basis. Die simulierten Flammengeschwindigkeitsprofile stimmen mit den Experimenten gut überein. Dies gilt insbesondere für Fälle, in denen die Messungen einen ausgeprägten DDT mit anschließender stabiler Detonationsausbreitung zeigen. In allen Simulationen der Validierung sagt der CFD Löser ein sicherheitstechnisch konservatives Ergebnis voraus. Nichtsdestotrotz stellen langsame Flammen in teilweise offenen Geometrien ein Limit für die Vorhersage durch das Berechnungsverfahren dar. Eine nichtreflektierende Randbedingung modelliert den Austritt von Druckwellen aus teilweise offenen Geometrien und ermöglicht damit die Explosionssimulation in derartigen Geometrien. Die Anwendbarkeit des CFD Lösers wird dadurch im Vergleich zu den Vorgängerentwicklungen erweitert.

Der Einsatz von empirischen Kriterien zur Bestimmung des Detonationsrisikos ist nicht generell anwendbar oder in der Praxis häufig unhandlich. Die präsentierte CFD-basierte Risikoanalyse bildet die Flammenbeschleunigung, den DDT und die anschließende Detonationsausbreitung in einer einzelnen zusammenhängenden Berechnung ab. Da die Flammenbeschleunigung durch Vorkonditionierung des Frischgases die Grundlage für den DDT bildet, werden durch die explizite Berücksichtigung dieser Verbrennungsphase in der CFD-basierten Risikoanalyse Abhängigkeiten von der Geometrie sowie der Gemischreaktivität explizit beachtet. Daraus ergibt sich ein allgemeiner anwendbares Vorgehen zur Risikobewertung von Unfällen mit H_2-CO-Luftverbrennung.

Contents

List of Figures **xiii**

List of Tables **xix**

Nomenclature **xxi**

1 Introduction **1**
1.1 Motivation 1
1.2 Challenges for Explosion Risk Assessment 3
1.3 Outline of the Thesis 5

2 Explosion Fundamentals **7**
2.1 Gas-Dynamic Relation of Combustion Waves 7
2.2 Deflagration and Flame Acceleration 11
2.2.1 Laminar Flame Characteristics 12
2.2.2 Turbulent Flame Characteristics 16
2.2.3 Combustion Instabilities 22
2.2.4 Flame Acceleration 24
2.3 Detonation 28
2.3.1 One-Dimensional Theories 29
2.3.2 Multi-Dimensional Detonation Structure 32
2.4 Deflagration-to-Detonation Transition 34
2.4.1 Phenomenology 34
2.4.2 Transition Criteria 37

3 Numerical Explosion Modeling for Risk Assessment **39**
3.1 Overview of Combustion-Related Risk Assessment Codes 41

3.2 CFD Framework for Stratified H_2-CO-Air Explosions on Multiple Geometrical Scales . . . 44
3.2.1 Governing Equations . . . 47
3.2.2 Inhomogeneous Multi-Component Fuel . . . 52
3.2.3 Solver Architecture and Discretization . . . 53
3.3 Combustion Model for Explosion Simulation with Stratified H_2-CO-Air Mixtures . . . 56
3.3.1 Multi-Scale Flame-Propagation Transport Equations . . . 57
3.3.2 Coupling of Flame and Flow . . . 63
3.3.3 Deflagration Source Term . . . 69
3.3.4 Detonation Source Term . . . 89
3.4 Efficiency-Related Solver Development . . . 104
3.4.1 Adaptive Mesh Refinement . . . 105
3.4.2 Load-Balanced Geometrical Volume-of-Fluid Method . . . 108

4 Validation and Verification 119
4.1 Simulation Initialization . . . 120
4.2 Small-Scale GraVent Explosion Channel . . . 123
4.2.1 Homogeneous H_2-CO-Air Mixtures . . . 125
4.2.2 Stratified H_2-CO-Air Mixtures . . . 131
4.3 Large-Scale Semi-Confined A1-Vessel . . . 135
4.3.1 Homogeneous Semi-Confined H_2-CO-Air Mixtures . . . 139
4.3.2 Inhomogeneous Semi-Confined H_2-CO-Air Mixtures . . . 141

5 Summary and Outlook 147
5.1 Summary . . . 147
5.2 Outlook . . . 150

Bibliography 153

Appendix 177

A H_2-CO-Air Reaction System Related Coefficients and Parameters 178

B Initialization of Vertical Fuel Concentration Gradients 180
B.1 GraVent-Facility . . . 180

B.2 A1-Vessel 182

C Load-Balanced Geometrical Volume-of-Fluid Method 185
C.1 Geometrical Volume-of-Fluid Method 185
C.1.1 Interface Reconstruction 189
C.1.2 Interface Advection 192
C.2 OpenFOAM Specific Implementation of the Load-Balancing Algorithm 195
C.3 Generic Validation of the Load-Balancing Algorithm 203

D OpenFOAM's waveTransmissive Boundary Condition in the Density-Based CFD Framework 208

E Supervised Student Thesis and Projects 211

F Previous Publications 212

List of Figures

2.1 One-dimensional control volume of a stationary reaction front. 7

2.2 Rankine-Hugoniot diagram showing Hugoniot curves (red) and Rayleigh lines (blue) with upper and lower Chapman-Jouguet solution at CJ-condition $u_2 = a_2$. 9

2.3 Schematic structure of a freely-propagating unstretched laminar flame. 12

2.4 Influence of Lewis number on the flame-stretch dependency of an adiabatic laminar flame [adopted from [1]]. 14

2.5 1D twin-flame burner setup with stagnation-point flow for numerical evaluation of stretched laminar flame speeds. 15

2.6 Evaluation of unstretched fuel consumption speed from stretched 1D twin-flame simulation data at standard reference condition (Plots from 20 % fuel in air - 75/25 H_2/CO). 16

2.7 Flame regimes of turbulent premixed combustion based on Borghi [2] and Peters [3] [adopted from [4] and [5]]. 19

2.8 Illustration of turbulent eddies with the flame front [adopted from [6]]. 21

2.9 Schematic of Landau-Darrieus (LD) instability (left) and thermo-diffusive (TD) instability (right). The dashed flame shape demonstrates TD instability evolution between time steps t_1 and t_2 [adopted from [5, 7]]. 23

2.10 Transient evolution of flame acceleration in obstructed and unobstructed channels. 25

2.11 One-dimensional control volume of the detonation complex consisting of the reaction zone and the shock front. 29

2.12 Rankine-Hugoniot diagram with Hugoniot curve (red) and Rayleigh lines (blue) illustrating overdriven and CJ detonation solutions. 30
2.13 The one-dimensional ZND detonation structure characterizing von Neumann (vN) and Chapman-Jouguet (CJ) state. 32
2.14 Two-dimensional schematic of the three-dimensional detonation structure. 33
2.15 Schematic of transition modes in obstructed channels typical for accident scenarios. 36

3.1 Overview of the modeling strategy for FA and DDT in stratified H_2-CO-air mixtures on multiple geometrical scales in the CFD solver developed in the thesis. (Major contributions compared to the previous solvers [4, 8] are indicated by red frames). 46
3.2 Combustion modeling strategy with different flame-propagation transport equations for small-scale and large-scale geometries as well as the source term models for deflagrations and detonations. 56
3.3 Overview of geometry-scale-dependent flame-propagation transport equations available in the multi-scale combustion model of the CFD framework. 58
3.4 Overview of the flame-to-flow coupling methodology including the evaluation sequence for the reacting and non-reacting mixture. 63
3.5 Selection matrix for the auxiliary variables T_{comp} and p_{comp} depending on the flame regime and the reaction progress variable. 66
3.6 Specification of the deflagration source term including evaluation methods for the most-important modeling parameters. . . 70
3.7 $S_{\mathrm{L},0}$ interpolation table generation based on cubic splines computed with the SLM toolbox. 71
3.8 Experimental $S_{\mathrm{L},0}$ data used for the derivation of cubic splines. The colormap visualizes amount of H_2 in the fuel varying from pure CO (blue) to pure H_2 (red). 73
3.9 Numerical $S_{\mathrm{L},0}$ data and flammability limits used for the derivation of cubic splines. 74

3.10 $S_{L,0}$ evaluated from derived cubic splines using the Matlab SLM toolbox. 75
3.11 Validation of $S_{L,0}$ evaluation from the created interpolation table against $S_{L,0}$ measured by ProScience GmbH [9]. 76
3.12 Intermittent shape of a flame front (red) and the corresponding flow field (grey) [adopted from [3]]. 77
3.13 Effective Lewis number Le_{eff} according to the polynomial expression and additional plane with constant value $Le_{eff} = 1$. . . . 81
3.14 Critical velocity gradients evaluated from 1D reactive flow simulations and Zimont's model [6] with 50/50, 75/25 and 100/0 H_2/CO fuels. 84
3.15 Schematic of 2D computational domain in highly resolved simulations (dimensions in mm). 86
3.16 Temperature contour with iso-surface (blue) of exceeding flow strain in comparison to the critical velocity gradient (100/0 H_2/CO). 87
3.17 Temperature contour with iso-surface (blue) of exceeding flow strain in comparison to the critical velocity gradient (75/25 H_2/CO). 87
3.18 Impact of the g_{cr} evaluation method on the flame tip velocity profile of a 20 vol.-% fuel-air mixture with 50/50 H_2/CO in the GraVent explosion channel (BR60S300). 88
3.19 Specification of the detonation source term, including a two-step heat release mechanism. 90
3.20 Length and time scales for a detonation front traversing a single cell. 95
3.21 Temporal c-profile evaluated with the volumetric source term scaling methodology with generic input variables c_{lim} and t_{def} ($\phi = 1$ in 75/25 H_2/CO). 97
3.22 Simulated detonation velocities of varying cell sizes in comparison to D_{CJ} (30 vol.-% fuel in air - 75/25 H_2/CO). 100
3.23 Simulated detonation velocities of varying Co number in comparison to D_{CJ} (20 vol.-% fuel in air - 75/25 H_2/CO). 100

3.24 Temporal evolution of pressure p, temperature T and reaction progress c tracked at the fixed axial position of 10.0 meter (20 vol.-% fuel in air (75/25 H_2/CO) and a cell size of 20 mm). . . 102
3.25 A non-uniform mesh before (left) and after AMR (right), including static domain decomposition with four parallel processors. . 108
3.26 Processing time of two consecutive time steps in a six processor system without (left) and with (right) load-balancing algorithm [adopted from [10]]. 110
3.27 Workflow of the LB-geoVoF load-balancing algorithm. 114
3.28 Cumulative computational speedup over the integral volumetric fuel conversion in the industrial-scale RUT facility (30 vol.-% H_2 in air). 117
3.29 Computational speedup of fuel conversion increments in the industrial-scale RUT facility (30 vol.-% H_2 in air). 118

4.1 GraVent explosion channel including the positing of pressure transducers (green), photodiodes (red) and spark plug ignition location (yellow) [adopted from [11]]. 123
4.2 Impact of the *rloess* method's span coefficient on the resulting flame velocity profile of the simulations. 125
4.3 Flame tip velocities of varied fuel compositions and fuel contents in the GraVent explosion channel for the geometry configuration BR30S100. 127
4.4 Variation of obstruction BR and obstacle spacing S in a 22.5 vol.-% fuel in air mixture (75/25 H_2/CO). 131
4.5 Gradient formation in the GraVent facility's explosion channel [adopted from [11]]. 132
4.6 Flame tip velocities of homogeneous and inhomogeneous 75/25 H_2/CO fuel-air mixture for BR30S100 and BR60S300 obstacle configurations (waiting time 3s). 134
4.7 Mesh geometry of the A1-vessel explosion channel, including an additional meshed box below the channel. Open surfaces with an assigned *waveTransmissive* boundary condition are colored yellow (different grades of yellow only for a better 3D perspective).137

4.8 Time sequence of a 2D pressure contour of a generic 3D simulation with *waveTransmissive* BC on the bottom. 138
4.9 Simulated flame tip velocity profiles of homogeneous 50/50, 75/25 and 100/0 H_2/CO fuels compared to experimental data for the minimum fuel content necessary for DDT. 140
4.10 Simulated and measured flame tip velocity profiles from fuel concentration gradients with the maximum fuel content of $x_{f,max} = 22$ vol.-% and of $x_{f,max} = 27$ vol.-% (75/25 H_2/CO). 142
4.11 2D contour plots of fuel mole fraction and pressure of a fast deflagration in an inhomogeneous 75/25 H_2/CO mixture with maximum fuel fraction $x_{f,max} = 27$ vol.-% including a flame front iso-surface with $c = 0.5$ highlighted in magenta. 144
4.12 Time sequence of 2D pressure contour plots during DDT and detonation propagation in an inhomogeneous 75/25 H_2/CO mixture with maximum fuel fraction $x_{f,max} = 27$ vol.-% including a flame front iso-surface with $c = 0.5$ highlighted in magenta. . . . 145

C.1 Continuous interface with mean cell values of α (left) and interface reconstruction with SLIC (middle) and PLIC method (right) [adopted from [12]]. 187
C.2 Stencil for computing α at face center fc of face f in the NAG gradient scheme [adopted from [13]]. 189
C.3 Truncation of the cell by an interface plane (colored dark orange) with orientation $\boldsymbol{n}$. The truncated volume is colored. Intersection points are marked as × [adopted from [4]]. 190
C.4 Truncation of the right-hand face's flux polyhedron (dotted lines) by an interface plane (colored orange) with orientation $\boldsymbol{n}$ [adopted from [13]]. 194
C.5 Work flow of the load balancing algorithm in the LB-geoVoF method. 200
C.6 *Simple* mesh decomposition of general cubic mesh with an additional projection of the ignition kernel on the cube surfaces (pink circles). 204
C.7 Computational speedup (left) and scaling (right) of the LB algorithm in a generic deflagration simulation. 205

D.1 Schematic of the boundary pressure evaluation of the *wave-Transmissive* BC. 209

List of Tables

3.1 Criteria expressions for the three different flow features of interest for AMR execution. 106
3.2 Fraction of the overall computation time consumed by the geoVoF method in a generic large-scale simulation with varying degrees of parallelization. 109

4.1 Turbulent Reynolds numbers and turbulent length scales used for turbulence initiation. 122

A.1 Sutherland coefficients for the H_2-CO-air reaction system. 178
A.2 Schmidt numbers Sc_k of species k in the H_2-CO-air reaction system according to Li et al. [14] at reference conditions. 179

C.1 Computational speedup and scaling values of the LB algorithm with increasing parallelization. 205

Nomenclature

Latin Letters

A	$[\mathrm{m}^2]$	Area
A	$[-]$	Empirical correlation constant
a	$[\mathrm{m}]$	Thermal diffusivity
a	$[\mathrm{m/s}]$	Speed of sound
B	$[-]$	Empirical correlation constant
B	$[-]$	Trigonometric scaling coefficient
c	$[-]$	Reaction progress variable
c	$[\mathrm{J/(kg\,K)}]$	Specific heat capacity
D	$[\mathrm{m}^2/\mathrm{s}^2]$	Mass diffusion coefficient
D	$[\mathrm{m/s}]$	Detonation velocity
d	$[\mathrm{m}]$	Diameter
e	$[\mathrm{J/kg}]$	Internal energy
f	$[-]$	Mixture fraction
G	$[-]$	Quenching factor
G	$[1/\mathrm{s}]$	Flame wrinkling generation rate
g	$[1/\mathrm{s}]$	Velocity gradient
g	$[\mathrm{m/s}^2]$	Gravitational acceleration
h	$[\mathrm{J/kg}]$	Enthalpy
h	$[\mathrm{m}]$	Layer thickness
K	$[-]$	Channel characteristic constant
k	$[\mathrm{m}^2/\mathrm{s}^2]$	Turbulent kinetic energy
l	$[\mathrm{m}]$	Dimensional length
L	$[-]$	Total number of send tasks

m	[−]	Power-law exponent of pressure dependency
N	[−]	Total count
n	[−]	Power-law exponent of temperature dependency
n	[−]	Running variable
P	[−]	Physical number of processors
p	$[\mathrm{N/m^2}]$	Pressure
q	$[\mathrm{J/kg}]$	Heat release
Q	[−]	Non-dimensional heat coefficient
R	[J/(mol K)]	Ideal gas constant
R	[1/s]	Flame wrinkling removal rate
R	[−]	Total number of received tasks
S	[m/s]	Flame Speed
s	[m]	Obstacle spacing
T	[K]	Temperature
t	[s]	Time
u	[m/s]	Velocity
V	$[\mathrm{m^3}]$	Volume
W	[−]	Computational work load
w	[−]	Weighing factor
x	[m]	Cartesian coordinate direction
x	[m]	cell width
x	[−]	Mole fraction
Y	[−]	Mass fraction
y	[−]	Vertical position

Greek Letters

α	[−]	Burnt volume fraction
β	[−]	Volume fraction on the cell surface
Δ	[−]	Difference
δ_{ij}	[−]	Kronecker delta
δ	[−]	Coefficient of additional communication load

ϵ	$[m^2/s^3]$	Dissipation rate
θ	$[-]$	Detonation criterion
κ	$[-]$	Isentropic coefficient
λ	$[m]$	Detonation cell size
μ	$[kg/(m\,s)]$	Molecular dynamic viscosity
ν	$[m^2/s]$	Kinematic viscosity
Ξ	$[-]$	Flame wrinkling term
ρ	$[kg/m^3]$	Density
σ	$[-]$	Expansion ratio
σ	$[-]$	Turbulent length scale ratio
τ	$[s]$	Time scale
τ	$[kg/(s^2m)]$	Shear stress tensor
τ	$[-]$	Non-dimensional ignition delay time
Φ	$[-]$	Normalized equivalence Ratio
ϕ	$[-]$	Equivalence Ratio
ϕ	$[-]$	Scalar variable
Ψ	$[1/s]$	Scalar flame wrinkling flux
ω	$[1/s]$	Specific dissipation rate
$\dot{\omega}$	$[W/m^3]$	Volume specific source term

Subscripts

0	Standard reference conditions
0	Initial state
1	pre-combustion/post-shock state
2	post-combustion state
δ	Reaction zone
η	Kolmogorov scale
Ξ	flame wrinkling
Ω	Entire domain
$\perp$	Macroscopic orthogonally projected
acc	Acoustic

aicc	Adiabatic isochoric complete combustion
air	Air
avg	Average
b	Burnt
bl	Blockage
C	Carbon monoxide
CJ	Chapman-Jouguet
c	Cell
c	Fuel consumption
calc	Calculation
cell	Cell related
comp	Composition
cr	Critical
def	Deflagration
det	Detonation
eff	Effective
eq	Equilibrium
exo	Exothermic
f	Fuel
fn	Face neighbors
g	Gas cloud
H	Hydrogen
h	hydraulic
i	Cartesian coordinate direction
ign	Ignition
inf	Far-field
j	Describing the sum
k	Species index
LFL	Lean flammability limit
L	Laminar
lim	Limit
M	Mixture
m	Mass specific
max	Maximum

opt	Optimal
p	Isobaric
p	Processor
pr	Combustion products
RFL	Rich flammability limit
RMS	Root mean square
re	Reactants
ref	Reference
S	Sutherland
t	Total
T	Turbulent
t	Time
u	Unburnt/Non-reacting
v	Isochoric
vN	von-Neumann
vol	Volumetric
w	Waiting
wave	Wave

Superscripts

$\dot{()}$	First derivative, i.e. flux/source
$\overline{()}$	Ensemble-averaged mean value
$\widetilde{()}$	Favre-averaged mean value
$()^0$	unstretched
$()^*$	stretched
$()'$	Ensemble-averaged fluctuation
$()''$	Favre-averaged fluctuation
$()^f$	Formation
$()^{\mathrm{LB}}$	Load-balanced
$()^{\mathrm{NLB}}$	Non-load-balanced
$()^s$	Sensible

$()^t$	Time step

Non-dimensional Numbers

Co	Courant-Friedrich-Lewy number / Courant number
Da	Damköhler number
Ka	Kalowitz number
Le	Lewis number
Ma	Mach number
Pr	Prandtl number
Re	Reynolds number
Sc	Schmidt number

Abbreviations

1D	One-dimensional
2D	Two-dimensional
3D	Three-dimensional
AMR	Adaptive mesh refinement
BC	Boundary condition
CO	Carbon monoxide
CEA	Atomic Energy and Alternative Energies Commission
CFD	Computational fluid dynamics
CFL	Courant-Friedrich-Lewy
CJ	Chapman-Jouguet
DDT	Deflagration-to-detonation transition
DNS	Direct numerical simulation
EPR	European Pressurized Reactor
PWR	Pressurized water reactor
FA	Flame acceleration

FVM	Finite volume method
FZK	Forschungszentrum Karlsruhe
geoVoF	geometrical Volume-of-Fluid
H_2	Hydrogen
HLLC	Harten-Lax-van Leer with contact
HPC	High performance cluster
IRSN	Radiological Protection and Nuclear Safety
KH	Kelvin-Helmholtz
KIT	Karlsruher Institute of Technology
LB	Load-balancing
LD	Landau-Darrieus
LES	Large-eddy simulation
OpenFOAM	Open Field Operation and Manipulation
MCCI	Molten-corium-concrete-interaction
N_2	Nitrogen
NAG	Node-averaged Gaussian
NASA	National Aeronautics and Space Administration
NIST	National Institute of Standards and Technology
NPP	Nuclear power plant
O_2	Oxygen
PAR	Passive auto-catalytic recombiner
PISO	Pressure implicit with splitting of operators
RM	Richtmyer-Meshkov
SIMPLE	Semi-implicit method for pressure linked equations
SLM	Shape-Language Modeling
SWACER	Shock wave amplification by coherent energy release
TD	Thermo-diffusive
TFC	Turbulent flame speed closure
TUM	Technical University of Munich
URANS	Unsteady Reynolds-averaged Navier-Stokes
vN	von Neumann
WENO	Weighted essentially non-oscillatory
ZND	Zeldovich-von Neumann-Döring

1 Introduction

1.1 Motivation

Man-made climate change is the inevitable reality that current and future generations face. The increase in the global mean temperature has a severe impact on everyone's life. While rising water levels and droughts make certain regions of the planet uninhabitable, extreme weather conditions become more likely elsewhere. The goal of the Paris climate treaty, signed by more than 190 nations, is to limit the global temperature rise to 1.5 °C [15]. This effort's key aspect is reducing greenhouse gases in the atmosphere, which primarily consist of carbon dioxide, water vapor, methane, nitrogen oxides and ozone [16].

As the intermittent nature of renewable solar and wind energy demands suitable energy storage solutions, the power-to-gas concept positions hydrogen (H_2) from electrolysis as a promising carbon-free energy carrier [16]. In the same way, gas mixtures of hydrogen and carbon-monoxide (CO), commonly known as syngas [17], can be utilized as a low-carbon energy carrier. The variety of hydrogen and syngas applications in the transport, production, and power generation sectors reflects the gases' importance. The gases are alternative fuels in fuel cells and gas turbine engines. Additionally, they are the basis of synthesis routes in the chemical and process industries.

Apart from the intended presence of the gases, large amounts of H_2-CO are also encountered during severe nuclear light water reactor accidents. The oxidation of the fuel rod cladding forms hydrogen. Additionally, molten-corium-concrete-interaction (MCCI) [18] generates CO once the reactor pressure vessel fails and the molten core reaches the concrete below. The investigation of the Fukushima-Daiichi accident by Gauntt et al. [19] showed that several tones of CO can be generated by MCCI in addition to H_2 during a severe acci-

dent. Passive auto-catalytic recombiners (PAR) are a countermeasure, mitigating the formation of a combustible atmosphere. However, CO can poison the catalytic surface shutting the PARs' operation. As a consequence, unexpectedly high amounts of H_2 and CO can accumulate and form explosive mixtures in uninertized sections of the containment or auxiliary buildings [20, 21]. Especially, the lighter H_2 tends to form a stratified fuel-air distribution under the building's ceiling.

Highly reactive gases pose an explosion hazard independent of the technical application or its occurrence. This is especially true for gases with ignition energies as low as H_2. Unintentional ignition of a combustible fuel-air mixture can lead to an explosion, which might significantly damage equipment, personnel, and environment [22–24]. Pressure evolution and flame velocity are directly coupled in explosions. In the worst-case scenario, flame acceleration allows for a transition from fast deflagration to detonation. Maximum pressure peaks can be expected at the deflagration-to-detonation transition (DDT) location, eventually causing the confining structure to fail. The mild deflagration at the Three Mile Island NPP in Harrisburg (1979 USA) [25] and the destructive detonations in the more recently Fukushima-Daiichi accident (2011 Japan) [19] demonstrated the potential hazard. From a global perspective, the importance of explosion risk assessment for nuclear power plants (NPPs) remains high because several new reactors are currently planned or constructed worldwide [26].

Risk assessment of fast deflagrations and detonations is mandatory in every application of highly reactive syngas (H_2-CO) [27–30]. Direct initialization of a detonation is unlikely in accident scenarios. Therefore, the explosion risk analysis has to focus on weak ignitions with subsequent flame acceleration, DDT, and detonation propagation. The need for an application-oriented risk assessment of H_2-air and H_2-CO-air mixtures is backed up by the increasingly important role of these gases in the upcoming energy transition.

1.2 Challenges for Explosion Risk Assessment

Following weak ignition, the expansion of burnt gas behind the flame front induces a flow ahead of the flame, similar to a moving piston. Hydrodynamic and thermo-diffusive intrinsic flame instabilities have the potential to force a cellular flame structure, which increases the flame surface. Consequently, the integral heat release rises, amplifying the pushing effect. The induced flow ahead of the flame generates turbulence in boundary layers or shear layers of obstacles in the flame path. As turbulent mixing increases fuel consumption, the flame emits stronger pressure waves due to its more rapid expansion. The waves, in turn, induce a faster flow ahead of the flame. Hence, a self-exciting feedback loop of the expanding flame causes continuous flame acceleration (FA). The emitted pressure waves precondition the fresh gas by compression until auto-ignition events occur, and a spontaneous wave eventually triggers DDT.

Two characteristic changes in the combustion regime can be identified during this process. The transition from slow to fast deflagration due to FA is the first. The regime of fast flames starts at a flame velocity close to the speed of sound of the reactants. If FA is sufficiently strong, a fast flame can reach the speed of sound of the combustion products. Corresponding flames allow for sufficiently strong fresh gas preconditioning able to trigger DDT. The onset of DDT represents the second characteristic change in the combustion regime.

Empirical criteria, which indicate possible FA and DDT, have been derived from small- and large-scale experiments for risk assessment purposes [5, 31, 32].

- Flame acceleration: σ-criterion
- DDT: λ-criterion

The FA criterion is based on the expansion ratio σ and the DDT criterion on the detonation cell size λ. Because DDT is a highly stochastic phenomenon, the λ-criterion only describes the potential for transition. Both criteria are dependent on the mixture reactivity and the confining geometry. Therefore, the

criteria are derived for fully- and semi-confined geometries separately [33–36]. Applying the criteria is not always unambiguous since their evaluation requires a characteristic geometric length. Overall, the empirical criteria lack generality. The complex interactions of combustion, gas-dynamic effects and geometrical confinement in accident scenarios cannot be expressed in simplified empirical criteria.

Computational fluid dynamics (CFD) simulations are viable for three-dimensional (3D) safety analysis of combustion phenomena. Its flexible applicability to different geometries is advantageous compared to the empirical criteria. With reactor safety research as a driving force [37], research institutes and companies developed CFD codes for transient H_2-air deflagration and detonation.

Using the unsteady Reynolds-averaged Navier-Stokes (URANS) equations in combination with an under-resolved computation mesh guarantees reasonable computation times on an industrial scale. Large-eddy simulations (LES) and direct numerical simulations (DNS) are unsuitable due to their much finer mesh resolutions requirement. URANS equations only determine mean flow variables and turbulence influences must be modeled. In comparison, the LES resolves a defined range of turbulent structures, and the DNS resolves all turbulent structures.

Deflagrations and detonations are typically calculated with different modeling strategies. Commonly, separate CFD codes consider each regime without representing the DDT phenomenon. The switch between deflagration and detonation CFD codes is often based on the described empirical λ-criterion. An exemplary CFD-based risk analysis in a light water reactor has been presented by Dimmelmeier et al. [38]. Not considering the influence of the fresh gas preconditioning by FA in the detonation simulation after switching codes neglects potential risk factors. Likewise, the peak pressures during DDT are not accounted for in the risk analysis.

Ettner [8] and Hasslberger [4] developed an OpenFOAM (*Open Field Operation and Manipulation*) based H_2-air explosion simulation framework, which applies to small and industrial scales. A single continuous simulation consid-

ers flame acceleration to fast flames, subsequent DDT, and stable detonation propagation. In this method, the transient evolution of the propagating flame and the associated fresh gas compression by flame-generated pressure waves determine the onset of DDT. A suitable description of the local interaction of the reaction front and the pressure wave enables DDT in the simulation.

The thesis aims to introduce an efficient multi-scale CFD framework for DDT risk assessment of stratified H_2-CO-air mixtures, which is applicable to realistic accident scenarios. The solver development builds on the previous work of Ettner and Hasslberger. The transient flame propagation in the confining structure, the DDT location and the corresponding pressure loads from detonations represent the key validation parameters for the CFD solver with a risk assessment purpose. The challenges for the solver development of the H_2-CO-air explosion risk assessment solver summarize as follows:

- Combustion modeling of deflagration, DDT and detonation for all initial H_2-CO-air compositions.
- Consideration of inhomogeneous fuel distributions in the computational domain.
- Applicability to all dimensional scales.
- Consideration of semi-confined geometries to extend the applicability of the CFD code to more realistic scenarios.
- Improvement of the computational efficiency for parameter studies in risk analysis.

1.3 Outline of the Thesis

In the following, the structure of the thesis is presented. Chapter 2 explains the fundamental background of explosions. Stable detonations are simplified based on the relations of one-dimensional (1D) steady-state reaction fronts. FA and DDT are explained on a phenomenological basis. Section 3.1 provides an overview of existing CFD codes for explosion risk assessment and their

modeling approaches. Section 3.2 introduces the governing equations of compressible flow and the handling of fuel inhomogeneity in the domain. Section 3.3 describes the reaction-progress-based flame-propagation transport equation for small-scale applications and the flame front tracking approach with the geometrical Volume-of-Fluid (geoVoF) method for large-scale scenarios. Deflagrations and detonations require individual source-term models in the flame-propagation transport equation. The source term models are introduced with respect to H_2-CO-air mixtures. Methods to provide necessary variables for the source term models are presented. They cover all possible compositions of H_2-CO-air mixtures. The phenomenon of turbulent flame quenching is discussed in the section. The volumetric heat release function of the detonation source term uses a mixture and cell-size-dependent scaling of the source term in order to preserve correct detonation velocities on all mesh sizes. Section 3.4 presents efficiency-related solver features. Additionally to the adaptive mesh refinement previously implemented by Hasslberger [4], a load-balancing algorithm for the geoVoF method is introduced. It significantly reduces the computation time of large-scale explosion simulations.

Chapter 4 covers the DDT solver validation with experiments at the small-scale GraVent facility and at the large-scale semi-confined A1-vessel. Temporal flame position data and the location of DDT are the key validation parameters. Fuel contents, fuel compositions, obstacle configurations and vertical concentration gradients are varied in both geometries to achieve a broad validation basis. Finally, Chapter 5 summarizes the accomplished developments and the outcome of the validation simulations. An outlook on further developments is provided.

2 Explosion Fundamentals

Explosions are transient propagating flames accompanied by a noticeable pressure increase. Deflagrations and detonations are considered explosions but differ in flame velocity and pressure loads. The following chapter provides the theoretical background on the deflagration and the detonation combustion regimes, as well as the transition mechanism leading from deflagration to detonation. The description is held brief and focuses on phenomena relevant to H_2-CO-air flames. A more detailed explanation can be found in extensive literature such as Ciccarelli and Dorofeev [5], Bartlmä [39] and Lee [40].

2.1 Gas-Dynamic Relation of Combustion Waves

Regardless of the three-dimensional (3D) structure of turbulent flames and detonations [40,41], a one-dimensional (1D) abstraction is well-suited for understanding the influence of a heat source, i.e., a reaction front, on the flow field. 1D models are viable if changes perpendicular to the flow direction are small compared to the changes in longitudinal direction and influences of boundaries are far away from the considered control volume. The fundamental behavior of the flow field during flame acceleration (FA) can be investigated by means of a 1D model, as illustrated by Figure 2.1 [5].

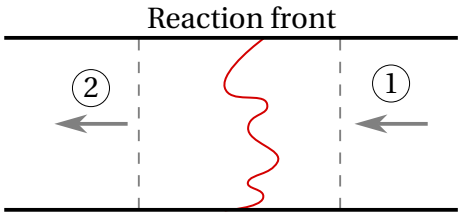

Figure 2.1: One-dimensional control volume of a stationary reaction front.

A steady-state, adiabatic, inviscid and compressible flow field with a discontinuous reaction front as the heat source is considered. The coordinate system is moving in reference to the reaction front. Hence, the reaction front is stationary, and the inflow corresponds to the reaction front's velocity. 1D steady-state equations of mass, momentum and energy conservation are according to Equations 2.1 to 2.3. Index 1 refers to the reactant side and Index 2 to the product side [39].

$$\rho_1 u_1 = \rho_2 u_2 \tag{2.1}$$

$$p_1 + \rho_1 u_1^2 = p_2 + \rho_2 u_2^2 \tag{2.2}$$

$$h_1^{\mathrm{s}} + \frac{u_1^2}{2} + q_{12} = h_2^{\mathrm{s}} + \frac{u_2^2}{2} \tag{2.3}$$

In the set of equations, ρ refers to the density, u to the velocity and p to the pressure. According to Equation 2.4, the absolute specific enthalpy h consists of the heat of formation at standard reference conditions h_0^{f} and the sensible heat h^{s}. Chemical and thermodynamic equilibrium is assumed on the product side.

$$h = h_0^{\mathrm{f}} + h^{\mathrm{s}} = h_0^{\mathrm{f}} + c_p(T - T_{\mathrm{ref}}) \tag{2.4}$$

The specific heat release of the reaction q_{12} can be evaluated from the difference in the heat of formation or temperature according to Equation 2.5. Straightforward application of this relation is only possible if constant heat capacities c_p are assumed and changes in the kinetic energy are negligible.

$$q_{12} = h_{0,2}^{\mathrm{f}} - h_{0,1}^{\mathrm{f}} = c_p(T_2 - T_1) \tag{2.5}$$

Utilizing the ideal gas law ($p = \rho RT$) and the Mach number ($\mathrm{Ma} = u/\sqrt{\kappa RT}$), the Rayleigh line in Equation 2.6 can be derived by combining Equations 2.1 and 2.2. The initial state ρ_1, p_1 and the speed of the reaction front, represented by Ma_1, define the slope of the Rayleigh line:

$$\frac{p_2}{p_1} = 1 + \kappa \mathrm{Ma}_1^2 \left(1 - \frac{\rho_1}{\rho_2}\right). \tag{2.6}$$

The energy equation 2.3 is transformed into the Hugoniot curve 2.7 by eliminating the velocity. κ represents the ratio of isobaric and isochoric heat capacities $\kappa = c_p/c_v$. Additionally, the non-dimensional heat coefficient $Q =$

$q_{12}/(c_p T_1)$ is introduced.

$$\frac{p_2}{p_1} = \frac{\frac{\kappa+1}{\kappa-1} - \frac{\rho_1}{\rho_2} + \frac{2\kappa}{\kappa-1}Q}{\frac{\kappa+1}{\kappa-1}\frac{\rho_1}{\rho_2} - 1} \tag{2.7}$$

Possible Rayleigh lines (blue) and Hugoniot curves (red) are presented in the p-$(1/\rho)$ plot of Figure 2.2, which is named the Rankine-Hugoniot diagram. The initial flow state (p_1,ρ_1) denotes unity in the diagram. A possible solution to the equations 2.1 to 2.3 refers to the change from the initial state to the state behind the reaction front (p_2,ρ_2). The state (p_2,ρ_2) represents an intersection of a Rayleigh line and a Hugoniot curve in the diagram. Equation 2.6 demands a negative slope of $-\kappa \mathrm{Ma}_1^2$ for all Rayleigh lines. Therefore, no possible solution exists in the gray-shaded regions of the plot. Depending on Ma_1, a supersonic ($\mathrm{Ma}_1 > 1$) or a subsonic ($\mathrm{Ma}_1 < 1$) solution exists. If the reaction front is

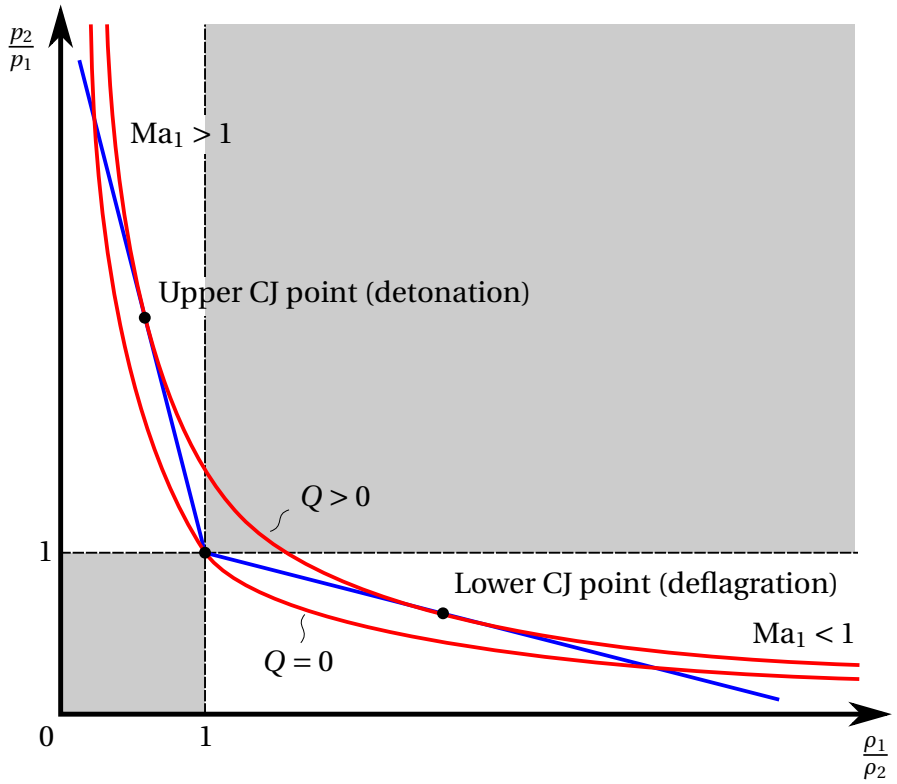

Figure 2.2: Rankine-Hugoniot diagram showing Hugoniot curves (red) and Rayleigh lines (blue) with upper and lower Chapman-Jouguet solution at CJ-condition $u_2 = a_2$.

considered a combustion wave, the subsonic branch (lower) resembles deflagrations and the supersonic branch (upper) detonations.

The Hugoniot curve without heat release ($Q = 0$) corresponds to a planar shock front, which causes a change of state without heat release. The curve of a reacting flow ($Q > 0$) has no intersection with the initial state at unity. The offset of the curve from the initial state increases with a higher non-dimensional heat input Q. The Hugoniot curve and Rayleigh line can have two points of intersection for each side in the diagram, deflagration and detonation regime. If the Rayleigh line is tangent to the Hugoniot curve, only a single intersection point remains, as illustrated in Figure 2.2. At this point, the Chapman-Jouguet (CJ) condition exists, in which the Ma number behind the reaction front becomes $\mathrm{Ma}_2 = 1$. In this condition, the state is thermally choked. The reaction front can propagate unaffected by any perturbations which travel at the local speed of sound. Hence, it is the only solution in the steady state.

When the CJ condition is met, only a single solution exists for each branch, deflagration and detonation. The Rankine-Hugoniot diagram 2.2 shows both single solutions. They are indicated as upper and lower CJ points. The reaction front speed under CJ condition can be evaluated with Equation 2.8 for a given heat release, i.e., a defined H_2-CO-air mixture [5]. The sign of the last term in the equation distinguishes the solution of the two branches:

$$\mathrm{Ma}_{1,\mathrm{CJ}} = \frac{u_1}{a_1} = \sqrt{1 + \frac{\kappa + 1}{2} Q} \pm \sqrt{\frac{\kappa + 1}{2} Q}. \tag{2.8}$$

Even though deflagrations can have slow velocities, the gas-dynamic-based relations describe the fundamental behavior of the flame acceleration during deflagration. Detonations on the supersonic branch appear as double discontinuities instead of a single reaction front. They consist of a planar shock and a reaction front. The solution for the change of state across the planar shock ($Q = 0$) is the intersection of the $Q = 0$ curve with the same Rayleigh line of the reaction front ($Q > 0$). If the Rayleigh line of the supersonic branch in Figure 2.2 has a stepper slope (higher inflow velocity), two intersection points would be present with the Hugoniot curve of the reaction front ($Q > 0$). In that case, only the upper intersection point is a possible solution for a detonation due to its double-discontinuity structure [39, 42]. However, this is no steady-

state solution because perturbations can interact with the inflow. Section 2.3 provides a more detailed look at the internal structure of detonations.

2.2 Deflagration and Flame Acceleration

The multi-species combustion reaction of H_2-CO-air mixtures is often simplified to a one-step overall reaction, which writes

$$H_2 + CO + O_2 \rightarrow CO_2 + H_2O. \tag{2.9}$$

CO_2 and H_2O are the main products of the reaction. If the intermediate species of the reaction system shall be considered, a detailed reaction mechanism is required [43]. In premixed combustion, reactants, i.e., fuel and oxidizer, are fully mixed before the reaction. The ratio of fuel and oxidizer determines whether one of the components is in excess according to the reaction in Equation 2.9. The reactants mixture is classified by the equivalence ratio ϕ as lean ($\phi < 1$), stoichiometric ($\phi = 1$) or rich mixture ($\phi > 1$). The equivalence ratio ϕ reads

$$\phi = \frac{x_{H_2} + x_{CO}}{2\, x_{O_2,\mathrm{air}}(1 - x_{H_2} - x_{CO})} \tag{2.10}$$

in a H_2-CO-air mixture. O_2 is the excess reactant in lean mixtures, while the fuel is the excess component in rich mixtures. In a H_2-CO-air mixtures, the equivalence ratio is usually expressed in terms of the mole fractions x_{H_2} of hydrogen and x_{CO} of carbon monoxide. $x_{O_2,\mathrm{air}}$ denotes to the mole fraction of oxygen (O_2) in atmospheric air. The mixture composition significantly impacts the deflagration and the hazards originating from the combustion process.

Deflagrations are associated with a moderate pressure drop across the flame front and a subsonic flame speed in the relative reference frame, as illustrated in the Rankine-Hugoniot diagram. Pressure perturbations originate from the expansion of the burnt gas behind the flame. They propagate into the fresh gas and induce a flow ahead of the flame. Consequently, the reaction front's velocity can reach supersonic speeds in the fixed reference frame [39, 44].

Following weak ignition, deflagration will precede the formation of a detonation. Typically, the flame will undergo self-generated acceleration, driven by turbulence-flame interaction and combustion instabilities. FA is decisive for conditioning the fresh gas sufficiently so that DDT occurs. The characteristics of laminar and turbulent premixed flames and combustion instabilities are discussed in the following sections.

2.2.1 Laminar Flame Characteristics

After weak ignition, deflagrations propagate as laminar flames. In premixed combustion, the mixing of fuel and oxidizer does not limit their reaction. Instead, the combustible mixture is heated until ignition and burned within a thin flame. The laminar flamelet can be distinguished in a preheat and a reaction zone. Figure 2.3 illustrates the laminar flamelet structure. The temperature rises significantly across the reaction zone.

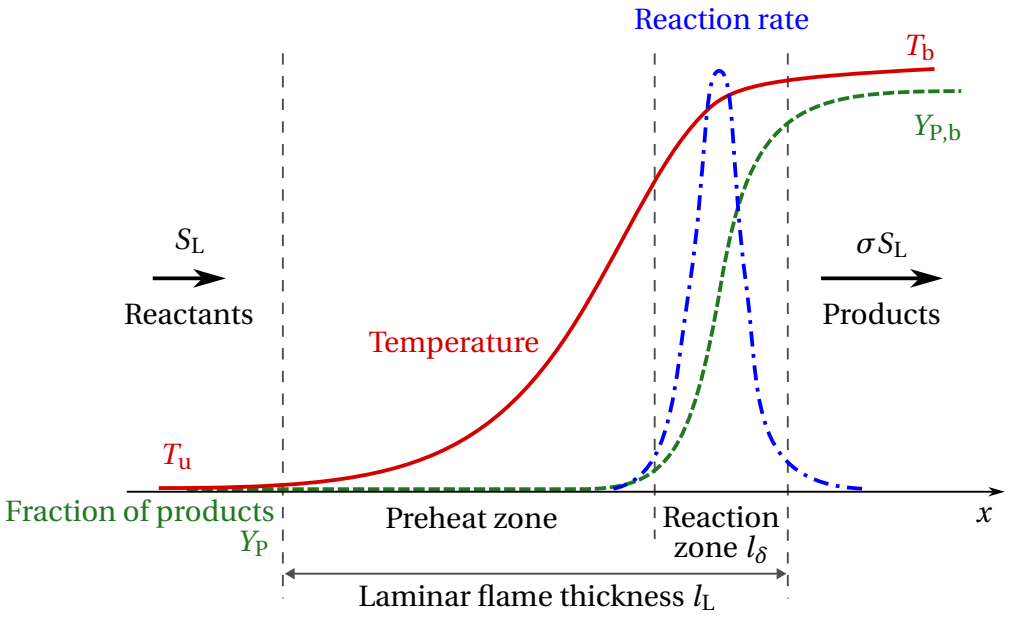

Figure 2.3: Schematic structure of a freely-propagating unstretched laminar flame.

The reaction progress variable expresses the conversion of reactants to products:

$$c = \frac{Y_\mathrm{P}}{Y_\mathrm{P,b}}. \tag{2.11}$$

It is the ratio of the local mass fraction of products Y_P and the fraction of products in the burnt gas $Y_\mathrm{P,b}$ [3]. The laminar flame thickness l_L, which includes the preheat and the heat release zone, reads

$$l_\mathrm{L} = \frac{a_\mathrm{u}}{S_\mathrm{L}}. \tag{2.12}$$

The expression uses the thermal diffusivity of the fresh gas a_u. The laminar flame speed S_L is the velocity of the fresh gas inflow approaching a stationary planar flame front [1, 3, 41]. In a freely-propagating 1D flame, depicted in Figure 2.3, S_L relates to the flow velocity anywhere in the fresh gas. It is the unstretched laminar flame speed. Due to a lower density of the burnt gas, the exhaust gas accelerates by the expansion ratio:

$$\sigma = \frac{\rho_\mathrm{u}}{\rho_\mathrm{b}}. \tag{2.13}$$

The flame front is subject to flame stretch in a multi-dimensional flow field. The two effects, flame strain and curvature, contribute to flame stretch. Both result in steeper gradients by reducing the flame thickness. The effect of flame stretch on the flame speed is ambiguous because heat and species transport is enhanced alike [1, 41]:

- Enhanced heat transport intensifies cooling of the flame and slows the flame down.
- Enhanced species transport leads to stronger fuel diffusion into the reaction zone, accelerating the flame.

The Lewis number indicates the predominant type of transport:

$$\mathrm{Le} = \frac{a_\mathrm{u}}{D}. \tag{2.14}$$

It is the ratio of thermal and molecular diffusion. The diffusion coefficient D is specified concerning the reaction limiting or deficient mixture component,

while the thermal diffusivity a_u is based on the unburnt mixture. The Lewis number of H_2-CO-air is dependent on the mixture composition. Figure 2.4 shows the dependency of flame speed on the flame stretch with respect to the Lewis number of the fuel-oxidizer mixture. The flame speed increases with the flame stretch in mixtures with Le < 1 due to enhanced fuel diffusion. In contrast, thermal diffusion dominates in mixtures with Le > 1 resulting in lower flame speeds with rising flame stretch. The flame can suddenly extinguish at very high stretching rates because the flame thickness becomes too thin. A sudden drop of flame speed at very high stretching rates can only be seen in mixtures with Le < 1. However, flame extinction due to flame stretch is present in all mixtures. Heat losses of the flame significantly reduce the critical stretch required for flame extinction [1].

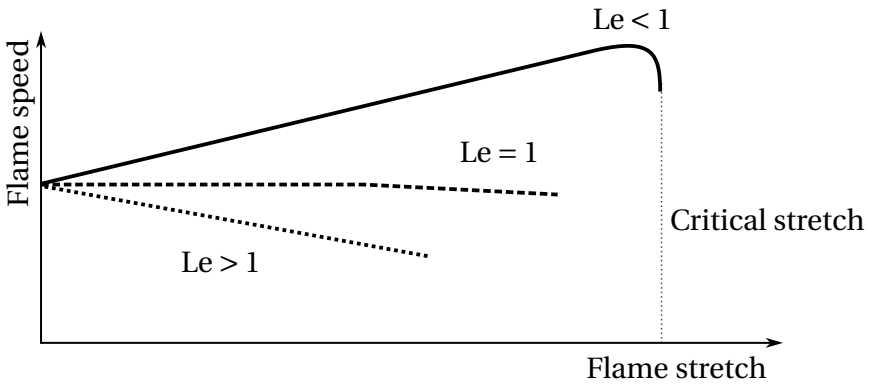

Figure 2.4: Influence of Lewis number on the flame-stretch dependency of an adiabatic laminar flame [adopted from [1]].

The laminar flame speed can be evaluated from 1D reaction kinetic simulations in the software Cantera [45]. The computation requires reaction kinetic information from a detailed reaction mechanism. Several reaction mechanisms exist for the H_2-CO-air reaction-system [14, 46–48]. While the unstretched laminar flame speed can be estimated directly from the inflow velocity in 1D simulations of freely-propagating flames, the simulation of lean mixtures close to the lower flammability limit is numerically challenging in this setup.

In the numerical setup of a 1D counterflow flame, a stagnation point exists in

the flow field in combination with a radial velocity component. Due to mass and momentum continuity, the axial velocity reduces with the distance from the burner. The flame is stationary at the location where flame speed and flow velocity are equal. In this setup, the numerical solution of lean premixed combustion is easier to accomplish. Figure 2.5 shows the setup of a counterflow flame in a fresh-to-fresh configuration, also called a twin-flame setup.

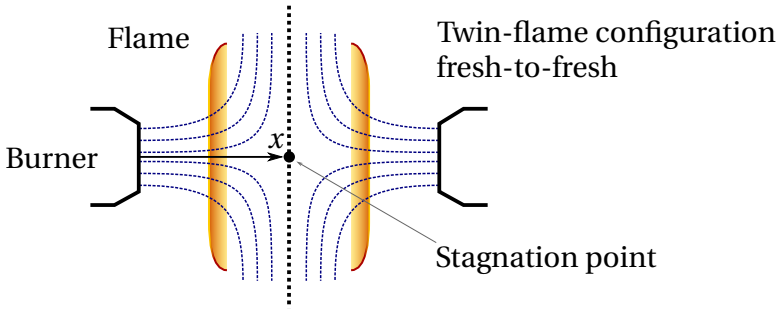

Figure 2.5: 1D twin-flame burner setup with stagnation-point flow for numerical evaluation of stretched laminar flame speeds.

In a twin-flame configuration, flow strain is present due to an axial velocity gradient. The left image of Figure 2.6 presents the axial flow velocity profile from the burner exit to the stagnation point (red dashed curve). It also displays the flow's local strain rate ahead of the flame's position (blue line). Because the stretched laminar flame speed S_L^* cannot be evaluated unambiguously in the changing velocity profile of a 1D counterflow flame, the use of the stretched fuel consumption speed $S_{L,c}^*$ is preferred. The stretched fuel consumption speed definition, shown in Figure 2.6, is unambiguous [1]. The unstretched fuel consumption speed at zero strain $S_{L,c}^0$ is extrapolated from stretched fuel consumption speeds at varying strain rates. The procedure is illustrated in the right image of Figure 2.6. The use of adaptive scaling for the 1D computational setup accelerates the repeated 1D simulations [49]. At zero stretch, the fuel consumption speed and the displacement speed have almost equal values. The fuel consumption speed does not account for the diffusion of burnt gas to fresh gas. In the context of the modeling strategy of the thesis, the difference between values from the two flame speed evaluations is small compared to the uncertainties associated with under-resolved CFD simula-

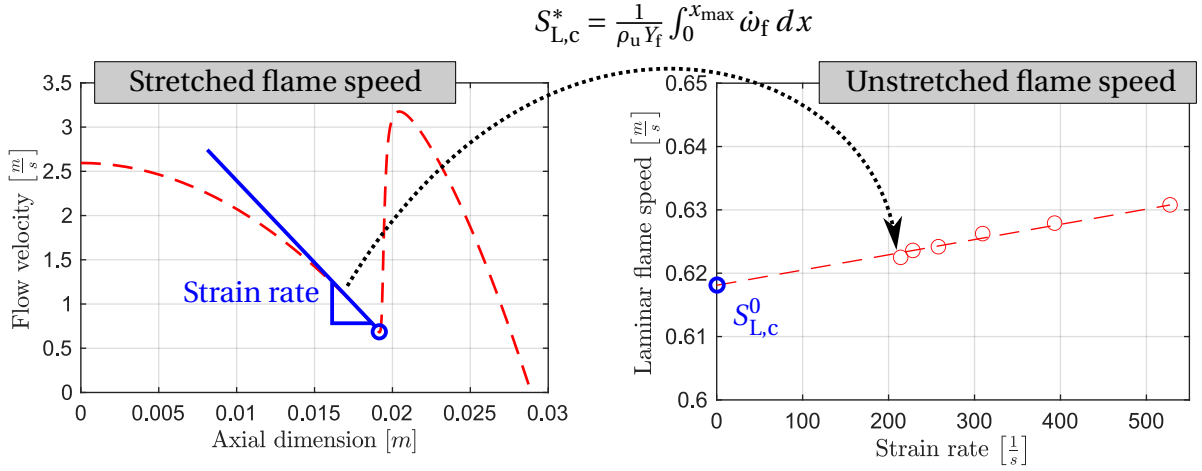

Figure 2.6: Evaluation of unstretched fuel consumption speed from stretched 1D twin-flame simulation data at standard reference condition (Plots from 20 % fuel in air - 75/25 H_2/CO).

tions. Therefore, the robust evaluation of fuel consumption speed is used for the required flame speed data of the combustion model.

The laminar flame speed can also be measured. Because the flame in the multi-dimensional flow of the experimental setup is always subject to flame stretch, the resulting data needs to be corrected for the flame-stretch influence with a similar evaluation procedure as presented in the numerical evaluation [50–52]. Mole-fraction-based correlations of the laminar flame speed at standard reference conditions are presented in the literature for H2-air [53] and H2-CO-air mixtures [54, 55]. If correlations are derived solely from experimental data, their validity is limited to the range of mixture compositions of the underlying database. Especially in the ternary mixture H2-CO-air, the small number of existing measurements poses a problem.

2.2.2 Turbulent Flame Characteristics

In premixed combustion, the turbulence-chemistry interaction intensifies the mixing of burnt and unburnt material on a molecular scale at the interface of small eddies. Thereby, the integral heat release of the turbulent flame grows.

The enhanced heat and mass transfer in turbulent combustion is the dominant contribution to the acceleration process in deflagrations.

Depending on the turbulence intensity, different combustion regimes can be classified. The laminar flame constitutes the basis for characterizing the turbulent premixed combustion regimes. From flame speed and flame thickness, a chemical or laminar time scale

$$\tau_{\mathrm{L}} = \frac{l_{\mathrm{L}}}{S_{\mathrm{L}}} \tag{2.15}$$

is defined. The reaction kinetics determine the laminar time scale τ_{L}. The ratio of inertia and friction forces in the flow indicates whether a turbulent flow is present. The non-dimensional Reynolds number

$$\mathrm{Re} = \frac{u\,l}{\nu}. \tag{2.16}$$

denotes this ratio. The product of velocity u and the geometrical dimension l, e.g., the tube diameter, represent the inertia forces. The kinematic viscosity ν denotes the internal shear friction. Laminar flow will likely transition into turbulent flow at a certain critical Reynolds number specific to the flow type. The turbulent flow has a chaotic and anisotropic nature. According to Reynolds [56], the intermittent velocity $u(t)$ in each dimension can be separated into a mean velocity $\overline{u}(t)$ and a fluctuation velocity $u'(t)$:

$$u(t) = \overline{u}(t) + u'(t). \tag{2.17}$$

Isotropic turbulence is assumed to characterize turbulent combustion regimes [1]. This assumption allows the evaluation of the velocity fluctuation from the turbulent kinetic energy k via $u' = \sqrt{2/3\,k}$. It should be mentioned that the intermittency of the flame locally influences u'. Hence, the root-mean-square (RMS) velocity of the free flow in some distance to the flame is used in many cases [1]:

$$\bar{u}' = u_{\mathrm{RMS}} = \sqrt{u'^2 + v'^2 + w'^2}. \tag{2.18}$$

The turbulence energy transfers along a cascade from large eddies on integral length scale l_{T} to the smallest eddies on Kolmogorov scale l_η, where the turbulent energy dissipates into internal energy. The energy is transferred with the

turbulent dissipation rate ε. Eddies contain turbulent kinetic energy dependent on their size. The eddies with the integral length scale hold the most energy. The interaction of the flow with the surrounding geometry forms them. Typically, a relation between l_T and a geometrical length exists, e.g., the mesh size in grids. The integral time scale

$$\tau_\mathrm{T} = \frac{l_\mathrm{T}}{u'} \tag{2.19}$$

is an estimate for the turnover time of large eddies at a certain level of turbulent kinetic energy. Because the Kolmogorov scale relates to the dissipation of kinetic energy into molecular motion, the Kolmogorov length scale

$$l_\eta = \left(\frac{\nu^3}{\varepsilon}\right)^{1/4} \tag{2.20}$$

and the Kolmogorov time scale

$$\tau_\eta = \left(\frac{\nu}{\varepsilon}\right)^{1/2} \tag{2.21}$$

both depend on the kinematic viscosity. The interpretation of the time scale τ_η is equivalent to the integral time scale τ_T. Flame-turbulence interaction can be classified using non-dimensional numbers derived from the previously defined length and time scales. Analogous to the Reynolds number in Equation 2.16, the turbulent Reynolds number

$$\mathrm{Re}_\mathrm{T} = \frac{u'\, l_\mathrm{T}}{\nu} \tag{2.22}$$

can be expressed using the velocity fluctuation u' and the integral length scale l_T. The Damköhler number is the ratio of turbulent and laminar time scales:

$$\mathrm{Da} = \frac{\tau_\mathrm{T}}{\tau_\mathrm{L}}. \tag{2.23}$$

The Kalowitz number is the ratio of laminar and Kolmogorov time scale:

$$\mathrm{Ka} = \frac{\tau_\mathrm{L}}{\tau_\eta}. \tag{2.24}$$

The laminar flame thickness l_L includes the flame preheat and heat release zone. A second Kalowitz number Ka_δ is specified based on the thickness of the

heat release zone of the laminar flame l_δ. For hydrocarbon and hydrogen fuels, the approximation of $l_\delta \approx 0.1\, l_\mathrm{L}$ is valid [3]. If the approximation is applied to the expression of the second Kalowitz number, it denotes

$$\mathrm{Ka}_\delta = \frac{\tau_\delta}{\tau_\eta} = \left(\frac{l_\delta}{l_\eta}\right)^2 \approx 0.01\mathrm{Ka}. \tag{2.25}$$

The two combustion regime diagrams of Borghi [2] and Peters [3] characterize combustion regimes during flame acceleration of deflagrations and self-ignition processes relevant to detonations. Peters exclusively considers a flamelet-like structure in all flame regimes, separating reactants and products. Borghi, however, includes a well-stirred regime without a visible flame front during the reaction. Figure 2.7 combines both diagrams and illustrates a trend line characteristic for flame acceleration. Concerning the effect of critically high flame stretch on the flame speed, the border of turbulent flame quench-

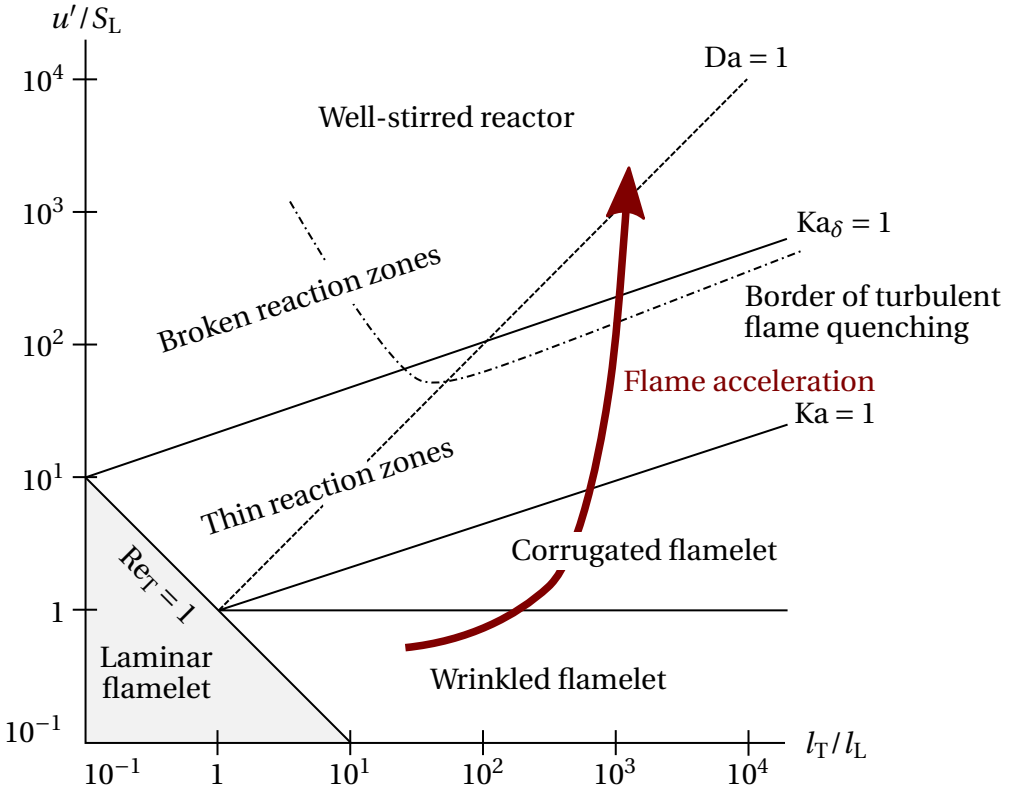

Figure 2.7: Flame regimes of turbulent premixed combustion based on Borghi [2] and Peters [3] [adopted from [4] and [5]].

ing is added in the diagram [1, 5].

As turbulence-chemistry interaction significantly increases the fuel consumption speed, its relevance to the transient FA process is obvious. However, turbulence can also cause flame extinction at extreme levels. Figure 2.8 illustrating the turbulent flame front supports understanding the combustion regimes. The combustion regimes presented in Figure 2.7 identify as:

- **Laminar flamelet:** For $\mathrm{Re_T} < 1$, the flame front remains laminar with its typical inner structure of preheat zone and heat release zone (see Section 2.2.1).
- **Wrinkled flamelet:** At low turbulence intensity, u' smaller than S_L, the burning speed is fast enough to counteract short-term flow fluctuations resulting in moderate wrinkling of the flame front.
- **Corrugated flamelet:** Once u' becomes larger than S_L, the continuous flame front corrugates because the flame's reaction rate does not damp aerodynamic deformations anymore. The laminar flamelet structure is maintained up to this turbulence intensity.
- **Thin reaction zones:** If $\mathrm{Ka} > 1$ holds, the smallest eddies (Kolmogorov eddies) penetrate the preheat zone of the flame structure. Larger eddies increase the macroscopic corrugation of the turbulent flame brush, while smaller eddies thicken the actual flame front, as depicted by Figure 2.8. The smallest eddies do not penetrate the heat release zone. Hence, temperature and species concentration profiles across the flame front maintain a quasi-laminar structure.
- **Broken reaction zones:** Once $\mathrm{Ka}_\delta > 1$ is reached, Kolmogorov eddies also enter the heat release zone, and the flamelet structure is broken up.
- **Border of turbulent flame quenching:** Intensive mixing of partially burnt gas in the heat release zone with cold reactants of the preheat zone potentially decreases the temperature below the ignition temperature and may result in local flame extinction. Corresponding mixing requires that the smallest eddies come close to the dimension of the heat

release zone. Poinsot et al. [57] introduced the limit for turbulent quenching using DNS simulations. The described flame extinction mechanism is flame-stretch-related. It is relevant to fast deflagrations, which have flame velocities equal to the speed of sound. Critical flame-stretch values for flame extinction are exceptionally high in mixtures with Le < 1, such as lean H_2-CO-air mixtures (see Section 2.2.1). Turbulent quenching has been discussed in the context of explosion scenarios in Reference [31]. In addition to stretch-related quenching, flames can also extinguish due to heat losses [58].

- **Well-stirred reactor:** The chemical reaction rate limits the fuel conversion, and turbulence has no further influence on the combustion rate. No reaction front is visible in this regime.

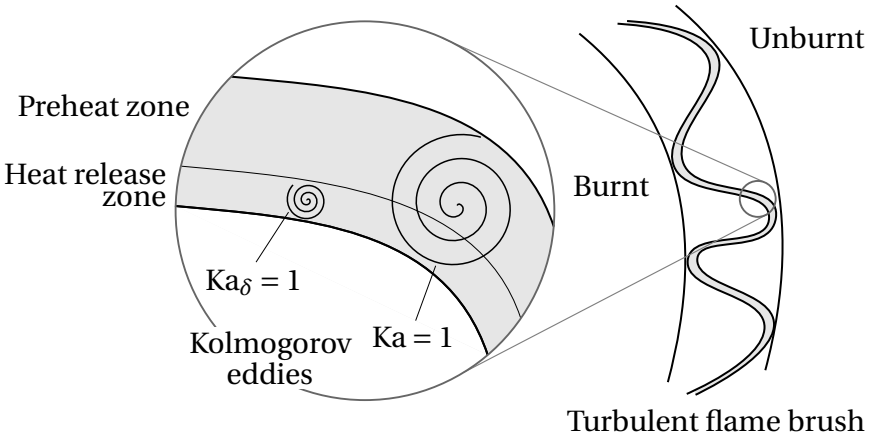

Figure 2.8: Illustration of turbulent eddies with the flame front [adopted from [6]].

The flame acceleration process refers to an upward trend towards the upper right corner in the combustion regime diagram of Figure 2.7 (red arrow). The reaction kinetics limit the fuel conversion in the auto-ignition dominated detonation. In contrast to Peters's flamelet-like combustion regime classification, the well-stirred reactor regime with Da < 1 introduced by Borghi allows the interpretation of the auto-ignition process in detonations. In the flamelet-like classification, turbulent quenching would occur instead of an auto-ignition reaction when turbulence continuously intensifies in a deflagration. Because drastically different combustion regimes characterize deflagra-

tions and detonations, the transition from a deflagration to a detonation can be interpreted as a sudden jump between the regimes.

2.2.3 Combustion Instabilities

In theory, planar reaction fronts become unstable when disturbed by any perturbation. In practice, diffusion effects stabilize the flame front to some extent resulting in a minimal perturbation wavelength or radius at which flame wrinkling begins [5]. Wrinkled flames have a larger surface, increasing the overall burning rate and accelerating the flame. In the following, the intrinsic instabilities of a flame front are listed:

- **Landau-Darrieus instability:** Hydrodynamic distortion amplification due to the expansion-related streamline congestion behind the flame front.
- **Thermo-diffusive instability:** Amplification or damping of distortion as a consequence of unequal heat and species diffusivity.

Besides intrinsic instabilities, external forces and effects can create combustion instabilities. The most important instabilities are:

- **Kevin-Helmholtz instability:** Shear-stress-related vortex evolution between two fluid layers at different velocities.
- **Taylor-Rayleigh instability:** Instability due to the nonparallel density gradient and gravitation vector direction. Typically present when a heavier fluid is on top of a lighter fluid.
- **Richtmyer-Meshkov instability:** Instability caused by the nonparallel density and pressure gradient direction. Interpretation as momentum-related Taylor-Rayleigh instability due to flow induction by the pressure gradient instead of gravitation. Different acceleration of burnt and unburnt gas when a shock wave passes a flame front in a non-orthogonal direction.

- **Accoustic instability:** Coherence between acoustic pressure perturbations and the flame's heat release. It is more relevant to slow flames in obstacle-free environments.

Figure 2.9 schematically illustrates the evolution of Landau-Darrieus (LD) and thermo-diffusive (TD) flame instabilities. The left image shows that streamlines diverge close to a curved flame front. Continuity demands a reduced flow velocity in the unburnt gas in front of the flame. First, the convex flame section pushes further into the unburnt gas because the laminar flame speed remains unchanged. Second, the flow acceleration due to the thermal expansion leads to a convergence of the streamlines behind the flame front. Both effects amplify the distortion of the curved flame front over time. The LD instability is omnipresent and independent of the mixture composition.

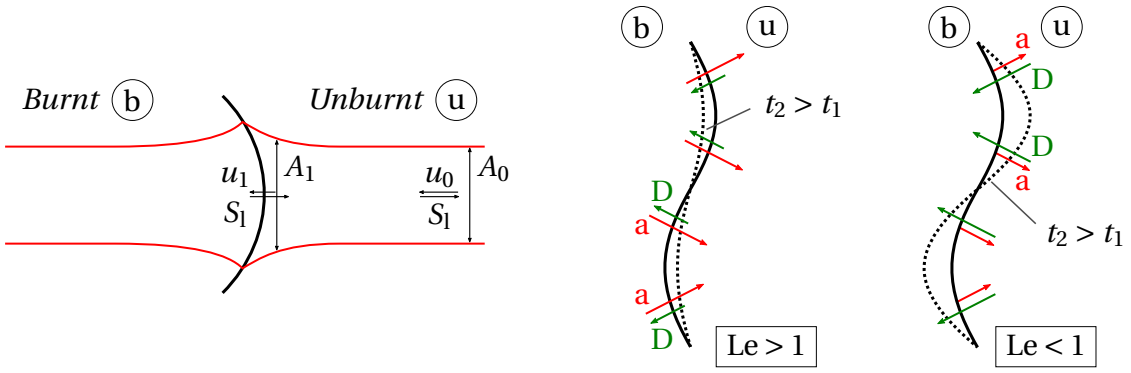

Figure 2.9: Schematic of Landau-Darrieus (LD) instability (left) and thermo-diffusive (TD) instability (right). The dashed flame shape demonstrates TD instability evolution between time steps t_1 and t_2 [adopted from [5, 7]].

Depending on the Lewis number, a weakly wrinkled flame front is either damped or amplified by the TD instability. At Le > 1, the thermal diffusion exceeds the species diffusion. Preheating in the concave flame section is intensified, resulting in a faster burning rate. At the same time, the dominating heat transport cools down the hot product side in the convex flame section because heat is distributed to a larger surface. As a consequence, the perturbations are damped. In reverse, the flame displacement is amplified when Le < 1. In convex flame sections, intensified diffusion of the deficient reactant into

the flame bulge amplifies the burning rate. Diffusion of the deficient species into a larger area on concave sections decreases hot side temperature due to a more distributed reaction.

Both intrinsic flame instabilities can be present at the same time. The TD effect can enhance or counteract the LD influence. Therefore, the onset of cellular flame structures is often characterized by a critical radius [59]. The critical radius of mixtures with Le < 1, e.g., 15 vol.-% H_2/CO in air, is significantly smaller than for a mixture with Le ≥ 1, e.g., stoichiometric H_2-CO-air. Separating the LD and TD influence is hardly possible in experiments [60]. Some combustion models account for the effect of flame instabilities by including terms based on the Lewis number or the flame radius [7, 61, 62]. The onset of cellular flame structures will occur at smaller critical radii with increasing pressure [63, 64]. The reduction of flame thickness with increasing pressures causes the noticeable pressure dependency of the flame instabilities.

Richtmyer-Meshkov (RM) instabilities [65, 66] can contribute to a high DDT probability. RM instabilities will only be relevant once fast flames are present because required strong pressure waves originate from a rapid flame acceleration. The combined effect of pressure rise due to the shock front and intensified flame front wrinkling due to instabilities promotes the transition [67–69].

2.2.4 Flame Acceleration

If a flame front's burning rate, i.e., the propagation speed, changes in time, a pressure wave will be emitted from the flame front, adjusting the flow velocity accordingly. Consequently, rapid flame acceleration can result in the formation of strong pressure waves ahead of the flame. They have the potential to damage the confining geometry. The formation of fast deflagrations has to be understood to design a CFD-based explosion risk analysis. Detailed descriptions of the mechanism of flame acceleration are presented in References [5, 40]. Because direct initialization of DDT is unlikely in accidents, flame acceleration following weak ignition is discussed exclusively.

Figure 2.10 demonstrates the flame acceleration. After ignition, a quasi-

laminar flame propagates spherically away from the ignition source (image A). Geometrical confinement will distort the spherical flame shape once the flame comes close to the walls. Once the critical radius described in the previous subsection is reached, a cellular flame structure forms. It significantly increases the flame surface. A pronounced cellular flame structure will only be present for mixtures with a small critical radius. The effects of flame stretch by curvature, LD and TD instabilities determine the critical radius [7]. The integral heat release of the flame rises with the increase in flame surface area. The expansion of hot combustion products induces a flow in the fresh gas. The information of a faster flame front is transported to the fresh gas by small pressure perturbations, similar to an accelerating piston [70]. Hence, the pressure rises. A boundary layer forms in the fresh gas flow (image B). The flame becomes finger-shaped. It has an increased flame surface due to the different flow velocities in the bulk flow and the boundary layer.

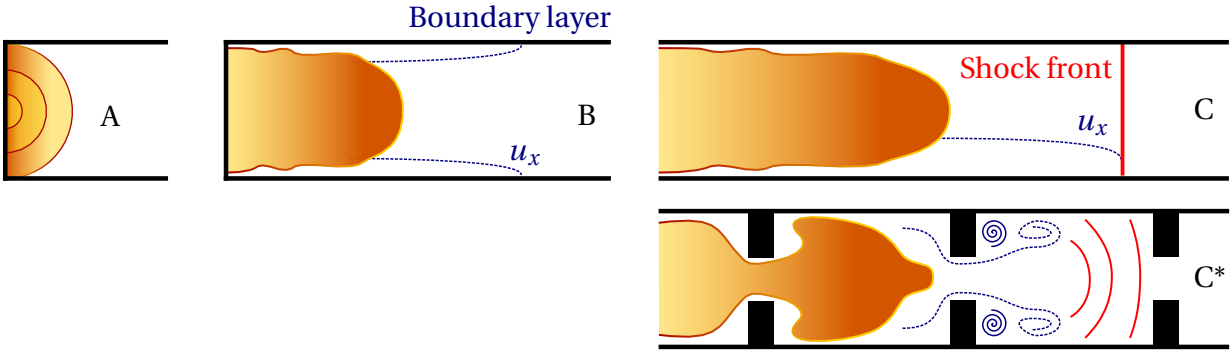

Figure 2.10: Transient evolution of flame acceleration in obstructed and unobstructed channels.

Turbulence generated in the shear flow of the boundary layer enhances the burning rate significantly. Consequently, stronger pressure perturbations are emitted from the flame front, increasing pressure, temperature and velocity in the fresh gas flow. In turn, the turbulence production rises again, creating a feedback loop capable of continuously accelerating the flame. With increasing temperatures in the fresh gas, each perturbation propagates faster than the previous one. Over time the emitted pressure waves accumulate and develop a shock front (image C). Once the flame is faster than the speed of sound, the wall's no-slip condition no longer influences the flame tip [5], and the flow

velocity in the combustion products begins to rise. The flame accelerates until the flow velocity in a relative coordinate system moved with the flame front chokes at Ma = 1 in the combustion products. The choked condition relates to the speed of sound of combustion products a_{pr}. The observed flame velocity for a fixed observer is also close to a_{pr} at this stage [71]. The choked flame can generate a shock front with an overpressure up to 10 bar. In fast deflagrations propagating through smooth tubes, an intermittent "tulip" flame shape has frequently been observed [72].

In contrast to smooth tubes, the obstruction of the flame path by obstacles causes a more rapid higher flame acceleration for several reasons (image C* of Figure 2.10):

- The deflection of streamlines around obstacles increases the flame surface compared to a finger-shaped flame.
- Steep velocity gradients in the shear layers behind obstacles intensify turbulence production.
- Shock reflection at obstacles promotes Richtmyer-Meshkov instabilities.

Experimental studies [5, 73] display images of accelerating flames in obstructed channels. Investigating flame acceleration due to obstacles with small blockage ratios (≈ 3%) like the Shchelkin spiral [74] showed that FA to fast deflagrations can be reached in any fully confined geometry as long as turbulence production is strong enough for the available channel length.

A flame is considered a fast deflagration once the observed propagation speed reaches the speed of sound of the reactants a_{re}. The observed propagation speed comprises the flame speed S and the unburnt gas velocity u_1. The possibility of acceleration to a fast deflagration is commonly characterized by the empirical σ-criterion in Equation 2.26 [31]. The ratio of unburnt ρ_{u} to burnt density ρ_{b} gives the expansion ratio σ. Fast deflagrations can be expected once the critical expansion ratio $\sigma_{\mathrm{cr},0}$ is exceeded. The criterion was derived for symmetrical flames and flames propagating in a duct from a closed end. In fully confined spaces, the criterion is equally valid for obstructed and unobstructed duct geometries. For homogeneous H_2-air flames $\sigma_{\mathrm{cr},0} = 3.75$ has

been determined [31]:

$$\sigma = \frac{\rho_\mathrm{u}}{\rho_\mathrm{b}} > \sigma_{\mathrm{cr},0}. \tag{2.26}$$

The criterion is a necessary but insufficient characteristic to reach a fast deflagration since the channel may be too short for the transition. Because the presented σ-criterion only relies on fluid properties, it does not consider geometry-related influences on the acceleration process, like venting or stratified mixtures. Therefore, Kuznetsov et al. [75] modified the critical expansion ratio to the expression

$$\sigma_\mathrm{cr} = \sigma_{\mathrm{cr},0}\left(1 + K\frac{s}{h}\right). \tag{2.27}$$

It was derived from data obtained at the medium to large-scale, semi-confined A1-vessel at Karlsruher Institute of Technology (KIT). Uniform and stratified mixtures were investigated [34, 75]. Equation 2.27 uses a facility-specific empirical constant K, the obstacle spacing s and the layer thickness h. The layer thickness h refers only to the layer height of the flammable mixture. While the obstacle spacing relates to turbulence production, the fuel layer thickness introduces the effect of lateral losses to the relation. Validation of the correlation against small-scale experiments led to adjustments of the criterion by Grune et al. [35, 36], which read

$$\sigma_\mathrm{cr} = \sigma_{\mathrm{cr},0} + 35/h_\mathrm{eff}\,, \tag{2.28}$$

$$h_\mathrm{eff}^2 = h^A - ([\mathrm{BR}]\cdot s)^B\,. \tag{2.29}$$

The equations are numerical value equations, which are expressed with SI units. The derived criterion follows the concept of maximum reactivity. It uses the most reactive mixture composition of the stratified layer to evaluate $\sigma_{\mathrm{cr},0}$. The effective height h_eff is calculated from the layer thickness h, the blockage ratio [BR] ([BR] = A_bl/A_0) and the obstacle spacing s. The empirical constants A and B are estimated to be $A = 1.3$ and $B = 1.1$. The concept of maximum reactivity might not generally be applicable because it could not be verified in the fully confined GraVent facility of the Technical University of Munich (TUM) for inhomogeneous H_2-air mixtures [76].

While FA with H_2 as fuel was investigated experimentally many times [31, 35, 36, 77, 78], only a few investigations on H_2-CO fuels exist [11, 79]. Generally,

CO has a lower laminar flame speed. However, the volumetric substitution of H_2 by CO can lead to faster acceleration because the piston-like pushing effect of the burnt gas expansion intensifies [80]. Recently, a blending function between σ-criteria for the individual fuels H_2 and CO was proposed based on Equation 2.27 in order to determine FA in semi-confined large-scale geometries filled with homogeneous H_2-CO-air mixtures [81]. In the expression

$$\sigma_{\mathrm{cr}} = a_{\mathrm{H_2}}\, x_{\mathrm{H_2,f}}\, \sigma_{\mathrm{cr,0,H_2}} \left(1 + K\frac{s}{h}\right) + a_{\mathrm{CO}}\, x_{\mathrm{CO,f}}\, \sigma_{\mathrm{cr,0,CO}} \left(1 + K\frac{s}{h}\right) \tag{2.30}$$

$a_{\mathrm{H_2}}$ and $a_{\mathrm{H_2}}$ denote coefficients, which resemble the tendency of FA to fast deflagrations of each fuel component. $x_{\mathrm{H_2,f}}$ and $x_{\mathrm{CO,f}}$ are the mole fraction of each component in the fuel. While the known value of $\sigma_{\mathrm{cr,0,H_2}} = 3.75$ is used for H_2, $\sigma_{\mathrm{cr,0,CO}}$ is estimated from the investigation of Veser et al. [79] to $\sigma_{\mathrm{cr,0,CO}} = 4.65$. The approach was validated against large-scale semi-confined experimental data from the A1-vessel of KIT. Because the already existent criterion for H_2-air provides the basis, $a_{\mathrm{H_2}}$ is specified as unity. $a_{\mathrm{CO}} = 1.18$ is determined from the experiments at the A1-vessel. The σ-criterion for multi-component fuels has yet to be verified on other test facilities.

2.3 Detonation

In contrast to deflagrations, detonations are dominated by gas-dynamic effects. Therefore, detonations can be abstracted as a double discontinuity of a shock wave and a reaction front [40]. The shock wave compresses the fresh gas to temperatures, which can trigger auto-ignition. The rapid heat release of the auto-ignition maintains the shock wave, while the shock wave initiates the auto-ignition process. The double discontinuity can be described in a 1D model. In reality, detonations propagates in a 3D structure with a distinct pattern of longitudinal and transverse shock waves. The following section provides theoretical background information on the one-dimensional and multi-dimensional propagation of detonations.

2.3.1 One-Dimensional Theories

Two 1D theories with varying detail on the detonation's structure are discussed to understand the detonation's dependency on mixture composition and initial fresh gas state.

2.3.1.1 Chapman-Jouguet theory

The relations derived from the Euler equations in Section 2.1 can be directly applied to the double discontinuity. Figure 2.11 illustrates the double discontinuity consisting of a shock front and a reaction zone. This structure is often referred to as a detonation complex. Compared to a single reaction front, the notation of states in the double discontinuity is altered to index 0 as the initial, 1 as the post-shock and 2 as the post-reaction state.

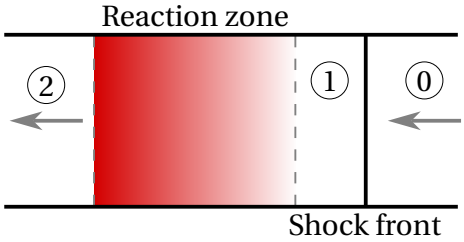

Figure 2.11: One-dimensional control volume of the detonation complex consisting of the reaction zone and the shock front.

Chapman [82] and Jouguet [83] proposed the 1D theory describing the propagation of stable detonations. In the CJ theory, no length or time scales are associated with the different states in Figure 2.11. Hence, the reaction zone is treated as a discontinuous reaction front. Figure 2.12 shows the detonation branch (supersonic) in the Rankine-Hugoniot diagram in more detail to support the theory explanation. If the double discontinuity satisfies the CJ condition ($Ma_2 = 1$), the Rayleigh line (lower blue line) is tangential to the Hugoniot curve of the reaction front ($Q > 0$). The intersection of the Hugoniot curve of the shock front ($Q = 0$) with the same Rayleigh line determines the CJ post-shock state 1. The post-reaction state 2 is the upper CJ point on the Hugoniot

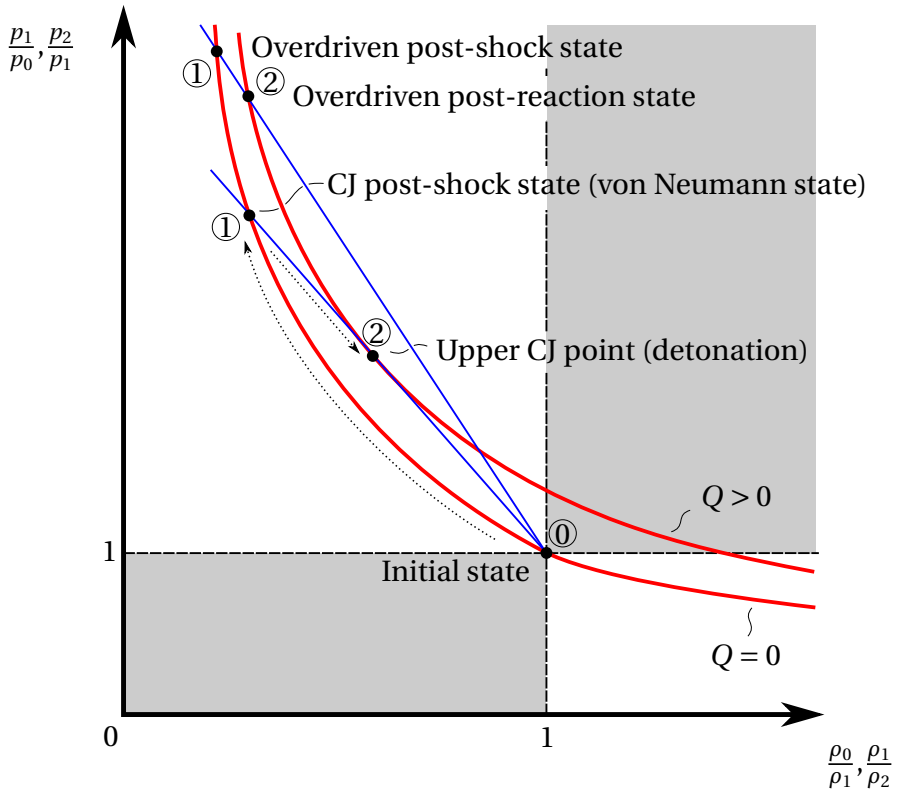

Figure 2.12: Rankine-Hugoniot diagram with Hugoniot curve (red) and Rayleigh lines (blue) illustrating overdriven and CJ detonation solutions.

curve of the reaction front ($Q > 0$). The dotted arrows indicate the change of states along the detonation structure.

The Taylor expansion fan propagates in the reaction zone's wake [84]. It forms due to the boundary condition on the burnt side of the flame front, e.g., the close end of a duct. If the CJ condition is satisfied, the expansion fan will not interfere with the leading shock and the reaction front. Rapid heat release can cause the shock wave to become stronger than the corresponding von Neumann state of a CJ detonation. In this case, the reaction front's heat release will not accelerate the flow sufficiently to satisfy the CJ condition ($u_2 < a_2$). An overdriven detonation originates. The post-shock and post-reaction states of the overdriven detonation exceed the von Neumann and CJ point in the Rankine-Hugoniot diagram 2.12. A temporary overdriven detonation is typical for the deflagration-to-detonation transition. The expansion fan

will interfere with the detonation complex, continuously decreasing the shock front's strength until the corresponding post-shock state of the CJ detonation is reached. At this point, the Taylor expansion fan cannot interfere with the detonation complex anymore. Hence, the CJ point represents the only steady-state solution of the double discontinuity. The CJ velocity $D_{0,\mathrm{CJ}}$ of the stable detonation can be estimated as follows

$$D_{0,\mathrm{CJ}} = \sqrt{\kappa R T_0 + \frac{\kappa^2 - 1}{2} q_{12}} \pm \sqrt{\frac{\kappa^2 - 1}{2} q_{12}}. \tag{2.31}$$

The steady-state solution only depends on the fresh gas's thermodynamic state and mixture composition. Due to the thermally choked flow, the 1D model predicts measured stable detonation velocities well [5].

2.3.1.2 Zeldovich-von Neumann-Döring (ZND) Theory

Zeldovich [85], von Neumann [86] and Döring [87] extended the CJ theory to the ZND theory, each independently from the others. The theory was named after its three original investigators. Using reaction kinetics, they evaluated an ignition delay time t_{ign} and a reaction time t_{exo}. A correctly tuned one-step Arrhenius model is sufficient to determine these parameters [88]. Hence, a detailed reaction mechanism is not required. However, it allows a more straightforward evaluation of t_{ign} and t_{exo} for varying mixture compositions. Both time scales transfer to a one-dimensional length scale in the detonation's structure shown in Figure 2.11. They result in an induction length behind the shock front and a reaction zone width.

Figure 2.13 shows a schematic of the detonation structure according to the ZND theory. Following the shock front, a plateau exists. The state only changes after the ignition delay time has passed. This plateau (index 1 in Figure 2.12) relates to the von Neumann (vN) state. During heat release over the time scale t_{exo}, the expansion relaxes the pressure to the level of the CJ-state (index 2 in Figure 2.12). While the density behaves similarly to the pressure, the temperature increases across both state changes.

While detonation velocities can be obtained from the CJ theory, the corre-

sponding time scales of the detonation's structure can be estimated with the ZND theory. Under-resolved simulations for risk assessment cannot reproduce the detonation complex on the correct length scale. However, the temporal sequence of states presented in Figure 2.13 can be reproduced by under-resolved detonation simulation codes quantitatively correct [89].

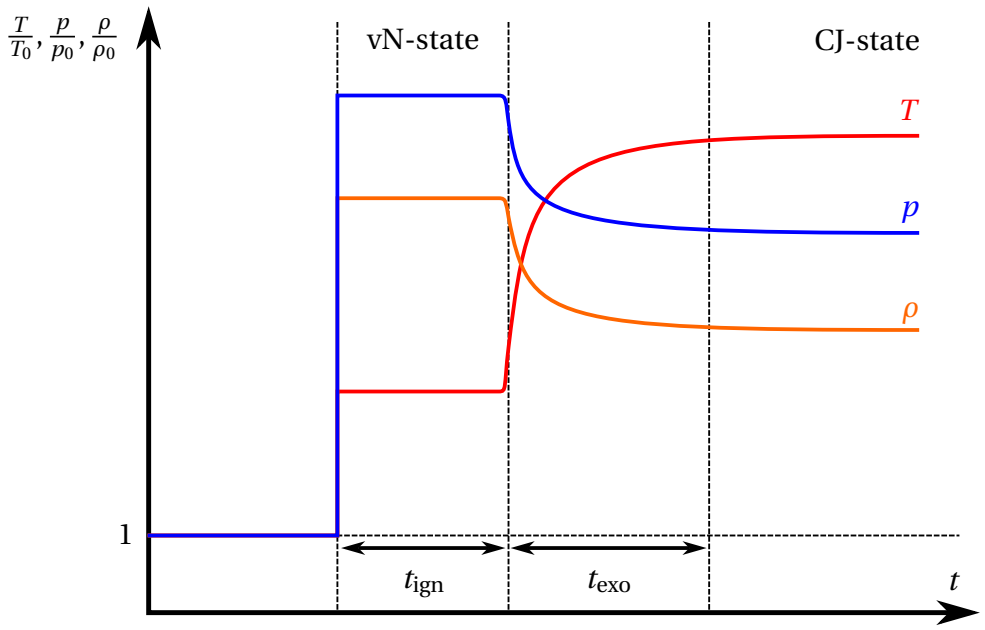

Figure 2.13: The one-dimensional ZND detonation structure characterizing von Neumann (vN) and Chapman-Jouguet (CJ) state.

2.3.2 Multi-Dimensional Detonation Structure

It has been shown mathematically that planar shock fronts are unstable when disturbed by any perturbation [90]. Consequently, detonations form a complex 3D structure with a distinct wave pattern on a macroscopic scale. Figure 2.14 depicts a simplified two-dimensional schematic of the 3D structure with rhombus-shaped cells.

Transverse waves (T) stabilize the planar shock front. The interaction of the leading shock wave (LS) and the transverse wave result in a Mach stem (M) formation. As streamlines have to pass the leading shock and the transverse

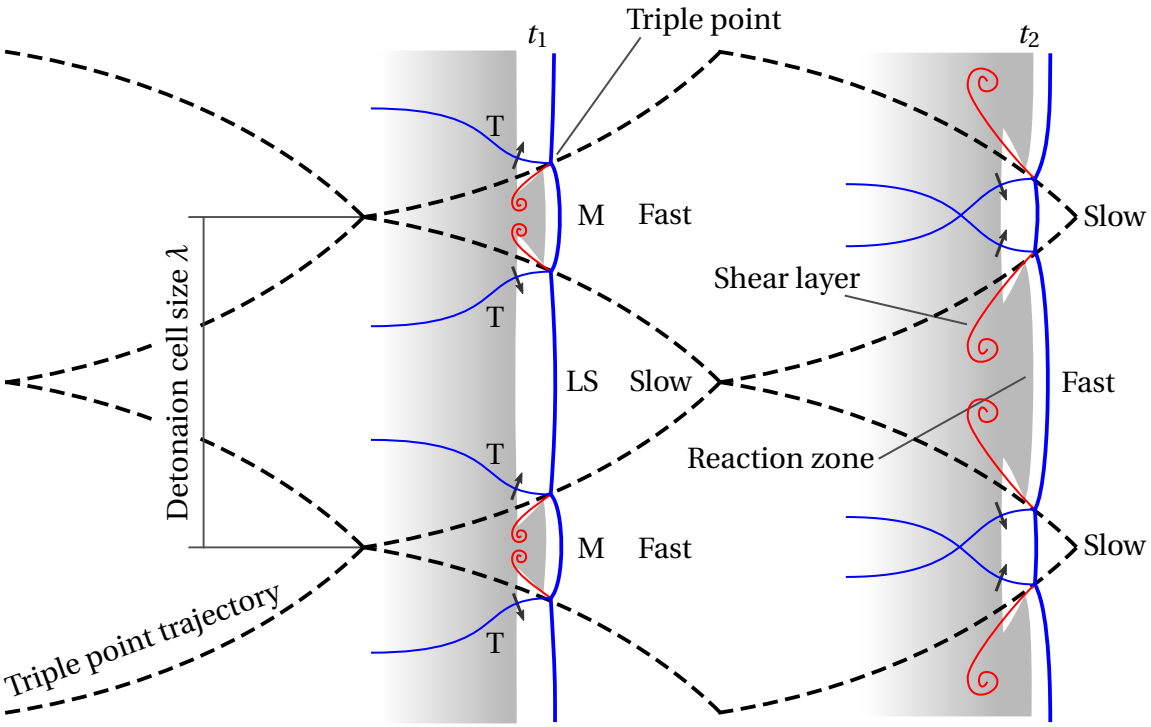

Figure 2.14: Two-dimensional schematic of the three-dimensional detonation structure.

wave to reach the same location as passing the Mach stem, the Mach stem is stronger than each of the other waves. Therefore, the induction length behind the Mach stem is shorter, and the reaction zone begins closer to the shock. The intersection of all three waves is the so-called triple point at which the highest pressure levels are present. Soot foils can visualize the triple point trajectory experimentally [91]. A similar visualization can also be obtained numerically [92]. The triple point trajectory forms the characteristic rhombus-shaped detonation cell with its detonation cell size λ.

A new detonation cell originates from the collision or the reflection of triple points. The triple point superposition generates an intensive local explosion creating a new Mach stem. The shock front is referred to as Mach stem (M) only in the first half. In the middle of the cell, a triple point collision forms a new Mach steam in the adjacent cell. Hence, the shock front becomes the leading shock (LS) in the second half of the cell. The shock wave's intensity decays from left to right of the detonation cell. The time steps t_1 and t_2 visualize the temporal evolution of the detonation propagation pattern in Figure 2.14.

The detonation's velocity decreases across the length of a cell similar to the intensity, but the mean velocity is close to the 1D estimate of the CJ theory $D_{0,\mathrm{CJ}}$.

Depending on the mixture's reactivity, the detonation structure exhibits a regular or irregular pattern. More reactive mixtures show more irregular patterns [40]. Furthermore, the detonation cell size is linked to the mixture reactivity. Because the fundamentals of multi-dimensional detonations still need to be fully understood, theory-based quantification of the detonation cell size is difficult. Nonetheless, the influence of the activation energy on the mixture reactivity led to the attempt to evaluate λ from chemical kinetics [93]. Since the results are associated with large uncertainties [94], experiments remain the primary data source for detonation cell sizes.

Because the 3D detonation structure needs to propagate self-sustained within a confining geometry, λ represents the most suitable parameter for deflagration-to-detonation transition criteria. The numerical simulation of the 3D structure requires the resolution of the induction length [95]. Thus, the simulation of fully resolved detonations is impractical for combustion-related risk assessment due to immense computational resource requirements.

2.4 Deflagration-to-Detonation Transition

2.4.1 Phenomenology

Direct initiation of detonation is highly unlikely in accidents. Therefore, only the DDT mechanism originating from a weak ignition and flame acceleration to fast deflagrations is discussed in the following. Several experimental and numerical studies [40, 67, 96] described the DDT mechanism.

The Rankine-Hugoniot diagram only allows two steady-state solutions, the CJ-deflagration and CJ-detonation. The transition between the two solutions requires a jump in the simplified 1D model. While the transition is much more complex in detail, the macroscopic effect of DDT is associated with a sud-

den jump in the observed flame velocity from the speed of sound of combustion products a_{pr} to the stable detonation velocity D_{CJ}. Typically, the observed flame velocity temporarily overshoots D_{CJ} (overdriven detonation) during the transition before it relaxes to D_{CJ} for a stable propagation [97]. The Rankine-Hugoniot diagram of Figure 2.12 already illustrated the corresponding overdriven detonation state.

Brehm and Mayinger [42] showed that with sufficiently strong pressure waves, the acceleration feedback loop becomes unstable, and the flame velocity rises exponentially, which can ultimately lead to DDT. A significant difference between deflagrations and detonations is that heat and mass transport drive deflagrations and gas-dynamic effects dominate detonations. Therefore, auto-ignition due to shock compression continuously becomes more relevant along the complex transition process.

Due to rapid FA to a thermally choked fast deflagration, a strong pressure shock forms far ahead of the flame front. The compression of the fresh gas by a shock wave corresponding to a choked fast deflagration does not lead to comparably low ignition delay times as anticipated for the detonation in the ZND theory [98]. Consequently, a single auto-ignition event triggered by the mentioned pressure wave is insufficient for successful DDT. Instead, a zone with matched self-ignition heat releases and preconditioning of the fresh gas allowing the auto-ignitions is necessary to achieve the shock strength specified in the ZND theory. The transition process is described in more detail in the following.

Local fresh gas zones capable of auto-ignition, referred to as hot spots, form in the unburnt flow ahead of the flame. They originate from local fluctuations of the thermodynamic state. Eventually, a pressure wave leads to self-ignition of a hot spot called 'explosion inside the explosion' [99]. After the first hot spot ignition, a transition to a stable detonation is only successful if a matching gradient in the ignition delay time exists in the surrounding [100]. A spontaneous pressure wave, which is stronger than the initial wave, stems from the rapid heat release of the auto-ignition at the hot spot location. The wave triggers auto-ignition in a nearby kernel whose preconditioned temperature is lower than the initial hot spot's temperature, i.e., it has a higher ignition de-

lay time. The auto-ignition initiates a new spontaneous wave. In this process, the quick heat release and the proximity of auto-ignition kernels cause the leading pressure wave intensity to grow constantly. The pressure waves during FA can create the required ignition delay time gradient. The auto-ignition sequence eventually forms a shock front, which is strong enough to initiate auto-ignitions in the unconditioned fresh gas [88]. A stable propagating detonation complex establishes, consisting of a shock front followed by a reaction zone. This transition mechanism is described as *Shock Wave Amplified Coherent Energy Release* (SWACER) [100, 101]. A mathematical description of this sensitive process is complicated due to its highly stochastic nature. The SWACER mechanism is accepted as the transition process for almost all DDT scenarios [5].

Figure 2.15 illustrates the two transition modes following either shock-focusing or transition in the vicinity of the flame. Reflection of shock waves and especially the focusing of shock waves in corners of the confinement is referred to as *strong solution* [102]. Successful DDT can be determined quite accurately through the ignition delay time in this scenario because, here, auto-ignition exclusively relies on the compression of the fresh gas.

DDT in the flame vicinity is considered the *weak solution*. Determining the onset of DDT in weak solutions is very challenging due to the complex interaction of different influencing parameters, like heat transfer, turbulence fluctu-

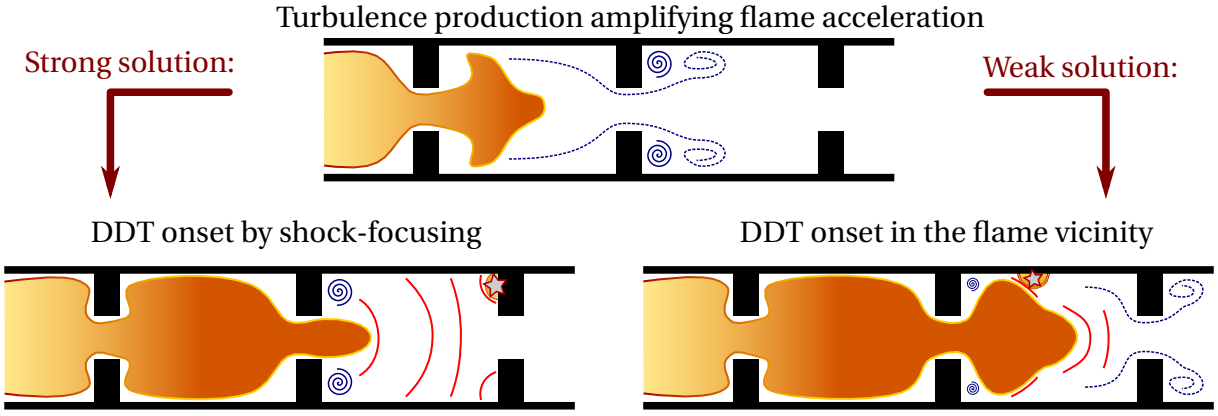

Figure 2.15: Schematic of transition modes in obstructed channels typical for accident scenarios.

ations and the preconditioned state of the fresh gas. This becomes especially difficult because the preconditioned fresh gas's state requires an accurate FA prediction. Different DDT scenarios are considered weak solutions:

- Abrupt reignition by mixing fresh gas with hot burnt gas after flame quenching [103, 104].
- Auto-ignition in a local hot spot close to the flame front resulting from the interplay of gas dynamics, turbulence and chemical reaction [88].

Apart from matching the state of the preconditioned fresh gas with the heat release from the auto-ignition reaction, the resulting spontaneous pressure wave and reaction front must propagate with related velocities to obtain a successful transition [105]. If the reaction speed is too high, the reaction front will overtake the pressure wave interrupting the auto-ignition process, and the flame reverts to a deflagration. Vise versa, the reaction will not be able to keep up if the wave velocity is too high. This scenario prohibits the pressure wave buildup according to the SWACER mechanism. The two gradients, the pressure wave and the reaction front, depend on each other. The pressure wave provides sufficiently low ignition delay times, and the reaction maintains the shock front with its heat release. Regarding modeling approaches, capturing and maintaining both gradients for DDT prediction is mandatory.

2.4.2 Transition Criteria

While the mixture reactivity poses a general limit for the onset of DDT, the confining geometry also restricts the propagation of stable detonations. The 3D detonation structure has to be sustained inside the geometry. The composition-dependent detonation cell size λ denotes a characteristic geometrical dimension of the detonation complex.

Relations between the geometrical dimension and the detonation cell size proved suitable as empirical criteria for the onset of detonations. The detonation cell size depends on the mixture composition and the initial state. The

λ-criterion for the onset of detonations has been derived from many DDT experiments in obstructed channels on various geometrical scales [32]. If the geometrical length scale l exceeds

$$l > 7\,\lambda \tag{2.32}$$

a stable detonation can propagate within the confinement, allowing the DDT. The criterion's simplicity is beneficial for practical use in safety assessment, but determining the characteristic length scale l is not straightforward in every geometry. Dorofeev et al. [32] provided length scale expressions for periodically obstructed channels. Using the gas cloud volume V_g a generalized length scale was specified, which reads

$$l = \sqrt[3]{V_\mathrm{g}}. \tag{2.33}$$

The criterion can be criticized for only being associated with stable detonations. Hot spot auto-ignitions without a successful DDT are not accounted for, even though their resulting pressure levels exceed those of fast deflagrations. Furthermore, the vague definition of the characteristic length scale lets the criteria appear situational, needing a generalized best practice guideline. Despite the uncertainties, the simplicity allows a fast evaluation of potential hazardous mixture compositions during CFD simulations [38, 106].

In the case of semi-confined layers of combustible gas [34,36,75], the criterion is adjusted using the layer thickness

$$h > 13.5\,\lambda. \tag{2.34}$$

The interpretation of the layer thickness h remains equivalent to it in Equation 2.27. The criterion in Equation 2.34 was recently adopted for H_2-CO-air mixtures. A blending function between individual criteria for H_2-air and CO-air was proposed:

$$\frac{h}{\lambda} > x_{\mathrm{H_2,f}}\,\frac{h}{\lambda}\bigg|_{\mathrm{H_2}} + x_{\mathrm{CO,f}}\,\frac{h}{\lambda}\bigg|_{\mathrm{CO}}. \tag{2.35}$$

While $\frac{h}{\lambda}\big|_{\mathrm{H_2}}$ is specified by Equation 2.34, $\frac{h}{\lambda}\big|_{\mathrm{CO}} = 26$ was determined from experiments in the A1-vessel at KIT. The criterion is derived for homogeneous H_2-CO-air mixtures, and it has not yet been validated against experiments at other test facilities.

3 Numerical Explosion Modeling for Risk Assessment

A reliable combustion-related safety assessment is necessary when explosive gas mixtures are present in any technical application. Using the experimentally derived flame acceleration and detonation criteria, described in Chapter 2, is often challenging in the complex geometries of real-world accident scenarios. In contrast, CFD codes allow risk analysis in arbitrarily complex geometries. Moreover, FA and DDT result from the interplay between reactivity, turbulence and gas-dynamic effects in CFD simulations [37, 107]. The simulations incorporate the FA influence on the fresh gas state before DDT and provide information about the DDT location. However, the design of CFD-based risk assessment codes for combustion phenomena encounters several challenges:

- **Combustion regimes:** Following weak ignition, the flame evolves from a slow to a fast deflagration during FA. Subsequently, gas-dynamic effects trigger auto-ignition events, which lead to DDT. If DDT is successful, a stable detonation forms ultimately. Because the different regimes are linked, all regimes must be properly captured.
- **Disparity of speeds:** Explosion scenarios range from a quiescent state at ignition to a supersonic flow in the detonation regime. While the flow can be considered incompressible at slow velocities, the supersonic flow is compressible.
- **Discontinuities:** Gas-dynamic effects like shock waves represent discontinuities. They play an essential role for FA, DDT and detonations. The flame front resembles a reactive discontinuity on very coarse meshes, which are typical for industrial-scale simulations. Capturing flow and reactive discontinuities requires the adequate design of a low-dissipative

discretization, an appropriate solver architecture and suitable combustion models.

- **Disparity of length and time scales:** Relevant Length scales in combustion accidents range from the smallest Kolmogorov eddies associated with turbulence to the geometrical length scales of the confining structure. Similarly, the time scales of reaction kinetics and the total time for flame propagation through the domain differ by several orders of magnitude. Appropriate modeling is unavoidable for the smallest scales to maintain reasonable computation times of DDT risk analysis simulations.

- **Combustion model:** Turbulence significantly influences the flame structure, and different interaction regimes must be considered during transient explosion simulations. Due to an excessive computation time demand, turbulence-chemistry interactions cannot be resolved in risk analysis simulations. Hence, sub-grid modeling is required. Moreover, regime-dependent models are necessary for the deflagration and the detonation regime due to the vastly different flame structures.

- **Fuel flexibility:** Due to its high hazard potential, highly reactive H_2 has played a predominant role as fuel in risk assessment code development. However, the relevance of multi-component mixtures like H_2-CO continuously increases for technical applications. Hence, risk assessment codes must be flexible concerning the mixture components present in the analyzed accident.

- **Efficiency:** Parameter studies are essential to accident risk analysis. Appropriate model selection, efficient evaluation methods and load-balancing algorithms can keep computational time low while increasing the code usability.

Existing risk assessment CFD codes apply different strategies for modeling transient explosion events. Their performance is compared in blind tests [108]. The tests prove the promising role of CFD in risk assessment. At the same time, the tests unveil limits that need to be addressed in the future.

An overview of existing codes is provided in the following. It allows the comparison of the CFD framework developed in the present thesis with existing codes.

3.1 Overview of Combustion-Related Risk Assessment Codes

In combustion risk analysis, the initial step is to predict mixture formation. The fuel distribution significantly influences FA and DDT. The explosion-related empirical criteria can be checked based on the fuel and oxidizer mixture distribution. The formation and distribution of combustible mixtures [38, 109–111] are commonly simulated utilizing lumped-parameter codes with a coarse nodalization or CFD solvers with a higher computational effort, i.e., GASFLOW-MPI [112] or ContainmentFOAM [113]. In addition to the mixture distribution, CFD simulations provide information on turbulence intensity due to the developed flow in the formation process. Both fields are relevant input parameters for combustion simulations.

The length and time scales relevant to combustion are significantly smaller than those during the mixture formation. Therefore, separate CFD codes usually address the mixture formation and the combustion to capture the respective dominating physical effects. All application-oriented solvers are applied on under-resolved computational meshes since the required resolution for mesh-independent computations cannot be satisfied for industrial scenarios. In consequence, the degree of modeling is very high in these combustion simulations. The CFD code development for combustion risk analysis by companies and research institutes focuses primarily on H_2 as fuel.

The codes COM3D [114] for slow and fast deflagrations and DET3D [115] for detonations were developed at the Forschungszentrum Karlsruhe (FZK), which is part of today's Karlsruhe Institute of Technology (KIT). Deflagrations and detonations are treated separately because the combustion regimes constitute different modeling requirements. Both codes use a structured block mesh topology. It limits the ability to discretize complex geometries on very coarse meshes. In addition, shock reflections, which are particularly impor-

tant to DDT, are reproduced inaccurately on curved surfaces with the block mesh topology. The empirical 7λ criterion determines the transition to a detonation (see Section 2.4.2). Once the criterion is satisfied, the user has to switch from the pressure-based COM3D to the density-based DET3D code for the detonation calculation. This procedure skips the transient DDT. Consequently, pressure loads during DDT leading to a potential failure of the confining structure might not be identified. Dimmelmeier et al. [38] demonstrated the procedure in a risk analysis study of the pressurized water reactor containment *EPR*.

The codes COM3D, DET3D and GASFLOW have been merged under the name GASFLOW-MPI [106, 112] to obtain an all-speed risk analysis CFD framework. GASFLOW-MPI solves the compressible 3D Navier-Stokes equations semi-implicitly in a pressure-based algorithm for all combustion regimes. The deflagration is modeled with a turbulent flame speed closure approach. A two-step Arrhenius-based chemistry model with an induction time criterion separating the shock front and the heat release zone describes the propagation of the detonation complex. DDT simulations are currently out of the framework's scope [106]. The consideration of conjugate heat transfer is a beneficial feature for slow flame simulations. Drawbacks of the code are its restriction to structured block meshes and the static switch between the deflagration and the detonation combustion model based on the empirical criterion.

The commercial CFD code FLACS, developed by GexCon, computes gas explosions in offshore oil and gas production platforms. A variety of fuels can be investigated by the code apart from H_2, which is mandatory for its application to gas production facilities. The 3D compressible Navier-Stokes equations are solved with the pressure-based algorithm (SIMPLE) [116]. A one-step Arrhenius approach combined with an artificial flame thickening method describes the flame propagation. The approach sustains a flame brush width of 3 to 5 cells. A porosity-distributed resistance model considers obstacles that the computational mesh does not resolve during simulation. Not all structures need to be represented by the mesh, simplifying the mesh generation. It allows a flexible application of the solver. On the downside, the solver setup becomes more complicated because the user must specify several additional model pa-

rameters. The pressure gradient across the flame brush determines the likelihood of DDT [117, 118]. The threshold of the pressure gradient is empirically derived, which lacks generality. Since detonation simulations are out of scope, the code does not contain a specific modeling strategy for detonations. However, detonation simulations have been attempted utilizing the code's modeling strategy for fast deflagrations [119]. Detailed user guidelines exist for the code because it is validated against many different explosion scenarios [120].

The EUROPLEXUS code of the *Atomic Energy and Alternative Energies Commission* (CEA) can be applied to all combustion regimes [121]. The code solves the 3D Euler equations. Hence, viscous effects are neglected. However, the effective numerical viscosity is scaled to include the corresponding molecular viscosity. In order to preserve discontinuities, convective terms are discretized with the reactive discrete equation method (RDEM) [122, 123], which employs a reactive Riemann solver [124]. In the flame-front tracking combustion model, the integral turbulent length scale appears in the closure term of the non-conservative transport equation of the reaction progress variable. The length scale is either treated as a static tuning parameter or is dynamically evaluated [121]. The solver simulates slow and fast flames as well as DDT. The framework was validated with homogeneous H_2-air mixtures on varying geometrical scales. Correctly tuning the model parameters for different scenarios makes a straightforward solver application challenging. Additionally, a high number of model tuning parameters can cause noticeably deviating simulation results when different users simulate the same accident scenario.

Developed by CEA in collaboration with the Institute for Radiological Protection and Nuclear Safety (IRSN), another CFD code named TONUS did emerge [125]. The combustion modeling with multi-component species transport is based on the CREBCOM [126] model, which utilizes a forest-fire mechanism. As a forest fire jumps from tree to tree, the flame propagates from one cell to the next in this model. A binary Heaviside function achieves this with a threshold temperature that specifies whether the control volume burns. The main drawbacks are its inability to represent the correct flame thickness and the requirement to prescribe the integral heat release rate, i.e., the flame speed, according to the mesh size. CREBCOM has also been employed in other

CFD codes for combustion accident risk assessment.

Almost all mentioned CFD solvers are designed to be applied explicitly to one of the three flame regimes - slow deflagration, fast deflagration or detonation. The onset of DDT is primarily based on empirical criteria instead of the locally present interplay of the heat release, turbulence and gas-dynamic effects in the simulated scenario. If the codes can be applied to different flame regimes, the simulation is stopped once the corresponding empirical criterion is satisfied. Another simulation with a different modeling strategy is started for the next flame regime. The numerical simulation of DDT following weak ignition, and subsequent flame acceleration remains a difficult challenge for combustion modeling with an under-resolved approach. In addition, H_2-air mixtures represent the primary interest in the solver development for explosion risk analysis. Only the FLACS code allows a flexible selection of fuels. None of the codes takes multi-component fuels into account.

3.2 CFD Framework for Stratified H_2-CO-Air Explosions on Multiple Geometrical Scales

Ettner [8] and Hasslberger [4] developed a CFD solver for combustion simulations of FA and DDT at the Technical University of Munich (TUM). The solver utilizes the open-source CFD library package OpenFOAM (Open source Field Operation and Manipulation) [127]. Discretization in OpenFOAM is based on the finite volume method (FVM). It supports the topology of unstructured computational meshes with arbitrary polyhedra, which allows the detailed reproduction of complex geometries. Moreover, OpenFOAM is capable of massive parallelization, as demonstrated in a DDT analysis in a Konvoi-type pressurized water reactor containment [128]. The previously developed CFD solver has the following key characteristics:

- Incorporates H_2-air combustion modeling capable of simulating FA, DDT and subsequent detonation in a single continuous calculation.
- Can be applied to small and industrial-scale geometries.

- Includes low-dissipative numerical methods for under-resolved simulations, which is especially beneficial for large geometrical scales.
- Utilizes broadly validated models in order to limit user-dependent uncertainties introduced by the need to specify model input variables.

The scope of the thesis is to extend the existing combustion-related CFD solver for FA and DDT risk assessment to H_2-CO-air mixtures and to apply it to small as well as large-scale geometries. Figure 3.1 gives an overview of the CFD framework's modeling strategy to calculate FA and DDT. In Figure 3.1, numerical methods and models of the developed solver are associated with the aspect they contribute to in the modeling strategy. Additionally, red lines link the methods to their appropriate section of the explosion simulation in the image. Aspects of the modeling strategy, which require adjustments due to the H_2-CO fuel or have been improved by model extensions, are framed in red. Appropriate methods for flame propagation have been implemented to evaluate required combustion modeling parameters, like the laminar flame speed, the Lewis number and the critical velocity gradient for turbulent flame quenching. The detonation modeling strategy has been improved by introducing a dynamic scaling of the source term. The following three aspects summarize the key contributions of the development of the thesis:

- Extension of the flame propagation simulation methodology to the multi-component mixture of H_2-CO-air, including improvement of the methodology.
- Introduction of numerical methods to consider inhomogeneous multi-component fuel distributions and partially confined structures in order to cover more accident scenarios with the modeling strategy.
- Improvement of computational efficiency by introducing a load-balancing method.

The developed H_2-CO-air CFD solver for FA and DDT risk assessment is based on the previous work by Ettner [8] and Hasslberger [4]. Since the governing equations are almost identical in the newly developed solver compared to the

previous work, they are only briefly described in the following sections. The developed solver handles the inhomogeneous distribution of the fuel components H_2 and CO through individual mixture fractions. Moreover, the combustion model for deflagrations and detonations is described in detail, emphasizing adjustments concerning the fuel extension from the previously investigated H_2 to H_2-CO. The efficiency improvement via a load-balancing algorithm is presented in depth at the end of the chapter.

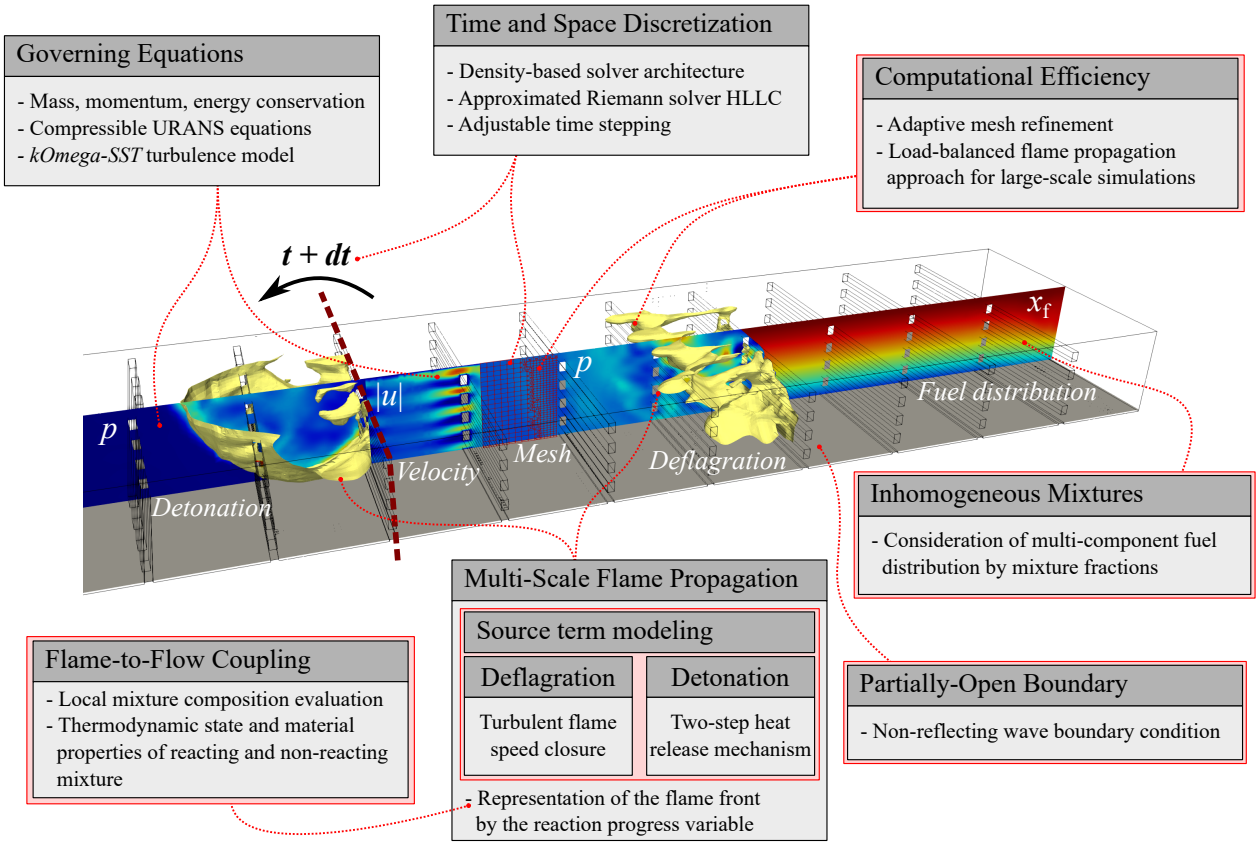

Figure 3.1: Overview of the modeling strategy for FA and DDT in stratified H_2-CO-air mixtures on multiple geometrical scales in the CFD solver developed in the thesis. (Major contributions compared to the previous solvers [4, 8] are indicated by red frames).

3.2.1 Governing Equations

The unsteady 3D Navier-Stokes equations are solved together with the mass and energy conservation equations. More detail on the equations can be found in the literature [56, 129]. Due to the transonic velocities present during detonation propagation, the equations account for compressible reactive flow.

Turbulent fluctuations contribute significantly to FA and must thus be considered in the simulation. Direct Numerical Simulations (DNS) resolve the entire turbulent spectrum, which requires very small cell sizes. Large-Eddy Simulations (LES) resolve the turbulent structures above a cut-off length. Due to the large geometrical dimensions and the high Reynolds numbers characteristic of explosion accidents, the necessary spatio-temporal resolution of LES and DNS cannot be calculated with reasonable computational effort. Unsteady Reynolds-averaged Navier-Stokes (URANS) equations only resolve mean flow quantities and model the turbulence influence, which makes it very suitable for explosion simulations for risk assessment. The use of under-resolved meshes agrees with the URANS methodology, but the accuracy of turbulence modeling decreases with coarser meshes.

The URANS equations express any flow variable ϕ as a superposition of a mean and a fluctuating value. Equation 3.1 demonstrates the decomposition. Ensemble-averaging of N values at the same position x and time t has to be used to obtain the mean value $\overline{\phi}$ in transient simulations:

$$\phi(x,t) = \overline{\phi}(x,t) + \phi'(x,t) \qquad \text{with} \qquad \overline{\phi}(x,t) = \lim_{N\to\infty} \frac{1}{N} \sum_{n=1}^{N} \phi_{(n)}(x,t). \tag{3.1}$$

For compressible or reactive flows with non-constant density, the URANS equations are simplified by employing mass-weighted mean values according to Favre [130]. Equation 3.2 shows the weighting and the resulting decomposition in mass-weighted mean values $\widetilde{\phi}$ and fluctuation values ϕ'':

$$\widetilde{\phi} = \frac{\overline{\rho\phi}}{\overline{\rho}} \qquad \text{resulting in:} \qquad \phi(x_i,t) = \widetilde{\phi}(x_i,t) + \phi''(x_i,t). \tag{3.2}$$

The decomposition into mean and fluctuation value introduces the Reynolds

stress terms $\left(\overline{\rho}\widetilde{u_i''u_j''}\right)$ to the momentum equations and turbulent scalar flux terms $\left(\overline{\rho}\widetilde{\phi''u_j''}\right)$ to scalar transport equations, respectively. The Reynolds stresses and scalar fluxes appear as unknown terms in the URANS equations, which prevents a straightforward computation. Instead, a turbulence model is employed to approximate the turbulent flux terms. A detailed derivation of the URANS equations applied in the solver can be found in the previous work [4] or a more general view in the literature [1, 129, 131].

3.2.1.1 Conservation Equations of Mass, Momentum and Energy

The Favre-averaged continuity equation in Einstein's summation convention reads

$$\frac{\partial}{\partial t}\overline{\rho} + \frac{\partial}{\partial x_j}\left(\overline{\rho}\widetilde{u}_j\right) = 0. \tag{3.3}$$

ρ denotes the density and u the velocity. The momentum conservation of the reactive flow is described by the compressible 3D unsteady Reynolds-averaged Navier-Stokes equations, which read

$$\begin{aligned}\frac{\partial}{\partial t}\left(\overline{\rho}\widetilde{u}_i\right) + \frac{\partial}{\partial x_j}\left(\overline{\rho}\widetilde{u}_i\widetilde{u}_j + \frac{2}{3}\delta_{ij}\overline{\rho}k\right) = \\ \frac{\partial}{\partial x_j}\left(\mu_{\text{eff}}\left(\frac{\partial\widetilde{u}_i}{\partial x_j} + \frac{\partial\widetilde{u}_j}{\partial x_i} - \frac{2}{3}\delta_{ij}\frac{\partial\widetilde{u}_m}{\partial x_m}\right)\right) - \frac{\partial\overline{p}}{\partial x_i} + \overline{\rho}g_i.\end{aligned} \tag{3.4}$$

The mathematical operator δ_{ij} is the Kronecker delta, p denotes the pressure, and k is the turbulent kinetic energy. Gravity is considered the only external volume force with the gravitational acceleration vector g_i. The Boussinesq hypothesis [129] is applied to model the Reynolds stresses. The molecular viscosity μ and the turbulent eddy viscosity μ_{T} introduced by the Boussinesq hypothesis are combined to an effective viscosity μ_{eff}:

$$\mu_{\text{eff}} = \mu + \mu_{\text{T}}. \tag{3.5}$$

Semi-empirical turbulence models have been published to describe μ_{T}. The well-established *k-ω Shear Stress Transport* (SST) turbulence model by Menter [132] is applied in the present explosion simulations. It is discussed in

more detail in Section 3.2.1.2. The mass-weighted average of the molecular dynamic viscosity of each species μ_k in the multi-component gas mixture yields the mixed molecular dynamic viscosity μ. The molecular dynamic viscosity of each species is determined by the Sutherland equation [133]:

$$\mu_k = A_{k,\mathrm{S}} \frac{T^{3/2}}{T + T_{k,\mathrm{S}}}. \tag{3.6}$$

In a multi-component mixture, the Sutherland temperature $T_{k,\mathrm{S}}$ and the Sutherland coefficient $A_{k,\mathrm{S}}$ must be provided for each species. The Sutherland parameters are not always directly available. However, they can be obtained by fitting the function of Equation 3.6 to viscosity-temperature profiles from databases, e.g., NIST[1]. Sutherland parameters for each species in the H_2-CO-air reaction system are listed in Appendix A.1.

A conservation equation for energy needs to be solved in reactive flows. For compressible flow, the kinetic energy needs to be considered. Hence, the conservation of energy is expressed in terms of the total internal energy e_t composed of the static internal energy e and the kinetic component. The static part can be further separated into the energy of formation at reference conditions $e^{\mathrm{f},0}$ and the sensible internal energy e^s. The latter can be calculated through each species' isochoric specific heat capacity $c_{v,k}(T)$. Equation 3.7 shows the decomposition of the total internal energy of a multi-component gas mixture. Index k resembles all species of the mixture:

$$e_\mathrm{t} = e + \frac{u_i u_i}{2} = \sum_{k=1}^{N_\mathrm{sp}} y_k \underbrace{\left(e^\mathrm{f}_{k,0} + \int_{T_\mathrm{ref}}^{T} c_{v,k}(T)\, \mathrm{d}T \right)}_{e_k} + \frac{u_i u_i}{2}. \tag{3.7}$$

In practice, the temperature-dependent internal energy of each species e_k is evaluated employing NASA polynomials with seven coefficients [134] derived from the NIST-JANAF thermochemical tables[2]. The JANAF coefficients that are part of the detailed reaction mechanism of Li et al. [14] are used for the present simulations. The NASA polynomial yields the enthalpy of the species

[1] National Institute of Standards and Technology (NIST) WebBook - URL: https://webbook.nist.gov/chemistry/

[2] NIST thermochemical tables - URL: https://janaf.nist.gov/

h_k, which is transformed into the internal energy ($e_k = h_k - R_{m,k}(T - T_{\text{inf}})$). The unsteady Reynolds-averaged conservation equation of the total internal energy writes

$$\frac{\partial}{\partial t}\left(\overline{\rho}\widetilde{e}_t\right) + \frac{\partial}{\partial x_j}\left(\left(\overline{\rho}\widetilde{e}_t + \overline{p}\right)\widetilde{u}_j\right) = \frac{\partial}{\partial x_j}\left(\overline{\rho}\, a_{\text{eff}} \frac{\partial(\widetilde{e} + \overline{p}/\overline{\rho})}{\partial x_j} + \mu\left(\frac{\partial \widetilde{u}_j}{\partial x_i} - \frac{2}{3}\delta_{ij}\frac{\partial \widetilde{u}_m}{\partial x_m}\right)\right). \tag{3.8}$$

The enthalpy flux via species diffusion is neglected. Radiation, the Dufour effect and the Soret effect are considered to be of minor importance and thus neglected as well. Analogous to the effective dynamic viscosity for the molecular and turbulent viscosity, the effective thermal diffusivity a_{eff} combines molecular and turbulent thermal diffusivity a_{T}. In order to reduce the number of modeling parameters of the turbulence model to only μ_{T}, the turbulent Prandtl number ($\text{Pr}_{\text{T}} = \mu_{\text{T}}/(a_{\text{T}}\,\rho)$) introduces a relation between a and μ, which yields

$$a_{\text{eff}} = a + a_{\text{T}} = a + \frac{1}{\text{Pr}_{\text{T}}}\frac{\mu_{\text{T}}}{\overline{\rho}} \tag{3.9}$$

in terms of the effective thermal diffusivity a_{eff}. Pr_{T} is a constant, predefined value specified as unity in all simulations. The set of equations for mass, momentum and energy conservation is closed with the equation of state for ideal gases in Equation 3.10. R_m refers to the mass-specific gas constant of the mixture:

$$p = \rho R_m T. \tag{3.10}$$

3.2.1.2 Turbulence Modeling

Turbulence models of varying complexity were developed to address the closure problem of Reynolds stresses and turbulent fluxes in the URANS equations [56, 129]. With the Boussinesq approximation in place, the well-established k-ω SST turbulence model of Menter [132] is used in the solver. References [132, 135, 136] provide detailed information about the model. It must be mentioned that the author of the model derived the coefficients for inert and not reactive flows. The k-ω SST turbulence model describes the eddy

viscosity μ_T as a function of the turbulent kinetic energy k defined in isotropic turbulence as

$$k = \frac{\widetilde{u_i'' u_i''}}{2} \tag{3.11}$$

and the specific dissipation rate ω. The k-ω SST model combines the advantageous behavior of the k-ε turbulence model in the bulk flow and the k-ω model of Wilcox in the near-wall region [131]. It uses a blending function to smoothly transition between the models for bulk flow and the near-wall region. This flexibility is beneficial in the investigation of different geometries for explosion risk analysis. The transport equations of the turbulent quantities k and ω read

$$\frac{\partial}{\partial t}\left(\overline{\rho} k\right) + \frac{\partial}{\partial x_j}\left(\overline{\rho} k \widetilde{u}_j\right) - \frac{\partial}{\partial x_j}\left(\Gamma_{k,\text{eff}} \frac{\partial k}{\partial x_j}\right) = P_k^* - \overline{\rho} \underbrace{\beta^* \omega k}_{\varepsilon} \tag{3.12}$$

and

$$\begin{aligned} \frac{\partial}{\partial t}\left(\overline{\rho}\omega\right) + \frac{\partial}{\partial x_j}\left(\overline{\rho}\omega \widetilde{u}_j\right) - \frac{\partial}{\partial x_j}\left(\Gamma_{\omega,\text{eff}} \frac{\partial \omega}{\partial x_j}\right) = \\ \frac{\overline{\rho}\gamma(F_1)}{\mu_T} P_k - \overline{\rho}\beta(F_1)\omega^2 + 2(1-F_1)\overline{\rho}\alpha_{\omega 2} \frac{1}{\omega} \frac{\partial k}{\partial x_j} \frac{\partial \omega}{\partial x_j}. \end{aligned} \tag{3.13}$$

Turbulent kinetic energy is generated by the production term P_k^* and P_k, respectively. F_1 is the aforementioned blending function. Both equations include an effective diffusivity of their quantity, $\Gamma_{k,\text{eff}}$ and $\Gamma_{\omega,\text{eff}}$. The model-specific coefficients proposed by the author of the k-ω SST turbulence model are used without adjustment [132]. The user requires no tuning of model parameters because the k-ω SST model is validated against a broad variety of cases. The decision for the k-ω SST model agrees with the goal of designing the solver to minimize the uncertainty due to user-dependent inputs on the simulation results.

In the under-resolved approach, the mesh resolution is insufficient to compute the near-wall region explicitly. Wall functions can be applied as boundary conditions to represent this region of strong gradients. This method remains valid as long as the first grid point lies within the logarithmic domain of the near-wall region. As boundary layer thickness is reduced with increasing ve-

locities, the wall functions most likely lose validity in the transonic flow of detonations. However, gas-dynamic effects become the driving physical mechanism in detonations, and the potential inaccuracy in turbulence production only marginally affects DDT's onset. The Reference [135] describes the theoretical basis of the applied wall functions in more detail.

3.2.2 Inhomogeneous Multi-Component Fuel

Homogeneous mixtures are highly unlikely in realistic accident scenarios. Fuel concentration gradients form due to various reasons:

- Convective mixing of ambient air and a fuel jet originating from a localized source [137].
- Formation of fuel layers due to varying density of mixture components.
- Different molecular diffusivity of mixture components.

Therefore, the CFD solvers must consider inhomogeneous fuel distributions. Vertical H_2fuel concentration gradients were already addressed in the previous work of Ettner [138] and Hasslberger [128], but their approach needs to be extended to H_2-CO-air mixtures. Due to the reasons listed above, different concentration gradients can exist for each fuel component, H_2 and CO, at the beginning of the combustion simulation. Hence, a scalar transport equation of the mixture fraction is introduced for each fuel component. The scalar transport equation in 3.14 describes the conservation of the hydrogen mixture fraction f_H and Equation 3.15 describes the conservation of the mixture fraction of carbon monoxide f_C:

$$\frac{\partial}{\partial t}\left(\overline{\rho}\widetilde{f}_\mathrm{H}\right)+\frac{\partial}{\partial x_j}\left(\overline{\rho}\widetilde{f}_\mathrm{H}\widetilde{u}_j\right)-\frac{\partial}{\partial x_j}\left(\overline{\rho}\,D_\mathrm{eff}\frac{\partial\widetilde{f}_\mathrm{H}}{\partial x_j}\right)=0, \tag{3.14}$$

$$\frac{\partial}{\partial t}\left(\overline{\rho}\widetilde{f}_\mathrm{C}\right)+\frac{\partial}{\partial x_j}\left(\overline{\rho}\widetilde{f}_\mathrm{C}\widetilde{u}_j\right)-\frac{\partial}{\partial x_j}\left(\overline{\rho}\,D_\mathrm{eff}\frac{\partial\widetilde{f}_\mathrm{C}}{\partial x_j}\right)=0. \tag{3.15}$$

The effective diffusion coefficient D_{eff} includes the molecular diffusion coefficient D and the turbulent diffusion coefficient D_{T}, according to

$$D_{\text{eff}} = D + D_{\text{T}} = D + \frac{1}{\text{Sc}_{\text{T}}} \frac{\mu_{\text{T}}}{\overline{\rho}}. \tag{3.16}$$

The non-dimensional turbulent Schmidt number ($\text{Sc}_{\text{T}} = \mu_{\text{T}}/(D_{\text{T}}\rho)$) expresses D_{T} in relation to μ_{T}, which the turbulence model computes. Sc_{T} is specified as unity for all simulations.

The inhomogeneous fresh gas composition of H_2-CO-air mixtures is evaluated from the mixture fractions. It should be noted that the mixture fraction is not affected by the flame. Therefore, the mixture composition of the reactants can be evaluated in all cells of the mesh, i.e., in cells with a partially burnt mixture. The combustion model described in Section 3.3 requires the fresh gas composition in all cells.

3.2.3 Solver Architecture and Discretization

According to the SWACER mechanism (see Section 2.4.1), the preconditioning of the fresh gas due to continuously amplifying pressure waves during FA determines the onset of DDT. Moreover, the DDT mechanism and the detonation propagation depend on strong shock waves. Therefore, the solver architecture and the spatio-temporal discretization methods are selected to preserve flow discontinuities.

3.2.3.1 Solver architecture

In the pressure-based *Pressure Implicit with Splitting of Operators* (PISO) solution algorithm, the pressure is computed via a pressure correction equation coupled with the momentum equation, which results in a second-order gradient for the pressure. The diffusive nature of this term causes smearing of discontinuities.

Therefore, Ettner proposed a density-based solver architecture to preserve discontinuities in the compressible reactive flow [8]. In contrast to a pressure-

based architecture, the continuity equation is solved in its conservative form. The solution is much less dissipative because the continuity equation only contains an advective and no diffusion term. Ettner [8] demonstrated the solver's ability to preserve shock waves through shock tube simulations on fine and coarse computational meshes. One downside of the approach becomes apparent at low flow velocities, however. In this case, the absence of numerical stabilization schemes (e.g., the diffusion term in the pressure correction equation) and small numerically induced fluctuations in the density or the velocity can cause significant responses in the other of the two coupled variables. In combustion accidents with fast flames and DDT, significantly low velocities are only present for a short period following ignition. The resulting uncertainty in the simulated flame velocity is reasonable regarding the solver's risk analysis application.

3.2.3.2 Spatial discretization of advection terms

In CFD, the gradient in the advection term of the transport equations is generally evaluated with the FVM from face values using Gauss' divergence theorem. In order to support the conservation of discontinuities, the Harten-Lax-van Leer contact (HLLC) scheme, a Godunov-type scheme, is appied [139]. The HLLC scheme solves a Riemann problem at the cell surface using an approximation. Godunov-type schemes are particularly suitable for preserving discontinuities in compressible flows since they distinguish between subsonic and transonic conditions at the cell surface. Ettner verified the robustness of the advection scheme by 1D shock tube simulations for non-reacting flows [8] and by DDT simulations for reacting flow [95]. The approximated Riemann solution is computed significantly faster than an iterative or direct Riemann scheme.

The advection scheme is generally designed for non-reacting flows. Under rare unfavorable conditions, the HLLC scheme can yield unphysical values and lead to the divergence of the simulation. These unwanted conditions are amplified by the detonation's rapid reaction-rate-limited heat release. The divergence is prevented by replacing the thermodynamic state of individual di-

vergent cells with the average state of all neighboring cells once a threshold temperature, density or velocity is exceeded. The influence on the onset of DDT by this bounding method for divergent cells is low because only single cells are affected on rare occasions. Recently, a reactive Riemann solver was developed [122–124], which can be applied as a more robust but more computational intensive gradient scheme in future projects.

3.2.3.3 Time-step discretization

In the present project, a hybrid implicit-explicit Euler time-stepping method is employed [4, 129]. The transport equations' advective terms are solved explicitly, guaranteeing a proper reconstruction of shock fronts. Diffusive terms are solved implicitly since it better represents the dissipative nature.

The time step size Δt is adjusted during the simulation employing the *Courant-Friedrich-Lewy* (CFL) criterion. With the use of an acoustic CFL number $\mathrm{Co}_{\mathrm{acc}}$, sufficiently small time steps are ensured to resolve wave propagation in time before detonation occurs. The criterion reads as

$$\mathrm{Co}_{\mathrm{acc}} = \frac{(|u| + a)\,\Delta t}{\Delta x_{\mathrm{c}}} \leq \mathrm{Co}_{\mathrm{acc,max}}. \tag{3.17}$$

The expression $|u| + a$ refers to the wave propagation velocity consisting of flow velocity and speed of sound a. The time step size adjustment saves computation time at low flow velocities and maintains sufficient temporal resolution at high velocities. In explicit methods, the restriction of the CFL number $\mathrm{Co}_{\mathrm{acc,max}} < 1$ must hold. It specifies that any information cannot travel further than the cell size within the next time step. The criterion's importance for a reliable explicit time stepping scheme is explained in References [129, 140].

The propagation velocity of stable detonations exceeds the acoustic wave velocity $|u| + a$. Therefore, a sufficiently small $Co_{\mathrm{acc,max}}$ limit must be chosen to resolve the temporal evolution of supersonic detonation waves. CFL numbers in the range of $Co_{\mathrm{acc,max}} = 0.1$ and $Co_{\mathrm{acc,max}} = 0.3$ are a good compromise of accuracy and computation time. In combination with the spatial discretization methods, the temporal discretization strategy supports the goal of capturing pressure waves and preserving their influence on FA and DDT.

3.3 Combustion Model for Explosion Simulation with Stratified H_2-CO-Air Mixtures

If the product gas is confined, the expansion of hot products induces a flow ahead of the propagating flame front. The combustion itself drives the feedback loop of FA since the induced flow generates turbulence in shear or boundary layers. The combustion model plays the dominant role in accurately predicting FA and DDT in realistic accident scenarios.

Figure 3.2 presents the structure of the combustion model. The CFD solver for risk assessment has to be applicable to different geometry sizes, from small to industrial scales. In the previous solver, Ettner [8] applied a volume reaction approach to describe flame propagation in small-scale geometries using the reaction progress variable c. Hasslberger [4] implemented a flame-front tracking approach based on the burnt volume fraction α for large-scale solver applications. Different transport equations are solved in the two flame propagation approaches. In the newly developed H_2-CO-air solver, the appropriate transport equation is selected from the two equations depending on efficiency and accuracy with respect to the scale of the scenario. Ultimately, the reaction progress variable c represents the flame in both approaches. This requires coupling of the α and the c field.

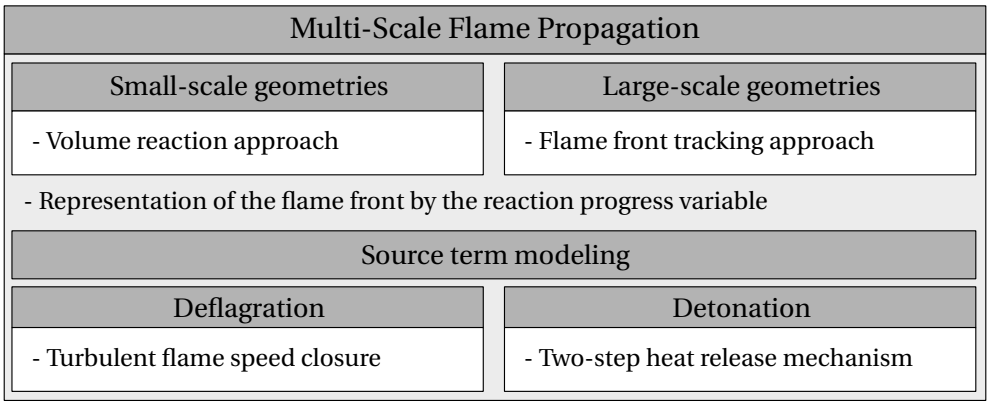

Figure 3.2: Combustion modeling strategy with different flame-propagation transport equations for small-scale and large-scale geometries as well as the source term models for deflagrations and detonations.

The deflagration and the detonation are treated with separate source terms in both flame-propagation transport equations because the dominating physics is fundamentally different in the two combustion regimes. In order to develop an efficient multi-scale CFD solver for explosion risk analysis in stratified H_2-CO-air mixtures, the previous solver's combustion model was adjusted and improved as follows:

- The treatment of a non-reacting mixture, which provides required thermodynamic state information for the source term calculation, was changed. This contributed to a better prediction of detonation velocities.
- The turbulent flame quenching model was revised concerning H_2-CO-air mixtures, and the quenching factor evaluation was adjusted to use precalculated critical velocity gradient values.
- Numerical evaluation methods for the laminar flame speed, effective Lewis number and critical velocity gradient have been implemented, providing possible results for all H_2-CO-air mixture compositions.
- The requirement of multi-scale applicability of the CFD solver demands a mesh-independent formulation of the detonation source term, which was implemented.

3.3.1 Multi-Scale Flame-Propagation Transport Equations

Consideration of all species and finite rate evaluation of all reactions in existing reaction mechanisms of H_2-CO-air [14, 46–48] is extremely computationally intensive. It requires additional transport equations for each species and very small time steps for the numerical solution of the stiff chemical reaction system.

Instead of tracking each species individually, the conversion of the multi-component gas mixture is described by a single variable in the developed CFD solver, the reaction progress variable c (see Section 2.2.1). Only one transport equation is required to describe the flame propagation, which is computationally very efficient. This demands that the mixture composition is provided

to the solver corresponding to the local reaction progress. The coupling of the reaction progress variable and the gas composition is discussed in Section 3.3.2. The procedure is referred to as flame-to-flow coupling because it also includes evaluating the thermodynamic state with respect to the reaction progress.

The multi-scale applicability of the solver is guaranteed by deploying individual flame-propagation transport equations according to the geometrical scale [1, 3]. Figure 3.3 shows the transport equation employed for small-scale and large-scale geometries, respectively. In the volume reaction approach, c is transported. The gas volume of each cell converts from fresh gas $c = 0$ to burnt gas $c = 1$. During the reaction, only the intermittent state $0 < c < 1$ exists in the cell volume. The flame front tracking approach for large-scale geometries transports the burnt volume fraction α. Its transport equation describes the motion of the reaction front itself, similar to a fluid particle. Therefore, it requires a reconstruction of the flame front inside the cell, separating the cell into a burnt and a fresh gas fraction. The reconstruction is computationally intensive but prevents the dissipation of the steep gradient in the flame front

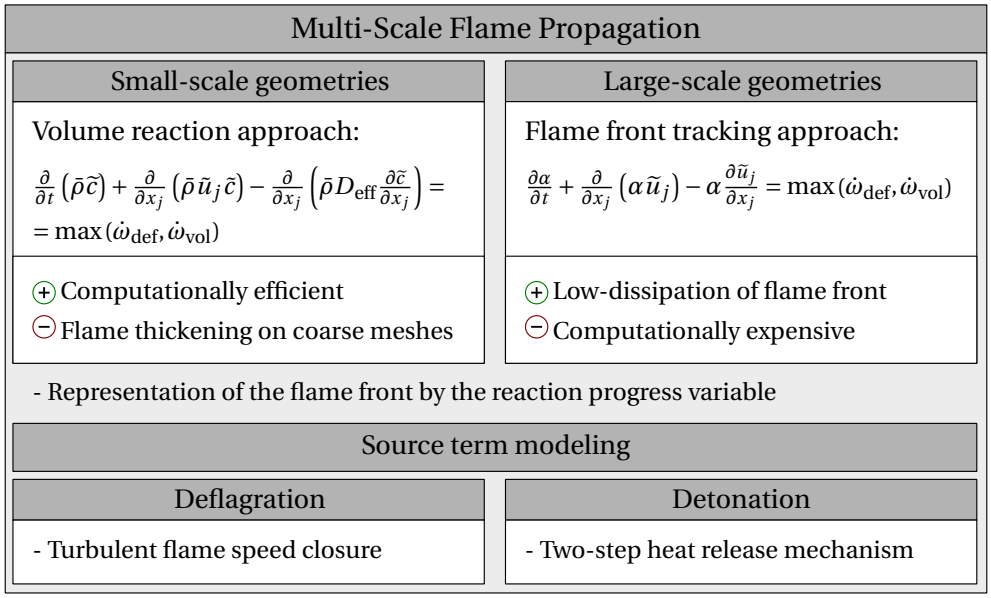

Figure 3.3: Overview of geometry-scale-dependent flame-propagation transport equations available in the multi-scale combustion model of the CFD framework.

on coarse meshes. Ultimately, the c field represents the flame for both transport equations.

Source terms describe the reaction with respect to the combustion regime and add its influence to the transport equations. A separate source term exists for deflagrations $\dot{\omega}_{\mathrm{def}}$ and detonations $\dot{\omega}_{\mathrm{vol}}$. Only the maximum of the two source term values is used for the solution in both flame-propagation transport equations. The source term modeling is addressed in Section 3.3.3 and Section 3.3.4 for the respective flame regime. A short description of the two flame-propagation transport equations is provided in the following before a guideline on the selection of the appropriate equation is given.

3.3.1.1 Volume Reaction Approach

In the volume reaction approach, the flame front is transported in reference to a fixed observer. Equation 3.18 takes the form of a Favre-averaged transport equation for a scalar quantity:

$$\frac{\partial}{\partial t}\left(\bar{\rho}\widetilde{c}\right)+\frac{\partial}{\partial x_j}\left(\bar{\rho}\,\tilde{u}_j\,\tilde{c}\right)-\frac{\partial}{\partial x_j}\left(\bar{\rho}\,D_{\mathrm{eff}}\frac{\partial\widetilde{c}}{\partial x_j}\right)=\max\left(\dot{\omega}_{\mathrm{def}},\dot{\omega}_{\mathrm{vol}}\right). \tag{3.18}$$

D_{eff} represents the sum of molecular and turbulent mass diffusion. Each cell is either burnt $c = 1$, partially-burnt $0 < c < 1$ or unburnt $c = 0$. The state stands for the entire cell volume. Since the transport equation contains a second-order derivative, the calculation is susceptible to non-physical thickening of the flame. Even though the intensity of the thickening depends on the source term modeling, it is particularly pronounced on coarse computational meshes.

Because mass diffusion is already considered in the transport equation, diffusive effects should strictly speaking not be included in the source terms. If source term models use the laminar flame speed to express the integral heat release of the flame, the fuel consumption speed should be used instead of the laminar flame speed. It refers to the conversion rate of fuel without diffusive transport [1]. However, compared to the uncertainties associated with the under-resolved simulation approach, the difference between the results from each flame speed expression is expected to be negligible.

3.3.1.2 Flame Front Tracking Approach

Interface tracking approaches have their origin in multiphase flow simulations. They describe the motion of an interface between two separated phases. In analogy, the flame front can be viewed as an interface between the burnt and unburnt gas state. The interface is treated as a discontinuity in this perspective. The assumption that the flame front resembles a discontinuity is justified when the flame thickness is small compared to the interface cell size. This condition is satisfied more accurately the larger the mesh's cell sizes are.

The position of the flame front is tracked by the burnt fraction of the cell volume α. The burnt state corresponds to $\alpha = 1$ and the unburnt state to $\alpha = 0$. The transport equation 3.19 describes the kinematic balance of flow velocity and burning speed of the discontinuous reaction front. It does not include a diffusive term, which benefits the application on coarse meshes [3]. In contrast to the volume reaction approach, the laminar flame speed, which incorporates mass diffusion, needs to be used in the source term formulation of this approach. The addition of a divergence correction term to the transport equation is derived in Appendix C.1. The conservative form of the transport equation yields

$$\frac{\partial \alpha}{\partial t} + \frac{\partial}{\partial x_j}\left(\alpha \widetilde{u}_j\right) - \alpha \frac{\partial \widetilde{u}_j}{\partial x_j} = \max\left(\dot{\omega}_{\mathrm{def}}, \dot{\omega}_{\mathrm{vol}}\right). \tag{3.19}$$

The Level-Set and Volume-of-Fluid (VoF) methods are popular interface tracking approaches. The Level-Set method considers separate thermodynamic states and flow velocities inside the interface cell's burnt and unburnt gas. In contrast, the VoF method assumes a single mixed velocity and thermodynamic state for the entire flame front cell [3]. The VoF method is more efficient than the Level-Set method, but its accuracy depends heavily on the advection scheme. Instead of evaluating the advection terms from differences to neighboring cell values as in standard VoF methods, the advected burnt volume can be computed by geometrical reconstruction of flux polyhedra on the cell faces and their truncation with the reconstructed flame front interface. Due to the use of geometrical volume reconstruction, this VoF method type is called the geometrical Volume-of-Fluid (geoVoF) method. It achieves a very

low numerical dissipation. Despite a higher computation effort for the geoVoF method than a standard-type VoF method, it remains more efficient than the Level-Set method.

In combination with the absence of a diffusive term in the transport equation, the geoVoF method allows the calculation of the flame front motion with minimal numerical dissipation on coarse meshes [141]. The necessary reconstruction of the interface position in the flame front cell maintains the discontinuity and prevents flame front thickening. An implementation of the geoVoF method for explosion simulations was achieved previously by Hasslberger and Ketterl [4, 13]. The developed CFD solver applies the geoVoF method as a flame front tracking approach. Appendix C.1 provides a detailed description of the method. The DDT simulation of a pressurized water reactor of a Konvoi-type NPP presented in [142] verifies the significant advantages of the geoVoF method when applied to industrial scales. As presented in Section 3.4.2, the computation efficiency of the geoVoF method was significantly improved through load-balancing the computationally intensive operations.

3.3.1.3 Coupling of Volume Fraction α and Reaction Progress Variable c

In reality the flame front is no discontinuity. It has steady mass fraction and temperature profiles with a finite turbulent flame thickness δ_T. Therefore, the α field of the geoVoF method cannot be used directly to evaluate the gas composition, state and material variables of the fluid flow. The c field represents the continuous flame profile, similar to the volume reaction approach. The α field is coupled with the c field using Equation 3.20. This methodology was adopted from Hasslberger [4]:

$$\overline{c} = \frac{1}{N_{\mathrm{fn}} w + 1} \left(w \sum_{n=1}^{N_{\mathrm{fn}}} \alpha_n + \alpha \right). \tag{3.20}$$

The reaction progress variable in a cell is calculated from the cell's α value and the values of the adjacent cells α_n. Only face neighbors of the cell are taken into account. N_{fn} denotes the number of face neighbors. The weighting factor w determines the smearing of the discontinuous α field across the neighboring cells. Smaller values of w result in a steeper gradient of the c field centered

at the interface cell. On coarse meshes, the turbulent flame brush and the cells can have a similar size, which prescribes a small w value. w is specified as 0.25 in the present simulations.

User-defined input variables like w are a source for uncertainties in risk analysis simulations. Hence, a dynamic evaluation of w based on the ratio of the turbulent flame thickness and cell size could be a subject for future research. Artificial flame thickening in the c field does not occur when flame front tracking is applied because it is reevaluated from the discontinuous α field every time step.

3.3.1.4 Selection of the Appropriate Flame-Propagation Transport Equation

A good practice for selecting the appropriate flame-propagation transport equation is to check whether the turbulent flame brush fits within one cell. The turbulent flame brush thickness δ_T can be calculated from different definitions [143, 144]. In the case of cell sizes of 10 mm and larger, the geoVoF method is suggested. Otherwise, the dissipation in the volume reaction approach causes a non-physically thickened turbulent flame brush. The repeated reconstruction of the mean flame front position in the geoVoF method counteracts any dissipation of the reactive gradient in the flame front. This advantage is bought with longer calculation times of the flame front tracking than the volume reaction approach.

If the mesh comprises cells with about 2 mm side length, the volume reaction approach is suggested for the flame-propagation transport equation. The turbulent flame brush covers several cells. Hence, the underlying assumption of the geoVoF method that the flame front can be treated as a discontinuity is not satisfied. The α-c-coupling in Equation 3.20 cannot represent the flame across several cells. Additionally, the solution of the flame-propagation transport equation of the volume reaction approach is more efficient than the computationally intensive geoVoF method. The model selection is a trade-off between accuracy, efficiency and minimizing dissipation.

3.3.2 Coupling of Flame and Flow

Since the flame-propagation transport equations only represent the flame via the reaction progress variable c, it does not directly provide the mixture's composition in the fresh and burnt gas. The composition must be evaluated with respect to the local c value. In addition to the mixture composition, the local thermodynamic state and material properties must be estimated. The sequential steps for evaluating the flow and mixture-related properties from the reaction progress variable c are referred to as flame-to-flow coupling. Figure 3.4 presents the necessary evaluation sequence of mixture composition, thermodynamic state and material properties.

Computing necessary input variables for the deflagration and the detonation source terms, like the laminar flame speed, requires the unburnt gas's thermodynamic state and material properties. The necessary input variables of the source terms must also be calculated inside the reaction zone. Therefore, a second non-reacting mixture is introduced in addition to the reacting mixture. It only accounts for the compression by pressure waves and does not include

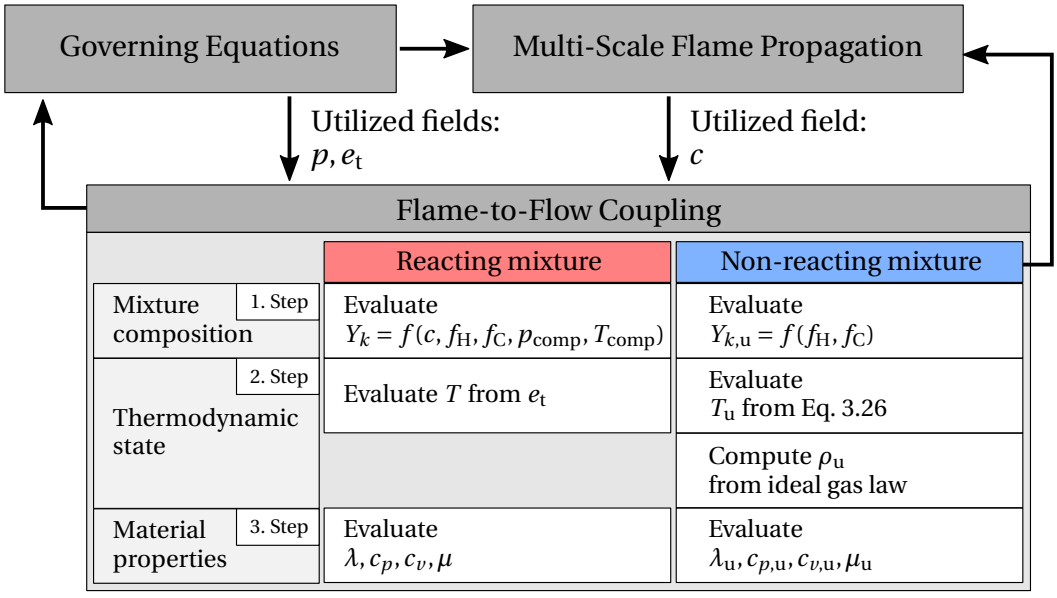

Figure 3.4: Overview of the flame-to-flow coupling methodology including the evaluation sequence for the reacting and non-reacting mixture.

the heat release of the reaction. Both mixtures have their individual mixture composition, thermodynamic state and material properties. The variables of the non-reacting mixture are indicated with the suffix u. The methodology of the flame-to-flow coupling requires the input of the pressure p, the total internal energy e_t and the reaction progress variable c. The approach to apply a non-reacting mixture has already been reported in the literature, e.g., in Weller's flame surface density combustion model [145], or the previous work on explosion CFD solvers by Ettner [8] and Wieland [146]. In the present solver, the flame-to-flow coupling methodology differs from the previous work in order to be suitable for multi-component fuels, i.e., H_2-CO, and to better predict the combustion products composition of stable detonations.

The overview in Figure 3.4 depicts the sequential steps for both mixtures. However, the computation of the required parameters differs between the mixtures in each step. The following sections describe each step with respect to both mixtures and introduce the non-explained variables in the overview.

3.3.2.1 Mixture Composition of the Reacting and Non-Reacting Mixture

The present CFD solver accounts for the species represented in the reaction mechanism of Li et al. [14]. A linear change of the composition is assumed between the burnt and unburnt state. Since the under-resolved simulation approach limits the resolution of the flame profile, the linear slope is sufficiently accurate. The equation

$$Y_k = (1 - c)\, Y_{k,\mathrm{u}} + c\, Y_{k,\mathrm{b}} \tag{3.21}$$

is evaluated for each species k of the multi-component mixture to obtain the local species mass fraction Y_k. This requires knowledge of the fresh gas composition $Y_{k,\mathrm{u}}$ and the fully burnt composition $Y_{k,\mathrm{b}}$.

Only the components hydrogen H_2, carbon monoxide CO, oxygen O_2 and nitrogen N_2 exist in the fresh gas. The local fresh gas composition $Y_{k,\mathrm{u}}$ is estimated from the mixture fractions of hydrogen f_H and carbon monoxide f_C (see Section 3.2.2). $Y_{\mathrm{O_2,air}}$ denotes the O_2 mass fraction in atmospheric air specified as 0.23295. N_2 is calculated from the closure condition that all species' mass

fractions must add up to unity. In the case of the non-reacting mixture, Equation 3.22 to 3.25 determine the gas composition in every cell:

$$Y_{H_2,u} = f_H, \tag{3.22}$$

$$Y_{CO,u} = f_C, \tag{3.23}$$

$$Y_{O_2,u} = Y_{O_2,air}(1 - f_H - f_C), \tag{3.24}$$

$$Y_{N_2,u} = 1 - Y_{H_2,u} - Y_{CO,u} - Y_{O_2,u}. \tag{3.25}$$

The equilibrium gas composition after adiabatic isobaric combustion represents the burnt composition $Y_{k,b}$. The composition is calculated with *Cantera* [45] using the reaction mechanism of Li et al. [14]. The reaction mechanism shows an overall good performance in the comparison study of syngas reaction mechanisms by Olm et al. [147]. It performs particularly well in estimating ignition delay times, which are relevant for the detonation source term modeling described in Section 3.3.4. The program requires a detailed reaction mechanism for the solution even though the calculation of the equilibrium state does not rely on reaction kinetic information.

In transient explosions with inhomogeneous fuel distributions, the fresh gas composition and the thermodynamic state before combustion change over time. An interpolation table is filled with precalculated burnt gas compositions $Y_{k,b}$. The table entries depend on the four input variables fuel mole fraction x_f, molar hydrogen fraction in the fuel $x_{H_2,f}$, composition temperature T_{comp} and composition pressure p_{comp}. Interpolation tables pose a very efficient method for evaluating a variable with multiple dependencies. It holds the advantage that the table only needs to be created once during preprocessing.

The mole fractions x_f and $x_{H_2,f}$ can be estimated from the mixture fractions f_H and f_C. Like the mixture fractions, they are not affected by the reaction. T_{comp} and p_{comp} are auxiliary variables employed as temporary input variables for the interpolation table. They depend on the flame regime and reaction progress c. T_{comp} and p_{comp} are always associated with the thermodynamic state before combustion. Figure 3.5 shows the selection matrix for T_{comp} and p_{comp}.

Because reacting and non-reacting mixtures are equivalent in the fresh gas

($c = 0$), T and p are selected for T_{comp} and p_{comp} there. Once $c > 0$ holds and the flame regime remains a deflagration, T_{comp} and p_{comp} are not changed throughout the simulation indicated as *const* in Figure 3.5. This treatment prevents the influence of large pressure rises over the flame front on the combustion products.

<table>
<tr><th></th><th>Fresh gas
$c = 0$</th><th>Flame front
$0 < c < 1$</th><th>Burnt gas
$c = 1$</th></tr>
<tr><td>Deflagrations
$\theta = 0$</td><td rowspan="3">$p_{\text{comp}} = p$
$T_{\text{comp}} = T$</td><td>$p_{\text{comp}} = \text{const}$
$T_{\text{comp}} = \text{const}$</td><td>$p_{\text{comp}} = \text{const}$
$T_{\text{comp}} = \text{const}$</td></tr>
<tr><td rowspan="2">Detonations
$\theta = 1$</td><td rowspan="2">$p_{\text{comp}} = p_{\text{vN}}$
$T_{\text{comp}} = T_{\text{vN}}$</td><td>*if:* DetInd = true</td></tr>
<tr><td>$p_{\text{comp}} = p_{\text{vN}}$
$T_{\text{comp}} = T_{\text{vN}}$</td></tr>
<tr><td></td><td></td><td>*set* DetInd = true</td><td></td></tr>
</table>

Figure 3.5: Selection matrix for the auxiliary variables T_{comp} and p_{comp} depending on the flame regime and the reaction progress variable.

In a detonation complex, the thermodynamic state before the auto-ignition reaction is the post-shock von Neumann state according to the ZND theory (see Section 2.3). If the detonation criterion $\theta = 1$ holds, T_{comp} and p_{comp} are substituted with the von Neumann state variables T_{vN} and p_{vN}. This way, the combustion products of a stable detonation are estimated, and hence, the correct corresponding heat release of a detonation results. Because the heat release significantly influences the propagation speed of the detonation complex D_{CJ}, a correct heat release prediction is essential. In practice, the detonation criterion θ (see Section 3.3.4) is only satisfied within the heat release zone ($0 < c < 1$) due to the under-resolved simulation approach. Once a detonation has been registered, the boolean indicator DetInd is specified as true. Since the ignition delay time is eventually reached in all burnt cells, θ always becomes unity at some point. The indicator DetInd restricts the burnt composition associated with detonations to cells where a detonation actually occurred. T_{comp} and p_{comp} is updated with T_{vN} and p_{vN} every time step. Considering the von Neumann state in the burnt gas composition evaluation for det-

onations poses a difference from previous solvers [4, 146]. The von Neumann state variables are obtained from Cantera calculations utilizing the script library *Shock and Detonation Toolbox*[3] [45]. The von Neumann state variables are precalculated and tabulated with x_f and $x_{\mathrm{H_2,f}}$ as input variables to obtain an efficient runtime evaluation.

The maximum values possible in accidents with fast deflagrations and DDT bound the values of the table input variables T_comp, p_comp, x_f and $x_{\mathrm{H_2,f}}$ for the tabulation of $Y_{k,\mathrm{b}}$. Pure H_2, pure CO or pure air are the limits regarding the fresh gas composition. The von Neumann post-shock state characterizes the maximum pressures and temperatures. Hence, temperatures are in the interval from 260 K to 1580 K and pressures in the interval from 0.7 bar to 100 bar. The reaction mechanism of Li et al. [14] is validated in the mentioned temperature and pressure range. The wide intervals allow a flexible application of the solver to various accident scenarios, which is one of the key goals for the developed CFD framework. The number of intermediate values of each input variable determines the accuracy of the burnt gas composition evaluation by interpolation tables. Because adding further input variables to the tabulation procedure potentiates the table size, the number of intermediate values of the interval must be reduced compared to a binary mixture.

3.3.2.2 Thermodynamic State and Material Properties

After evaluating the gas composition in the reacting and non-reacting mixture, the thermodynamic state must be determined. In the reacting mixture, the temperature T is calculated from the total internal energy e_t iteratively. The continuity equation in 3.3 and the equation of state in 3.10 provide the density ρ and the pressure p.

The non-reacting mixture does not include the heat release of the reaction. Hence, its thermodynamic state is only affected by the compression due to pressure waves. As shown in Equation 3.26, the non-reacting temperature T_u is determined differently in the fresh gas ($c = 0$) and in the flame region ($c > 0$):

[3] Shock and Detonation Toolbox URL: https://shepherd.caltech.edu/EDL/PublicResources/sdt/

$$T_\mathrm{u} = \begin{cases} T & \text{if: } \overline{c} = 0, \\ T_\mathrm{u}|^{t-1} \left(\frac{p|^t}{p|^{t-1}} \right)^{\frac{\kappa-1}{\kappa}} & \text{if: } \overline{c} > 0. \end{cases} \tag{3.26}$$

In the fresh gas region ($c = 0$), the non-reacting temperature T_u is equal to the temperature T of the reacting mixture. In contrast to the isentropic relation used in the previous solver by Hasslberger [4], the present evaluation method captures the effect of strong shock waves on T_u accurately in the fresh gas. In the flame region and the burnt gas ($c > 0$), compression effects on T_u are calculated with an isentropic relation. Isentropic relations are suitable during FA because emitted waves have a small incremental pressure amplitude in the flame vicinity. In this stage, strong pressure waves occur only further away as a consequence of the superposition of the weak waves. Moreover, the thermodynamic state of the non-reacting mixture is exclusively required by the deflagration source term in the present CFD solver. Equation 3.26 applies the pressure increment between the current time step t and the previous time step $t-1$ instead of on a static reference pressure. This way, no user input is required, reducing potential user-related sources of uncertainties. Ultimately, the density of the non-reacting mixture ρ_u is calculated through the equation of state for ideal gases.

In the under-resolved simulation approach, the strong precursor shock wave of the detonation complex resides within the reaction front ($c > 0$). The isentropic relations cannot capture the von Neumann post-shock state in T_u and p of the non-reacting mixture. This justifies the use of the tabulated von Neumann state variables for the evaluation of the burnt gas composition $Y_{k,\mathrm{b}}$ in the flame region, as has already been described in Section 3.3.2.1. An appropriate method to capture T_vN and p_vN by the non-reacting mixture within the heat release zone could significantly improve the accuracy of under-resolved DDT simulations and enhance the flexibility of the CFD solver application.

After estimating the mixtures' gas compositions and thermodynamic states, the material properties of both mixtures are determined. No empirical correlations are required to calculate the non-reacting material properties. The implemented code of the non-reacting mixture can access the same functions in OpenFOAM as the reacting mixture to calculate material properties. This im-

proves the general applicability and usability of the CFD solver in comparison to previous solvers [146]. Subsequently, the viscosity μ and μ_u as well as the thermal conductivity λ and λ_u are updated for both mixtures with the Sutherland Equation 3.6. Additionally, the heat capacities c_p, c_v and $c_{p,\mathrm{u}}$, $c_{v,\mathrm{u}}$ are calculated using the JANAF coefficients and a mass-weighted mixing law.

3.3.3 Deflagration Source Term

The source terms of the deflagration $\dot{\omega}_\mathrm{def}$ and the detonation $\dot{\omega}_\mathrm{vol}$ introduce the influence of reactions into both flame-propagation transport equations. Two source terms exist because the predominant physical influences differ between the flame regimes. Only the maximum value of the two source terms is considered for the solution of the transport equation (see Equations 3.18 and 3.19).

The deflagration source utilizes the gradient ansatz of the *(extended) turbulent flame speed closure* (eTFC) model [148, 149] in Equation 3.27. Its formulation depends on which flame-propagation transport equation is used. The integral heat release of the eTFC model is mesh-independent. Ettner demonstrated this mesh-independence in comparison to Schmid's quadratic source term model [8, 150]. The formulation of the eTFC model for the flame front tracking transport equation 3.19 needs to be divided by the density in order to be consistent (right-hand side term):

$$\dot{\omega}_\mathrm{def} = \underbrace{\rho_\mathrm{u} G \underbrace{\Xi S_\mathrm{L}}_{S_\mathrm{T}}}_{S_\mathrm{eff}} \left| \frac{\partial \widetilde{c}}{\partial x_j} \right| \quad \text{or} \quad \dot{\omega}_\mathrm{def} = \underbrace{\frac{\rho_\mathrm{u}}{\overline{\rho}} G \underbrace{\Xi S_\mathrm{L}}_{S_\mathrm{T}}}_{S_\mathrm{eff}} \left| \frac{\partial \alpha}{\partial x_j} \right| . \tag{3.27}$$

The density correction ρ_u/ρ accounts for the expansion of the burnt gas. Correcting the burning velocity across the flame front with the expansion ratio is required to satisfy the mass balance (see Section 2.2.1). G denotes the quenching factor, which accounts for flame extinction at very high degrees of turbulence. Ξ is the flame wrinkling factor and S_L the laminar flame speed. The resulting effective flame velocity of the turbulent premixed flame is denoted as S_eff.

Figure 3.6 shows the turbulent flame speed closure model, which describes the deflagration source term for both flame-propagation transport equations. Additionally, it summarizes the calculation methods for the three required variables of the eTFC model S_L, Ξ and G. The eTFC model was already applied to small-scale and large-scale H_2-air DDT simulations [4, 8]. The S_L and Lewis number computation is adjusted for H_2-CO-air mixtures in the present thesis. The Lewis number contributes to Ξ. The critical velocity gradient evaluation, relevant for estimating the quenching factor G, was revised regarding the impact of the CO addition to the fuel. The computation methods for the variables S_L, Ξ and G are described separately in the following subsections.

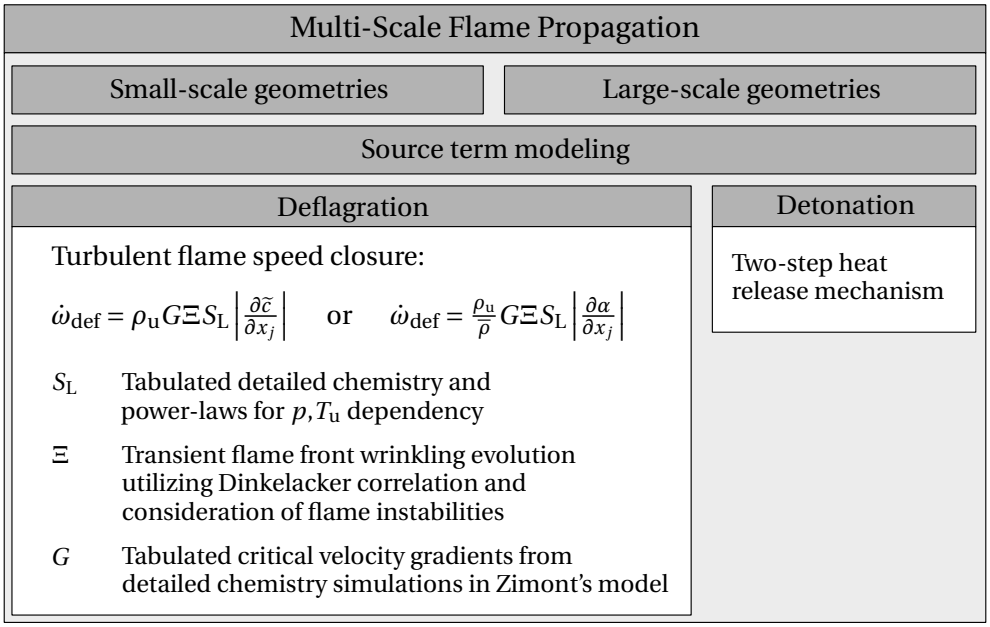

Figure 3.6: Specification of the deflagration source term including evaluation methods for the most-important modeling parameters.

3.3.3.1 Laminar Flame Speed

Typically, unstretched laminar flame speeds $S_{L,0}$ are evaluated at standard reference conditions (p_0=1.013 bar/ T_0=298.15 K), and the temperature and pressure dependencies are addressed separately. Hence, S_L is calculated with

Equation 3.28. A power law accounts for temperature and pressure dependencies:

$$S_L = S_{L,0}(x_f, x_{H_2,f}) \left(\frac{T_u}{T_0}\right)^n \left(\frac{p}{p_0}\right)^m . \tag{3.28}$$

The majority of CFD solvers for explosion risk analysis only consider binary mixtures. In that case, polynomial correlations are sufficient to calculate $S_{L,0}$ [146], e.g., the correlation of Koroll for H_2-air [8, 53]. In ternary H_2-CO-air mixtures, two fuel component dependencies of $S_{L,0}$ must be considered instead of just one. This renders polynomial correlations unpractical and computationally expensive because several nested polynomials are required to capture the influence of two input variables [54,151]. Deriving a polynomial becomes even more challenging when the $S_{L,0}$ evaluation needs to be applied to all possible compositions of the ternary mixture. Hence, a different method is introduced for the newly developed H_2-CO-air CFD solver.

An interpolation table for $S_{L,0}$ is created during pre-processing. It is filled with $S_{L,0}$ entries corresponding to the two input variables fuel mole fraction x_f and H_2 mole fraction in the fuel $x_{H_2,f}$. The use of interpolation tables has two advantages over nested polynomials. Firstly, their evaluation is very fast. Secondly, there are no restrictions to the algorithmic complexity of the required intermediate correlations since they do not have to be evaluated during CFD simulation. Figure 3.7 illustrates the procedure of the interpolation table generation. Intermediate cubic splines are derived from experimental data, numerically generated data and flammability limits. Splines are fitted to the data

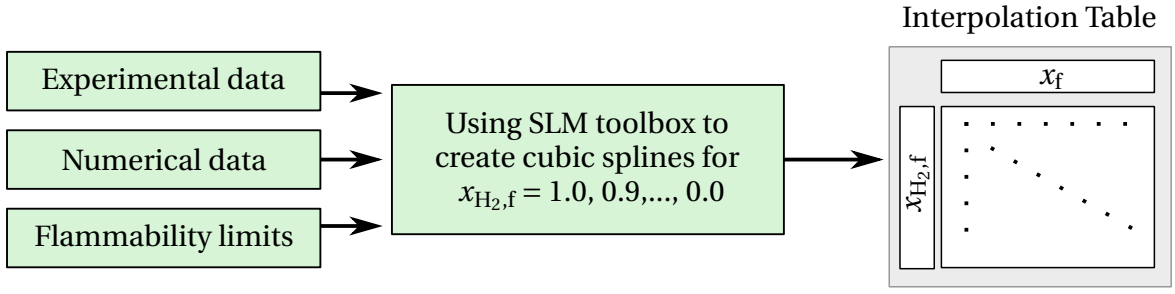

Figure 3.7: $S_{L,0}$ interpolation table generation based on cubic splines computed with the SLM toolbox.

with the freely available Matlab *Shape-Language Modeling* (SLM) toolbox[4]. Finally, the $S_{L,0}$ table entries are computed from the cubic splines.

The interpolation table structure requires that the number of x_f values and their distribution in the x_f array are uniform for all $x_{H_2,f}$ in the table. The existing experimental flame speed data is scattered regarding the input variables and, hence, cannot be used directly as $S_{L,0}$ table entries. Deriving any correlation at constant $x_{H_2,f}$ values requires a densely populated database at varying x_f. However, the existing experimental investigations have focused primarily on specific fuel compositions in H_2-CO-air mixtures, e.g., 50/50, 75/25 or 95/5 H_2/CO. Additionally, the resulting correlations must be valid for all possible mixture compositions to ensure general applicability. Therefore, the database for the derivation of cubic splines comprises flame speed data from different sources:

- **Experimental data:** The research company ProScience GmbH recently provided laminar flame speed measurements covering a wide variation of gas compositions with a focus on lean conditions [9]. Additional measurements from various authors are gathered as a database for the spline derivation [9,51,54,152–161]. Measurements are essential for the derivation of a reliable correlation, especially for lean mixture with fuel contents below 20 vol.-%. Figure 3.8 presents the experimental data set. The color map indicates $x_{H_2,f}$, which is red for pure H_2 fuel and blue for pure CO fuel. The measurement data mainly covers lean H_2-CO-air mixtures.

- **Flammability limit data:** Derived correlations must account for the flammability limits to predict flame extinction due to a deficient reactant correctly. The limits are estimated with the lever rule of Le Chatelier [162, 163] based on the limits of the pure fuel components H_2 and CO. Choudhuri et al. [164] verified the validity of the lever rule with measurements. The lean flammability limits (LFL) are $x_{H_2,LFL} = 0.0485$ and $x_{CO,LFL} = 0.12$. The rich flammability limits (RFL) are $x_{H_2,RFL} = 0.750$ and $x_{CO,RFL} = 0.745$ [17, 43].

[4]SLM toolbox URL: https://de.mathworks.com/matlabcentral/fileexchange/24443-slm-shape-language-modeling

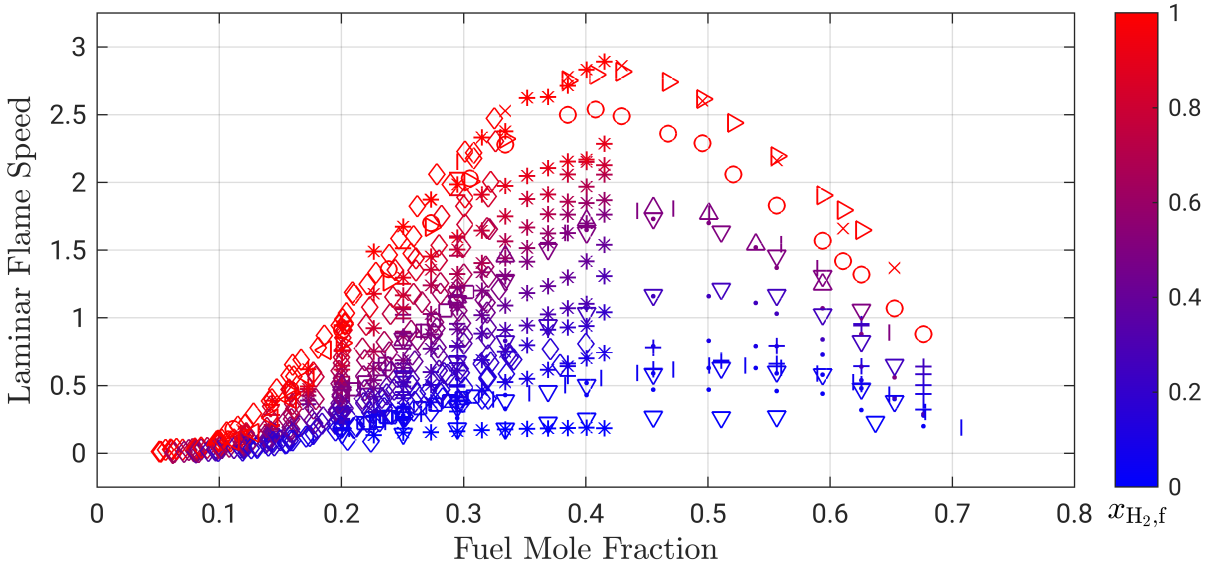

Figure 3.8: Experimental $S_{L,0}$ data used for the derivation of cubic splines. The colormap visualizes amount of H_2 in the fuel varying from pure CO (blue) to pure H_2 (red).

- **Numerical data:** Unstretched fuel consumption speeds are computed in 1D twin-flame simulations using the program Cantera [45] with the reaction mechanism of Davis et al. [46]. The comparative study of H_2-CO-air reaction mechanisms by Olm et al. [147] indicates the mechanism of Davis et al. [46] as the most appropriate for laminar flame speed computation. The twin-flame configuration was chosen for the flame speed computation since it is the only stagnation-point flame configuration used for measurements [52, 164]. Computed $S_{L,0}$ from this configuration agreed better with measurements than those from a fresh-to-burnt configuration. Section 2.2.1 already discussed advantages of a stagnation-point flame over a freely-propagating flame for $S_{L,0}$ computation at lean conditions. x_f is altered with an increment of 0.01 and $x_{H_2,f}$ with an increment of 0.1. Figure 3.9 shows the computed unstretched laminar fuel consumption speeds. The present solver employs the laminar flame speed and fuel consumption speed interchangeably, even though both are required in their own right (see Section 3.3.1). However, the difference between their values is small compared to the uncertainties associated with under-resolved CFD simulations. Moreover, using only one

simplifies the interpolation table generation.

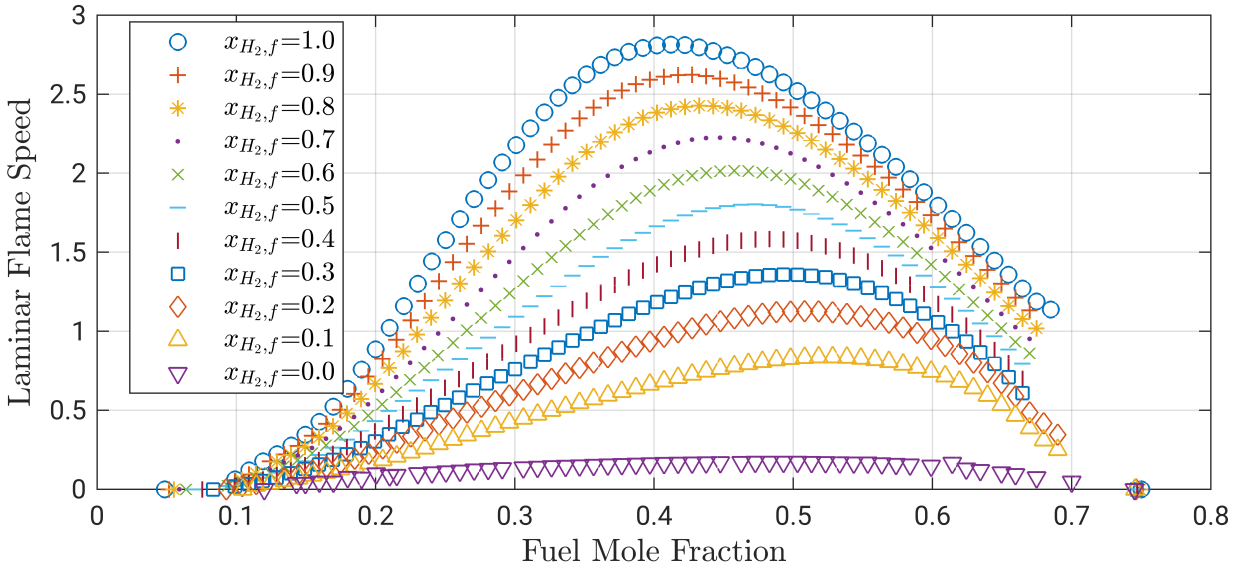

Figure 3.9: Numerical $S_{L,0}$ data and flammability limits used for the derivation of cubic splines.

Cubic splines are derived based on the described database. A correlation is created for every 10 vol-% of $x_{H_2,f}$. Data points within a ±2.5 % deviation from the desired $x_{H_2,f}$ are selected, and cubic spline functions are fitted to the data using the Matlab SLM[5] toolbox. The flammability limits can be specified as constraints for the spline generation, which guarantees flame extinction at the flammability limits. As cubic splines represent a series of cubic polynomials interconnected by nodes, splitting the x_f array into smaller segments improves the input data representation. Figure 3.10 shows $S_{L,0}$ values evaluated with the derived cubic splines of all $x_{H_2,f}$ entries used in the interpolation table.

Ultimately, the interpolation table is generated from the values presented in Figure 3.10. The x_f arrays must have the same array size, and zero values need to be inserted eventually. In Figure 3.11, the $S_{L,0}$ prediction with the interpolation table is validated against measurements by ProScience [9]. The interpolated values agree well with measurement data for most data points. In the

[5]SLM toolbox URL: https://de.mathworks.com/matlabcentral/fileexchange/24443-slm-shape-language-modeling

range of 15 to 20 vol.-% of fuel, deviations are evident at the highest flame speeds. The bomb experiment data from ProScience were not corrected for flame-stretch effects [9, 165], which explains the discrepancies. Most H_2-air data points used for the table generation are flame-stretch-corrected. The experimental flame velocities overshoot because flame stretch increases the laminar flame speed when Le < 1, i.e., for high H_2 contents in the fuel of lean mixtures. Since the results from the generated interpolation table show good agreement with unstretched flame speed measurements for 100 vol.-% H_2 fuels by other authors, the interpolation methodology is considered robust and accurate. The approach of the interpolation table satisfies the flammability limits strictly. This is particularly beneficial in semi-confined simulations, where pure air layers surround the fuel-air vapor cloud.

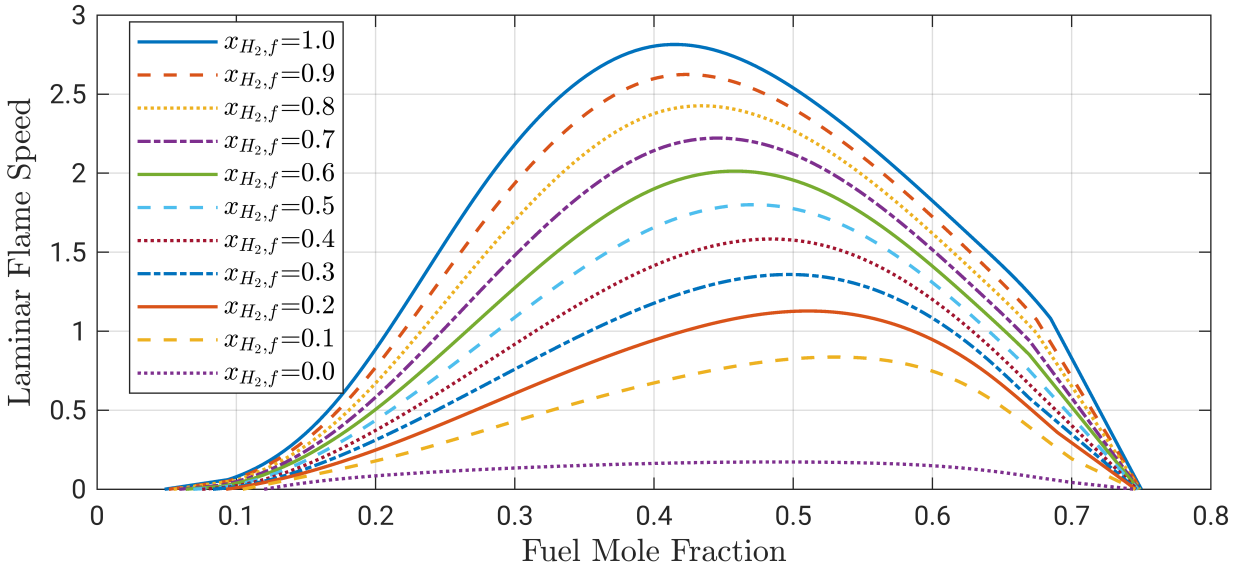

Figure 3.10: $S_{L,0}$ evaluated from derived cubic splines using the Matlab SLM toolbox.

Following the $S_{L,0}$ evaluation, the flame speed dependencies on temperature and pressure are calculated by power laws in Equation 3.28. The laminar flame speed is typically referenced to the unburnt fresh gas state ahead of the flame. Therefore, T_u of the non-reacting mixture is applied for the temperature dependency. The exponents of the temperature and pressure dependencies are derived following the methodology of Szabo et al. [166]. They are extracted

from a double logarithmic plot of numerically calculated flame speeds for varying fresh gas temperatures and pressures. Additionally, the sensitivity of the temperature and pressure dependencies on x_f and $x_{H_2,f}$ must be considered. The temperature exponent n is specified as $n = 1.85$. It is determined as the average of all compositions studied since the sensitivity of n to the mixture composition appears to be generally small compared to the influence of temperature changes. Above 550 K, $n = 2.25$ is proposed. Reliable experimental verification of the exponent is impossible due to the small number of corresponding experiments available [157]. For the pressure dependency, the exponent $m = -0.20$ is adopted from the H_2-air mixtures from previous projects [8]. The pressure exponent from numerically estimated flame speeds in H_2-CO-air mixtures shows no significant deviation from the well-tested value.

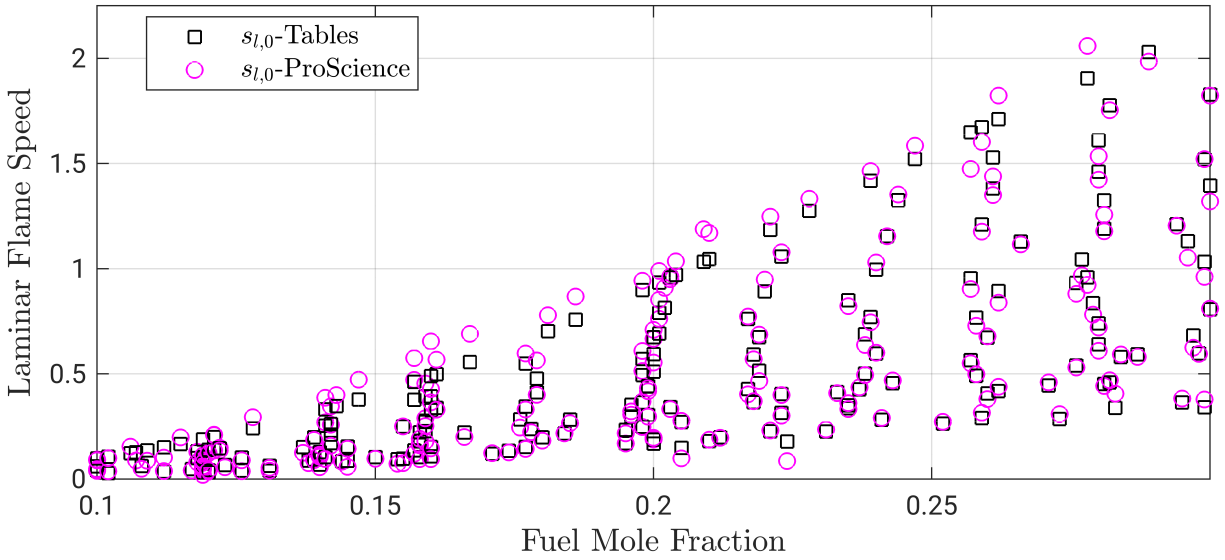

Figure 3.11: Validation of $S_{L,0}$ evaluation from the created interpolation table against $S_{L,0}$ measured by ProScience GmbH [9].

3.3.3.2 Flame Front Wrinkling

Figure 3.12 presents the intermittent shape of a flame front in a turbulent flow. A purely kinetic interaction is assumed between the turbulent flow and the flame front. Hence, the flame front and the flow velocity profile display the

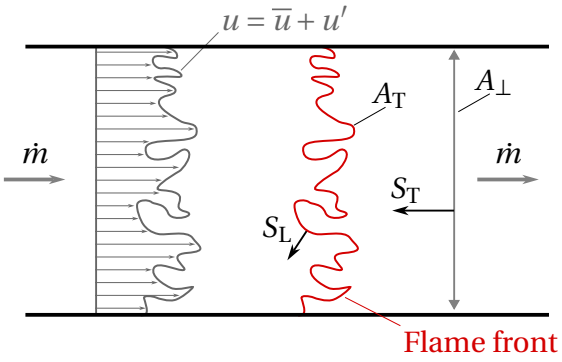

Figure 3.12: Intermittent shape of a flame front (red) and the corresponding flow field (grey) [adopted from [3]].

same shape in Figure 3.12. This assumption is justified as long as a quasi-laminar flamelet structure exists. A relation between laminar and turbulent flame speed can be expressed by reordering the mass continuity equation [3]:

$$\frac{S_T}{S_L} = \frac{A_T}{A_\perp} = \Xi. \tag{3.29}$$

The area ratio of the intermittent, turbulent flame surface A_T to the macroscopic flame surface $A_\perp$ denotes the flame folding term Ξ. It becomes unity for laminar flames. According to Equation 3.29, S_T can be expressed as the product of the flame wrinkling term Ξ and the laminar flame speed S_L. The relation is valid for flames with a Lewis number of $Le \geq 1$. Because the Lewis-number-related deviations become apparent on very fine meshes, the relation is used without restriction in the present CFD solver. On the large cell sizes used in under-resolved simulations, the interpretation of S_T is all the more accurate, as the deviations are averaged over a larger flame surface section in each cell.

Within a single cell of the computational mesh, the macroscopic flame can be interpreted as a surface perpendicular to the reaction progress gradient. This is analogous to the piece-wise linear reconstruction of the flame front in the geoVoF method (see Appendix C.1). According to Equation 3.29, the wrinkling factor Ξ incorporates the complex turbulence-chemistry interaction of premixed combustion. It captures the turbulence influence when turbulent structures are not resolved on coarse meshes.

Weller [145] proposed the transport equation in 3.30 in order to evolve the

flame wrinkling factor Ξ in time. It is based on the concept of flame surface density models [1], but uses Ξ as a transported scalar. The model was adopted without adjustments by Ettner and Hasslberger [4, 167] and successfully applied to H_2-air DDT simulations on different geometrical scales. Hence, it is also used for H_2-CO-air DDT simulations:

$$\frac{\partial}{\partial t}\left(\overline{\rho}\Xi\right) + \frac{\partial}{\partial x_j}\left(\overline{\rho}\Xi\widetilde{u}_j\right) + \Psi_\Xi \frac{\partial \Xi}{\partial x_j} = \overline{\rho}\Xi G_\Xi - \overline{\rho}\left(\Xi - 1\right) R_\Xi + \overline{\rho}\Xi \max\left(0; \sigma_s - \sigma_r\right). \tag{3.30}$$

The transport equation contains the scalar flux Ψ_Ξ, the wrinkling generation rate G_Ξ and the wrinkling removal rate R_Ξ. The last term in Equation 3.30 denotes the influence of flame stretch resolved on the computational mesh. A detailed description of the transport equation is omitted, and the interested reader is referred to the original reference of Weller [145].

The transport equation represents the transient evolution of flame folding as the flame becomes increasingly more turbulent. Starting from a laminar flame with the value $\Xi = 1$, the growth term G_Ξ dominates initially during FA. The smoothing term R_Ξ dampens the flame-wrinkling increase when the flame becomes thermally choked. An equilibrium value Ξ_{eq} is reached once growth and reduction rates are equal. The terms G_Ξ and R_Ξ are both formulated as a function of Ξ_{eq}. In the fresh gas, the value of unity is maintained for Ξ_{eq} by manipulating the growth G_Ξ with a correction for Ξ_{eq}. In contrast to an analytical model, the transient evolution of Ξ can represent non-equilibrium behavior inherent to a rapid FA. The faster the flame accelerates, the more the evolution of flame wrinkling lags behind initially, and the more it overshoots when DDT suddenly reduces flame folding. However, the influence on the onset of DDT is limited, since gas dynamic effects determine DDT. The equilibrium value Ξ_{eq} is calculated by the turbulent flame speed correlation of Dinkelacker et al. [61], which reads

$$\Xi_{eq} = \frac{S_T}{S_L} = 1 + \frac{0.46}{Le_{eff}} Re_T^{0.25} \left(\frac{u'}{S_L}\right)^{0.3} \left(\frac{p}{p_0}\right)^{0.2}. \tag{3.31}$$

According to Equation 3.29, the turbulent flame speed correlation is equal to the equilibrium flame wrinkling factor Ξ_{eq}. The Dinkelacker correlation is selected because its formulation incorporates several aspects relevant for FA:

- **Turbulence influence:** The turbulent Reynolds number Re_T and the velocity fluctuation u' account for flame folding due to turbulent eddies. In fast flames, turbulence is the dominant influencing factor on flame wrinkling. In real-world accident scenarios, the flame path is often obstructed, which significantly promotes turbulence production.

- **Flame instabilities:** Intrinsic flame instabilities wrinkle or smooth the flame surface. While the Landau-Darrieus (LD) instability amplifies flame wrinkling independent of the mixture composition, the thermodiffusive (TD) instability's influence is dependent on the mixture composition (see Section 2.2.3). The TD instability influence is represented in the Dinkelacker correlation 3.31 through the effective Lewis number Le_{eff}. Le_{eff} must be provided in the solver as a correlation regarding H_2-CO-air mixtures. LD instabilities are not explicitly considered in the Dinkelacker correlation. Approaches to describe the LD instability influence on flame speeds are typically based on the self-similarity of the cellular structure of wrinkled flames. It can be expressed by fractal theory [62, 77]. A weak point of Dinkelacker's correlation is that with vanishing turbulence ($u' \rightarrow 0$) the flame speed equals the laminar flame speed. Instead, the influence of intrinsic instabilities on the flame speed should remain present.y

- **Pressure dependency of flame wrinkling:** With increasing pressure, the flame brush is compressed and its thickness reduced. The critical radius for the onset of the cellular breakup of the wrinkled flame decreases (see Section 2.2.3). This intensifies flame wrinkling as laser-optical measurements have shown [7, 63]. The pressure power law in Dinkelacker's correlation 3.31 represents the compression effect on flame wrinkling. However, the correlation does not consider the asymptotic behavior of the pressure dependency at high pressure. It should be included because the flame brush cannot be compressed beyond the limits of the laminar flame thickness [7, 63].

The Dinkelacker correlation is well-suited in describing FA to fast deflagrations before DDT. It accounts for the pressure dependency and the intrinsic

flame instabilities. It performs particularly well for lean mixtures in geometries with strong turbulence promoters, i.e., obstacles in the flame path [168]. All influences of the deflagration in H_2-air mixtures remain relevant when the mixture is extended to H_2-CO-air. Therefore, Dinkelacker's correlation is applied in the developed H_2-CO-air CFD solver for explosion risk assessment.

3.3.3.3 Combustion Instabilities - Effective Lewis Number

The effective Lewis number Le_{eff} must be estimated for the Dinkelacker correlation in Equation 3.31 for all H_2-CO-air mixture compositions. The appropriate Lewis number is defined by the deficient component in the mixture, fuel or oxidizer, identified by the equivalence ratio ϕ.

In the presence of fuel concentration gradients, the limit of a stoichiometric mixture ($\phi = 1$) can be crossed somewhere in the computational domain. Once this happens, the deficient mixture component switches, and the value of Le_{eff} changes abruptly. The resulting sudden change in Ξ_{eq} of the Dinkelacker correlation is non-physical. Hence, a smooth transition between the effective Lewis number of the fuel $Le_{f,eff}$ and the oxidizer Le_{O_2} is introduced, which reads

$$Le_{eff} = Le_{f,eff}(1 - \Phi) + Le_{O_2}\,\Phi. \tag{3.32}$$

The transition formulation is based on the normalized equivalence ratio

$$\Phi = \frac{\phi}{1+\phi}, \tag{3.33}$$

which is bound to the interval from 0 to 1. A stoichiometric mixture ($\phi = 1$) is given by $\Phi = 0.5$. Using the normalized equivalence ratio, an equally weighted mixing of the effective fuel and oxidizer Lewis number is achieved. The methodology described has been applied by Hasslberger [4], and Le_{eff} for H_2-air mixtures is estimated from a polynomial correlation. The approach was adopted here, but the polynomial was derived differently for the multi-component fuel in the H_2-CO-air mixture.

Le_{O_2} of the oxidizer O_2 can be evaluated easily. Dinkelacker et al. [61] propose Equation 3.34 for the effective Lewis number of a multi-component fuel $Le_{f,eff}$.

Bouvet et al. [153] tested different relations to determine $\mathrm{Le}_{\mathrm{f,eff}}$ for a H_2-CO fuel. The relation

$$\mathrm{Le}_{\mathrm{f,eff}} = \frac{a_{\mathrm{M}}}{x_{\mathrm{H_2,f}} D_{\mathrm{H_2,M}} + (1 - x_{\mathrm{H_2,f}}) D_{\mathrm{CO,M}}} \tag{3.34}$$

showed the best agreement with measurements. a_{M} denotes the mean thermal diffusivity of the mixture. The diffusion coefficient in the denominator is evaluated from a mixing law based on the hydrogen mole fraction in the fuel $x_{\mathrm{H_2,f}}$. The diffusion coefficient $D_{\mathrm{i,M}}$ of each fuel component H_2 and CO is defined for the mass diffusion of component i into the present mixture. This definition differs from binary diffusion coefficients used in multi-component mixture diffusion.

A multi-dimensional polynomial is fitted to data evaluated with Equation 3.32 in order to allow a quick evaluation of $\mathrm{Le}_{\mathrm{eff}}$ during simulations. The data covers H_2-CO-air mixture compositions from pure air to pure fuel and all possible

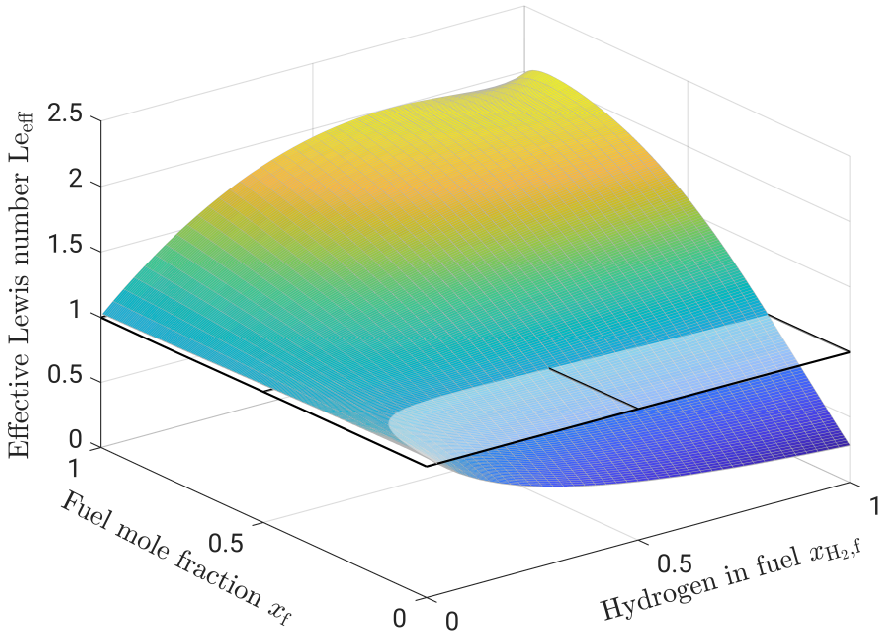

Figure 3.13: Effective Lewis number $\mathrm{Le}_{\mathrm{eff}}$ according to the polynomial expression and additional plane with constant value $\mathrm{Le}_{\mathrm{eff}} = 1$.

fuel compositions. The polynomial is a function of x_f and $x_{H_2,f}$ and reads

$$\begin{aligned} Le_{eff} = 1.044439 &- 1.685161\, x_{H_2,f} - 0.2404606\, x_f + 0.9229039\, x_{H_2,f}^2 \\ &+ 6.073742\, x_{H_2,f}\, x_f + 0.6705638\, x_f^2 - 2.507565\, x_{H_2,f}^2\, x_f \\ &- 1.892691\, x_{H_2,f}\, x_f^2 - 0.4050405\, x_f^3. \end{aligned} \tag{3.35}$$

The resulting Le_{eff} from the polynomial 3.35 are presented in Figure 3.13 together with a transparent plane of Le = 1. The TD instability amplifies flame wrinkling in mixtures whose Le is below the plane. This occurs predominantly in lean H_2-CO-air mixtures. An interesting finding is that even small amounts of hydrogen in the fuel of lean mixtures cause $Le_{eff} < 1$.

3.3.3.4 Turbulent Quenching

The combustion-driven feedback loop of FA generates high flow velocities in the fresh gas. Obstacles in the flame path create strong shear layers, including vortex shedding. This, in turn, induces strong turbulence. At very high turbulence intensities, the smallest eddies, i.e., eddies at the Kolmogorov length scale, are able to perturb the reaction zone of the flame [1, 3]. The high flame stretch in the vortices can lead to turbulent flame quenching (see Section 2.2.2). Thereby, the increase of the integral heat release is limited, damping the combustion-driven feedback loop of FA. Consequently, the onset of detonation can be delayed or even suppressed.

Zimont [6] proposed Equation 3.36 to account for turbulent flame quenching in the TFC model with the quenching factor G. The relation is derived from the log-normal distribution of the turbulent dissipation rate ε [148]. The standard deviation σ of the log-normal distribution is calculated from the ratio of the integral length scale and the Kolmogorov length scale $\sigma = 0.26 \ln(l_T / l_\eta)$. Once the critical dissipation rate ε_{cr} is reached, the value of the error function in Equation 3.36 starts to decrease significantly.

The critical dissipation rate ε_{cr} in Equation 3.37 is determined from the kinematic viscosity ν_u of the non-reacting mixture and the critical flame stretch g_{cr}. In the eddy viscosity concept employed in URANS equations, the turbulence influence, i.e., the Reynolds stress term, is linked to the velocity gradi-

ents. In turbulent flows, the flame stretch is mainly caused by the flow strain. The influence of flame surface curvature can be neglected [7, 169]. Hence, g_{cr} can also be interpreted as the critical velocity gradient at which the flame extinguishes. Dimensional analysis [6] has been used by Zimont to derive Equation 3.38:

$$G = \frac{1}{2}\mathrm{erfc}\left\{-\frac{1}{\sqrt{2\sigma}}\left(\ln\left(\frac{\varepsilon_{cr}}{\varepsilon}\right)\right)+\frac{\sigma}{2}\right\}, \tag{3.36}$$

$$\varepsilon_{cr} = 15\nu_u g_{cr}^2, \tag{3.37}$$

$$g_{cr} = \frac{S_L^2}{a}. \tag{3.38}$$

Turbulent flame quenching must be considered in the DDT modeling strategy to limit FA at very high turbulence. The quenching model of Zimont [6] was applied in the previous solver by Hasslberger [142, 168] for H_2-air DDT simulations. Sufficiently high laminar flame speeds in the binary H_2-air mixtures kept the quenching factor's influence on simulated velocity profiles small in the legacy code versions. Compared to pure H_2 as a fuel, lower laminar flame speeds with fuels containing CO significantly increase the fraction of extinguished flame front, according to Equation 3.38. This raises the question of whether the g_{cr} expression of Equation 3.38 is also appropriate for H_2-CO-air mixtures in FA and DDT simulations.

Evaluating g_{cr} values from 1D simulations with detailed chemistry allows a better understanding of the influence of CO-containing fuels on g_{cr}. The g_{cr} values are computed in 1D twin-flame simulations in Cantera [45](see Section 2.2.1). Instead of extrapolating to zero strain to obtain the unstretched laminar flame speed, the inflow velocity is continuously increased until flame extinction occurs. Flame extinction is identified once the OH radical concentration drops below a threshold larger than the OH equilibrium concentration. This procedure has already been applied to steady-state simulations in gas-turbine combustion chambers with good results [149]. Figure 3.14 compares the resulting values of g_{cr} evaluated with 1D simulations and Equation 3.38 for fuel compositions of 50/50, 75/25 and 100/0 H_2/CO. The velocity gradients are calculated at 1 bar pressure.

Critical velocity gradients g_{cr} estimated from the two approaches yield similar

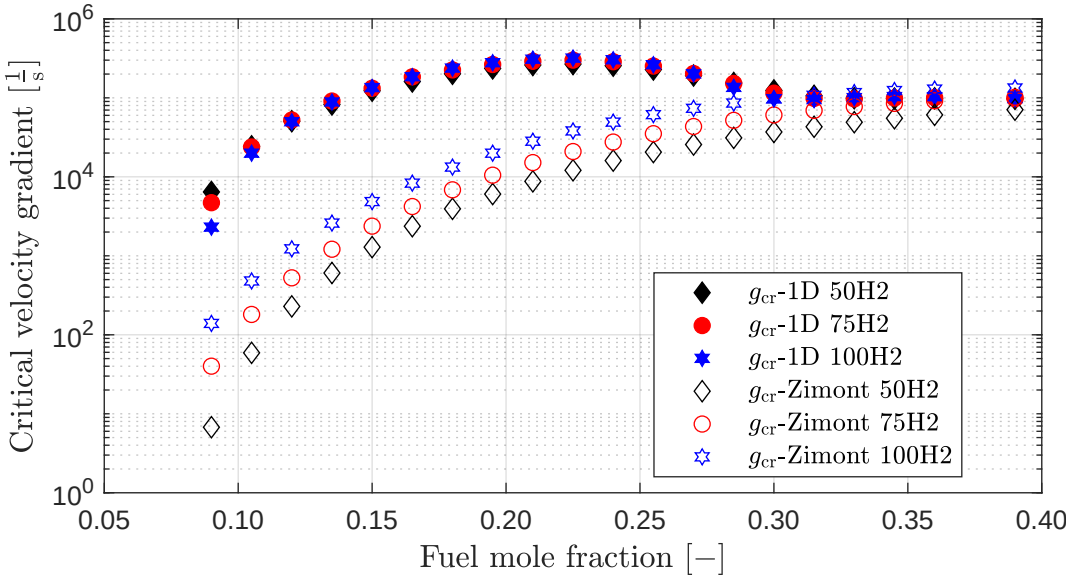

Figure 3.14: Critical velocity gradients evaluated from 1D reactive flow simulations and Zimont's model [6] with 50/50, 75/25 and 100/0 H_2/CO fuels.

values for stoichiometric and rich mixtures ($x_f > 0.3$). At lean mixtures, significant deviations appear regarding trends and values. Proportionally lower laminar flame speeds with increasing CO content in the fuel cause a uniform spacing between curves estimated from relation 3.38 for 50/50, 75/25 and 100/0 H_2/CO. In contrast, the fuel composition has only a minimal impact on the results of the 1D simulations. The g_{cr} values from 1D twin-flame simulations are higher between 15 to 30 vol.-% of fuel than in rich mixtures. The deviations can be explained by the laminar flame speed increase due to flame stretch in lean mixtures with Le < 1. Consequently, higher stretch rates are required for flame extinction when considering the Le influence. Below $x_f < 0.15$, the reactivity declines disproportionately, causing a rapid decrease in the resulting critical velocity gradient of both calculation methods. However, g_{cr} values from Zimont's relation in Equation 3.38 remain several orders of magnitude smaller.

Similar to the previous solver by Ettner and Hasslberger, the S_L evaluation in the present solver only determines the unstretched laminar flame speed (see Section 3.3.3.1). Hence, flame-stretch influences on S_L are not considered in Zimont's relation 3.38 for any of the solvers. The relation cannot repro-

duce the trend indicated by the 1D twin-flame simulations results. Noticeably smaller g_{cr} values can lead to an overpredicted flame front quenching in CO-containing fuels when Zimont's relation 3.38 would be used. Alternatively, g_{cr} values from the 1D twin-flame simulations can substitute Equation 3.38.

Additionally, increasing pressure accompanying FA compresses the flame brush, which steepens the temperature gradient. The flame becomes more robust against flame extinction as a consequence. This pressure dependency can be easily considered in 1D simulation with detailed chemistry. In Zimont's model, it is included indirectly via the laminar flame speed relation in Equation 3.38.

A conclusion on whether turbulent flame quenching should be considered in modeling H_2-CO-air FA and DDT is required. Hence, the general occurrence of turbulent flame quenching is studied for H_2-air and H_2-CO-air mixtures. High-resolution 2D simulations (DNS) of an obstructed explosion channel were performed to address this topic. The framework of the *rhoReactingFoam* available in OpenFOAM has been adopted. The unsteady Navier-Stokes equations are solved in a pressure-based architecture. Adjustable time steps are estimated from the acoustic CFL number of $Co_{acc,max} = 0.1$. Combustion reactions are modeled with a *finite rate* approach, which requires individual transport equations for each species of the reaction system. The kinetic data is taken from the reaction mechanism of Li et al. [14]. Individual diffusion coefficients are specified for each species to account for the different molecular diffusivity (see Appendix A.2). Hence, combustion phenomena based on the high mass diffusion of hydrogen, i.e., TD instabilities, can be captured in the simulation. The 2D consideration is sufficiently accurate since the flame-turbulence interaction leading to flame extinction occurs primarily in tubular structures [1, 58]. The simulation setup mimics the study of Gamezo et al. [170]. Their study only reveals little discrepancies between 2D and 3D numerical results for accelerated H_2-air flames. Figure 3.15 illustrates the 2D computational domain, which has been discretized with a uniform mesh resolution of $\Delta x_{cell} = 0.04\,mm$. The flame front is resolved with a minimum of 10 cells throughout the simulation. This study [171] gives additional detail on the setup.

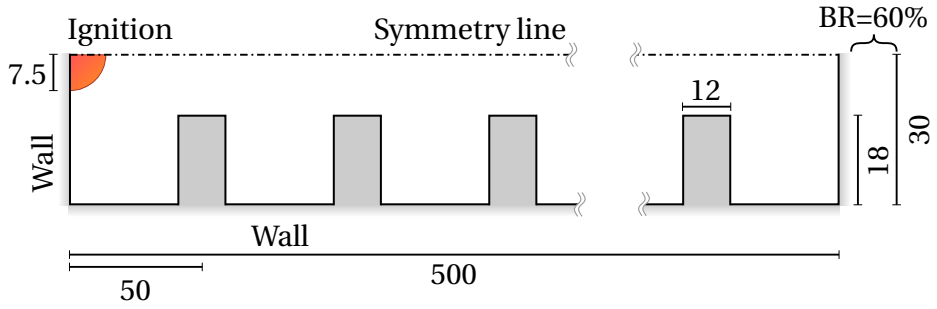

Figure 3.15: Schematic of 2D computational domain in highly resolved simulations (dimensions in mm).

The high-resolution simulations were performed for 22.5 % fuel in air with a fuel composition of 100/0 H_2/CO and 75/25 H_2/CO. Figure 3.16 and 3.17 present temperature contours of the channel section at about 250 mm for different timings. The images include blue iso-surfaces, which indicate regions where the flow velocity gradient exceeds the critical flame stretch g_{cr} estimated from 1D twin-flame simulations. The g_{cr} threshold of the iso-surface is adjusted for the local pressure in Figure 3.16 and 3.17.

The observed flame velocity at the 250 mm position is similar for both fuel mixtures. Nevertheless, the vortices develop further downstream from the obstacle in the CO-containing flame. Once the flame vortices have formed, they penetrate deeper into the fresh gas pocket behind the obstacle compared to the case with pure H_2 fuel. The volumetric substitution of H_2 with CO increases the momentum of the jet flow through the free cross-section between obstacles due to a higher density. Therefore, the shear layer, in which the vortices exist, is extended. Velocity gradients exceeding the g_{cr} values (blue iso-surface) are found primarily in the flame vortices. No significant portion of flame extinction is visible in the areas identified by the blue iso-surfaces for either of the fuel compositions. Only a slight tendency towards increased stretch in H_2-CO fuels exists, which is explained by the higher momentum flow.

Figure 3.16 and 3.17 show that velocity gradients higher than g_{cr} are present in fast deflagrations of H_2-CO-air mixtures in obstructed channels. The flame tip velocity is around 300 m/s for both fuels. Flow velocities and velocity gradients become even higher in thermally choked deflagrations. Therefore, tur-

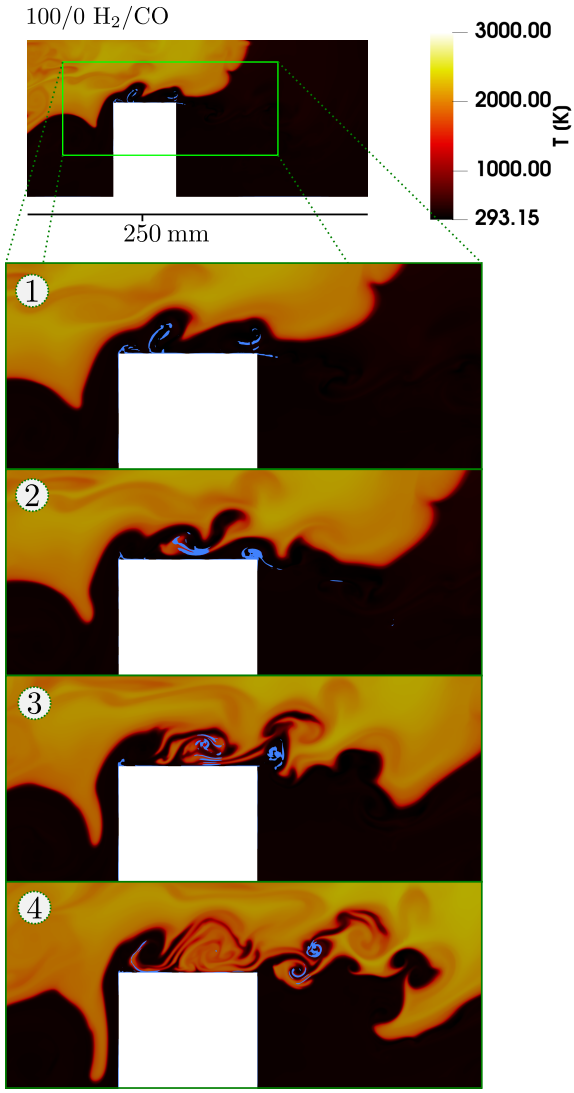

Figure 3.16: Temperature contour with iso-surface (blue) of exceeding flow strain in comparison to the critical velocity gradient (100/0 H_2/CO).

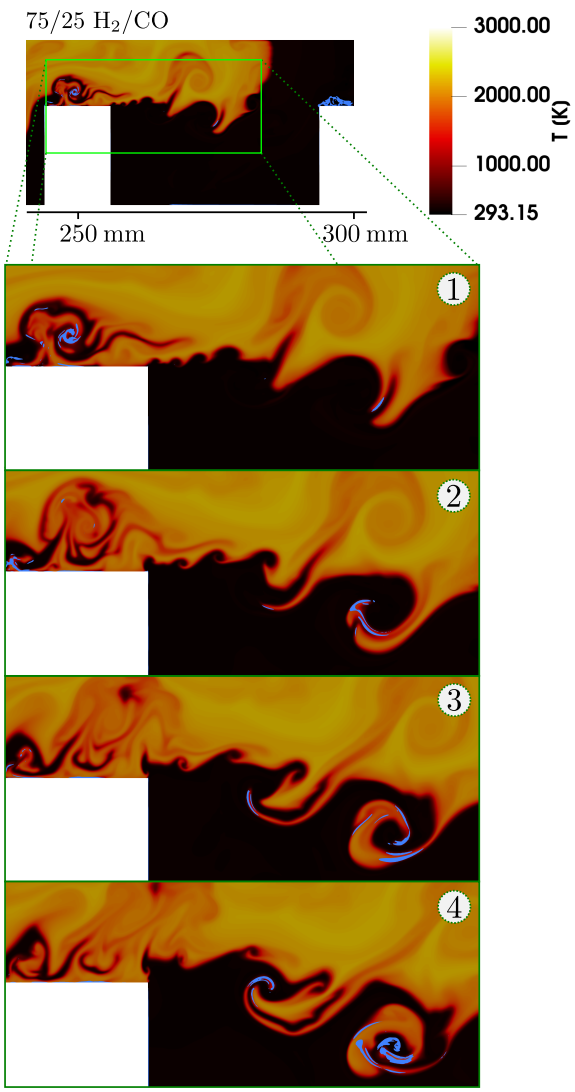

Figure 3.17: Temperature contour with iso-surface (blue) of exceeding flow strain in comparison to the critical velocity gradient (75/25 H_2/CO).

bulent flame quenching cannot be neglected [171]. Zimont's model for turbulent flame quenching is applied in the developed solver. However, the critical velocity gradient g_{cr} is tabulated from 1D twin-flame simulations during preprocessing to account for Lewis number and pressure dependencies. Zimont's expression 3.38 is substituted with a direct evaluation of g_{cr} from the created interpolation table during simulations.

The input variables of the table are x_f, $x_{H_2,f}$ and p. Analogous to the laminar flame speed, all compositions from pure fuel to pure air can be evaluated. Since the quenching factor G is only relevant to deflagrations, the pressure input is varied from 0.7 bar to 10 bar. The fresh gas temperature also influences g_{cr}. The number of input variables for the table generation is reduced by approximating the fresh gas temperature with isentropic relations according to the specified pressure. The standard reference conditions are employed as a basis in the isentropic relations. This practice assumes that primarily weak pressure waves are present during most parts of the flame acceleration phase. The relevance of turbulent quenching declines once flame velocities close to the sound speed of the combustion products a_{pr} are reached, and gas-dynamic effects start to dominate the flame propagation.

Figure 3.18 presents simulated flame tip velocity profiles obtained from the two different g_{cr} evaluations. Two simulated flame velocity profiles are compared to measurements in the obstructed explosion channel of the GraVent facility filled with 20 vol.-% of 50/50 H_2/CO in air.Section 4.2 describes the test rig in more detail. The experimental data indicates several auto-ignition events. The resulting quasi-detonation exhibits a flame velocity between a_{pr} and D_{CJ}. Zimont's g_{cr} relation in Equation 3.38 falsely suppresses DDT because

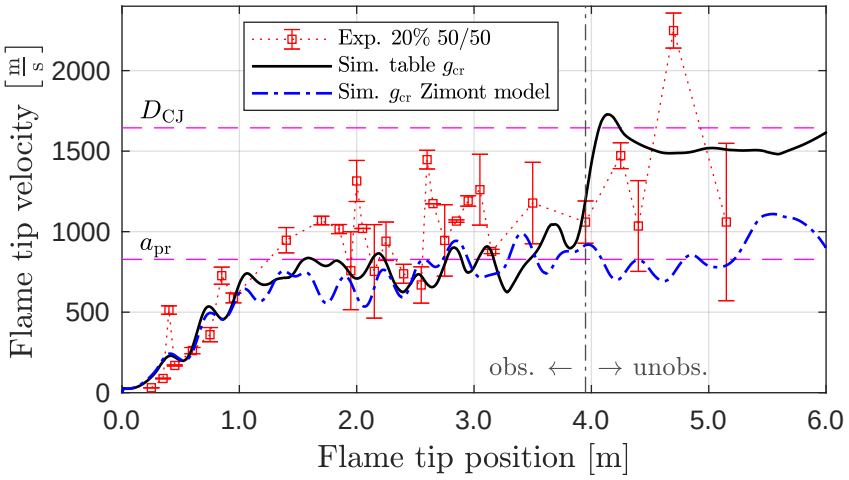

Figure 3.18: Impact of the g_{cr} evaluation method on the flame tip velocity profile of a 20 vol.-% fuel-air mixture with 50/50 H_2/CO in the GraVent explosion channel (BR60S300).

the velocity of a thermally choked fast deflagration a_{pr} is only reached close to the end of the obstructed channel section. Using the interpolation table with detailed chemistry information allows the prediction of DDT. Subsequently, a stable detonation establishes in the unobstructed channel section. This behavior is in agreement with the measurement. If the measurements indicate a potential DDT, CFD codes for risk assessment should predict DDT deterministically. The g_{cr} evaluation from the interpolation table with detailed chemistry information contributes to this behavior of the CFD solver.

3.3.4 Detonation Source Term

Gas-dynamic effects dominate detonations. The compression of fresh gas by pressure waves causes self-ignition. The continuous heat release after self-ignition maintains a shock wave in front of the reaction zone. At the same time, the pressure wave compresses fresh gas to levels beyond the auto-ignition temperature. As a consequence, a self-sustaining detonation complex forms.

Because the combustion regime of detonations differs fundamentally from flamelet-like combustion, a suitable combustion model is required for the volumetric heat release after auto-ignition. Figure 3.19 outlines the modeling strategy for the detonation source term $\dot{\omega}_{vol}$. A two-step mechanism is applied, which consists of a detonation criterion and a quadratic heat release function. The two-step mechanism represents the detonation's structure consisting of a shock wave and a reaction zone.

A spatial and temporal resolution of the detonation complex is unfeasible in CFD simulations for safety analysis. However, the thermodynamic states of the detonation complex described in the ZND theory (see Section 2.3) can be captured quantitatively correctly. The corresponding length scales, e.g., the induction length, do not need to be accurately represented. This primarily works because the Chapman-Jouguet point resembles a stable state for the detonation, which fluctuations relax to.

A gradient approach similar to the deflagration source term is inadequate for

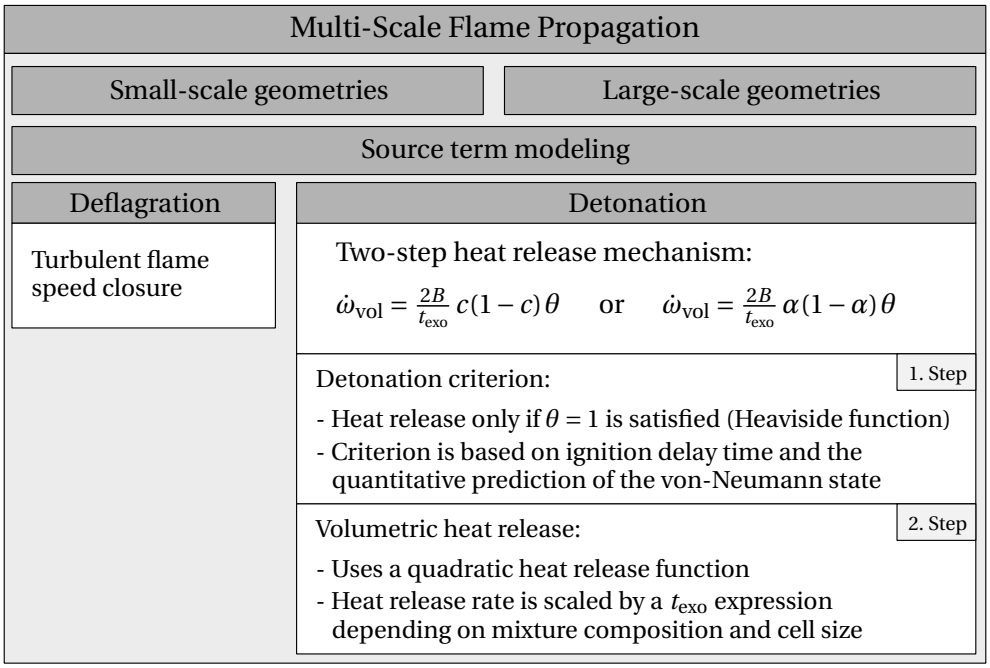

Figure 3.19: Specification of the detonation source term, including a two-step heat release mechanism.

detonations because the reaction zone always covers 3 to 5 cells. A thickened detonation reaction front gives inaccurate pressure loads when waves are reflected at walls [89]. Hence, a quadratic heat release function is applied combined with a detonation criterion. This approach is based on the forest-fire mechanism of the CREBCOM code [126]. In that code, the reaction jumps from one cell to the next. The two-step mechanism with quadratic heat release was implemented in the legacy code versions [4, 8]. However, the detonation criterion and the heat release function are improved to create a more accurate and generally applicable detonation source term model. A cell-size and mixture-composition-dependent dynamic scaling of the heat release function is implemented. It guarantees a correct heat release rate in detonations.

3.3.4.1 Detonation Criterion

The rapid volumetric heat release due to detonation occurs once the detonation criterion θ is satisfied. The criterion guarantees that the fresh gas is suffi-

ciently preconditioned for DDT. In other words, it ensures that the shock front ahead of the reaction zone and its thermodynamic state is captured quantitatively correctly. The shock front, required for adequate conditioning of the gas mixture, is sustained by the rapid auto-ignition combustion of the detonation. Because under-resolved simulations cannot capture the induction length, the shock front cannot be sustained ahead of the reaction zone. Hence, the shock front and the reaction zone coincide in the same cell with a temporal offset. This influences the formulation of the detonation criterion θ, which reads

$$\begin{aligned}\theta = \max(&\mathrm{H}(\tau-1)\cdot\mathrm{H}(T-T_{\mathrm{vN}})\cdot\mathrm{H}\left(p|^{t-1}-p|^{t}\right)\cdot\mathrm{H}(c-0.001)\,;\\ &\mathrm{H}(\tau-1)\cdot\mathrm{H}\left(10^{-16}-c\right)).\end{aligned} \tag{3.39}$$

The criterion relies on multiple Heaviside step functions. It is only formulated with respect to c in Equation 3.39. If the flame tracking approach is used for the flame-propagation transport equation, c is simply substituted with α. The two terms of the maximum argument resemble the scenarios of DDT in the flame vicinity (weak solution) and DDT due to shock-focusing (strong solution), respectively. The criterion covers several conditions for the onset of the detonation source term:

- **Detonation in the flame vicinity or due to shock-focusing:** The criterion separates the phenomena of DDT in the flame vicinity with the condition $c > 0.001$ and of DDT due to shock-focusing with the condition $c < 10^{-16}$.
- **Ignition delay time:** The fresh gas must be compressed sufficiently by pressure waves to trigger auto-ignition. The non-dimensional ignition delay time τ indicates the possibility of auto-ignition based on the thermodynamic state of the gas mixture.
- **Representation of the von Neumann plateau:** In order to capture the maximum pressure loads of detonations, the von Neumann plateau has to be captured in under-resolved simulations. It has been shown that an early heat release suppresses the formation of the von Neumann pressure peak in the under-resolved approach [172]. Because the shock front and the reaction zone coincide in the same cell in the simulation, the pressure quickly approaches the CJ value. Therefore, the heat release needs to be

delayed until the maximum pressure is reached. Thereby, the von Neumann peak of stable detonations is captured. The corresponding condition $H(p|^{t-1} - p|^{t})$ is met once the pressure decreases in the current time step t in comparison to the previous time step $t-1$.

The condition for the cell temperature T to be above the von Neumann temperature T_{vN} contributes to the robustness of the θ criterion. Since $c > 1$ holds in the concerned cells, the cell temperature will eventually exceed the von Neumann temperature T_{vN} (see Section 2.3). The T_{vN}-based Heaviside function safeguards against premature auto-ignition. T_{vN} values can be obtained from the methodology used for the evaluation of the local gas composition (see Section 3.3.2.1).

The detonation criterion 3.39 is similar to the implementation of Hasslberger [4]. However, it is designed to be more robust by treating the DDT scenarios separately and accounting for T_{vN}. The ignition delay time indicates the onset of the auto-ignition based on kinetic data. It is fundamental for the presented two-step heat release mechanism. The non-dimensional ignition delay time

$$\tau = \frac{t_{\mathrm{calc}}}{t_{\mathrm{ign}}(x_{\mathrm{f}}, x_{\mathrm{H_2,f}}, T, p)} = \frac{Y}{Y_{\mathrm{cr}}} \tag{3.40}$$

is defined as the ratio of the simulation calculation time t_{calc} and the ignition delay time $t_{\mathrm{ign}}(x_{\mathrm{f}}, x_{\mathrm{H_2,f}}, T, p)$. It can also be understood as a measure of the radical pool necessary for the branching reactions of the reaction system to dominate. This condition holds above a critical mass fraction of radicals Y_{cr}. Once Y_{cr} is reached, rapid conversion to the products takes place. The ignition delay time resembles the period of time until the critical limit is present. The dimensionless ignition delay time τ is evolved in time with the transport equation 3.41 to account for the fresh gas preconditioning during FA [4]. The transient evolution of τ [173] indicates the influence of the flame history on the onset of detonation:

$$\frac{\partial}{\partial t}\left(\overline{\rho}\widetilde{\tau}\right) + \frac{\partial}{\partial x_j}\left(\overline{\rho}\widetilde{u}_j\widetilde{\tau}\right) - \frac{\partial}{\partial x_j}\left(\overline{\rho}D_{\mathrm{eff}}\frac{\partial\widetilde{\tau}}{\partial x_j}\right) = \frac{\overline{\rho}}{t_{\mathrm{ign}}(x_{\mathrm{f}}, x_{\mathrm{H_2,f}}, T, p)}. \tag{3.41}$$

Above a critical auto-ignition temperature, the ignition delay time drops significantly, and the term on the right-hand side of the equation increases. At

$\tau = 1$ auto-ignition is possible. The ignition delay time depends on the composition and thermodynamic state in the gas $t_{\mathrm{ign}}(x_{\mathrm{f}}, x_{\mathrm{H_2,f}}, T, p)$. The time scale t_{ign} is provided to the solver efficiently via interpolation tables. The table entries are precalculated using the *Shock and Detonation Toolbox*[6], a script library for Cantera [45]. Based on the conclusion of the comparative study of Olm et al. [147], the reaction mechanism of Li et al. [14] performs best for ignition delay time evaluation. It is thus used to compute t_{ign}. The interpolation table has four input variables. The created table covers all mixture compositions from pure air to pure fuel with fuel compositions from pure H_2 to pure CO. Since the shock front coincides with the reaction zone, the temperature changes due to shock compression cannot be captured accurately by the non-reacting temperature T_{u} (see Section 3.3.2). Hence, the ignition delay time is evaluated based on the cell-averaged temperature.

3.3.4.2 Quadratic Heat Release Function

Once the detonation criterion is satisfied, the volumetric source term releases heat via a quadratic function. The auto-ignition combustion in the detonation's reaction zone is reaction-rate-limited, like the reaction in a perfectly mixed isochoric reactor [1]. The typical profile of the reaction progress in this reactor can be approximated by a tanh-function, which reads

$$c(t) = \alpha(t) = \frac{1}{2} + \frac{1}{2}\tanh\left(\frac{B}{t_{\mathrm{exo}}}t\right). \tag{3.42}$$

The tanh-function becomes self-similar when the scaling factor B/t_{exo} is tuned according to a specified interval of c or α. The value $B \approx 4.5951$ refers to the interval $c \in [0.01; 0.99]$ [4]. With this function scaling, c or α increase from 0.01 to 0.99 in the exothermal time scale t_{exo}.

The quadratic heat release function in Equation 3.43 is the time derivative of the tanh-function (Equation 3.42) [4]. The formulation of the equation depends on the selected flame-propagation transport equation. The parabolic profile of the function has a maximum at $c = 0.5$. The equation is similar to the quadratic deflagration model derived by Schmid et al. [150]. Like Schmid's

[6] Shock and Detonation Toolbox URL: https://shepherd.caltech.edu/EDL/PublicResources/sdt/

model, the quadratic function is generally not mesh-independent [8]. The correction in Equation 3.44 prevents that the quadratic function always remains zero when $c = 0$:

$$\dot{\omega}_{\mathrm{vol}} = \frac{2B}{t_{\mathrm{exo}}} c^* \left(1 - c^*\right) \theta \qquad \text{or} \qquad \dot{\omega}_{\mathrm{vol}} = \frac{2B}{t_{\mathrm{exo}}} \alpha^* \left(1 - \alpha^*\right) \theta, \tag{3.43}$$

$$c^* = c + 0.001 \cdot H(10^{-15} - c) \cdot H(\tau - 1) \qquad [\text{same for } \alpha^*]. \tag{3.44}$$

The high conversion rates of the quadratic function lead to a compact detonation complex with a maximum width of two cells in the under-resolved approach. However, the conversion rate needs to be scaled with t_{exo} to maintain a correct detonation velocity D_{CJ} on all mesh sizes. The scaling is dependent on the cell size and the local mixture reactivity.

In stable detonations, the reaction front and the pressure wave must propagate with corresponding velocities to each other [5]. If not, the reaction gradient can overtake the shock wave, and the detonation decays or the shock wave decouples from the reaction front [174, 175]. Accurate simulation of the onset of detonations not only requires capturing the coupling between the reaction front and the shock wave. Prediction of failed DDT attempts or decoupling of shock and reaction front must also be possible.

In principle, even an unphysically fast reaction front could sustain the shock wave in front of the reaction. The detonation criterion θ always keeps the reaction behind the shock ($H(p|^{t-1} - p|^t)$). At the same time, no possibility exists for decoupling the shock and reaction front with an overestimated conversion rate. Consequently, the solver would create an overly conservative DDT prediction if the conversion rate is not scaled appropriately with t_{exo}. However, if it is scaled correctly, the possibility exists that the reaction cannot follow the shock and, hence, the detonation decays into a deflagration. This shows the relevance of an accurate t_{exo} scaling for the simulation of DDT and detonation propagation.

3.3.4.3 Cell-Size and Mixture-Composition-Dependent Scaling of the Source Term

Figure 3.20 illustrates the propagation of a stable detonation front through a computational cell of size Δx_{c} at the propagation speed of stable detonations

D_{CJ} [39,82,83]. The volumetric source term $\dot{\omega}_{vol}$ must be scaled by t_{exo} in order to guarantee a mean conversion of the cell volume that is equivalent to the scenario in Figure 3.20. If only the volumetric source term would be used in the flame-propagation transport equation, t_{exo} would represent the time for the detonation to traverse the cell. In practice, the deflagration source term partially converts the cell before the detonation criterion $\theta = 1$ is reached. Hence, $\dot{\omega}_{vol}$ needs to be higher in order to maintain a mean propagation velocity of D_{CJ} across the cell.

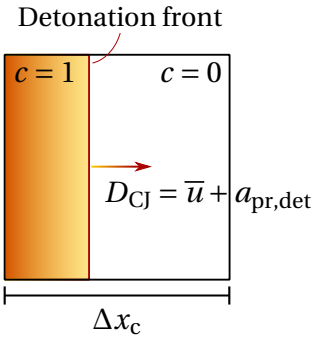

Figure 3.20: Length and time scales for a detonation front traversing a single cell.

The observed detonation speed D_{CJ} consists of the convective bulk flow $\overline{u}$ and the burning speed of the reaction. According to the ZND theory, the reaction front's relative propagation speed is equal to the speed of sound of the detonation products $a_{pr,det}$ [5, 39]. As the source terms in the flame-propagation transport equations (see Section 3.3.1) describe the reaction front propagation only relative to the fluid flow, the appropriate time scale for the reaction reads

$$t_{CJ} = \frac{\Delta x_c}{a_{pr,det}}. \tag{3.45}$$

The D_{CJ} as well as $a_{pr,det}$ can be calculated using Cantera with the *Shock and Detonation Toolbox*. The velocity $a_{pr,det}$ is precalculated and provided to the solver through an interpolation table. The convective flow necessary to reach D_{CJ} does not have to be considered since the corresponding heat release induces it.

The time measure t_{CJ} depends on the traveled distance Δx_c by the detonation

front, i.e., the cell size. As a consequence, the propagation direction matters to the time scale. However, the flame-propagation transport equations describe a volumetric conversion of the cell from unburnt to burnt. Consequently, the traveled distance needs to be conveyed into a volume profile of the cell along the projected flame propagation direction. In order to reduce complexity, a mean cell distance Δx_c is estimated from the cell volume V_c according to

$$\Delta x_c = \sqrt[3]{V_c}. \tag{3.46}$$

The more uniform the cell aspect ratios are, the more accurate the method becomes. By using Δx_c from Equation 3.46 in Equation 3.45 the source term $\dot{\omega}_{vol}$ is dynamically adjusted via t_{exo} and the source term model becomes mesh-independent. In addition, the dependency on the mixture reactivity is accounted for by the tabulated values of $a_{pr,det}$.

An appropriate expression for the scaling quantity t_{exo} based on t_{CJ} is derived in the following. c and α can be substituted by each other without any adjustments in the equations of the volumetric source term model. The derivation of the source term scaling is only expressed in terms of c for the sake of simplicity.

Figure 3.21 illustrates a typical temporal evolution of the c-profile in a single computational cell during under-resolved detonation simulation. The overall conversion of the cell needs to remain within t_{CJ}. The blue dashed line indicates the required mean progression. As the shock front and the detonation front coincide in the same cell, the detonation criterion θ is reached at a reaction progress limit c_{lim}. Beforehand, c rises due to the deflagration source term and convection. c_{lim} is reached in the corresponding time period t_{def}. Only values of c_{lim} and t_{def} contribute to the scaling function. Thus, the trend is depicted as linear for the sake of simplicity. The linear progression can be interpreted as a mean convective source. The time scale t_{def} is tracked for each cell, starting with the value $c = 0.01$.

The time t_{def} has passed before the detonation criterion is reached. Therefore, the time left for the detonation source term to convert the remaining fresh gas to fully burnt reduces to $t_{det} = t_{CJ} - t_{def}$. The required mean conversion rate of

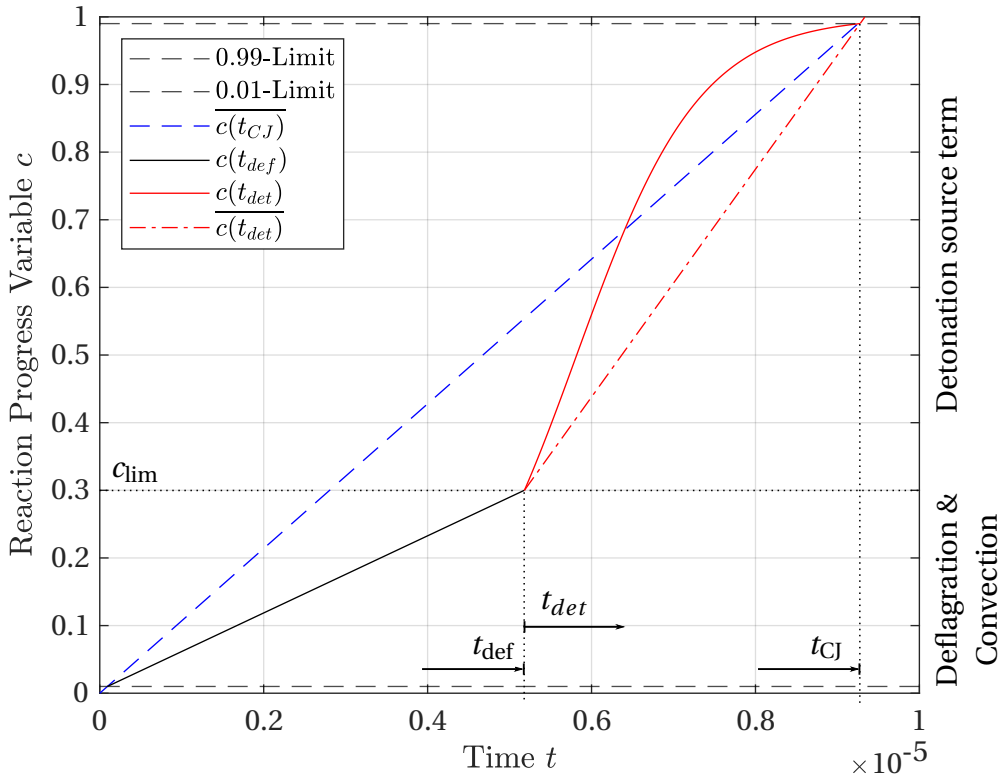

Figure 3.21: Temporal c-profile evaluated with the volumetric source term scaling methodology with generic input variables c_{lim} and t_{def} ($\phi = 1$ in 75/25 H_2/CO).

the detonation source term $\overline{\dot{\omega}}_{\mathrm{vol}}$ needs to be adjusted according to

$$\overline{\dot{\omega}}_{\mathrm{vol}} = \frac{0.99 - c_{\mathrm{lim}}}{t_{\mathrm{CJ}} - t_{\mathrm{def}}}. \tag{3.47}$$

The corresponding mean progression of c is shown in Figure 3.21 as a red dash-dotted line. Knowing $\overline{\dot{\omega}}_{\mathrm{vol}}$, an expression for t_{exo} can be derived from the mean gradient of the quadratic heat release function 3.43. The relation reads

$$\overline{\dot{\omega}}_{\mathrm{vol}} = \frac{1}{t_{\mathrm{exo}} - t(c_{\mathrm{lim}})} \int_{t(c_{\mathrm{lim}})}^{t_{\mathrm{exo}}} \dot{\omega}_{\mathrm{vol}}\, dt = \frac{1}{t_{\mathrm{exo}} - t(c_{\mathrm{lim}})} \left[\underbrace{c(t_{\mathrm{exo}})}_{0.99} - \underbrace{c(t(c_{\mathrm{lim}}))}_{c_{\mathrm{lim}}} \right]. \tag{3.48}$$

The integral function of the volumetric source term $\dot{\omega}_{\mathrm{vol}}$ is the reaction progress tanh-profile in Equation 3.42 itself. Since $\dot{\omega}_{\mathrm{vol}}$ is only relevant in detonations, $\theta = 1$ is assumed for the derivation of the scaling function. It does not influence Equation 3.48. The c progression function in Equation 3.49 can be

rearranged with the relation in Equation 3.50 to solve for the time $t(c)$, which yields Equation 3.51. The tanh-function in Equation 3.49 is an adjustment of Eqauation 3.42 to prescribe the condition of $c = 0.01$ at $t = 0$. It should be noted that the time $t(c_{\text{lim}})$ needs to be evaluated in reference to Equation 3.49:

$$c(t) = \frac{1}{2} + \frac{1}{2}\tanh\left(\left(\frac{t}{t_{\text{exo}}} - \frac{1}{2}\right)B\right), \tag{3.49}$$

$$\text{artanh(x)} = \frac{1}{2}\ln\left(\frac{1+x}{1-x}\right), \tag{3.50}$$

$$t(c) = \left(\frac{1}{2} + \frac{1}{2B}\ln\left(\frac{c}{1-c}\right)\right)t_{\text{exo}} \qquad \text{with:} \qquad B \approx 4.5951. \tag{3.51}$$

Substituting $t(c_{\text{lim}})$ in 3.48 by the expression 3.51 and transforming the equation in order to solve for t_{exo} yields in the final scaling function

$$t_{\text{exo}} = \frac{0.99 - c_{\text{lim}}}{\overline{\dot{\omega}}_{\text{vol}}\left(\frac{1}{2} - \frac{1}{2B}\ln\left(\frac{c_{\text{lim}}}{1-c_{\text{lim}}}\right)\right)}. \tag{3.52}$$

The appropriately scaled c-profile (solid red curve) in Figure 3.21 is obtained by applying $\overline{\dot{\omega}}_{\text{vol}}$ from Equation 3.47 to the scaling function in Equation 3.52 and evaluating the c-profile of Equation 3.49. The volumetric source term is only scaled to reach the upper limit $c = 0.99$ within t_{exo}. In practice, full conversion is reached quickly without requiring any additional modeling. Two exceptions need to be considered:

- If t_{def} exceeds the time t_{CJ}, $\overline{\dot{\omega}}_{\text{vol}} = 1/t_{\text{CJ}}$ is used as an exception to Equation 3.47. In that case, $\overline{\dot{\omega}}_{\text{vol}}$ resembles the blue dashed line in Figure 3.21.
- In the unlikely case that a cell with fresh gas ($c = 0$) burns only in the detonation regime, the t_{exo} evaluation can be simplified according to

$$t_{\text{exo}} = \left(c_{\text{upper}}(B) - c_{\text{lower}}(B)\right)t_{\text{CJ}} = (0.99 - 0.01)\,t_{\text{CJ}}. \tag{3.53}$$

  The time scale for the complete conversion of the cell t_{CJ} needs to be reduced to the time range the self-similar tanh-function in Equaiton 3.43 is specified on ($c \in [0.01; 0.99]$ for $B \approx 4.5951$). A possible occurrence of this scenario is the initial auto-ignition following shock-focusing.

In contrast to the static expression $t_{exo} = k\Delta t_{calc}$ used in the previous CFD code implementation [4], the analytically derived scaling function 3.52 provides a cell-size and mixture-composition-dependent conversion rate. It satisfies the condition that the reaction reaches complete conversion in a cell within the time scale t_{CJ}. As a consequence, the coupling of the shock front and the reaction zone is based on a precisely scaled conversion rate. In addition, the current analytical scaling of the heat release function reduces the number of user-dependent input variables, i.e., k, which enhances the code usability.

3.3.4.4 1D Validation of the Detonation Source Term Model

The model is verified with generic 1D detonation simulations. Stable detonations are directly initialized by setting 20 % of the 1D domain to the CJ state. This includes initializing the flow velocity in the combustion products according to the ZND theory in the absolute reference frame. The sides of the 1D mesh are configured as a *empty*-type boundary and the front and back as solid walls.

The main goal of the scaling procedure is to obtain a correct volumetric conversion rate - independent of the cell size. In Figure 3.22, flame tip velocities of simulations with varying cell sizes are compared with each other. A horizontal line of $D_{CJ} = 1886.5\,m/s$ is added. The fuel content in the simulations is 30 vol.-% fuel in air (75/25 H_2/CO). The mesh in all simulations comprises the same number of cells. Hence, the axial flame tip position is normalized with the length x_{ign} initialized as CJ state to allow a direct comparison of the simulations.

The position of the flame tip is tracked over time in the simulations. The spatial derivative of the resulting flame trajectory gives the observed flame tip velocity. A smoothing function is applied to eliminate outliers originating from the discrete nature of the data. The findings of the cell-size comparison study are:

- Almost exact flame velocity curves for all simulations prove the mesh in-

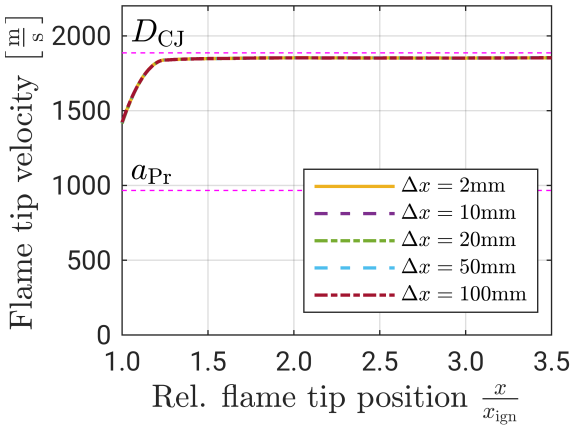

Figure 3.22: Simulated detonation velocities of varying cell sizes in comparison to D_{CJ} (30 vol.-% fuel in air - 75/25 H_2/CO).

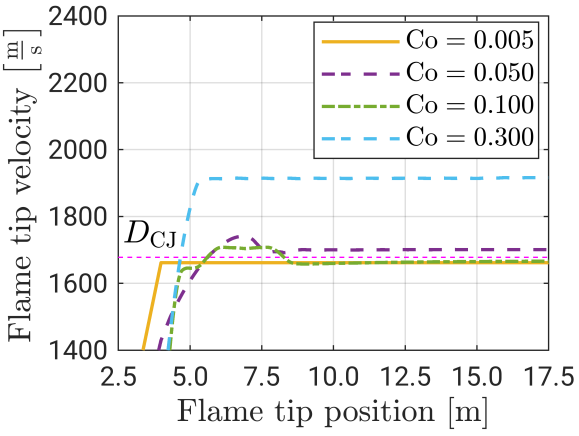

Figure 3.23: Simulated detonation velocities of varying Co number in comparison to D_{CJ} (20 vol.-% fuel in air - 75/25 H_2/CO).

dependence of the scaled volumetric heat release model.

- Only a small deviation of max. 36 m/s from the calculated D_{CJ} is found, which indicates good model accuracy.
- The deviation from D_{CJ} is similar to those reported in other under-resolved detonation simulations [8, 89, 172]. However, none of the mentioned detonation modeling strategies consistently reproduce the flame velocity when cell sizes vary.

The influence of the temporal resolution on the scaling function performance is also analyzed. Flame velocities obtained from simulations with varying limiting CFL numbers are compared in Figure 3.23. In all simulations, the mesh has the same uniform cell size of 20 mm. The findings of the CFL number comparison study are summarized:

- Apart from Co = 0.30, all curves remain within an acceptable deviation from D_{CJ}. Deviations between the simulated curves are expected because the influence of varying time step size is not compensated by the scaling function in contrast to the cell size.
- Simulations with varying CFL numbers differ in their number of time

steps, which cover the volumetric heat release of the detonation source term. If $\Delta t > t_{\mathrm{det}}$ holds, the resulting conversion rate after the solution of the flame-propagation transport equation ($c_{\mathrm{lim}} \rightarrow c = 1$) is smaller than determined by the scaling function.

- An early auto-ignition at a low c_{lim} causes the strong deviation of the Co = 0.30 flame velocity profile. This leads to a large amount of released heat within a single time step. The resulting detonation is similar to an over-driven detonation with a significantly higher propagation velocity.
- A sufficiently small CFL number is required for accurate simulation of detonation propagation. Most importantly, the CFL number must be small enough to capture the convective and deflagrative increase of c to c_{lim} without overshooting. The minimum scale $\Delta t \approx t_{\mathrm{det}}$ appears as a good practice. However, the scaling function works as intended and can be applied without restrictions.
- The investigation cannot be transferred directly to the onset of DDT because the corresponding flame velocities around a_{pr} are close to the wave propagation velocity considered by the acoustic CFL number definition. Consequently, the temporal resolution at the onset of DDT is finer than at the stable detonation propagation. Hence, higher limiting CFL numbers can be selected at the onset of DDT.

The temporal evolution of p, T and c are tracked at a fixed location during a 1D detonation simulation. Figure 3.24 presents the corresponding profiles. All plots show profiles obtained with the previously applied constant value scaling $k\Delta t$ and the presented dynamic scaling of t_{exo}. The profiles stem from a detonation simulation with 20 vol.-% fuel in air (75/25 H_2/CO). The 1D mesh is 20 meters long, consisting of cubic cells with an edge length of 20 mm. The CFL number is specified as $\mathrm{Co}_{\mathrm{acc}} = 0.1$, which resembles a typical setting for FA and DDT simulations. The profiles are tracked in time at the axial position of 10.0 m, which is located far away from potential ignition or wall influences.

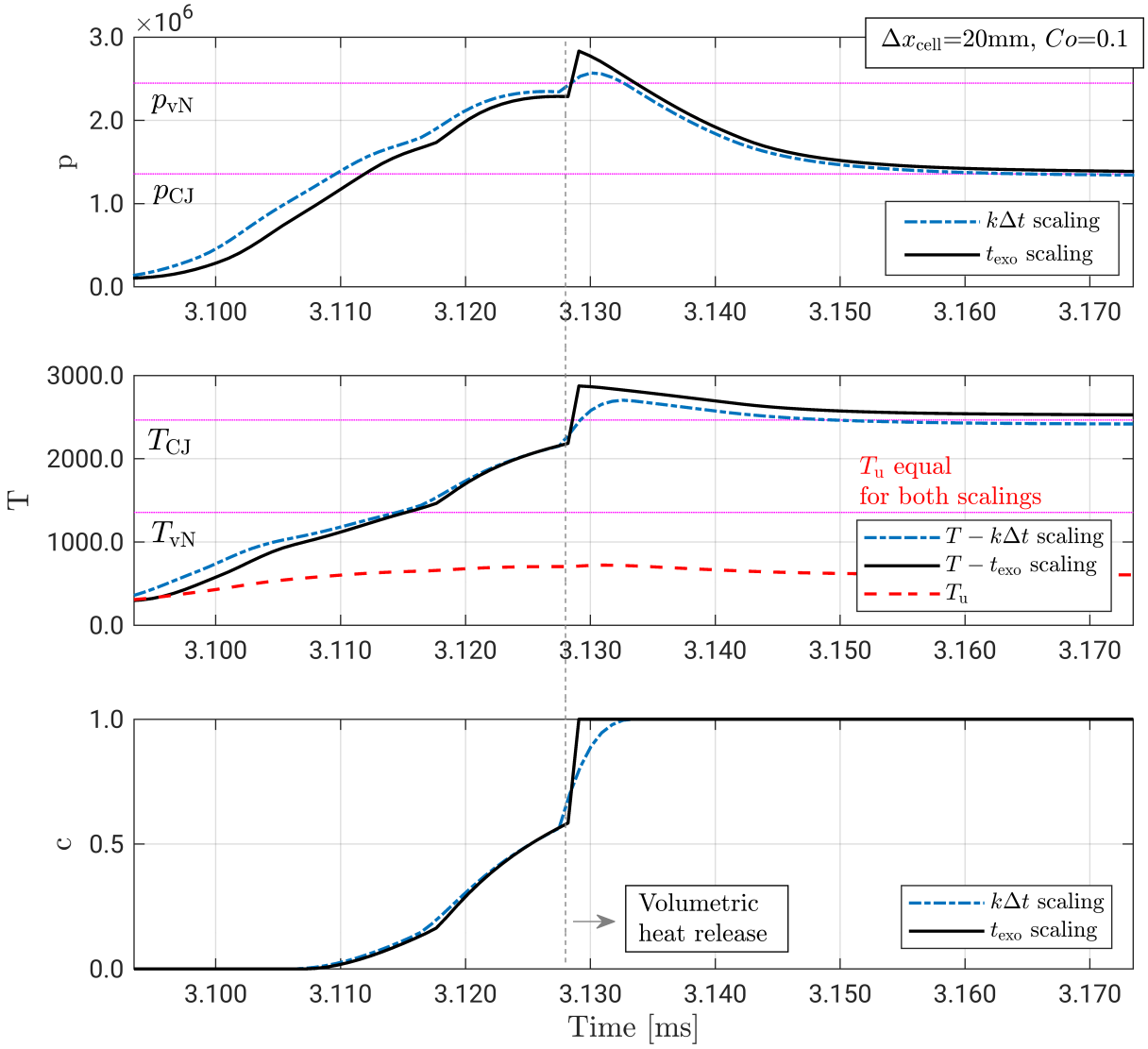

Figure 3.24: Temporal evolution of pressure p, temperature T and reaction progress c tracked at the fixed axial position of 10.0 meter (20 vol.-% fuel in air (75/25 H_2/CO) and a cell size of 20 mm).

The convection of burnt gas and the subsequent rapid volumetric heat release can be identified by their drastically different slope in the c profiles for both scaling methods. The quadratic heat release function activates once the detonation criterion θ is satisfied. In the stable detonation regime, the pressure-related criterion of θ is the most restrictive. The pressure is required to decrease between two time steps. The vertical gray dashed line indicates that

moment. However, the pressure does not quite reach p_{vN} before volumetric heat release. Due to the rapid heat release of the auto-ignition, the pressure eventually rises above p_{vN}. Compared to simulations without the pressure-related criterion in θ, the onset of volumetric heat release is delayed. Higher c_{lim} values are the consequence. At the same time, the pressure condition in θ ensures that the von Neumann pressure peak p_{vN} is reached [172]. Capturing the von Neumann pressure peak is essential for the risk analysis of the confining structure. As expected, the pressure relaxes to p_{CJ} behind the reaction zone for stable detonations. The p profile of the ZND theory can be reproduced by the detonation source term model with acceptable accuracy.

c increases before self-ignition occurs. Hence, no temperature increase due to compression alone can be identified in the T profiles. The von Neumann temperature T_{vN} is not explicitly captured in the T profiles in Figure 3.24. The expected temperature after the reaction zone T_{CJ} is closely met by the T profiles. Because the temperature change of the non-reacting T_u due to shock compression cannot be described easily within the heat release zone (see Section 3.3.2), T_u remains far below T_{vN}. Only temperatures around T_{vN} would be sufficiently high to trigger auto-ignition. Consequently, the ignition delay time needs to be evaluated with the average cell temperature.

While the static $k\Delta t$-scaling with $k = 20$ always distributes the volumetric heat release over several time steps, the dynamic t_{exo}-scaling results in a single time step for the heat release under the presented conditions as indicated by the c profiles. This profile difference is also visible in the p and the T plots. The composition of the combustion products specifies the amount of released heat by the reaction. Because the tabulated von Neumann state, T_{vN} and p_{vN}, is used to evaluate the burnt gas composition in the simulations of both scaling methods, the resulting thermodynamic states are very similar. The only noticeable difference is present at the onset of volumetric heat release. A stretched-out heat release over several time steps damps the overshoot in the pressure profile. The expansion of hot combustion products counteracts the pressure increase due to the rapid conversion rate rise. The overshoot of p and T in the simulation with dynamic t_{exo}-scaling is more pronounced since the heat release occurs within one time step. Utilizing t_{exo}-scaling, D_{CJ} is barely

under-predicted in Figure 3.23 by only 13 m/s. Since the reaction front's relative propagation speed is scaled correctly, the kinetic energy of the bulk flow has to be lower. Consequently, more sensible energy is kept, and the temperature slightly exceeds T_{CJ}.

The main advantage of the novel dynamic t_{exo}-scaling over the previously used static scaling is maintaining D_{CJ} on all mesh sizes and time steps for varying gas compositions. The static scaling resulted in a 60-150 m/s offset from the expected D_{CJ} with varying cell sizes and compositions. The dynamic t_{exo}-scaling allows minimum deviations of 10-20 m/s. The lower mean conversion rate due to the stretched-out volumetric heat release by the static scaling can cause a failed DDT attempt, as the reaction front might not be able to follow the shock wave. Hence, predicting heat release within one time step by the dynamic t_{exo}-scaling is considered necessary under these conditions.

3.4 Efficiency-Related Solver Development

The applicability of the developed CFD solver to real-world H_2-CO-air explosion risk assessment depends on the solver's computational efficiency. Typically, risk assessment requires parameter studies. Hence, the computation time of single simulations has to be kept as low as possible. This aspect is essential for large-scale scenarios where the number of cells is significantly higher. Especially in industrial-scale scenarios, the computation times can become restrictive. In the development of the present solver, computational efficiency has been improved primarily in three areas:

- **Efficient model design:** The reaction-progress-variable-based representation of the flame is an efficient CFD solver design. Additionally, detailed chemistry information is provided through interpolation tables instead of correlations for combustion parameters with multiple dependencies. Corresponding parameters are laminar flame speeds or critical velocity gradients. For example, using interpolation tables instead of nested correlations for the $S_{L,0}$ evaluation in H_2-CO-air mixtures result in a 10% faster computation.

- **Adaptive mesh refinement:** Adaptive mesh refinement (AMR) was introduced to the CFD solver by Hasslberger [4]. The mesh is refined only in three regions of interest, the flame vicinity, regions of pronounced turbulence production and gas-dynamic effects. AMR significantly lowers computation times compared to refining the entire domain [128]. The method is improved in the current work to better suit the application of the solver to semi-confined geometries.
- **Load-balancing algorithm for the geoVoF method:** The computationally intensive geoVoF method used in the flame-propagation transport equation for large-scale geometries only requires computation in flame front cells. Consequently, an imbalance of computational workload between processors in a parallelized simulation originates because flame front cells are typically present in only a few processor domains. Simple massive parallelization is very ineffective in reducing computation time. A newly implemented load-balancing algorithm for the geoVoF method (LB-geoVoF) achieves significantly better efficiency - already at low processor counts. As the LB-geoVoF method's performance scales with the number of flame front cells, a synergy is created between the LB-geoVoF method and AMR.

The last two areas of improvements are described in more detail in the following.

3.4.1 Adaptive Mesh Refinement

Adaptive mesh refinement (AMR) is suitable for transient computation of flame fronts to effectively save computation time by only resolving regions of interest. OpenFOAM only supports AMR for hexahedra in its unstructured mesh topology [176]. Therefore, the applicability of the solver to complex geometries is not restricted by AMR as long as meshes with hexahedra are used.

Flame-dynamics, turbulence and gas-dynamic effects primarily dominate FA and DDT. Therefore, AMR should increase the mesh resolution at the flame front, regions of high turbulence production and pressure waves. A threshold

criterion triggers mesh refinement. It is specified to suit the purpose of explosion simulations. Table 3.1 summarizes the criteria for the three regions of interest depending on the flame-propagation transport equation used. The presented terms are evaluated in every cell. Their results are summed up, and once the threshold of 0.1 is exceeded, the corresponding cell is refined. AMR reverts to the original mesh if the threshold is no longer met. A maximum refinement level of two provides a good compromise between accuracy and additional computation time due to the higher load on individual processors.

Table 3.1: Criteria expressions for the three different flow features of interest for AMR execution.

	Volume reaction model (c-equation)	Flame front tracking model (α-equation incl. geoVoF)
Flame vicinity	$H\left((c-0,001)\wedge(0,999-c)\right)$	$H\left(\dfrac{\left\lvert\left(\dfrac{\partial\alpha}{\partial x_j}\right)^{\mathrm{NAG}}\right\rvert}{\max_{\Omega}\left[\left\lvert\left(\dfrac{\partial\alpha}{\partial x_j}\right)^{\mathrm{NAG}}\right\rvert\right]}-0,01\right)$
Turbulence production	$\dfrac{\left\lvert\dfrac{\partial\lvert u_i^*\rvert}{\partial x_j}\right\rvert}{\max_{\Omega_\mathrm{u}}\left[\left\lvert\dfrac{\partial\lvert u_i^*\rvert}{\partial x_j}\right\rvert\right]}$	$\dfrac{\left\lvert\dfrac{\partial\lvert u_i^*\rvert}{\partial x_j}\right\rvert}{\max_{\Omega_\mathrm{u}}\left[\left\lvert\dfrac{\partial\lvert u_i^*\rvert}{\partial x_j}\right\rvert\right]}$
Gas-dynamic effects	$H\left(\dfrac{\left\lvert\dfrac{\partial p}{\partial x_j}\right\rvert}{\dfrac{p_\mathrm{aicc}}{3\cdot\Delta\overline{x}_\mathrm{c}}}-0,025\right)$	$H\left(\dfrac{\left\lvert\dfrac{\partial p}{\partial x_j}\right\rvert}{\dfrac{p_\mathrm{aicc}}{3\cdot\Delta\overline{x}_\mathrm{c}}}-0,025\right)$
Sum of effects	>0.1	>0.1

Hasslberger introduced the flame vicinity term and the turbulence production term [4,168]. The use of a Heaviside function forces the refinement in the reaction zone. At the same time it ensures that the refinement is reversed as soon as a cell is completely burnt ($c=1$). If the geoVoF method is used, the thresh-

old term for the flame vicinity is based on the normalized flame front gradient. It is evaluated with the node-averaged Gaussian (NAG) gradient scheme of the geoVoF method. Normalization is carried out with the maximum value in the entire domain, indicated by the subscript Ω.

The region of pronounced turbulence production is included via the normalized velocity gradient. The gradient is computed on a manipulated velocity field u_i^*. A *zeroGradient* boundary condition is applied to walls instead of a zero velocity condition. This prevents disproportional refinement at the walls.

In Hasslberger's implementation [168], gas-dynamic effects were considered based on the non-reacting density ρ_u. The applicability of the present CFD solver is extended to semi-confined geometries. In this case, the interface between pure air and combustible mixture introduces a density gradient unrelated to gas-dynamic effects. In order to prevent unwanted refinement, the threshold term for gas-dynamic effects is formulated based on pressure instead. The pressure gradient is normalized with a pseudo-gradient in Table 3.1. The denominator is a static expression. This holds the advantage that refinement can be restricted to sufficiently strong pressure waves. Hence, weak acoustic waves in the slow early phase can be excluded from refinement. This behavior compliments the density-based solver as the solver tends to overestimate waves at very slow flow velocities. The pseudo-gradient for normalization is specified as a pressure change over three times the mean cell width $\Delta\overline{x}_\mathrm{c}$, calculated from the cell volume ($\Delta\overline{x}_\mathrm{c} = \sqrt[3]{V_\mathrm{c}}$). For the pressure change, the pressure after adiabatic isochoric complete combustion p_aicc is applied. The two-dimensional fitting function in Equation 3.54 is used to evaluate p_aicc during the simulation run. The function accounts for the dependencies of p_aicc on x_f and $x_{\mathrm{H_2,f}}$. For very lean mixtures below $x_\mathrm{f} < 0.05$, a constant value of $p_\mathrm{aicc} = 2.8452 \cdot 10^5\,\mathrm{Pa}$ and for rich mixtures above $x_\mathrm{f} > 0.70$ a value of $p_\mathrm{aicc} = 5.3033 \cdot 10^5\,\mathrm{Pa}$ is used instead. As soon as the normalized value exceeds 0.025, the Heaviside function allows cell refinement:

$$\begin{aligned} p_\mathrm{aicc} =& 5.038087 \cdot 10^4 - 2.493652 \cdot 10^4\, x_{\mathrm{H_2,f}} + 5.313911 \cdot 10^6\, x_\mathrm{f} \\ & - 1.226538 \cdot 10^4\, x_{\mathrm{H_2,f}}^2 - 4.343147 \cdot 10^4\, x_{\mathrm{H_2,f}}\, x_\mathrm{f} \\ & - 1.093893 \cdot 10^7\, x_\mathrm{f}^2 + 1.004991 \cdot 10^5\, x_{\mathrm{H_2,f}}^2\, x_\mathrm{f} \\ & - 5.353102 \cdot 10^4\, x_{\mathrm{H_2,f}}\, x_\mathrm{f}^2 + 6.270539 \cdot 10^6\, x_\mathrm{f}^3. \end{aligned} \tag{3.54}$$

3.4.2 Load-Balanced Geometrical Volume-of-Fluid Method

According to Amdahl's law, an infinite number of processors reduces the overall computation time of a parallelized program to the time taken by the serial code segments [177]. This assumption of perfect scaling implies an evenly distributed workload between all processors. If that is not the case, underloaded processors are waiting for overloaded processors to finish their tasks. A non-uniform load distribution can have three primary reasons:

- **Uneven distribution of cells per processor:** Some processors might have more cells to compute than others. This scenario is commonly encountered in CFD simulations with highly localized phenomena, which are resolved with a finer mesh during the simulation, e.g., AMR in explosion simulations. AMR refines the region of interest and increases the imbalance of workload. Figure 3.25 illustrates the generation of an imbalance of workload due to the refinement of a region of interest (marked in red). A static domain decomposition is considered, which is typical for most CFD frameworks.

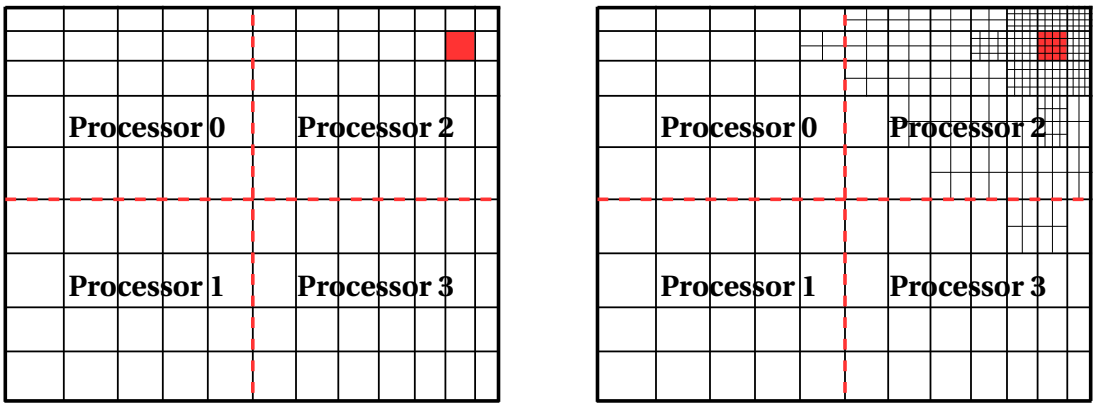

Figure 3.25: A non-uniform mesh before (left) and after AMR (right), including static domain decomposition with four parallel processors.

- **Calculation tasks with different computational effort:** Imbalance of workload between processors also stems from the different complexity of their computation task. The geoVoF method, by its very nature, cre-

ates vastly different computational complexity for each cell because certain computations are only required in flame front cells. Hence, processors containing flame front cells exhibit a higher workload. The geometric evaluation of the convective fluxes is computationally very demanding.

- **Heterogeneous hardware:** The processor types or the communication between individual machines in a cluster setup can differ. While load-balancing regarding the computation environment is a field of ongoing research [178], it is rarely addressed in application programs. Hence, this source of imbalance is not considered in the present work.

Noticeable imbalance exists in large-scale simulations with the previous CFD solver for explosion risk assessment due to the first two reasons. The computationally intensive geoVoF evaluation, in combination with AMR, puts a heavy load on processors, which contain sections of the flame front. The number of flame front cells per processor directly scales with the imbalance of the workload. Table 3.2 indicates that a minimum of 57% of the overall computation time is consumed by the geoVoF method. This time fraction decreases with increasing processor count because more processors cover the flame front cells after the finer domain decomposition at the simulation start. Hence, the number of flame front cells in heavily loaded processors is reduced, and the time for underloaded processors waiting for the geoVoF evaluation to finish reduces. However, the imbalance remains high, as the computation time of geoVoF dominates the overall computation.

Table 3.2: Fraction of the overall computation time consumed by the geoVoF method in a generic large-scale simulation with varying degrees of parallelization.

Processor	Time fraction taken by geoVoF method [%]
16	80.1
32	74.45
48	64.37
64	57.22

Straightforward massive parallelization is an ineffective way to reduce computation time. The imbalanced workload is split among more processors, but it persists nonetheless. The possible speedup by merely increasing the parallelization is limited. The imbalance leads to idle times for underloaded processors, which must wait until overloaded processors finish their computation. A load-balancing (LB) algorithm evenly distributes the workload between processors and thereby reduces overall computation time. Figure 3.26 demonstrates a generic parallelized computation with and without an LB algorithm. It displays the time periods required for necessary operations during computation. The overall computation time is determined through the time required by the most heavily loaded processor. The LB algorithm distributes the workload evenly. The exchange of additional data packages from overloaded to underloaded processors demands additional communication. The additional communication time can be taken into account as an additional load. A small residual waiting time remains even when LB methods are applied. However, significant speedup gains are achieved already at low processor counts. The computation time reduction by the LB algorithm can be interpreted as an enhanced efficiency or the option to compute the same simulation on fewer processors. Especially the latter perspective increases the framework's applicability.

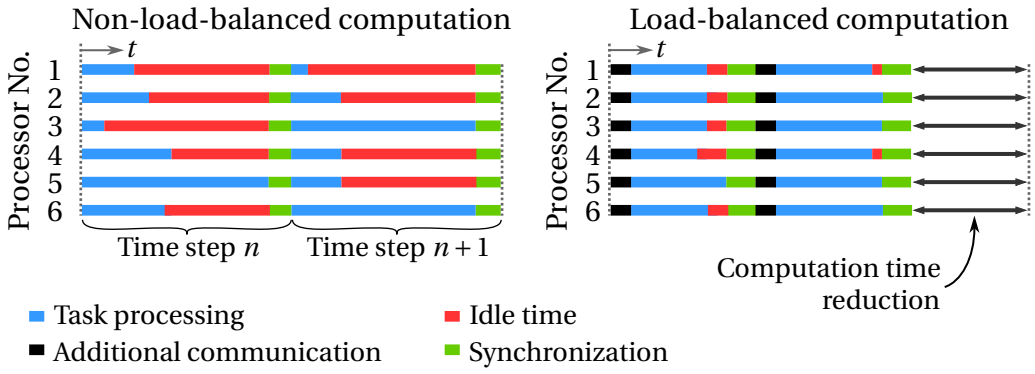

Figure 3.26: Processing time of two consecutive time steps in a six processor system without (left) and with (right) load-balancing algorithm [adopted from [10]].

3.4.2.1 Load Balancing Algorithm LB-geoVoF

Jofre et al. introduced an LB algorithm for the geoVoF method [179], which was implemented in a self-developed CFD code employing structured meshes. So far, no implementation of an LB algorithm for the geoVoF method has been presented for OpenFOAM applications in the literature. Therefore, an LB algorithm is introduced to the H_2-CO-air CFD solver in the present thesis. The implementation is based on the process steps described by Jofre et al. [179]. However, it was adjusted to fit the communication and the unstructured mesh topology of OpenFOAM for parallel computation.

In order to better understand the interaction of the LB algorithm with the geoVoF method, the solution steps of the flame-front-tracking flame-propagation transport equation are briefly summarized:

- **Flame front orientation:** The node-averaged Gaussian (NAG) gradient scheme is applied on the burnt volume fraction field α to evaluate the flame front orientation.
- **Reconstruction:** The flame front position is reconstructed by iterative positioning of a cutting plane inside the flame front cell in the flame propagation direction. The cell is geometrically truncated, and α is determined each iteration until the desired burnt volume is achieved. Larger cells require more iterations to meet the tolerance of accuracy.
- **Advection:** Flux polyhedra are geometrically constructed on the cell surfaces. The transported volume of burnt gas across each surface is evaluated by geometrical truncation of the flux polyhedra with the reconstructed flame front plane.
- **Flame-propagation transport equation:** The flame-propagation transport equation given in Section 3.3.1 is solved.
- **Redistribution:** When the bounding limits of the interval $\alpha \in [0;1]$ are violated in a cell, the burnt volume fraction α exceeding the limit is redistributed between adjacent cells in order to preserve the combustion progress.

- **Coupling of flame and flow:** The discontinuous α field is transferred to a steady profile of the reaction progress variable c in order to represent the flame front.

A detailed description of the geoVoF operation steps can be found in Appendix C.1. The computation time of the geoVoF method is almost entirely determined by the three operations NAG, reconstruction and advection. While NAG and advection hold similar shares with 10-20% of the geoVoF computation time, reconstruction takes up 60-80%. The shares of the computation times strongly depend on the geometry, the ignition source and the cell size of the specific simulation.

In contrast to the NAG gradient scheme, the reconstruction and advection steps are only carried out in flame front cells. Hence, the workload imbalance is much higher for the reconstruction and advection steps. Consequently, the LB algorithm is designed to distribute the workload of the reconstruction and advection steps. It sends computation packages from overloaded processors to underloaded processors. Two key aspects to accomplish this task are the design of the inter-processor communication and the provision of the required mesh data to each processor. The implementation in the present thesis is specifically adapted to the OpenFOAM framework regarding these two aspects. These efforts represent substantial contributions to the introduction of the LB algorithm outlined by Jofre [179]. The LB-geoVoF method can be outlined as follows:

- **Static LB algorithm:** Domain decomposition between processors remains unchanged, and all computational tasks are considered equally intensive. Additional communication cost due to the LB algorithm is taken into account as additional workload.
- **Hybrid local/global mesh topology:** Each processor contains its local decomposed mesh and a global mesh. The global mesh consists of a coherent list of mesh data from each processor. The coherent list of the global mesh is created and distributed only at the simulation start and once upon each mesh update. This procedure reduces communication steps but comes at the cost of high memory usage.

- **Collective inter-processor communication:** Few large data packages are distributed between all processors. Every processor gets process data about all other processors using *all-to-all* communication with *OpenMPI* based functions inherent to the OpenFOAM framework (*gatherList/scatterList*).

The LB-geoVoF method is programmed as an object-oriented OpenFOAM class, which provides good reusability of the developed method. It can be easily transferred to other OpenFOAM solvers. The subsequent process steps of the LB algorithm are presented in an abbreviated form to keep the focus of this thesis on the explosion simulations and to display the LB method as a feature improving the applicability of the CFD solver. A detailed description, including the OpenFOAM-specific implementation, can be found in Appendix C.2 or the contributing work of Pathak [10].

The workflow of the LB algorithm is graphically presented in Figure 3.27. A step-wise description of the LB-geoVoF schematic explains the functionality of the LB-geoVoF algorithm:

1. The mesh is checked to determine whether it has been refined to ensure the LB algorithm's compatibility with AMR. If the mesh has changed, the global mesh list is updated and distributed again between all processors. Subsequently, surface area weights required for the NAG scheme evaluation are calculated and cached as variables. Saving the cell surface data allows an efficient calculation of the NAG scheme. The global mesh data is only utilized by the LB-geoVoF operations.

2. The flame front orientation is estimated with the NAG gradient scheme based on the volume fraction gradients $\nabla\alpha$. The operation is carried out on all cells of the mesh.

3. The workload of each processor is equal to the number of flame front cells in its local domain. The individual workloads are shared between all processors. Considering a computational overhead for communication δ, the total count of sent tasks L and the total count of received tasks R

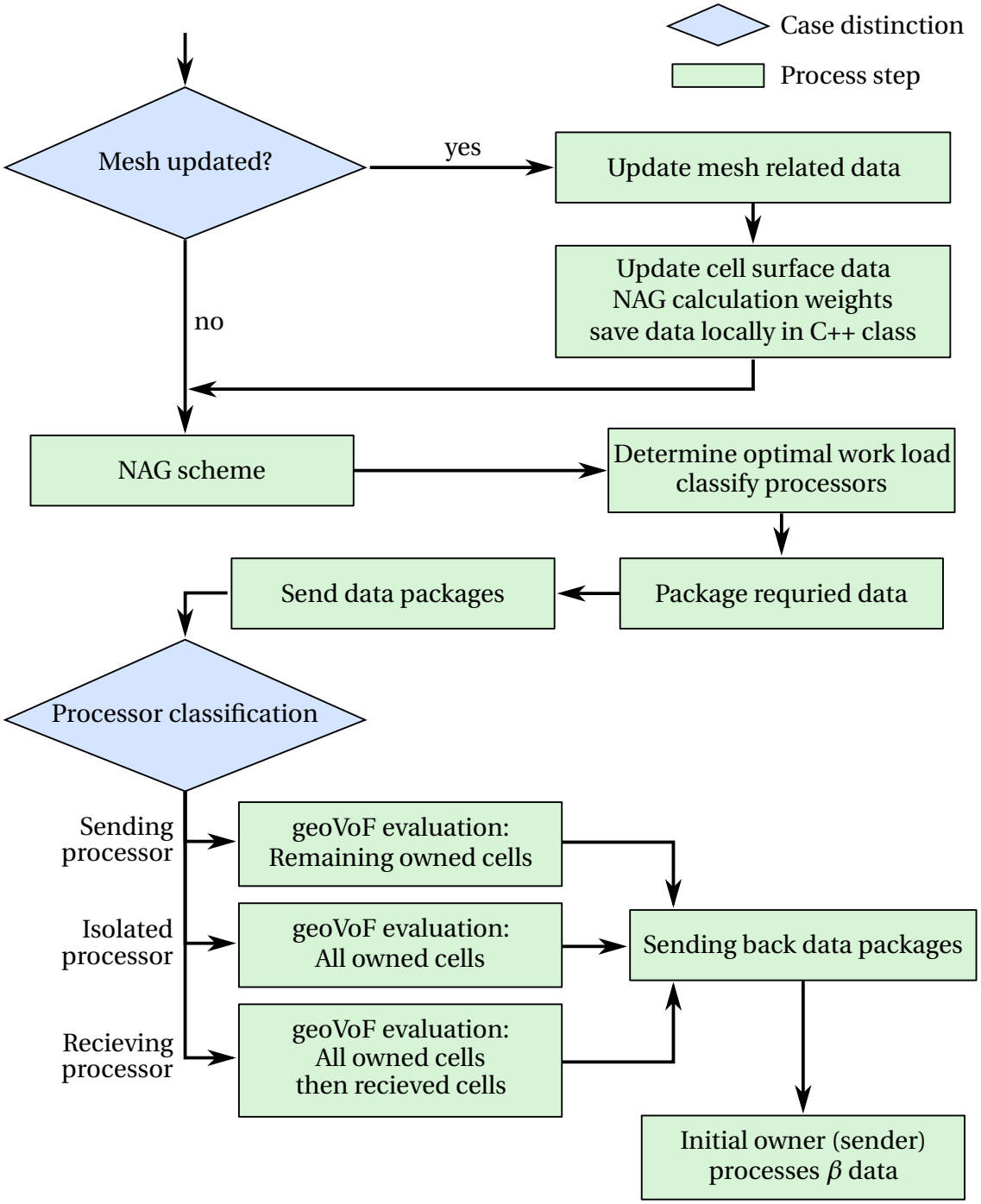

Figure 3.27: Workflow of the LB-geoVoF load-balancing algorithm.

can be balanced in order to obtain the optimal workload W_{opt} per processor. The balance reads

$$(1+\delta)\cdot L(W_{\mathrm{opt}}) = R(W_{\mathrm{opt}}). \tag{3.55}$$

A static communication overhead of $\delta = 0.1$ is specified as suggested by Jofre et al. [179]. The balance is solved with an iterative root-finding method, i.e., bisection. Knowing the optimal workload W_{opt}, each processor can evaluate its corresponding number of tasks to be sent or received. Each processor can be classified as sending, receiving or isolated by comparing its workload with the optimal value.

4. A sending and a receiving processor is assigned to each task. This information needs to be exchanged. According to the assignment, the necessary process data for the geoVoF evaluation is arranged in an OpenFOAM-specific nested *list*-type data structure. The nested *list* structure combines all information in large data chunks. However, the handling of the data structures is algorithmically complex. The process data, which is necessary for the geoVoF evaluation, consists of the cell index of the transmitted tasks, the α values, the NAG gradient of α and the velocity vectors on the cell surfaces of the flame front cells. Detailed information on the data structure can be found in Appendix C.2.

5. The process data is shared between all processors for reconstruction and advection step evaluation. The *all-to-all* communication functions of OpenFOAM are utilized to transmit large data packages efficiently.

6. If present, the processors execute self-owned tasks (reconstruction and advection) first, followed by the received tasks. Necessary geometrical data is obtained from the global mesh list in combination with the cell index of the transmitted task. The advected burnt volume fractions across the cell surfaces β are finally evaluated.

7. The data field β is packaged as a nested list structure analogously to the process data previously and distributed between all processors. Subsequently, the flame-propagation transport equation of the flame front tracking approach is solved by each processor on its local decomposed

mesh with the updated β field in the advection term. Similarly, all following geoVoF steps are carried out locally by each processor.

3.4.2.2 Speedup Validation of the LB-geoVoF Method on a Realistic Explosion Simulation

The present CFD solver is developed for FA and DDT explosion risk analysis in real-world accident scenarios. The flame front tracking approach, including the geoVoF method, has already been applied to the industrial-scale RUT facility with convincing results in an earlier investigation [168]. Therefore, the same industrial-scale obstructed explosion channel (62 m length and $420\,m^3$ volume) is also used for validating the LB algorithm. The reader is referred to References [168, 180] for a detailed description of the RUT facility. FA with subsequent DDT is simulated in a 30 vol.-% H_2-air mixture with single-staged AMR. Two-staged AMR could not be computed in a reasonable time with the hardware resources available. The simulation was run with 64 processors.

The speedup is defined as the ratio of the overall computation times with the non-load-balanced geoVoF and the load-balanced geoVoF method. Figure 3.28 shows the speedup as a function of the overall volumetric fuel conversion in the channel. The speedup data resembles the cumulative evolution of speedup over the simulation. With increasing volumetric fuel conversion, the flame transitions from FA over DDT to a subsequent stable detonation. During FA, the flame surface and, thus, the number of flame front cells increases. On a macroscopic scope, the distortion of the flow streamlines due to obstacles in the flame path cause the flame surface growth. On a microscopic level, turbulent flame wrinkling contributes to the increased flame surface. Only the macroscopic number of interface cells matters in terms of speedup. As a result, the speedup continuously increases to a factor of 4.05 at an overall conversion of 50 %. This illustrates the direct proportionality of the number of flame front cells and the load imbalance.

The flame surface area decreases rapidly with the onset of DDT because the fast self-ignition reaction smooths the flame front [5, 168]. Contrary to expectation, the cumulative speedup does not drop after DDT occurs at about 50% fuel conversion. It remains at around 4.0 until the fuel is completely burnt.

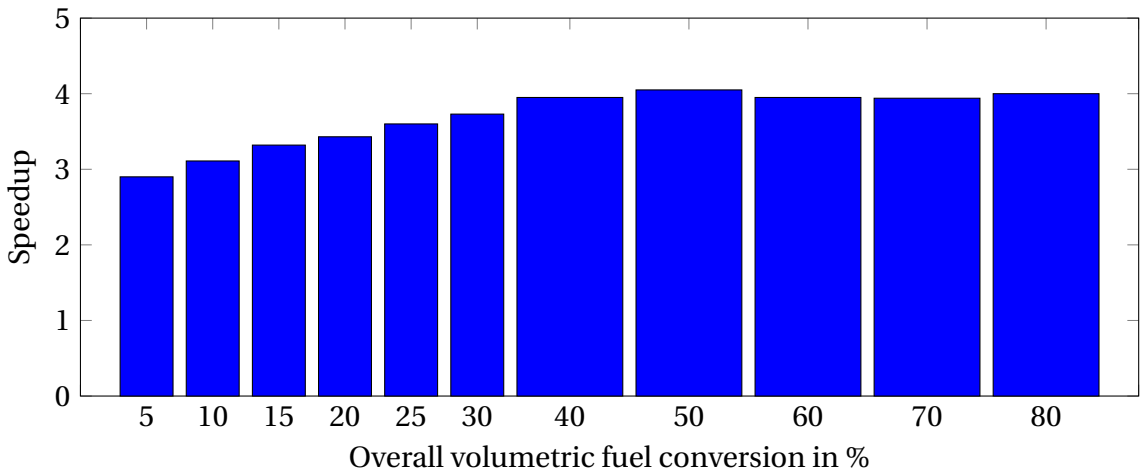

Figure 3.28: Cumulative computational speedup over the integral volumetric fuel conversion in the industrial-scale RUT facility (30 vol.-% H_2 in air).

The detonation phase covers only a short period of the overall calculation time due to the detonation's high propagation velocity. Consequently, adverse temporary speedup values during detonation only marginally affect the overall speedup of the simulation run. Thereby, the LB-geoVoF method proves itself as a very useful tool to increase the efficiency and applicability of the CFD solver for DDT risk assessment.

Evaluating the speedup within increments of the overall fuel conversion allows a more distinct identification of the different combustion regimes. This incremental perspective of the speedup is presented in Figure 3.29. A ramp-up of the speedup is apparent until the maximum of 6.49 is reached in the interval of 20-25 %. The flame front surface increase during FA causes this, as described earlier. The speedup remains at roughly 6 until the fuel conversion increment 30-40 %. The speedup drops to 2.88 in the interval of 50-60 % fuel conversion, as DDT leads to a rapid reduction of flame front cells. Due to the limited influence of the reduced speedup during detonation on the cumulative speedup, the LB-geoVoF method should be applied in all DDT simulations without restriction. Nonetheless, the best speedup results are obtained with a large number of flame front cells with simultaneous highly unequal distribution of the cells across the available processors. These conditions are valid for an explosion scenario in a duct geometry with long deflagrative flame propagation.

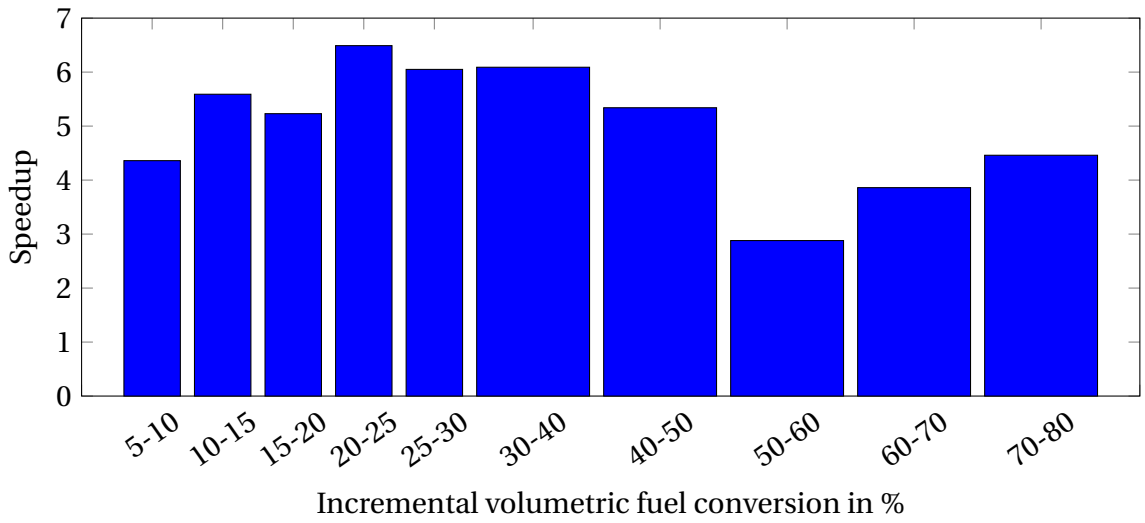

Figure 3.29: Computational speedup of fuel conversion increments in the industrial-scale RUT facility (30 vol.-% H_2 in air).

Test simulations in the RUT facility with 64 processors indicated that higher speedup values could be achieved at lower fuel concentrations. For example, an overall speedup of almost 6 has been achieved within the first 20% of overall fuel conversion for a mixture of 20 vol.-% H_2 in air [10]. The higher speedup is due to the larger flame surface required to obtain the necessary conditions for DDT. The speedup is highly dependent on the investigated scenario. A more generic validation, including a description of the fundamental LB-geoVoF performance trends, is attached in Appendix C.3. In general, the application of the LB-geoVoF method provides the potential to reduce computational time noticeably. Therefore, the LB-geoVoF flame front tracking approach is recommended as the flame-propagation transport equation for all large-scale DDT simulations. The OpenFOAM class LB-geoVoF is not limited to combustion simulations but can also be applied to multi-phase simulations when transferred to a corresponding OpenFOAM solver.

4 Validation and Verification

In the following chapter, the validation of the CFD solver for DDT simulations in stratified H_2-CO-air mixtures is presented. In real-world accident scenarios, the flame path is often obstructed. Therefore, the validation is carried out using experimental data from obstacle-laden explosion test rigs. The two main objectives are:

- Quantitative verification of the presented methodology's ability to correctly predict the onset of DDT, the flame trajectory and the thermodynamic states in the detonation complex.
- Demonstration of the applicability to a wide range of accident scenarios.

The key validation parameter for comparing simulation and experimental data is the observed propagation velocity of the flame front. Only macroscopic quantities are suitable for validating the under-resolved simulation approach because uncertainties on microscopic quantities like turbulent kinetic energy are too high. The flame can be characterized as a fast deflagration or a detonation based on the observed flame velocity profile. The drastic change in flame velocity indicates the onset of DDT. Two DDT-related aspects relevant for risk assessment are the location of DDT and the corresponding fuel content at which DDT is first encountered. Therefore, the fuel content and composition are varied over a wide range in the validation.

Real-world explosion accidents occur on various geometrical scales. Therefore, the experimental data from the small-scale GraVent facility and the large-scale semi-confined A1-vessel are used for validation. Depending on the geometrical scale of the test rig, the appropriate flame-propagation transport equation must be selected (see Section 3.3.1.4). The volume reaction approach is applied in simulations of the GraVent facility experiments. The flame

front tracking approach, including LB-geoVoF, is used in simulations of the A1-vessel experiments. As both test rigs are obstructed explosion channels, the obstacle configuration is varied in the validation. Inhomogeneous distributions of the fuel components often occur in real-world accidents. Hence, the validation also includes the investigation of vertical H_2-CO fuel concentration gradients.

The small-scale GraVent explosion channel [11, 76, 80, 181] at the Chair of Thermodynamics (TUM) provides the flexibility to investigate a wide range of H_2-CO-air mixture compositions as well as different obstacle configurations. A vertical fuel concentration gradient can be created in the channel. Thus, homogeneous and inhomogeneous fuel-air mixtures are investigated. In addition, the rapid repeatability of the experiments is a significant benefit of the small-scale test rig. Statistical significance of the experimental data can be obtained by rerunning the experiments several times at each test condition [11, 80]. The processed experimental results consist of the repeated measurements' average and standard deviation.

The A1-vessel operated by ProScience GmbH and KIT [33, 34] is a medium to large-scale test facility. Its explosion channel is a scale-up of the GraVent facility's channel by a factor of 10 based on its cross-section dimensions. The bottom and the back of the A1-vessel's channel is open to the environment. H_2-CO-air explosion experiments were conducted to identify fuel contents leading to the onset of effective FA and DDT [81]. Large-scale validation of the CFD solver focuses on the fuel contents associated with the onset of DDT. As in the GraVent facility, homogeneous and inhomogeneous mixtures were experimentally investigated. A non-reflecting boundary condition, which is native to the OpenFOAM framework, handles necessary relations at the open venting surfaces of the channel in the simulation.

4.1 Simulation Initialization

The initialization of each simulation follows the same procedure, independent of the geometry. Thus, it is only explained once in a general manner. Case-

specific settings are discussed in Section 4.2 and 4.3 for the respective facility.

The initial temperature of the reacting and non-reacting mixture is specified as 293.15 K. The initial pressure is 1.013 bar. The solver evaluates the multi-component fresh gas composition from the two mixtures fractions f_{H} and f_{C} according to the equations described in Section 3.3.2. For homogeneous mixtures, uniform fields of initial mixture mass fractions are patched onto the entire mesh. In the case of inhomogeneous mixtures, profiles of the two mixture fractions must be specified.

Initially, the gas mixture in the explosion channel is completely at rest. The density-based solver architecture is designed for fast flames and causes sudden density changes to create pressure waves. This behavior is inaccurate at low flow velocities. Therefore, the complex ignition process is simplified by initializing an ignition kernel as entirely burnt ($c = \alpha = 1$). The solver evaluates the thermodynamic state of the burnt gas as adiabatic, isobaric combustion itself. This procedure has proven more flexible and applicable than the previously applied procedure of statically assigning a fixed burnt state in the whole ignition kernel [4, 146]. It is especially beneficial in cases with fuel concentration gradients. The ignition kernel should be sized accordingly to depict the general shape of the expanding flame (cylinder, plane, or sphere). This avoids the preference of a single propagation direction.. Enforcing $c = \alpha = 1$ within the ignition kernel at all times prevents problems caused by the gradient approach of the deflagration source term for kernel sizes of less than three cells.

In addition to mixture and ignition initialization, the turbulent kinetic energy k and the specific dissipation rate ω must be given. The following set of equations allows the estimation of the required quantities as a function of the turbulent Reynolds number Re_{T} and the turbulent integral length scale l_{T}:

$$u' = \frac{\mathrm{Re}_{\mathrm{T}}\,\mu}{l_{\mathrm{T}}}, \tag{4.1}$$

$$k = \frac{3}{2}u'^2, \tag{4.2}$$

$$\omega = \frac{1}{0.09}\frac{\sqrt{k}}{l_{\mathrm{T}}}. \tag{4.3}$$

These equations are valid for fully developed turbulence [131]. In general, the initialized Re_T is kept low because the turbulence level at the beginning of the simulation corresponds only to residual turbulence from fuel injection into the test rig and weak flame-induced turbulence from the initial flame propagation. The latter depends on the size of the ignition kernel.

Table 4.1 lists the turbulent Reynolds numbers and the turbulent lengths used in the solver validation. Taking half of the injection nozzle's hydraulic diameter d_h as an integral length scale ensures a consistent initialization for all investigated geometries. The largest eddies of the initial turbulence generated during the filling process relate to the nozzle diameter. d_h of the open cross-section at obstacles is much larger than that of the nozzles, leading to a larger integral length. Consequently, the flow around the obstacles does not significantly affect the initial turbulence intensity. A high proportionality factor between turbulent and geometric length keeps the turbulence level low.

Table 4.1: Turbulent Reynolds numbers and turbulent length scales used for turbulence initiation.

	GraVent facility	A1-vessel homogeneous	A1-vessel inhomogeneous
Re_T	10	30	20
$l_T = 0.5\,d_h$	3.44 mm	3.75 mm	0.7 mm

All GraVent explosion simulations are initialized with a low level of turbulence. In the A1-vessel channel, the ignition kernel is typically bigger due to the coarse large-scale mesh. Thus, the already present flame-induced turbulence becomes more influential at the start of the simulation. Re_T is slightly increased for the large-scale simulations.

Moreover, two different injection systems with varying nozzle diameters were used for homogeneous and inhomogeneous experiments. For homogeneous mixtures, the combustible gas is injected at the head plate and ignited once the outflow composition at the end plate matches the desired value. On the contrary, in the inhomogeneous experiments, evenly distributed nozzles along the channel length and width simultaneously fill the entire channel

from top to bottom [81]. Turbulence is assumed to be higher in the homogeneous case due to the established continuous flow before ignition.

4.2 Small-Scale GraVent Explosion Channel

The explosion channel of the GraVent facility [11, 80] is a 6.0 m long rectangular duct. The channel cross-section has a width of 300 mm and a height of 60 mm. It is obstructed on a 3.95 m length followed by an obstacle-free section. Different obstacles regarding the blockage ratio (BR) and the obstacle spacing (S) can be installed. They are mounted on the ceiling and the bottom of the channel covering the entire channel width. The label *BRxxSxxx* identifies the obstacle configuration. The blockage ratio *BR* can be 30 or 60%, and the obstacle spacing *S* is specified as 100 mm or 300 mm. A spark plug is placed in the end plate adjacent to the obstructed section. The position of the first is 50 mm downstream of the spark plug head plate.

The data acquisition consists of pressure transducers and photodiodes. While photodiodes track the flame front propagation, the pressure transducers measure the dynamic pressure history. Figure 4.1 illustrates the layout of the GraVent explosion channel (top view). The data acquisition system remains at the same location independent of the obstacle configuration.

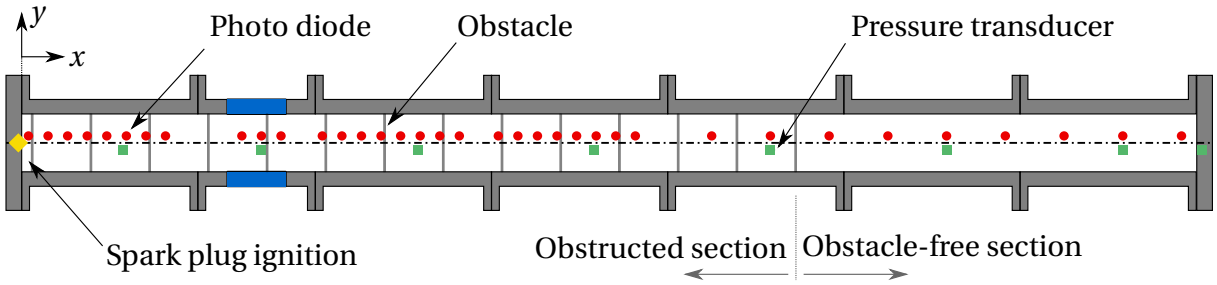

Figure 4.1: GraVent explosion channel including the positing of pressure transducers (green), photodiodes (red) and spark plug ignition location (yellow) [adopted from [11]].

The flame dynamics were experimentally studied for varying fuel contents, fuel compositions and obstacle configurations. In detail, fuel contents of 15,

17.5, 20, 22.5, 25, 27.5, 30, 35 and 40 vol.-% with a composition of 100/0, 75/25 and 50/50 H_2/CO have been tested. The experimental fuel injection procedure can result in a possible derivation of $\Delta x_f = \pm 0.5$ vol.-% from the desired fuel content. Measurements with homogeneous and inhomogeneous mixtures were conducted. In the case of inhomogeneous mixtures, the specified fuel content resembles the average value over the channel height.

In the numerical investigation, approximately 150000 cells comprise the GraVent explosion channel mesh for all configurations. All four possible obstacle configurations BR30S100, BR30S300, BR60S100 and BR60S300 are studied. Using a two-level AMR during the simulations results in cell sizes of 2 mm in refined regions. According to Ettner [8], mesh convergence is accomplished in the GraVent simulation at a minimum cell size of 2 mm. The Courant number is given as $CO_{acc} = 0.3$. The c-based transport equation describes the small-scale flame propagation. A hemisphere with a radius of 15 mm specifies the ignition kernel at the spark plug location. Adiabatic, no-slip walls are the wall boundaries of the fully confined geometry.

The validation primarily compares flame tip trajectory data. In the numerical investigation, the most advanced flame tip position in the longitudinal channel direction is tracked over time. The flame tip velocity corresponding to the flame tip's axial position in the channel is derived from the time-position raw data. The flame tip velocity profile allows a more straightforward classification of the flame's combustion regime than the time-position raw data.

The fixed cell center locations in the mesh give the time-position data of simulated flames a discretized nature, resulting in noisy velocity-position data. Hence, a smoothing function is applied based on the *rloess* (robust local regression using weighted linear least squares) method. Figure 4.2 shows the impact of the *rloess* method's span coefficient on the resulting flame tip velocity profile. While the flow acceleration through the open passage area at obstacle locations is visible at lower span values, run-up distances and the DDT location can be identified more clearly with the span of 0.1. Since the validation focuses on macroscopic parameters, precise identification is prioritized, and the span is given as 0.1.

Each explosion experiment was repeated three to five times under the same conditions. The measured data has been combined into a single data array with a local mean value and a standard deviation at each measurement position along the channel.

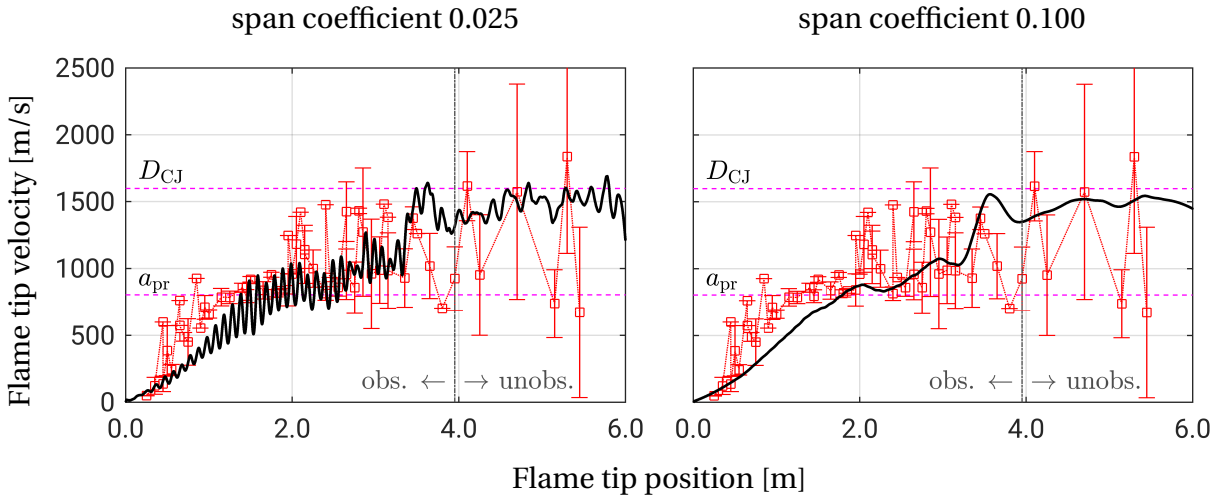

Figure 4.2: Impact of the *rloess* method's span coefficient on the resulting flame velocity profile of the simulations.

4.2.1 Homogeneous H_2-CO-Air Mixtures

In this section, fuel contents of 17.5, 20.0 and 22.5 vol.-% in air are investigated. This is based on the experimental identification of the most relevant fuel content range for the onset of DDT in homogeneous H_2-CO-air mixtures. Fuel compositions are varied as well. The numerical analysis focuses on accurately predicting the DDT location and the minimum fuel content necessary for DDT to occur. First, simulations are run for each fuel content with all three fuel compositions 100/0, 75/25 and 50/50 H_2/CO in the fixed geometry configuration BR30S100. Second, the ability to predict DDT accurately in all four obstacle configurations is investigated at a constant fuel content of 22.5 vol.-% of 75/25 H_2/CO.

4.2.1.1 Variation of fresh gas composition

Figure 4.3 shows flame tip velocities over the flame tip's longitudinal position in the explosion channel for various fresh gas compositions. The fuel content varies in the images from left to right from 17.5 to 22.5 vol.-%. The fuel composition alters from top to bottom from 100/0 to 50/50 H_2/CO mixtures. The obstacle configuration is BR30S100. In all plots, horizontal lines for the speed of sound of the combustion products a_{pr} and the stable detonation velocity D_{CJ} are added. The gray vertical line separates the obstructed from the obstacle-free section of the channel.

Generally, the standard deviations of the measurements are small during the FA phase, indicating a good consistency of the data. Once the maximum speed of the deflagration a_{pr} is reached, the possibility of sudden auto-ignition events grows. Large standard deviations in the obstructed section result from these auto-ignition events. When large deviations occur in the velocity range between a_{pr} and D_{CJ}, two interpretations for a simulated DDT are possible:

- **Spatial region of potential transition:** A detonation is unambiguously identified when the mean velocity in the measurements is close to D_{CJ} and the standard deviation is minimal. If the preceding spatial region shows large standard deviations, DDT occurs at slightly different locations in the repeated experiments. Due to the stochastic nature of DDT indicated by measurements, simulated DDT locations are considered correct as long as they reside in this region.
- **Temporary quasi-detonation:** Sometimes, no detonation can be identified unambiguously in the measurements following the region of large standard deviations. If so, a temporary quasi-detonation with velocities between a_{pr} and D_{CJ} or single auto-ignition events caused the high deviations in the measurements. The flame decays to a fast deflagration after some distance. A simulated DDT in the corresponding region is a conservative estimate for risk assessment since it considers the pressure peaks of the temporary auto-ignition events.

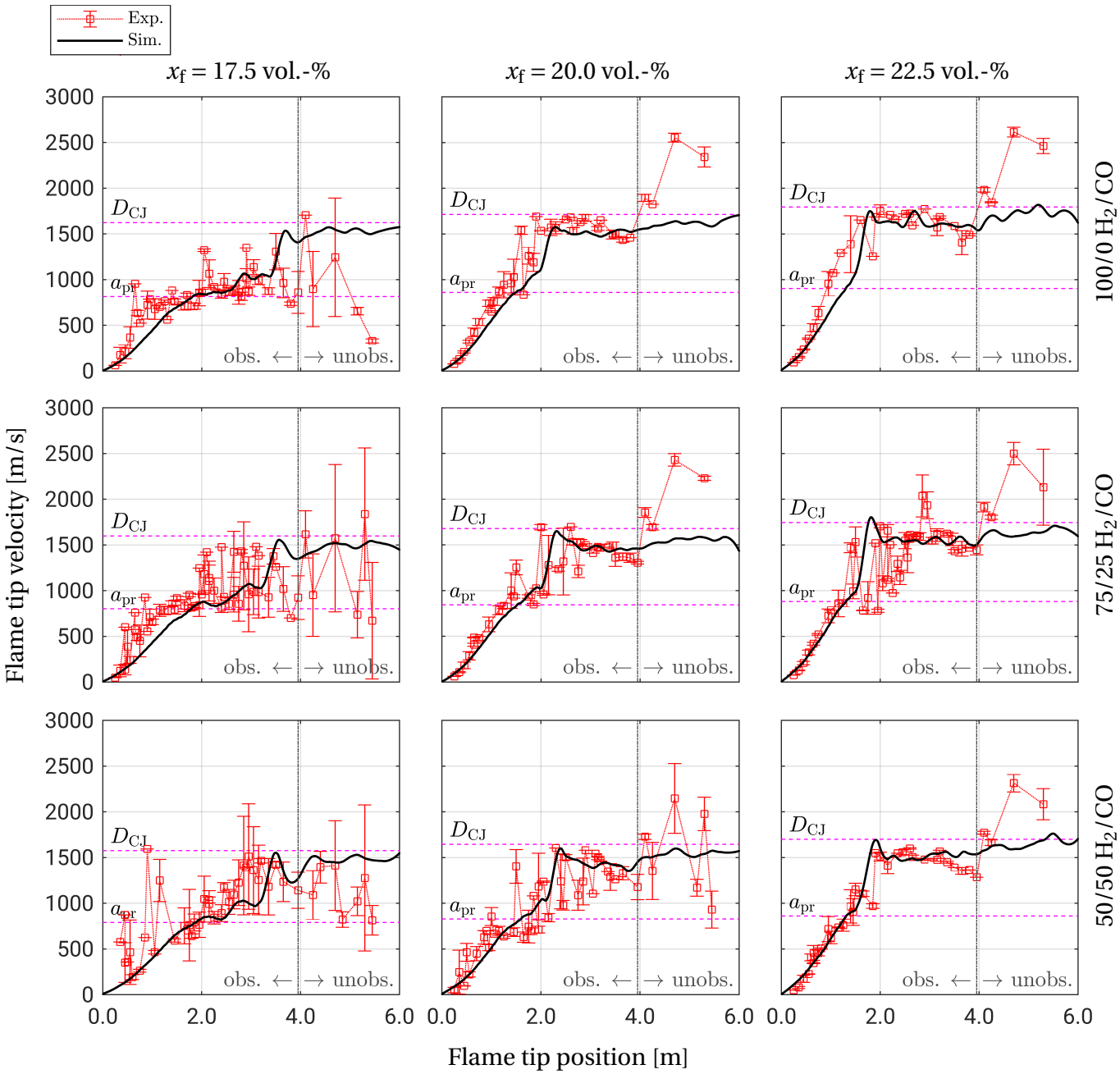

Figure 4.3: Flame tip velocities of varied fuel compositions and fuel contents in the GraVent explosion channel for the geometry configuration BR30S100.

Stable detonations can be identified in the obstacle-free section for all mixtures with a fuel content $x_f \geq 20.0$ vol.-%. The CFD solver predicts DDT well in these cases. After DDT, the detonation velocity remains slightly below D_{CJ} in the obstructed channel section for simulation results and measurements. Studies by other researchers [33] confirm this observation. In contrast, the propagation velocity of the detonation increases in the obstacle-free section. Here, the detonation complex is no longer slowed down by reflected waves.

The DDT location is either met very closely by the simulation, i.e., 20.0 vol.-% of 100/0 H_2/CO, or well within the region of high standard deviations, i.e., 20.0 vol.-% of 75/25 H_2/CO. In the simulation, the velocity overshoot indicates an over-driven detonation at the DDT. The over-driven detonation causes high dynamic pressures. The simulations reproduce the experiments' trend of earlier DDT with increasing fuel content, independent of the fuel composition. The DDT location shifts only slightly downstream with increasing CO content.

The flame velocity profiles of the simulations agree with the measurements in the initial phase of FA, especially for cases with rapid acceleration and successive DDT. At a fuel content of 17.5 vol.-%, the measured flame velocity reaches a_{pr} faster than in the simulation. While DDT occurs immediately after reaching a_{pr} at higher fuel contents, at 17.5 vol.-% of fuel the flame front remains at a_{pr} for an extended distance in the obstructed channel section. The choked flame at a_{pr} can only further accelerate by auto-ignition combustion. It is not triggered immediately because the interplay of reactivity and pressure waves is insufficient at this fuel content. The simulation predicts the choked flame velocity at maximum deflagration velocity a_{pr} until DDT occurs close to the end of the obstructed section. The coupling of the reaction front and the shock front only occurs if the volumetric heat release can keep up with the pressure wave triggering auto-ignition. The newly implemented cell-size and mixture-dependent scaling of the volumetric heat release function guarantees appropriate heat release rates.

At 17.5 vol.-%, large standard deviations and mean velocities between a_{pr} and D_{CJ} indicate auto-ignition events or quasi-detonations. Hence, the mixture reactivity at 17.5 vol.-% of fuel is close to the necessary limit for a self-sustaining detonation. Because mean velocities above a_{pr} and high deviations

are present in the obstacle-free section, the simulated self-sustaining detonation is considered a conservative estimate. The transition coincides with regions of large standard deviations for all fuel compositions. This match is more distinct for CO-containing fuels. However, the measured flame tip velocities decay to fast flames with a_{pr} for all fuel compositions towards the end plate of the channel. This trend can be seen particularly well for 17.5 vol.-% of 100/0 H_2/CO. The simulated DDT with subsequent stable detonation is reasonable for risk assessment simulations. The presence of auto-ignition events with temporary velocities of quasi-detonations in the experiments affirms this conservative perspective. At 15 vol.-%, the experiments show no sign of auto-ignition events, and CFD simulations do not show DDT either.

Overall, simulated and measured velocity profiles agree well for varied fresh gas compositions. The simulated velocity profiles remain within the deviation of the experimental data over almost the entire channel length. Simulation results can be considered a conservative estimate for gas compositions that do not clearly indicate DDT.

4.2.1.2 Geometry Variation

Because the channel geometry significantly influences FA and DDT, the CFD solver is validated against data obtained on various obstacle configurations. All four possible GraVent explosion channel obstacle configurations are investigated. The fresh gas composition of 22.5 vol.-% fuel with 75/25 H_2/CO remains unchanged for the simulations. The previous validation of fresh gas compositions demonstrated that this fuel content is sufficient to obtain DDT.

Heilbronn et al. presented an experimental study [80] concerning the geometry influence on DDT at the GraVent facility. The obstacle configuration can support or even suppress DDT. Generally, higher blockage ratios and shorter obstacle spacings decrease the run-up distance to a_{pr}. At the same time, the dimension of the open obstacle passage needs to be larger than a critical value for a stable detonation to be sustained. Investigations of the critical dimensions at different blockage ratios can be found in different studies [182–184].

Figure 4.4 presents measured and simulated flame velocity profiles for all four obstacle configurations. The BR60S100 configuration stands out because DDT is effectively suppressed in the experiments by the combined effects of a high blockage ratio and small obstacle spacing. The choked fast deflagration only exhibits the propagation speed a_{pr}. The simulation is not capable of reproducing the suppressed DDT. The high blockage ratio promotes FA, which quickly generates strong pressure waves. In the simulation, self-ignition initiates directly due to a sufficiently strong compression of the fresh gas. Compared to the smaller blockage ratio of 30%, the velocity deficit of the detonation in the obstructed section is more significant. Consequently, the flame speed increase is larger when reflected shock waves no longer influence the detonation in the obstacle-free section. However, the simulated flame speed profile is conservative because the mixture is sufficiently reactive for DDT.

The initial FA phase obtained from simulations agrees with the measurements in all configurations. The obstacle locations are visible in the velocity profile for 300 mm spacing from the temporary accelerations and decelerations. The simulation results replicate the trend of a more rapid FA with higher blockage ratios and smaller obstacle spacing. Altering the blockage ratio has a greater effect on the results than changing the obstacle spacing.

Stable detonations can be identified in the obstacle-free section of all configurations, apart from BR60S100. The simulation closely matches the DDT location when the measurements clearly show a detonation with continuous flame velocities at D_{CJ}, i.e., BR60S300. While the experiments indicate a transition closer to the end of the obstructed channel section in the two BR30 configurations, the DDT locations obtained by simulation are further upstream. Still, they reside in regions of high standard deviation. This result is conservatively correct since auto-ignition events or DDT occurred in some experiments at the simulated DDT location.

A good agreement exists between simulated and measured velocity profiles when the obstacle configuration is varied. In the case of the suppressed DDT in scenario BR60S100, the simulation result's conservative nature agrees with the CFD solver's risk assessment purpose.

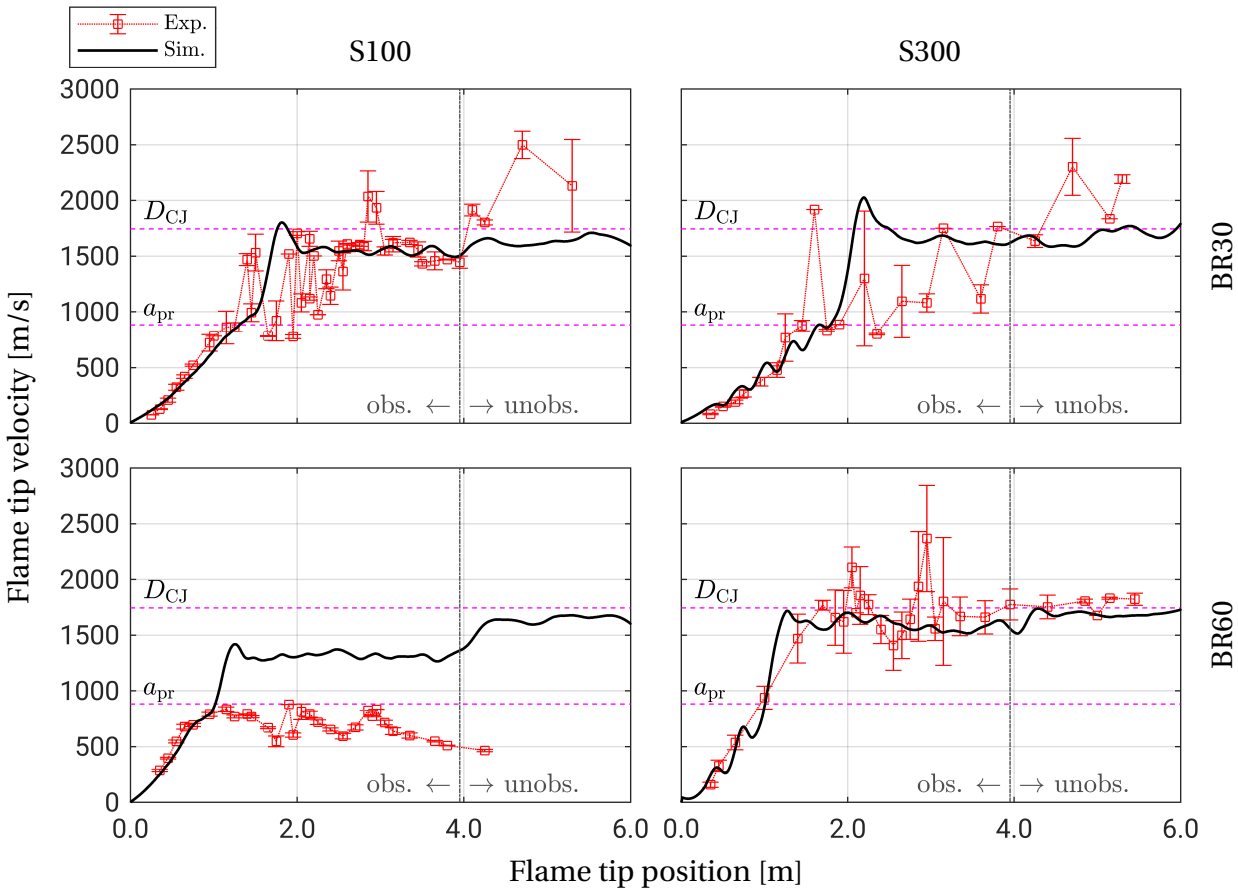

Figure 4.4: Variation of obstruction BR and obstacle spacing S in a 22.5 vol.-% fuel in air mixture (75/25 H_2/CO).

4.2.2 Stratified H_2-CO-Air Mixtures

Since homogeneous mixtures are very unlikely in real-world accidents, vertical concentration gradients of the H_2-CO fuel is analyzed as a part of the solver validation. The influence of vertical concentration gradients on the flame dynamics in H_2-air mixtures has been investigated experimentally and numerically in the GraVent facility [167, 181, 185]. Experimental investigations of inhomogeneous H_2-CO-air mixtures were conducted recently [186].

The generation of vertical concentration gradients in the GraVent explosion channel is primarily based on molecular diffusion. After the fuel injection is finished, a homogeneous fuel layer is present underneath the channel ceiling

as Figure 4.5 illustrates. During the waiting time t_w, fuel diffuses towards the bottom and a vertical fuel concentration gradient forms. Generally, the fuel components must be considered separately due to the different molecular diffusivity of H_2 and CO. Because almost no convective mixing is present, the H_2 and the CO fuel concentration gradient differ significantly in the GraVent explosion channel [186].

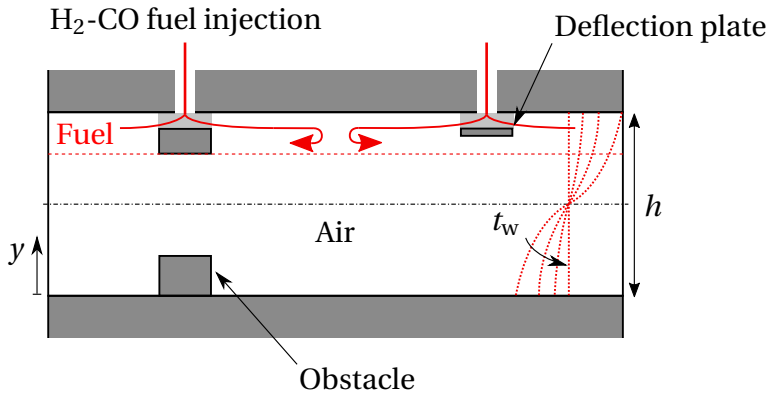

Figure 4.5: Gradient formation in the GraVent facility's explosion channel [adopted from [11]].

For simulation initialization, the correlation

$$\frac{x_k(y)}{\overline{x_k}} = 1 + \frac{K_k(t_w)}{0.9} \tanh\left(C\frac{y_c}{h}\right) \tag{4.4}$$

specifies the vertical distribution of the mole fractions x_k over the channel height y. It is normalized with the mean molar fraction over the channel height $\overline{x_k}$. The distribution is a function of the vertical cell center position y_c. The vertical position y_c is normalized with the channel height h. The constant C is given as $C \approx 2.9444$. The correlation is evaluated for each fuel component k separately. The correlated parameter $K_k(t_w)$ determines the slope of the concentration profile corresponding to the waiting time. It is derived from experimental and numerical investigations of the filling process [186]. Detailed information on the derivation of Equation 4.4 as well as the coefficients $K_k(t_w)$ are provided in Appendix B.1.

The effect of inhomogeneous fuel distributions on flame dynamics is investigated on the two geometry configurations BR60S300 and BR30S100. The same

mean fuel composition of 75/25 H_2/CO is used for all simulations. The mean fuel content is varied between 17.5, 20.0 and 22.5 vol.-%. The slope of the vertical fuel concentration gradient depends on the waiting time. It is steeper at shorter waiting times. A minimum waiting time is necessary to allow sufficient time for the diffusion process to form a smooth vertical concentration gradient over the channel height. The data obtained from ignition after a minimum waiting time of 3 s is used in the validation.

Figure 4.6 compares the simulated flame tip velocity with the experimental data. For comparison, plots of the corresponding homogeneous mixture have been added to Figure 4.6. However, the discussion focuses on inhomogeneous mixtures. All simulation results with inhomogeneous mixtures closely meet the measured run-up distances to a_{pr}. Compared to the homogeneous mixture results, stable detonations cannot be identified clearly in the obstacle-free section for any inhomogeneous experiments. However, the solver predicts stable detonations in the unobstructed channel section for all simulated cases. Regions with auto-ignition events with velocities close to D_{CJ} exist in the obstructed channel section. Because the mixture's reactivity appears high enough for local quasi-detonations, the simulated onset of DDT can be considered a conservative estimate for risk assessment. Once a stable detonation forms in the most reactive leading flame front tip under the ceiling, it does not decouple and decay to a fast deflagration in the obstacle-free section. In the BR30S100 configuration, the simulated onset of DDT is located further upstream in the inhomogeneous mixture than in the homogeneous mixture due to a more reactive mixture at the leading flame tip under the ceiling.

The higher blockage ratio of 60 % causes a shorter run-up distance to a_{pr} due to increased turbulence production and a more elongated flame shape [4]. The likelihood of auto-ignitions and quasi-detonations is not enhanced in the obstructed section. More minor standard deviations indicate that trend for the BR60S300 compared to the BR30S100 configuration. The leading flame tip, located in the most reactive layer of the inhomogeneous mixture, propagates underneath the ceiling for most lean average fuel contents. It is assumed that the inhomogeneous mixture's most reactive layer determines the likelihood of FA and DDT. Hence, corresponding empirical FA and DDT criteria for inho-

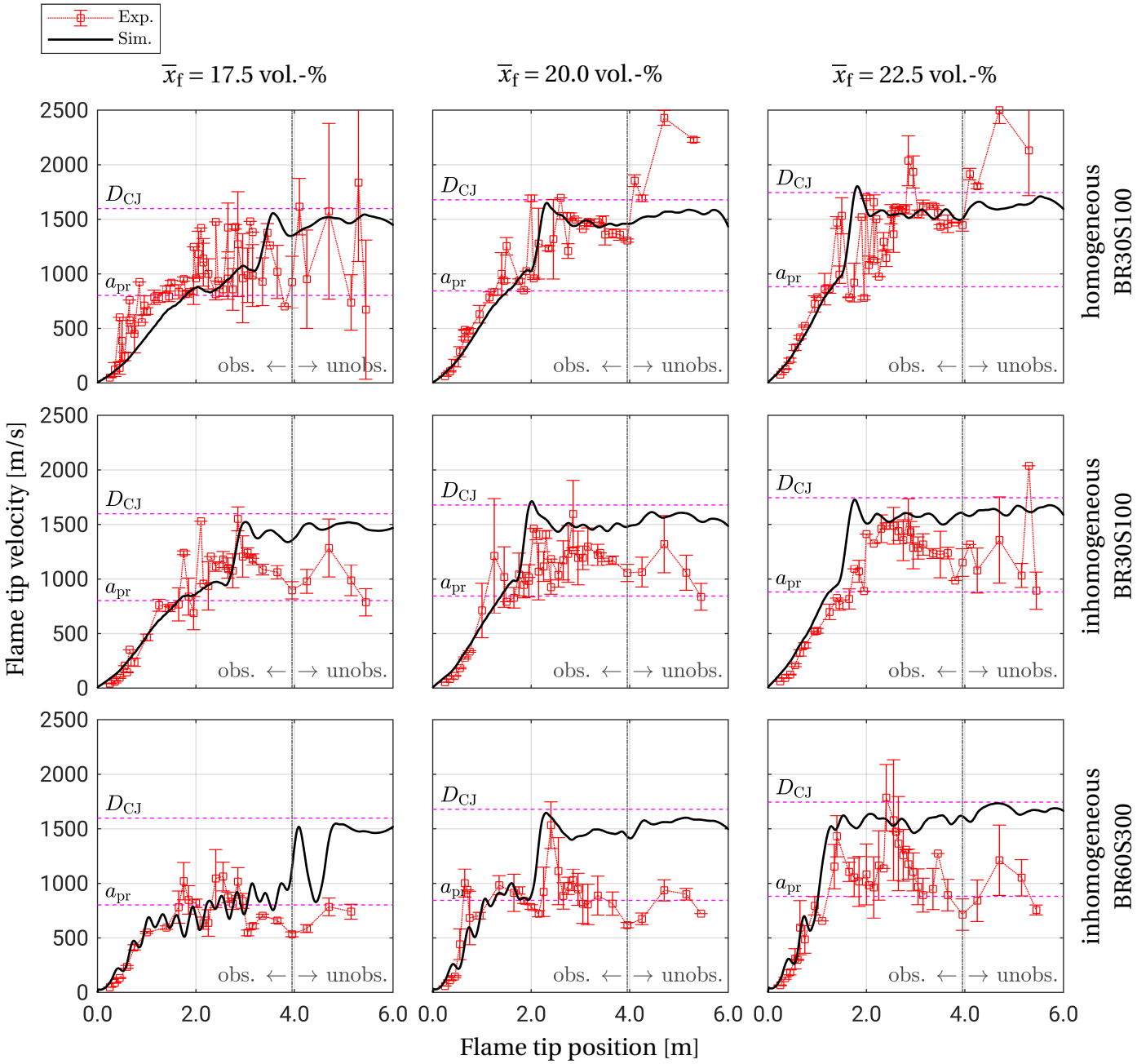

Figure 4.6: Flame tip velocities of homogeneous and inhomogeneous 75/25 H_2/CO fuel-air mixture for BR30S100 and BR60S300 obstacle configurations (waiting time 3s).

mogeneous mixtures are based on the fuel content of the leading flame tip (see Section 2.2.4 and Section 2.4.2). This concept for empirical criteria was tested in small-scale experiments with inhomogeneous H_2-air mixtures [36, 76, 181]. The reduced likelihood of auto-ignitions in the BR60S300 compared to the BR30S100 configuration can have two reasons:

- Larger obstacles at a BR60 blockage ratio of 60 % disrupt the most reactive layer more drastically. The flame front must pass fuel layers with lower fuel content at each obstacle, reducing the local reaction rate.
- The expansion of the burnt gas generates the strongest pressure waves at the leading flame tip in the most reactive mixture layer. Stronger obstruction of the layer causes an intensified push-back of the flame from reflected waves.

Consequently, the flame sustains the maximum deflagrative propagation speed a_{pr} for a longer distance in BR60S300. This it particularly visible for the average fuel fractions $\overline{x}_{\mathrm{f}} = 17.5$ and $\overline{x}_{\mathrm{f}} = 20.0$ vol.-%. The simulation captures the sustained flame propagation at a_{pr}. For $\overline{x}_{\mathrm{f}} = 20.0$ vol.-%, the predicted transition takes place once the measurement shows auto-ignition events. The simulated stable detonation is a conservative estimate. In the case of $\overline{x}_{\mathrm{f}} = 17.5$ vol.-%, transition takes place once the flame enters the obstacle-free section. Because the measured flame profile displays no velocities close to D_{CJ} over the entire channel length, the simulated behavior is contradictory to the respective experimental findings.

4.3 Large-Scale Semi-Confined A1-Vessel

As the solver development aims at an industrial application for risk assessment of FA and DDT, the CFD solver is additionally validated on large-scale geometries. Unlike H_2-air mixtures in the RUT facility [180], H_2-CO-air mixtures have yet to be investigated on the industrial scale. Recently, H_2-CO-air explosion experiments have been conducted in the medium to large-scale semi-confined A1-vessel. The large-scale DDT simulation validation employs the

measured flame tip velocity data. As the A1-vessel comprises a semi-confined explosion channel, the validation extends the CFD solver's applicability to accidents involving a semi-confined flame enclosure.

Homogeneous and inhomogeneous mixtures have been experimentally studied in the A1-vessel to identify the minimum fuel content at which FA and DDT are first encountered [81]. The A1-vessel is a tank enclosing the actual explosion channel. The channel has a length of 9 meters, a width of 3 meters and a height of 600 mm [33, 34]. The bottom and back of the explosion channel are open to reduce pressure loads on the channel structure during explosion experiments. The loss of mass and momentum caused by pressure waves leaving the channel damps the FA feedback mechanism. The channel is repeatedly obstructed by obstacles with a 50 % blockage ratio of the cross-section. The obstacles consist of several 60 mm high wooden beams with an even distribution over the channel height. In the longitudinal direction, the obstacles are spaced 600 mm apart. The ignition source is a tube filled with a combustible auxiliary gas located in the corner between the ceiling and the head plate. The mixture is ignited by a spark plug. The burning gas exits the tube through holes facing the corner, igniting the H_2-CO-air mixture.

Figure 4.7 depicts the computational mesh. It comprises roughly 1 million uniform hexahedral cells with the dimensions 40x30x30 mm (LxWxH). Industrial-scale simulations of the RUT facility [168] or the containment of a nuclear Konvoi type reactor [128] used equivalent cell sizes. Hence, the A1-vessel is well suited for validation on large scales. In the simulation, the ignition kernel is given as a cylinder, which spans the whole channel width, with a radius of 85 mm positioned in the upper corner at the head plate. The flame front tracking approach with the LB-geoVoF method is applied for the flame-propagation transport equation. Although two-staged AMR is generally advised, only single-staged AMR is applied, as HPC resources have not been available. Only computing systems with a maximum of 64 processors were available. The overall computation times with single-staged AMR remain below two days for all simulated cases.

As a consequence of the partially-open sides of the explosion channel, the simulation case setup must account for two additional aspects :

- Combustible gas can be convected in flame propagation direction underneath the bottom obstacles by the induced flow in the fresh gas.
- Boundary conditions (BC) handle the in- and outflow conditions on the open surfaces of the mesh for the variables transported by the solver. Pressure waves, which accompany fast deflagrations and detonations, must be able to exit the computational domain without any reflections due to the BC.

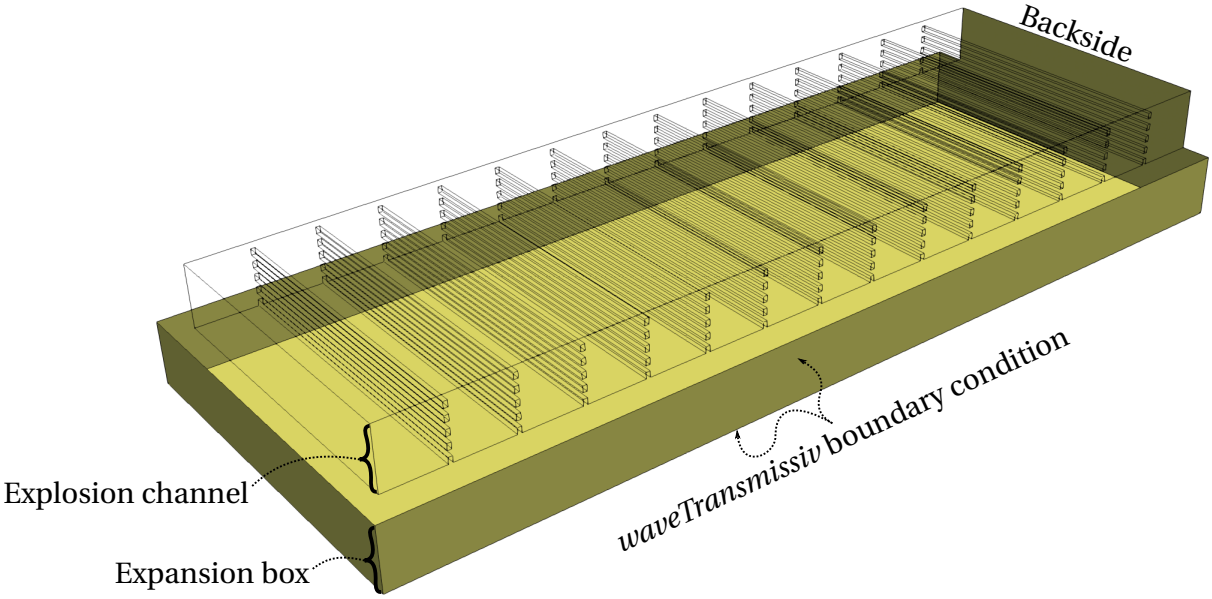

Figure 4.7: Mesh geometry of the A1-vessel explosion channel, including an additional meshed box below the channel. Open surfaces with an assigned *waveTransmissive* boundary condition are colored yellow (different grades of yellow only for a better 3D perspective).

First, the contribution of the combustion of the flammable gas cloud below the bottom obstacle to FA must be considered. Because the impact cannot be modeled easily in a BC, the computational mesh must be extended below the channel to include the described effect on FA. Figure 4.7 shows an extension of the mesh below the explosion channel denoted as an expansion box. The box is 600 mm high and protrudes five cells over the channel bounds to each side but the backside. The dimensions of the expansion box are large enough to ensure that no positive feedback on the FA is neglected.

Second, the BC on open surfaces of the mesh needs to ensure that no reflection of a pressure wave remains inside when it exits the domain. Therefore, the *waveTransmissive* BC, a native OpenFOAM implementation, is specified for pressure and velocity on the expansion box's bottom, sides and backside. The corresponding surfaces are highlighted yellow in Figure 4.7. The BC requires a far-field state ($p_{\text{inf}} = 1.013\,\text{bar}$ and $u_{\text{inf}} = 0\,\frac{\text{m}}{\text{s}}$) located in a far-field distance l_{inf} from the BC surface. The pressure and velocity value on a boundary face relaxes towards this state over the distance l_{inf}. When a vast distance is specified, pressure waves can exit the domain with minimal reflection. The method does not provide the most accuracy but is favorable due to its robustness [1, 187]. It allows correctly conditioned inflow. Appendix D provides more details on the BC's functionality and its density-based implementation.

A generic 3D simulation with an open bottom side is used to check the plausibility of the results obtained with the *waveTransmissive* BC. Figure 4.8 illustrates a time sequence of 2D pressure contours shortly after ignition. In the density-based solver architecture, a change in the flame front velocity induces low-amplitude pressure waves. Figure 4.8 shows that the initial wave due to the initial movement of the ignition kernel leaves the domain on the bottom side without a significant reflection in the normal direction to the boundary. The pressure remains unchanged (center at $t = 35\mu s$). The overall pressure level decreases due to spherical wave propagation. Two pressure peaks appear, which propagate to the sides parallel to the bottom. Because the *waveTransmissive* BC is strictly only valid for 1D flows, a weak residual reflection remains in 3D. In the case of the A1-vessel simulations, the expansion box was

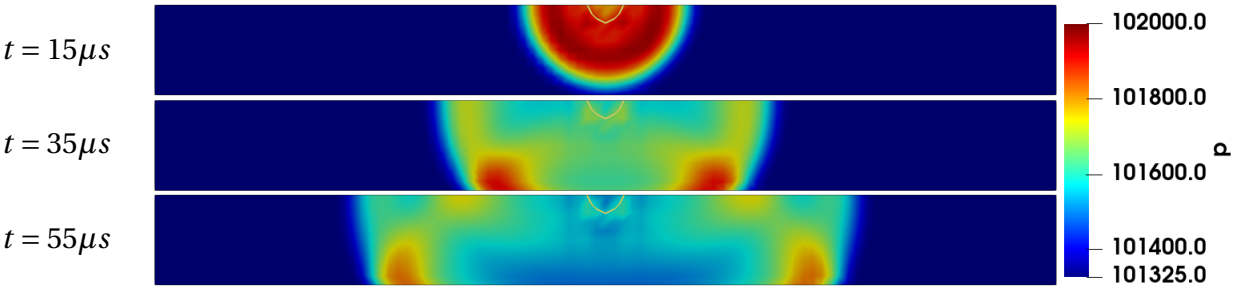

Figure 4.8: Time sequence of a 2D pressure contour of a generic 3D simulation with *waveTransmissive* BC on the bottom.

created large enough that no feedback from the residual waves on the bottom boundary to the flame is to be expected. In the A1-vessel simulation, the wave reflections eventually exit the computational domain in normal direction to the *waveTransmissive* BC on the sides of the expansion box.

4.3.1 Homogeneous Semi-Confined H_2-CO-Air Mixtures

Minimum fuel contents required for effective FA and DDT depend on the confining geometry. In the A1-vessel, they have been experimentally determined for homogeneous mixtures with the fuel compositions 50/50, 75/25 and 100/0 H_2/CO [33, 81]. For the three fuel compositions, simulations in the semi-confined A1-vessel explosion channel are conducted with the minimum fuel content for DDT. The simulated flame tip velocity is compared to the experimental data in Figure 4.9. The fuel content of each fuel composition is indicated next to the corresponding plot. It should be mentioned that DDT has been experimentally identified at 21 vol.-% of 100/0 H_2/CO fuel in air, but corresponding data was not available to the author. The mixture of 22 vol.-% of 100/0 H_2/CO fuel in air has been simulated instead.

The measurement instrumentation in the A1-vessel consists of ionization probes and pressure transducers. Three velocity profiles are obtained from measurement data. Each profile refers to measurement locations at a different lateral channel position along the longitudinal channel direction. The lateral positions are $y = -1.2\,\text{m}$, $y = 0\,\text{m}$ and $y = 1.2\,\text{m}$. The position 0 m denotes the center line. The previously described procedure for tracking the flame tip position in the longitudinal direction during simulation remains in use.

The speed of sound of the reactants a_{re} is the minimum velocity required for the characterization as a fast deflagration. Simulated and measured velocity profiles show long run-up distances to a_{re}, indicating that FA to fast deflagrations is less pronounced in the semi-confined channel than in the fully-confined GraVent channel. For all investigated fuel compositions, the maximum velocity of fast deflagrations a_{pr} is reached only in the second half of the channel. Mass and momentum losses over the channel's open surfaces yield slower FA. As long as the three measured profiles show similar behavior,

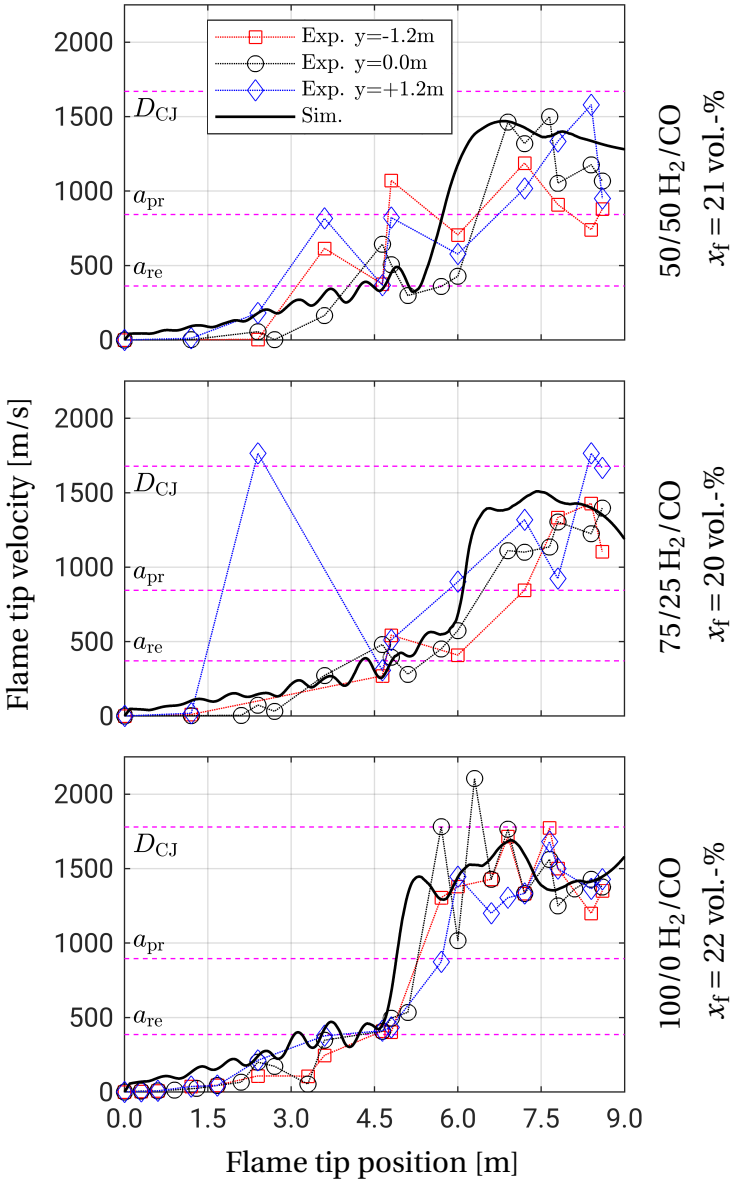

Figure 4.9: Simulated flame tip velocity profiles of homogeneous 50/50, 75/25 and 100/0 H_2/CO fuels compared to experimental data for the minimum fuel content necessary for DDT.

they can be considered a tolerance range for the simulation validation. Even though the simulation overpredicts flame velocities in the initial phase after ignition, the simulated flame speed remains within the deviation of the three experimental profiles in the subsequent acceleration phase for all mixtures.

The measured flame velocity profiles are obtained from single-shot experiments. However, the study in the GraVent facility showed that DDT occurs in the obstructed channel within a tolerance region for repeated experiments under the same conditions. Hence, reasonable deviations of simulated DDT locations from measured ones are acceptable for the solver validation in the A1-vessel. The simulation captures the DDT location with a reasonable deviation of less than half a meter for all fuel compositions. The predicted velocity curves do not overshoot at DDT but stay close to the experimental profiles. The simulation reproduces the subsequent quasi-detonation in the measurement, which is typical for obstructed channels. The flame velocity of the quasi-detonation is between a_{pr} and D_{CJ}. Compared to a fully-confined geometry, the velocity deficit between the quasi-detonation's velocity and D_{CJ} is larger due to mass and momentum losses at the open channel surfaces. The good agreement between simulated and measured DDT locations in the semi-confined A1-vessel geometry proves two aspects:

- The CFD solver predicts DDT within an acceptable tolerance on large-scale geometries with coarse meshes for homogeneous H_2-CO-air mixtures.
- FA and DDT simulations in semi-confined geometries are possible with the developed CFD solver by slightly extending the computational mesh to the surrounding of the channel and using OpenFOAM's *waveTransmissive* BC.

4.3.2 Inhomogeneous Semi-Confined H_2-CO-Air Mixtures

The validation of the CFD solver also covers vertical fuel concentration gradients in the semi-confined A1-vessel's explosion channel. Simulations are conducted with the minimum fuel contents necessary for FA to fast deflagrations and DDT. The flame velocity of a_{re} characterizes FA to a fast deflagration. The corresponding simulation aims to identify possible limitations of the solver's FA prediction ability under the challenging semi-confined conditions with vertical concentration gradient. Experimental and numerical flame

velocities obtained with a 75/25 H_2/CO fuel composition are compared.

In the A1-vessel, vertical concentration gradients are generated based on convective transport. The fuel mixture is injected with high-momentum jets against the ceiling. After flow deflection, a fuel concentration gradient forms due to the momentum decline towards the channel bottom. The fuel composition is assumed to remain uniform across the entire channel height [81]. The fuel concentration gradient is initialized during the case setup of the simulation using 2D interpolation tables with the cell center's vertical position y and the maximum fuel content $x_{f,max}$ underneath the ceiling as input variables. Based on measurements, different tables were derived for varying fuel compositions (see Appendix B.2). The vertical concentration gradient only covers the explosion channel height. Pure air fills the expansion box.

In Figure 4.10, numerically and experimentally obtained flame tip velocity profiles are compared for fuel concentration gradients with the maximum fuel content of $x_{f,max} = 22$ vol.-% and $x_{f,max} = 27$ vol.-%. For $x_{f,max} = 22$ vol.-%, the experimental data displays FA to a fast deflagration. The flame tip velocity exceeds a_{re}, but it does not reach a_{pr}. Hence, the mixture reactivity is insufficient to obtain a thermally choked flame. The flame propagates as a slow flame in

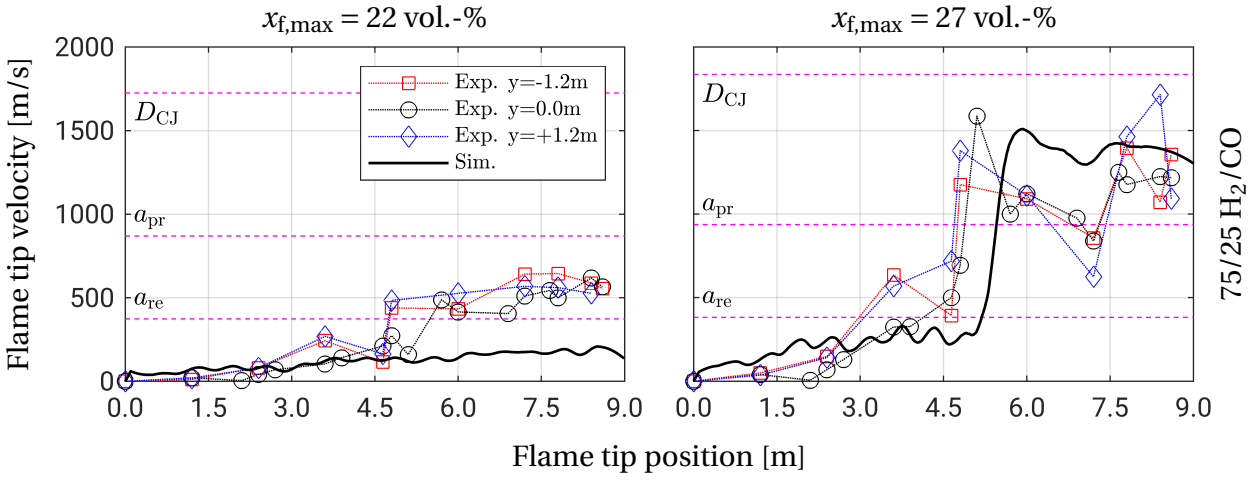

Figure 4.10: Simulated and measured flame tip velocity profiles from fuel concentration gradients with the maximum fuel content of $x_{f,max}$ = 22 vol.-% and of $x_{f,max}$ = 27 vol.-% (75/25 H_2/CO).

the first channel half. While the simulation captures the initially slow flame velocity, it misses the measured FA to a_{re} in the second channel half.

Significant deviations at slow velocities evolve from the density-based architecture combined with weaker velocity gradients on the under-resolved mesh, i.e., turbulence production. Hence, uncertainties in simulation results are high when the flame velocities are low. These inaccuracies add up continuously along the transient simulation when the flame propagates as slow deflagration (<200 m/s) over a long distance. The prediction of FA to fast deflagrations might not be possible due to the long propagation as slow deflagration. Two-stage AMR could improve the prediction of local turbulence production. However, due to the solver-architecture-related origin of the uncertainties, it is unclear whether FA would be predicted accurately on a finer mesh. Software incompatibility of the applied outdated OpenFOAM version with the operating system of available HPC resources at TUM prohibited using two-staged AMR with reasonable computation times in the present validation. As a result, it can be stated that applying the CFD solver to scenarios with FA to the lower velocity limit of fast deflagrations a_{re} is unreliable.

The simulated flame velocity profile for $x_{\mathrm{f,max}} = 27$ vol.-% shows quick acceleration close to a_{re} within the first meters due to a higher mixture reactivity in Figure 4.10. Like the experimental data, the simulation results show a sudden DDT followed by a subsequent quasi-detonation. The flame velocity jumps from around a_{re} to the quasi-detonation's velocity between a_{pr} and D_{CJ} in the experiment and the simulation alike. The simulated DDT location deviates from the experimental finding by less than half a meter. The interaction of the detonation complex with obstacles combined with the mass and momentum losses in the semi-confined geometry causes the noticeable velocity deficit to D_{CJ} in the quasi-detonation. Simulated values and trends of the flame velocity profile agree well with measured ones in the quasi-detonation regime.

For $x_{\mathrm{f,max}} = 27$ vol.-%, Figure 4.11 displays simulated 2D contour plots of the fuel mole fraction x_{f} and the pressure p. An iso-surface colored magenta indicates the flame front position. The 2D cutting plane is positioned off-center to capture the DDT location later. Figure 4.12 demonstrates the lateral positioning of the plane. The plots are taken during FA at the time $t = 28.732$ ms,

which corresponds to the flame tip position of 5.1 m in Figure 4.10.

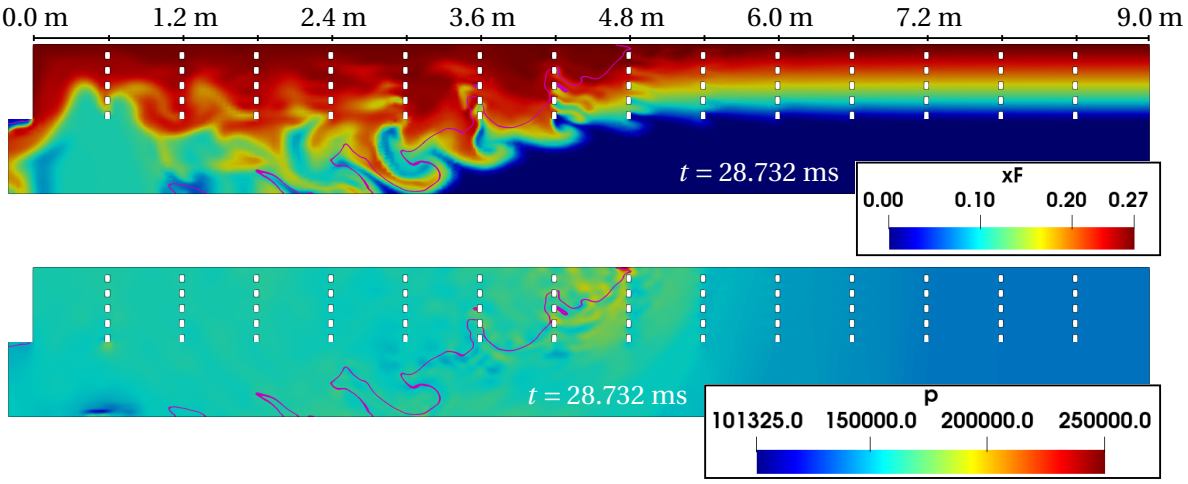

Figure 4.11: 2D contour plots of fuel mole fraction and pressure of a fast deflagration in an inhomogeneous 75/25 H_2/CO mixture with maximum fuel fraction $x_{f,max}$ = 27 vol.-% including a flame front iso-surface with $c = 0.5$ highlighted in magenta.

The fuel mole fraction contour plot shows that fresh combustible gas is convected downstream due to the induced flow. Combustible gas clouds pass the obstacles below the bottom obstacle. The flame front burns these gas clouds contributing to the FA of the flame tip. This underlines the need for an extended computational mesh beyond the bounds of the explosion channel. At flame velocities of a_{pr} or higher, the flame propagates too fast for the fresh gas convection to produce combustible gas clouds below the bottom obstacle that contribute to FA of the flame tip.

A fast flame is present at $t = 28.732$ ms. Hence, Figure 4.11 depicts several re- or deflected pressure waves in the pressure contour plot. The grid-like arrangement of the obstacles intensifies the reflection and deflection of pressure waves emitted from the flame front. The presented time step is short before DDT occurs. The interaction of several reflected waves can create a sufficiently strong preconditioning of the gas to trigger DDT either in the flame vicinity or by shock-focusing (see Section 2.4.1). The pressure peak, visible at 4.8 m in the most reactive mixture layer underneath the ceiling, results from the described positive pressure wave interaction.

Figure 4.12 visualizes the detonation front propagation in a time sequence of pressure contours following DDT. Contrary to Figure 4.11, peak pressures increase to roughly 19 bar, which relates to the shock wave leading the detonation complex. In the top-view pressure contour plot underneath the ceiling, it is visible at $t = 29.729$ ms that the detonation initially propagates spherically. The DDT occurred between the obstacles at 4.8 m and 5.4 m in the most reactive mixture layer underneath the ceiling. Hence, DDT probably originated as a weak transition solution in the flame vicinity instead of shock-focusing at obstacles.

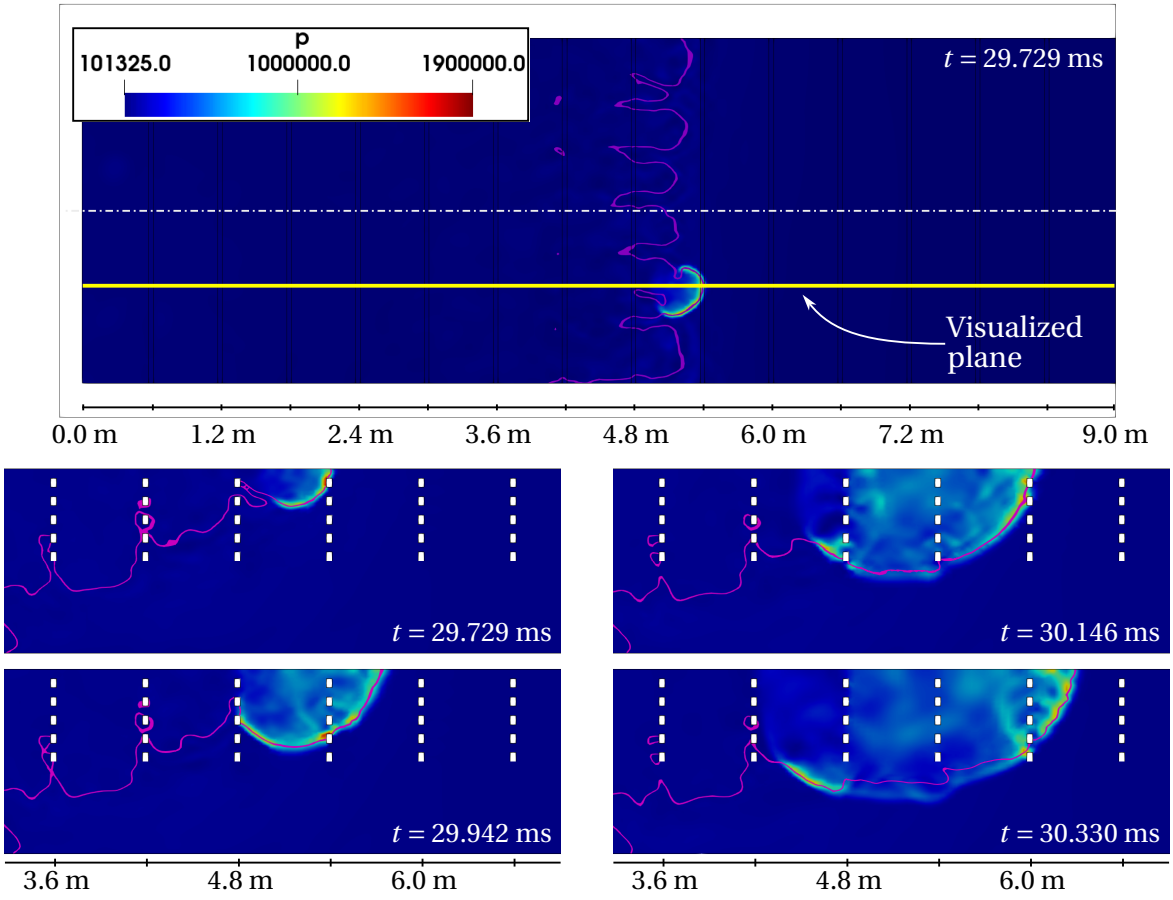

Figure 4.12: Time sequence of 2D pressure contour plots during DDT and detonation propagation in an inhomogeneous 75/25 H_2/CO mixture with maximum fuel fraction $x_{f,max} = 27$ vol.-% including a flame front iso-surface with $c = 0.5$ highlighted in magenta.

The time sequence of the contour plots in the cutting plane, presented in Figure 4.12, confirms the initial spherical propagation of the quasi-detonation following DDT. However, the pressure shock intensity decreases over time towards the channel bottom as the detonation propagates through less reactive mixture layers. The pressure wave decouples from the reaction front below the bottom obstacle at $t = 30.146$ ms. The lower local mixture reactivity reduces the heat release rate significantly, and the reaction front can no longer follow the shock front. The independently propagating pressure shock has a noticeably lower intensity. The newly introduced cell-size and mixture-dependent scaling of the detonation source term allows the solver to capture the decoupling of the detonation complex. At the time step $t = 30.330$ ms, the reaction front and the shock wave couple again in the region between 4.2 m and 4.8 m below the explosion channel forming a stable detonation. Convective transport of combustible gas led to a sufficiently reactive mixture there.

The mixture layers with different reactivity over the channel height result in varying detonation propagation velocities. Beginning from $t = 29.942$ ms, a curved shape of the macroscopic detonation front forms in the longitudinal propagation direction towards the explosion channel's end. The fastest detonation front remains in the mixture layer underneath the ceiling at all presented times. The scaling methodology of the volumetric source term guarantees the proper heat release rate, corresponding to the different reactivity in the vertical mixture layers (see Section 3.3.4). The simulation predicts the quasi-detonation's velocity with good accuracy, as indicated in Figure 4.10.

Overall, the validation with inhomogeneous mixtures proves that the solver can quantitatively predict FA, DDT and subsequent detonation propagation. Hence, the CFD solver can be applied for risk analysis in large-scale semi-confined geometries.

5 Summary and Outlook

5.1 Summary

The present thesis introduced an efficient multi-scale CFD framework for FA and DDT simulation in stratified H_2-CO-air mixtures for risk assessment of real-world accident scenarios. The development was based on the previous H_2-air explosion simulations of Ettner [8] and Hasslberger [4]. The presented solver development pursued three main objectives:

- The flame propagation simulation methodology was extended and adjusted to H_2-CO-air mixtures.
- The computational efficiency of the solver was improved, allowing parameter studies in the risk analysis.
- The solver was designed to be applicable to inhomogeneous multi-component fuel distributions and partially confined structures of different geometrical scales.

Depending on the geometrical scale of the accident scenario, the appropriate flame-propagation transport equation is selected in the multi-scale applicable framework. Due to its computational efficiency, the volume reaction approach (c transport equation) is used for small-scale geometries. The flame front tracking approach, including the geoVoF method (α transport equation), is applied to large-scale scenarios due to its low numerical dissipation on coarse meshes. For both flame-propagation transport equations, the source terms for deflagrations and detonations are modeled individually. While the deflagration source term employs a turbulent flame speed closure model, the detonation is modeled as a two-step mechanism consisting of a detonation

criterion and a heat release step. The introduction of H_2-CO fuels required the adjustment of the source term models compared to the previously investigated H_2 fuels. The achieved developments are summarized in the following:

- By considering the von Neumann pressure and temperature via interpolations tables for evaluating the burnt gas composition of detonations, the correct heat release for the detonation complex is guaranteed. This improves the accuracy of predicting the stable detonation velocity D_{CJ}.
- A virtual non-reacting mixture was introduced to track the material properties and the thermodynamic state, which are only affected by the compression. In contrast to previous implementations, shock relations are considered in the fresh gas. However, the deficit remains that shock-related change in the thermodynamic state cannot be reproduced inside the reaction zone. The non-reacting thermodynamic state influences FA via the deflagration source term.
- The necessary input variables to the turbulent flame speed closure model are provided for the simulation of H_2-CO-air mixtures. An interpolation table for unstretched laminar flame speeds at reference conditions $S_{\mathrm{L},0}$ was generated, which can be evaluated for any compositions of H_2-CO-air. Using interpolation tables is computationally more efficient than complex correlations for multi-component fuels. A new correlation was derived for the effective Lewis number $\mathrm{Le}_{\mathrm{eff}}$.
- The investigation of turbulent flame quenching demonstrated that the impact of quenching does not change significantly when H_2 is partially substituted with CO. Because the previously applied relation to calculate the decisive critical velocity gradient g_{cr} of the quenching model incorrectly predicts lower limits when CO is added, critical velocity gradients g_{cr} are computed from 1D simulations with detailed chemistry and tabulated for the simulations.
- The implementation of a scaling method for the volumetric source term maintains correct detonation velocities D_{CJ} independent of the mesh and mixture composition. The scaled volumetric source term combines the

advantage of a compact detonation front from the previously introduced detonation source term relation with consistent propagation velocities due to the scaling method for the under-resolved simulation approach.

- The introduction of a load-balancing algorithm for the computationally intensive geoVoF method (LB-geoVoF) provides a computational speedup of four for industry-scale DDT accident scenarios.

The simulation results were validated against experimental data from small-scale and large-scale facilities. Fuel content, fuel composition and obstacle configuration were varied in the validation. Moreover, the investigation covers fully and semi-confined structures with homogeneous and inhomogeneous fuel distributions. The outcome of the validation is as follows:

- The thermodynamic states of the detonation complex with respect to the ZND theory were represented quantitatively correctly in the validation, despite its non-physical spatial dimension in the under-resolved simulation approach. Capturing the von Neumann pressure peak is essential for risk assessment studies.
- Prediction of the DDT location and the flame velocity profiles agreed with the small-scale experiments in the GraVent facility for homogeneous H_2-CO-air mixtures of all three investigated fuel compositions 50/50, 75/25 and 100/0 H_2/CO.
- Apart from effectively suppressing detonation in the BR60S100 configuration, the simulation shows accurate DDT prediction when the obstacle configuration, i.e., blockage ratio and obstacle spacing, was varied.
- The simulation reproduces the experimentally found quasi-detonations in the presence of vertical concentration gradients in the GraVent channel. However, the quasi-detonations did not decay to fast flames in the obstacle-free channel section. This trend is adequate for a risk-assessment tool.
- The simulations capture the propagation of thermally choked fast deflagrations with flame tip velocities of the speed of sound of the combustion products a_{pr}. The newly implemented scaling of the detonation

source term correctly adjusts the heat release rate. Hence, the reaction front does not necessarily couple with any shock wave once the speed of sound of the combustion products a_{pr} is reached and DDT is delayed.

- Utilization of the *waveTransmissive* BC on open mesh boundaries is sufficiently accurate for explosion simulations with strong shock waves.
- The simulation of different homogeneous and inhomogeneous mixture compositions in the large-scale semi-confined A1-vessel achieved a reliable prediction of the DDT location.
- In the semi-confined A1-vessel explosion channel, simulations did not reproduce FA to the lower velocity limit of fast deflagrations, i.e., the speed of sound of reactants a_{re}. Uncertainties in the computation of the long-lasting slow deflagration before FA are high due to the solver's density-based architecture.

The generally reliable simulation of DDT in various geometrical configurations and mixture compositions allows the application of the efficient multi-scale CFD framework to DDT risk analysis in stratified H_2-CO-air mixtures.

5.2 Outlook

The presented development is a fundamental step towards a generally applicable risk analysis tool for H_2-CO-air combustion accidents. While two different approaches for the flame-propagation transport equation have been applied in the present study to handle the disparity of the dimensional scales in accident scenarios, future projects could introduce a dynamic link between the two transport equations instead of a static selection. A seamless multi-scale framework can be created that takes advantage of each approach. The dynamic switching can be based on the ratio of turbulent flame thickness and cell size. Methods to transfer the burnt volume fraction α field to the reaction progress variable c field and reverse are already existent in the present CFD solver, i.e., coupling of the fields in the flame front tracking approach (see Section 3.3.1.3) and the interface reconstruction of geoVoF (see Appendix C.1.1).

In order to minimize the potential uncertainty from user-defined input variables, the weighting coefficient w in the field coupling of the flame front tracking approach should be modeled based on a physical principle. A geometrically correct reconstruction of the flame brush thickness is very complex. Therefore, a distribution-based approach is suggested depending on the flame front's position inside the interface cell. Again, the relevant parameter is the ratio of the turbulent flame thickness and the local cell size.

The validation revealed two deficits of the DDT solver. First, the shock wave and reaction front of the detonation complex are linked by the detonation criterion of the simulation. Improvement of the coupling and decoupling mechanism of the shock wave and the reaction front can be obtained by explicitly tracking the von Neumann thermodynamic state within the reaction front during simulation. It can be achieved through the virtual non-reacting mixture. The non-reacting temperature must capture the compression by the shock wave. In that case, the burnt gas composition and the ignition delay time evaluation can directly utilize the non-reacting temperature.

Second, advancing the explosion modeling strategy towards an all-speed CFD solver requires that the solver captures FA to fast deflagrations at the speed of sound of reactants a_{re}. A hybrid pressure-density-based solver architecture could be used for that purpose. Static switching between solvers with a density-based and a pressure-based architecture has already led to good results for the simulation of FA in low turbulence tube geometries [146, 188]. However, it is preferable that a single framework covers all speeds similar to the FA and DDT prediction in the presented CFD solver for H_2-CO-air mixtures. Currently, efforts in this regard are underway [62, 189].

A migration of the CFD solver to an up-to-date version of OpenFOAM is a highly desirable step in the future. This way, HPC resources would be accessible to test the load-balancing algorithm to its full extent. More importantly, the applicability of the DDT solver on stratified H_2-CO-air mixtures could be demonstrated on industry-scale geometries like the containment of a Konvoi-type nuclear power plant.

Bibliography

[1] T. Poinsot and D. Veynante. *Theoretical and numerical combustion.* RT Edwards, Inc., 2005.

[2] R. Borghi. On the structure and morphology of turbulent premixed flames. In *Recent advances in the Aerospace Sciences*, pages 117–138. Springer, 1985.

[3] N. Peters. *Turbulent combustion.* Cambridge university press, 2000.

[4] J. Hasslberger. *Numerical simulation of deflagration-to-detonation transition on industry scale.* PhD thesis, Technische Universität München, 2017.

[5] G. Ciccarelli and S. B. Dorofeev. Flame acceleration and transition to detonation in ducts. *Progress in Energy and Combustion Science*, 34(4):499 – 550, 2008.

[6] V. L. Zimont. Gas premixed combustion at high turbulence. turbulent flame closure combustion model. *Experimental thermal and fluid science*, 21(1-3):179–186, 2000.

[7] P. Katzy. *Combustion model for the computation of flame propagation in lean hydrogen-air mixtures at low turbulence.* PhD thesis, Technische Universität München, 2020.

[8] F. Ettner. *Effiziente numerische Simulation des Deflagrations-Detonations-Übergangs.* PhD thesis, Technische Universität München, 2013.

[9] A. Friedrich, F. Necker, A. Veser, J. Grune, and M. S. Kuznetsov. Experiments on the combustion behaviour of hydrogen-carbon monoxide-air mixtures. In *Proc. 8th ICHS International Conference on Hydrogen Safety 2019*. Hydrogen Knowledge Centre, 2019.

[10] U. Pathak. Efficient simulation of medium to large scale DDT phenomena in H2-CO-air mixtures. Master's thesis, Lehrstuhl für Thermodynamik, Technische Universität München, 2020.

[11] D. Heilbronn, C. Barfuss, and T. Sattelmayer. Deflagration-to-detonation transition in H2-CO-air mixtures in a partially obstructed channel. *International Journal of Hydrogen Energy*, 46(23):12372–12383, March 2021.

[12] W. J. Rider and D. B. Kothe. Reconstructing volume tracking. *Journal of Computational Physics*, 141(2):112–152, April 1998.

[13] S. Ketterl. A conservative geometrical volume-of-fluid method with iterative interface reconstruction supporting unstructured meshes. Master's thesis, Technische Universität München, 2014.

[14] X. Li, X. You, F. Wu, and C. K. Law. Uncertainty analysis of the kinetic model prediction for high-pressure H2/CO combustion. *Proceedings of the Combustion Institute*, 35(1):617–624, 2015.

[15] European Comission. Übereinkommen von Paris. URL: https://ec.europa.eu/clima/policies/international/negotiations/paris.de, 2015. Last Accessed: 24.09.2021.

[16] IPCC. Climate change 2014: Synthesis report. Contribution of working groups I, II and III to the fifth assessment report of the intergovernmental panel on climate change [Core writing team, R.K. Pachauri and L.A. Meyer (eds.)]. Technical Report AR5, Intergovernmental Panel on Climate Change (IPCC), Geneva, Switzerland, 2014.

[17] T. Lieuwen, V. Yang, and R. Yetter. *Synthesis gas combustion: Fundamentals and applications*. CRC Press, 2009.

[18] T. Sevón. *Molten core - Concrete interactions in nuclear accidents: Theory and design of an experimental facility*. Number 2311 in VTT Tiedotteita - Meddelanden - Research Notes. VTT Technical Research Centre of Finland, Finland, 2005. Project code: 12S-SAAAN1MMCE.

[19] R. Gauntt, D. Kalinich, J. Cardoni, J. Phillips, A. Goldmann, S. Pickering, M. Francis, K. Robb, L. Ott, D. Wang, C. Smith, S. St. Germain, D. Schwieder, and C. Phelan. Fukushima Daiichi accident study. Technical Report SAND2012-6173, Sandia National Laboratories, July 2012.

[20] M. Klauck, E.-A. Reinecke, S. Kelm, N.Meynet, A.Bentaib, and H.-J. Allelein. Passive auto-catalytic recombiners operation in the presence of hydrogen and carbon monoxide: Experimental study and model development. *Nuclear Engineering and Design*, 266:137–147, January 2014.

[21] M. Klauck, E.-A. Reinecke, and H.-J. Allelein. Effect of PAR deactivation by carbon monoxide in the late phase of a severe accident. *Annals of Nuclear Energy*, 151:107887, February 2020.

[22] D. M. Johnson. The potential for vapour cloud explosions - lessons from the buncefield accident. *Journal of Loss Prevention in the Process Industries*, 23(6):921–927, November 2010.

[23] M. Maremonti, G. Russo, E. Salzano, and V. Tufano. Post-accident analysis of vapour cloud explosions in fuel storage areas. *Process Safety and Environmental Protection*, 77(6):360–365, November 1999.

[24] H.-J. Liaw. Lessons in process safety management learned in the Kaohsiung gas explosion accident in Taiwan. *Process Safety Progress*, 35(3):228–232, March 2016.

[25] M. Rogovin. *Three Mile Island: A report to the commissioners and to the public*, volume 1250. Nuclear Regulatory Commission, Special Inquiry Group, 1980.

[26] World Nuclear Association. World nuclear performance report 2021. Technical Report No. 2021/003, World Nuclear Association, 2021. URL: https://www.world-nuclear.org/getmedia/891c0cd8-2beb-4acf-bb4b-552da1696695/world-nuclear-performance-report-2021.pdf.aspxx.

[27] A. Bentaib, N. Meynet, and A. Bleyer. Overview on hydrogen risk research and development activities: Methodology and open issues. *Nuclear Engineering and Technology*, 47(1):26–32, February 2015.

[28] S. Collong and R. Kouta. Fault tree analysis of proton exchange membrane fuel cell system safety. *International Journal of Hydrogen Energy*, 40(25):8248–8260, July 2015.

[29] M. Molnarne and V. Schroeder. Hazardous properties of hydrogen and hydrogen containing fuel gases. *Process Safety and Environmental Protection*, 130:1–5, October 2019.

[30] A. Molino, G. Braccio, G. Fiorenza, F. A. Marraffa, S. Lamonaca, G. Giordano, G. Rotondo, U. Stecchi, and M. La Scala. Classification procedure of the explosion risk areas in presence of hydrogen-rich syngas: Biomass gasifier and molten carbonate fuel cell integrated plant. *Fuel*, 99:245–253, September 2012.

[31] S. B. Dorofeev, M. S. Kuznetsov, V. I. Alekseev, A. A. Efimenko, and W. Breitung. Evaluation of limits for effective flame acceleration in hydrogen mixtures. *Journal of Loss Prevention in the Process Industries*, 14(6):583 – 589, 2001.

[32] S. B. Dorofeev, V. P. Sidorov, M. S. Kuznetsov, I. D. Matsukov, and V. I. Alekseev. Effect of scale on the onset of detonations. *Shock Waves*, 10(2):137–149, May 2000.

[33] M. S. Kuznetsov, J. Grune, A. Friedrich, and T. Jordan. Combustion regimes in a stratified layer of hydrogen-air mixture. In *Proc. ICAPP*, pages 2–5, 2011.

[34] M. S. Kuznetsov, J. Yanez, J. Grune, A. Friedrich, and T. Jordan. Hydrogen combustion in a flat semi-confined layer with respect to the Fukushima Daiichi accident. *Nuclear Engineering and Design*, 286:36 – 48, 2015.

[35] J. Grune, K. Sempert, M. S. Kuznetsov, and T. Jordan. Experimental investigation of fast flame propagation in stratified hydrogen-air mixtures in semi-confined flat layers. *Journal of Loss Prevention in the Process Industries*, 26(6):1442 – 1451, 2011.

[36] J. Grune, K. Sempert, H. Haberstroh, M. S. Kuznetsov, and T. Jordan. Experimental investigation of hydrogen-air deflagrations and detonations in semi-confined flat layers. *Journal of Loss Prevention in the Process Industries*, 26(2):317 – 323, 2013. Selected Papers from the Eighth International Symposium on Hazards, Prevention, and Mitigation of Industrial Explosions (Yokohama, Japan, 2010).

[37] W. Breitung, C. K. Chan, S. B. Dorofeev, A. Eder, B. E. Gelfand, M. Heitsch, R. Klein, A. Malliakos, J. E. Shepherd, E. Studer, and P. Thibault. Flame acceleration and deflagration-to-detonation transition in nuclear safety. state-of-the art report by a group of experts. Technical Report NEA/CSNI/R(2000)7, OECD Nuclear Energy Agency, 2000.

[38] H. Dimmelmeier, J. Eyink, and M.-A. Movahed. Computational validation of the EPR combustible gas control system. *Nuclear Engineering and Design*, 249:118–124, 2012.

[39] F. Bartlmä. *Gasdynamik der Verbrennung*. Leitfäden der angewandten Mathematik und Mechanik. Springer, 1975.

[40] J. H. Lee. *The detonation phenomenon*. Cambridge University Press, Cambridge, 2008.

[41] S. R. Turns et al. *An introduction to combustion*, volume 499. McGraw-Hill New York, 1996.

[42] N. Brehm and F. Mayinger. *Ein Beitrag zum Phänomen des Überganges Deflagration-Detonation*. VDI-Verlag, 1989.

[43] F. Joos. *Technische Verbrennung*, volume 76. Springer, 2006.

[44] A. Eder. *Brennverhalten schallnaher und überschall-schneller Wasserstoff-Luft Flammen*. Dissertation, Technische Universität München, München, 2001.

[45] D. G. Goodwin, R. L. Speth, H. K. Moffat, and B. W. Weber. Cantera: An object-oriented software toolkit for chemical kinetics, thermodynamics, and transport processes. `https://www.cantera.org`, 2018. Version 2.4.0.

[46] S. G. Davis, A. V. Joshi, H. Wang, and F. Egolfopoulos. An optimized kinetic model of H2/CO combustion. *Proceedings of the combustion Institute*, 30(1):1283–1292, 2005.

[47] A. Kéromnès, W. K. Metcalfe, K. A. Heufer, N. Donohoe, A. K. Das, C.-J. Sung, J. Herzler, C. Naumann, P. Griebel, O. Mathieu, M. C. Krejci, E. L. Petersen, W. J. Pitz, and H. J. Curran. An experimental and detailed chemical kinetic modeling study of hydrogen and syngas mixture oxidation at elevated pressures. *Combustion and Flame*, 160(6):995–1011, June 2013.

[48] T. Varga, C. Olm, T. Nagy, I. G. Zsély, E. Valkó, R. Pálvölgyi, H. J. Curran, and T. Turányi. Development of a joint hydrogen and syngas combustion mechanism based on an optimization approach. *International Journal of Chemical Kinetics*, 48(8):407–422, May 2016.

[49] T. Fiala and T. Sattelmayer. Nonpremixed counterflow flames: Scaling rules for batch simulations. *Journal of Combustion*, 2014:1–7, 2014.

[50] J. Natarajan, T. Lieuwen, and J. Seitzman. Laminar flame speeds of H2/CO mixtures: Effect of CO2 dilution, preheat temperature, and pressure. *Combustion and flame*, 151(1-2):104–119, 2007.

[51] H.-M. Li, G.-X. Li, Z.-Y. Sun, Y. Zhai, and Z.-H. Zhou. Measurement of the laminar burning velocities and markstein lengths of lean and stoichiometric syngas premixed flames under various hydrogen fractions. *international journal of hydrogen energy*, 39(30):17371–17380, 2014.

[52] A. K. Das, K. Kumar, and C.-J. Sung. Laminar flame speeds of moist syngas mixtures. *Combustion and Flame*, 158(2):345–353, February 2011.

[53] G. W. Koroll and E. M. Kumar, R. K .and Bowles. Burning velocities of hydrogen-air mixtures. *Combustion and Flame*, 94(3):330–340, 1993.

[54] C. Dong, Q. Zhou, Q. Zhao, Y. Zhang, T. Xu, and S. Hui. Experimental study on the laminar flame speed of hydrogen/carbon monoxide/air mixtures. *Fuel*, 88(10):1858–1863, 2009.

[55] R. Shang, Y. Zhang, M. Zhu, Z. Zhang, and D. Zhang. Semiempirical correlation for predicting laminar flame speed of H2/CO/air flames with CO2 and N2 dilution. *Energy & Fuels*, 31(9):9957–9966, 2017.

[56] S. B. Pope. *Turbulent flows*. IOP Publishing, 2001.

[57] T. Poinsot, D. Veynante, and S. Candel. Quenching processes and premixed turbulent combustion diagrams. *Journal, Fluid Mechanics*, 228:561–605, 1991.

[58] C. Meneveau and T. Poinsot. Stretching and quenching of flamelets in premixed turbulent combustion. *Combustion and Flame*, 86(4):311–332, 1991.

[59] D. Bradley. Instabilities and flame speeds in large-scale premixed gaseous explosions. *Philosophical Transactions of the Royal Society of London. Series A: Mathematical, Physical and Engineering Sciences*, 357(1764):3567–3581, December 1999.

[60] P. Katzy, J. Hasslberger, L. Boeck, and T. Sattelmayer. The effect of intrinsic instabilities on effective flame speeds in under-resolved simulations of lean hydrogen-air flames. *Journal of Nuclear Engineering and Radiation Science*, 3(4), 2017.

[61] F. Dinkelacker, B. Manickam, and S. P. R. Muppala. Modelling and simulation of lean premixed turbulent methane/hydrogen/air flames with an effective lewis number approach. *Combustion and Flame*, 158(9):1742 – 1749, 2011.

[62] D. Zivkovic and T. Sattelmayer. Fractal-based RANS modeling of Darrieus-Landau and thermal-diffusive instability effects on lean hydrogen flames. In *28th International Colloquium on the Dynamics of Explosions and Reactive Systems*, Naples, Italy, June 2022. Combustion Institute.

[63] W. Kim, Y. Sato, T. Johzaki, T. Endo, D. Shimokuri, and A. Miyoshi. Experimental study on self-acceleration in expanding spherical hydrogen-air flames. *International Journal of Hydrogen Energy*, 43(27):12556–12564, July 2018.

[64] P. Katzy, J. Hasslberger, and T. Sattelmayer. On the effect of pressure on intrinsic flame instabilities in lean hydrogen-air mixtures - Part II: Experimental investigation based on OH-PLIF technique. In *26th International Colloquium on the Dynamics of Explosions and Reactive Systems (ICDERS)*, pages 1–6, Boston, USA, July 2017. FM Global in Boston.

[65] R. D. Richtmyer. Taylor instability in shock acceleration of compressible fluids. *Communications on Pure and Applied Mathematics*, 13(2):297–319, May 1960.

[66] E. E. Meshkov. Instability of the interface of two gases accelerated by a shock wave. *Fluid Dynamics*, 4(5):101–104, 1969.

[67] E. S. Oran and V. N. Gamezo. Origins of the deflagration-to-detonation transition in gas-phase combustion. *Combustion and Flame*, 148(1):4 – 47, 2007.

[68] W. Rakotoarison, B. Maxwell, A. Pekalski, and M. I. Radulescu. Mechanism of flame acceleration and detonation transition from the interaction of a supersonic turbulent flame with an obstruction: Experiments in low pressure propane–oxygen mixtures. *Proceedings of the Combustion Institute*, 37(3):3713–3721, 2019.

[69] M. Bambauer, J. Hasslberger, and M. Klein. Direct numerical simulation of the Richtmyer-Meshkov instability in reactive and nonreactive flows. *Combustion Science and Technology*, 192(11):2010–2027, May 2020.

[70] V. Bychkov, V. Akkerman, G. Fru, A. Petchenko, and L.-E. Eriksson. Flame acceleration in the early stages of burning in tubes. *Combustion and Flame*, 150(4):263–276, September 2007.

[71] J. H. Lee, R. Knystautas, and C. K. Chan. Turbulent flame propagation in obstacle-filled tubes. *Symposium (International) on Combustion*, 20(1):1663–1672, January 1985.

[72] M. S. Kuznetsov and V. I. Alekseev. DDT in a smooth tube filled with a hydrogen-air mixture. *Shock Waves*, 14(3):205–215, 2005.

[73] M. S. Kuznetsov, I. D. Matsukov, V. I. Alekseev, and S. B. Dorofeev. Photographic study of unstable turbulent flames in obstructed channels. In *Proc. 17th Int. Colloquium on the Dynamics of Explosions and Reactive Systems, Heidelberg, Germany*, 1999.

[74] K.I. Shchelkin. Influence of tube roughness on the formation and detonation propagation in gas. *Journal of Experimental and Theoretical physics*, 10(10):823–827, 1940.

[75] M. S. Kuznetsov, J. Grune, A. Friedrich, K. Sempert, W. Breitung, and T. Jordan. Hydrogen-air deflagrations and detonations in a semi-confined flat layer. In *Proceedings of the Sixth International Seminar on Fire & Explosion Hazards (FEH6)*, 2010.

[76] L. Boeck, J. Hasslberger, and T. Sattelmayer. Flame acceleration in hydrogen/air mixtures with concentration gradients. *Combustion Science and Technology*, 186(10-11):1650–1661, 2014.

[77] C. R. L. Bauwens, J. M. Bergthorson, and S. B. Dorofeev. Experimental investigation of spherical-flame acceleration in lean hydrogen-air mixtures. *International Journal of Hydrogen Energy*, 42(11):7691–7697, March 2017.

[78] L. Boeck, F. Berger, J. Hasslberger, F. Ettner, and T. Sattelmayer. Macroscopic structure of fast deflagrations and detonations in hydrogen-air mixtures with concentration gradients. In *24th ICDERS*, January 2013.

[79] A. Veser, G. Stern, J. Grune, W. Breitung, and W. Burgeth. Programm Nukleare Sicherheitsforschung Jahresbericht 2001 Teil 2: CO-H2-air combustion tests in the FZK-7m-tube. Technical Report FZKA 6742, Institut für Kern- und Energietechnik, 2002.

[80] D. Heilbronn, C. Barfuss, and T. Sattelmayer. Influence of geometry on flame acceleration and DDT in H2-CO-air mixtures in a partially obstructed channel. *Journal of Loss Prevention in the Process Industries*, 71:104493, July 2021.

[81] A. Friedrich, G. Necker, M. Moore, J. Grune, M. S. Kuznetsov, and T. Jordan. Verbundvorhaben: Entwicklung von Verbrennungsmodellen und Kriterien für H2-CO-Luft-Schichten mit partiellem Einschluss -Teilvorhaben: Grundlagenexperimente und experimentelle Untersuchungen auf großer Skala. Technical Report 1501545B, Bundesministerium für Wirtschaft und Energie (BMWi), 2022.

[82] D. L. Chapman. On the rate of explosion in gases. *The London, Edinburgh, and Dublin Philosophical Magazine and Journal of Science*, 47(284):90–104, 1899.

[83] E. Jouguet. Sur la propagation des réactions chimiques dans les gaz. *Journal de mathématiques pures et appliquées*, 6(1):347–425, 1905.

[84] G. I. Taylor. The dynamics of the combustion products behind plane and spherical detonation fronts in explosives. *Proceedings of the Royal Society of London. Series A. Mathematical and Physical Sciences*, 200(1061):235–247, January 1950.

[85] Y. B. Zeldovich. On the theory of the propagation of detonation in gaseous systems. *Journal of Experimental and Theoretical Physics*, 10(5):543–68, 1940.

[86] J. Von Neumann. Progress report on the theory of detonation waves. Technical Report ADB967734, Office of Scientific Research and Development, 1942.

[87] W. Döring. Über den Detonationsvorgang in Gasen. *Annalen der Physik*, 435:421 – 436, March 2006.

[88] E. S. Oran and A. M. Khokhlov. Deflagrations, hot spots, and the transition to detonation. *Philosophical Transactions of the Royal Society of London. Series A: Mathematical, Physical and Engineering Sciences*, 357(1764):3539–3551, December 1999.

[89] M. Zbikowski, D. Makarov, and V. Molkov. Numerical simulations of large-scale detonation tests in the RUT facility by the LES model. *Journal of Hazardous Materials*, 181(1-3):949–956, September 2010.

[90] J. J. Erpenbeck. Stability of steady-state equilibrium detonations. *The physics of Fluids*, 5(5):604–614, 1962.

[91] J. M. Austin. *The role of instability in gaseous detonation*. PhD thesis, California Institute of Technology, 2003.

[92] S. Shigeoka and A. Matsuo. Numerical investigation of detonation in stratified combustible mixture and oxidier with concentration gradients. In *Proceedings of the 8th International Conference on Hydrogen Safety*. Hydrogen Knowledge Centre, 2019.

[93] A. I. Gavrikov, A. A. Efimenko, and S. B. Dorofeev. A model for detonation cell size prediction from chemical kinetics. *Combustion and Flame*, 120(1):19 – 33, 2000.

[94] M. Kaneshige and J. E. Shepherd. Detonation database. Technical Report FM97-8, GALCIT, 1997.

[95] F. Ettner, K. Vollmer, and T. Sattelmayer. Mach reflection in detonations propagating through a gas with a concentration gradient. *Shock Waves*, 23(3):201–206, May 2013.

[96] J. E. Shepherd and J.H.S. Lee. On the transition from deflagration to detonation. In *Major research topics in combustion*, pages 439–487. Springer, 1992.

[97] J. E. Shepherd. Detonation in gases. *Proceedings of the Combustion Institute*, 32(1):83–98, 2009.

[98] J.W. Meyer, P.A. Urtiew, and A.K. Oppenheim. On the inadequacy of gasdynamic processes for triggering the transition to detonation. *Combustion and Flame*, 14(1):13–20, February 1970.

[99] P. A. Urtiew and A. K. Oppenheim. Experimental observations of the transition to detonation in an explosive gas. *Proceedings of the Royal Society of London. Series A. Mathematical and Physical Sciences*, 295(1440):13–28, November 1966.

[100] J. H. Lee, R. Knystautas, and N. Yoshikawa. Photochemical initiation of gaseous detonations. In *Gasdynamics of Explosions and Reactive Systems*, pages 971–982. Elsevier, 1980.

[101] J. H. Lee and I. O. Moen. The mechanism of transition from deflagration to detonation in vapor cloud explosions. *Progress in Energy and Combustion Science*, 6(4):359–389, January 1980.

[102] G. Thomas. Some observations on the initiation and onset of detonation. *Philosophical Transactions of the Royal Society A: Mathematical, Physical and Engineering Sciences*, 370(1960):715–739, February 2012.

[103] M. Jordan, A. Eder, B. Edlinger, F. Mayinger, M. Carcassi, M. Heitsch, F. Martin-Fuertes, R. Monti, and T. Kanzleiter. Turbulent quenching and acceleration of flamesby highly blocking obstacles. In *FISA Symposium*, 1999.

[104] R. Knystautas, J. H. Lee, I. Moen, and H. G. G. Wagner. Direct initiation of spherical detonation by a hot turbulent gas jet. *Symposium (International) on Combustion*, 17(1):1235–1245, January 1979.

[105] Y. B. Zeldovich, V. B. Librovich, G. M. Makhviladze, and G. I. Sivashinsky. On the development of detonation in a non-uniformly preheated gas. *Astronautica Acta*, 15:313–21, 1970.

[106] J. Xiao, W. Breitung, M. S. Kuznetsov, H. Zhang, J. R. Travis, R. Redlinger, and T. Jordan. GASFLOW-MPI: A new 3-D parallel all-speed CFD code for turbulent dispersion and combustion simulations - Part II: First analysis of the hydrogen explosion in Fukushima Daiichi Unit 1. *International Journal of Hydrogen Energy*, 42(12):8369–8381, 2017.

[107] W. Breitung and P. Royl. Procedure and tools for deterministic analysis and control of hydrogen behavior in severe accidents. *Nuclear Engineering and Design*, 202(2-3):249–268, December 2000.

[108] W. Breitung, S. B. Dorofeev, A. Kotchourko, R. Redlinger, W. Scholtyssek, A. Bentaib, J.-P. L'Heriteau, P. Pailhories, J. Eyink, M. Movahed, K.-G. Petzold, M. Heitsch, V. Alekseev, A. Denkevits, M. Kuznetsov, A. Efimenko,

M. V. Okun, T. Huld, and D. Baraldi. Integral large scale experiments on hydrogen combustion for severe accident code validation-HYCOM. *Nuclear Engineering and Design*, 235(2-4):253–270, February 2005.

[109] S. Kelm, M. Klauck, S. Beck, H.-J. Allelein, G. Preusser, M. Sangiorgi, W. Klein-Hessling, I. Bakalov, A. Bleyer, A. Bentaib, I. Kljenak, M. Stempniewicz, P. Kostka, S. Morandi, B. Ada del Corno, C. Bratfisch, T. Risken, L. Denk, Z. Parduba, S. Paci, A. Manfredini, A. Silde, P. Juris, J. Jancovic, H. G. Lele, and S. Ganju. Generic containment: Detailed comparison of containment simulations performed on plant scale. *Annals of Nuclear Energy*, 74:165–172, December 2014.

[110] M. Andreani. Simulation of gas stratification build-up in the containment under severe accident conditions. In *Volume 2B: Thermal Hydraulics*. American Society of Mechanical Engineers, July 2014.

[111] A. Filippov, S. Grigoryev, N. Drobyshevsky, A. Kiselev, A. Shyukin, and T. Yudina. CMFD simulation of ERCOSAM PANDA spray tests PE1 and PE2. *Nuclear Engineering and Design*, 299:81–94, April 2016.

[112] J. Xiao, W. Breitung, M. S. Kuznetsov, H. Zhang, J. R. Travis, R. Redlinger, and T. Jordan. GASFLOW-MPI: A new 3-D parallel all-speed CFD code for turbulent dispersion and combustion simulations - Part I: Models, verification and validation. *International Journal of Hydrogen Energy*, 42(12):8346–8368, 2017.

[113] S. Kelm, M. Kampili, X. Liu, A. George, D. Schumacher, C. Druska, S. Struth, A. Kuhr, L. Ramacher, H.-J. Allelein, K. A. Prakash, G. V. Kumar, L. M. F. Cammiade, and R. Ji. The tailored CFD package 'containmentFOAM' for analysis of containment atmosphere mixing, H2/CO mitigation and aerosol transport. *Fluids*, 6(3):100, March 2021.

[114] J. Yanez, M. S. Kuznetsov, and A. Souto-Iglesias. An analysis of the hydrogen explosion in the Fukushima-Daiichi accident. *International Journal of Hydrogen Energy*, 40(25):8261–8280, July 2015.

[115] R. Redlinger. DET3D - A CFD tool for simulating hydrogen combustion in nuclear reactor safety. *Nuclear Engineering and Design*, 238(3):610–617, March 2008.

[116] E. Vyazmina and S. Jallais. Validation and recommendations for FLACS CFD and engineering approaches to model hydrogen vented explosions: Effects of concentration, obstruction vent area and ignition position. *International Journal of Hydrogen Energy*, 41(33):15101–15109, September 2016.

[117] P. Middha and O. Hansen. Predicting deflagration to detonation transition in hydrogen explosions. *Process Safety Progress*, 27(3), 2008.

[118] C. Rosas, S. G. Davis, D. Engel, P. Middha, K. van Wingerden, and M. S. Mannan. Deflagration to detonation transitions (DDTs): Predicting DDTs in hydrocarbon explosions. *Journal of Loss Prevention in the Process Industries*, 30:263–274, July 2014.

[119] O. R. Hansen and D. M. Johnson. Improved far-field blast predictions from fast deflagrations, DDTs and detonations of vapour clouds using FLACS CFD. *Journal of Loss Prevention in the Process Industries*, 35:293–306, May 2015.

[120] O. R. Hansen, P. Hinze, D. Engel, and S. Davis. Using computational fluid dynamics (CFD) for blast wave predictions. *Journal of Loss Prevention in the Process Industries*, 23(6):885–906, November 2010.

[121] A. Velikorodny, E. Studer, S. Kudriakov, and A. Beccantini. Combustion modeling in large scale volumes using EUROPLEXUS code. *Journal of Loss Prevention in the Process Industries*, 35:104–116, 2015.

[122] K. Tang, A. Beccantini, and C. Corre. Combining discrete equations method and upwind downwind-controlled splitting for non-reacting and reacting two-fluid computations: One dimensional case. *Computers & Fluids*, 93:74–90, April 2014.

[123] K. Tang, A. Beccantini, and C. Corre. Combining discrete equations method and upwind downwind-controlled splitting for non-reacting

and reacting two-fluid computations: Two dimensional case. *Computers & Fluids*, 103:132–155, November 2014.

[124] A. Beccantini and E. Studer. The reactive Riemann problem for thermally perfect gases at all combustion regimes. *International Journal for Numerical Methods in Fluids*, 64(3):269–313, September 2009.

[125] S. Kudriakov, F. Dabbene, E. Studer, A. Beccantini, J. P. Magnaud, H. Paillère, A. Bentaib, A. Bleyer, J. Malet, E. Porcheron, and C. Caroli. The TONUS CFD code for hydrogen risk analysis: Physical models, numerical schemes and validation matrix. *Nuclear Engineering and Design*, 238(3):551–565, March 2008.

[126] A. A. Efimenko and S. B. Dorofeev. CREBCOM code system for description of gaseous combustion. *Journal of Loss Prevention in the Process Industries*, 14(6):575–581, November 2001.

[127] H. Jasak, A. Jemcov, and Z. Tukovic. OpenFOAM: A C++ library for complex physics simulations. In *International Workshop on Coupled Methods in Numerical Dynamics*, September 2007.

[128] J. Hasslberger, P. Katzy, L. Boeck, and T. Sattelmayer. Computational fluid dynamics simulation of deflagration-to-detonation transition in a full-scale konvoi-type pressurized water reactor. *Journal of Nuclear Engineering and Radiation Science*, 3(4):041014, 2017.

[129] J. H. Ferziger and M. Peric. *Computational methods for fluid dynamics*. Springer Science & Business Media, 2012.

[130] A. Favre. Equations des gaz turbulents compressibles. *J. de Mécanique*, 4(3), 1965.

[131] D. C. Wilcox et al. *Turbulence modeling for CFD*, volume 2. DCW industries La Canada, CA, 1998.

[132] F. Menter, M. Kuntz, and R. Langtry. Ten years of industrial experience with the SST turbulence model. *Turbulence, heat and mass transfer*, 4(1):625–632, 2003.

[133] B. E. Poling, j. M. Prausnitz, J. P. O'connell, et al. *The properties of gases and liquids*, volume 5. Mcgraw-hill New York, 2001.

[134] B. J. McBride, M. J. Zehe, and S. Gordon. NASA Glenn coefficients for calculating thermodynamic properties of individual species. Technical Report NASA/TP-2002-211556, National Aeronautics and Space Administration, John H. Glenn Research Center, 2002.

[135] F. Menter and T. Esch. Elements of industrial heat transfer predictions. In *16th Brazilian Congress of Mechanical Engineering (COBEM)*, volume 109, page 650, 2001.

[136] F. Menter. Two-equation eddy-viscosity turbulence models for engineering applications. *AIAA journal*, 32(8):1598–1605, 1994.

[137] C. R. L. Bauwens and S. B. Dorofeev. Quantifying the potential consequences of a detonation in a hydrogen jet release. In *Proceedings of the 8th International Conference on Hydrogen Safety*. Hydrogen Knowledge Centre, 2019.

[138] F. Ettner, K. Vollmer, and T. Sattelmayer. Numerical investigation of DDT in inhomogeneous hydrogen-air mixtures. In *8th International Symposium on Hazards, Prevention and Mitigation of Industrial Explosions*, Yokohama, Japan, 2010.

[139] E. F. Toro, M. Spruce, and W. Speares. Restoration of the contact surface in the HLL-Riemann solver. *Shock waves*, 4(1):25–34, 1994.

[140] J. F. Wendt. *Computational fluid dynamics: An introduction*. Springer Science & Business Media, 2008.

[141] T. Maric, H. Marschall, and D. Bothe. voFoam-A geometrical volume of fluid algorithm on arbitrary unstructured meshes with local dynamic adaptive mesh refinement using OpenFOAM, 2013.

[142] J. Hasslberger, P. Katzy, L. Boeck, and T. Sattelmayer. Massively parallelized simulation of deflagration-to-detonation transition in a Konvoi-type pressurized water reactor. In *24th International Conference on Nuclear Engineering*, volume Vol. 4, Charlotte, NC, USA, June 2016. ASME.

[143] M. Namazian, I. G. Shepherd, and L. Talbot. Characterization of the density fluctuations in turbulent V-shaped premixed flames. *Combustion and Flame*, 64(3):299–308, June 1986.

[144] A. N. Lipatnikov and J. Chomiak. Turbulent flame speed and thickness: Phenomenology, evaluation, and application in multi-dimensional simulations. *Progress in Energy and Combustion Science*, 28(1):1–74, January 2002.

[145] H. G. Weller. The development of a new flame area combustion model using conditional averaging, 1993.

[146] C. H. Wieland. *Efficient simulation of flame acceleration and deflagration-to-detonation transition in smooth geometries*. Dissertation, Technische Universität München, München, 2022.

[147] C. Olm, I. G. Zsély, T. Varga, H. J. Curran, and T. Turányi. Comparison of the performance of several recent syngas combustion mechanisms. *Combustion and flame*, 162(5):1793–1812, 2015.

[148] V. L. Zimont, W. Polifke, M. Bettelini, and W. Weisenstein. An efficient computational model for premixed turbulent combustion at high Reynolds numbers based on a turbulent flame speed closure. *Journal of engineering for gas turbines and power*, 120(3):526–532, 1998.

[149] W. Polifke, P. Flohr, and M. Brandt. Modeling of inhomogeneously premixed combustion with an extended TFC model. In *ASME Turbo Expo 2000: Power for Land, Sea, and Air*, pages V002T02A053–V002T02A053. American Society of Mechanical Engineers, 2000.

[150] H.-P. Schmid, P. Habisreuther, and W. Leuckel. A model for calculating heat release in premixed turbulent flames. *Combustion and Flame*, 113(1-2):79–91, 1998.

[151] C. Barfuss, D. Heilbronn, and T. Sattelmayer. Numerical simulation of deflagration and detonation in homogeneous hydrogen-carbon monoxide-air mixtures. In Combustion Institute, editor, *12th International Symposium on Hazards, Prevention, and Mitigation of Industrial Explosions*, Kansas City, MO, USA, Aug 2018. FIKE Corporation.

[152] K. T. Aung, M. I. Hassan, and G. M. Faeth. Flame stretch interactions of laminar premixed hydrogen/air flames at normal temperature and pressure. *Combustion and Flame*, 109(1-2):1–24, April 1997.

[153] N. Bouvet, F. Halter, C. Chauveau, and Y. Yoon. On the effective lewis number formulations for lean hydrogen/hydrocarbon/air mixtures. *International journal of hydrogen energy*, 38(14):5949–5960, 2013.

[154] M. I. Hassan, K. T. Aung, and G. M. Faeth. Properties of laminar premixed CO/H2/air flames at various pressures. *Journal of Propulsion and Power*, 13(2):239–245, March 1997.

[155] O. C. Kwon and G. M. Faeth. Flame/stretch interactions of premixed hydrogen-fueled flames: Measurements and predictions. *Combustion and Flame*, 124(4):590–610, March 2001.

[156] I. C. McLean, D. B. Smith, and S. C. Taylor. The use of carbon monoxide/hydrogen burning velocities to examine the rate of the CO-OH reaction. *Symposium (International) on Combustion*, 25(1):749–757, 1994.

[157] J. Natarajan, S. Nandula, T. Lieuwen, and J. Seitzman. Laminar flame speeds of synthetic gas fuel mixtures. In *ASME turbo expo 2005: power for land, sea, and air*, pages 677–686. American Society of Mechanical Engineers, 2005.

[158] C. Prathap, A. Ray, and M. R. Ravi. Effects of dilution with carbon dioxide on the laminar burning velocity and flame stability of H2-CO mixtures at atmospheric condition. *Combustion and Flame*, 159(2):482–492, February 2012.

[159] H. Sun, S. I. Yang, G. Jomaas, and C. K. Law. High-pressure laminar flame speeds and kinetic modeling of carbon monoxide/hydrogen combustion. *Proceedings of the Combustion Institute*, 31(1):439–446, January 2007.

[160] S. D. Tse, D. L. Zhu, and C. K. Law. Morphology and burning rates of expanding spherical flames in H2/O2/inert mixtures up to 60 atmospheres. *Proceedings of the Combustion Institute*, 28(2):1793–1800, January 2000.

[161] C. M. Vagelopoulos and F. N. Egolfopoulos. Laminar flame speeds and extinction strain rates of mixtures of carbon monoxide with hydrogen, methane, and air. *Symposium (International) on Combustion*, 25(1):1317–1323, 1994. Twenty-Fifth Symposium (International) on Combustion.

[162] H. Le Chatelier. Estimation of firedamp by flammability limits. *Annals of Mines*, 19(8):388–395, 1891.

[163] C. V. Mashuga and D. A. Crowl. Derivation of Le Chatelier's mixing rule for flammable limits. *Process Safety Progress*, 19(2):112–117, 2000.

[164] A. R. Choudhuri, M. Subramanya, and S. R. Gollahalli. Flame extinction limits of H2-CO fuel blends. *Journal of Engineering for Gas Turbines and Power*, 130(3), March 2008.

[165] M. S. Kuznetsov, R. Redlinger, W. Breitung, J. Grune, A. Friedrich, and N. Ichikawa. Laminar burning velocities of hydrogen-oxygen-steam mixtures at elevated temperatures and pressures. *Proceedings of the Combustion Institute*, 33(1):895–903, 2011.

[166] T. Szabó, J. Yáñez, A. Kotchourko, M. S. Kuznetsov, and T. Jordan. Parameterization of laminar burning velocity dependence on pressure and temperature in hydrogen/air/steam mixtures. *Combustion Science and Technology*, 184(10-11):1427–1444, 2012.

[167] F. Ettner, K. Vollmer, and T. Sattelmayer. Numerical simulation of the deflagration-to-detonation transition in inhomogeneous mixtures. *Journal of Combustion*, 2014:1–15, 2014.

[168] J. Hasslberger, L. Boeck, and T. Sattelmayer. Numerical simulation of deflagration-to-detonation transition in large confined volumes. *Journal of Loss Prevention in the Process Industries*, 36:371 – 379, 2015.

[169] N. Klarmann, T. Sattelmayer, W. Geng, and F. Magni. Flamelet generated manifolds for partially premixed, highly stretched and non-adiabatic combustion in gas turbines. In *54th AIAA Aerospace Sciences Meeting*. American Institute of Aeronautics and Astronautics, January 2016.

[170] V. N. Gamezo, T. Ogawa, and E. S. Oran. Numerical simulations of flame propagation and DDT in obstructed channels filled with hydrogen–air mixture. *Proceedings of the Combustion Institute*, 31(2):2463–2471, 2007.

[171] C. Barfuss, D. Heilbronn, and T. Sattelmayer. Impact of local flame quenching on the flame acceleration in H2-CO-air mixtures in obstructed channels. *Journal of Loss Prevention in the Process Industries*, 71:104491, July 2021.

[172] L. T. Kaiser. Under-resolved simulation of detonations in inhomogeneous hydrogen-air mixtures. Master's thesis, Technische Universität München, 2013.

[173] J.-B. Michel, O. Colin, and C. Angelberger. On the formulation of species reaction rates in the context of multi-species CFD codes using complex chemistry tabulation techniques. *Combustion and Flame*, 157(4):701–714, 2010.

[174] M. S. Kuznetsov, V. I. Alekseev, S. B. Dorofeev, I. D. Matsukov, and J. L. Boccio. Detonation propagation, decay, and reinitiation in nonuniform gaseous mixtures. *Symposium (International) on Combustion*, 27(2):2241–2247, January 1998.

[175] S. I. Kryuchkov, S. B. Dorofeev, and A. A. Efimenko. Critical conditions for detonation propagation through mixture with decreasing reaction rate. *Symposium (International) on Combustion*, 26(2):2965–2972, 1996.

[176] H. Jasak. Dynamic mesh handling in OpenFOAM. In *47th AIAA Aerospace Sciences Meeting Including The New Horizons Forum and Aerospace Exposition*, January 2009.

[177] G. M. Amdahl. Validity of the single processor approach to achieving large scale computing capabilities. In *Proceedings of the April 18-20, 1967, spring joint computer conference on - AFIPS '67 (Spring)*. ACM Press, 1967.

[178] I. Darmawan, Kuspriyanto, Y. Priyan, and I. M. Joseph. Integration of genetic and tabu search algorithm based load balancing for heterogenous

grid computing. In *2013 International Conference on Computer, Control, Informatics and Its Applications (IC3INA)*. IEEE, November 2013.

[179] L. Jofre, R. Borrell, O. Lehmkuhl, and A. Oliva. Parallel load balancing strategy for volume-of-fluid methods on 3-D unstructured meshes. *Journal of Computational Physics*, 282:269–288, 2015.

[180] S. B. Dorofeev, V. P. Sidorov, A. E. Dvoinishnikov, and W. Breitung. Deflagration to detonation transition in large confined volume of lean hydrogen-air mixtures. *Combustion and flame*, 104(1-2):95–110, 1996.

[181] K. Vollmer, F. Ettner, and T. Sattelmayer. Influence of concentration gradients on flame acceleration in tubes. *Science and Technology of Energetic Materials*, 72:1–11, May 2011.

[182] M. S. Kuznetsov, V. I. Alekseev, and S. B. Dorofeev. Comparison of critical conditions for DDT in regular and irregular cellular detonation systems. *Shock Waves*, 10(3):217–223, July 2000.

[183] M. S. Kuznetsov, V. I. Alekseev, and I. D. Matsukov. Deflagration-to-Detonation transition in H2-air and H2-O2-N2 mixtures in channels with obstructions. *Advances In Confined Detonations (eds. G. Roy, S. Frolov, R. Santoro, S. Tsyganov), Torus Press Ltd., Moscow*, pages 26–30, 2002.

[184] A. Teodorczyk, J. H. S. Lee, and R. Knystautas. Propagation mechanism of quasi-detonations. *Symposium (International) on Combustion*, 22(1):1723–1731, January 1989.

[185] L. Boeck, F. Berger, J. Hasslberger, and T. Sattelmayer. *Transient combustion and detonation phenomena: Fundamentals and applications*, chapter Propagating detonations - Detonation propagation in hydrogen-air mixtures with concentration gradients, pages 306–314. Torus Press Moscow, November 2014.

[186] C. Barfuss, D. Heilbronn, and T. Sattelmayer. Verbundvorhaben: Entwicklung von Verbrennungsmodellen und Kriterien für H2-CO-Luft-Schichten bei partiellem Einschluss - Teilvorhaben: Experimentelle

Untersuchungen auf Laborskala sowie Entwicklung komplementärer CFD-Verfahren. Technical Report 1501545A, Bundesministerium für Wirtschaft und Energie (BMWi), Lehrstuhl für Thermodynamik der Technische Universität München, 2022.

[187] T. J. Poinsot and S. K. Lelef. Boundary conditions for direct simulations of compressible viscous flows. *Journal of Computational Physics*, 101(1):104–129, July 1992.

[188] C. H. Wieland, F. Scharf, H.-P. Schildberg, V. Hoferichter, J. Eble, C. Hirsch, and T. Sattelmayer. Efficient simulation of flame acceleration and deflagration-to-detonation transition in smooth pipes. *Journal of Loss Prevention in the Process Industries*, 71:104504, July 2021.

[189] D. Zivkovic and T. Sattelmayer. Towards efficient and time-accurate simulations of early stages of industrial scale explosions. In *9th International Conference on Hydrogen Safety (ICHS) 2021*, Edinburgh, Scotland, September 2021. Health and Safety Executive.

[190] S. Popinet. An accurate adaptive solver for surface-tension-driven interfacial flows. *Journal of Computational Physics*, 228(16):5838–5866, September 2009.

[191] D. Fuster, A. Bagué, T. Boeck, L. Le Moyne, A. Leboissetier, S. Popinet, P. Ray, R. Scardovelli, and S. Zaleski. Simulation of primary atomization with an octree adaptive mesh refinement and VOF method. *International Journal of Multiphase Flow*, 35(6):550–565, June 2009.

[192] W. F. Noh and P. Woodward. SLIC (Simple Line Interface Calculation). In *Proceedings of the Fifth International Conference on Numerical Methods in Fluid Dynamics June 28 – July 2, 1976 Twente University, Enschede*, pages 330–340. Springer Berlin Heidelberg, 1976.

[193] D. L. Youngs. Time-dependent multi-material flow with large fluid distortion. *Numerical methods for fluid dynamics*, 24:273–285, January 1982.

[194] D. L. Youngs. An interface tracking method for a 3D Eulerian hydrodynamics code. *Atomic Weapons Research Establishment (AWRE) Technical Report*, 44(92):35, 1984.

[195] S. Mosso, C. Garasi, and R. Drake. A smoothed two- and three-dimensional interface reconstruction method. *Computing and Visualization in Science*, 12(7):365–381, April 2008.

[196] X. Yang and A. J. James. Analytic relations for reconstructing piecewise linear interfaces in triangular and tetrahedral grids. *Journal of Computational Physics*, 214(1):41–54, May 2006.

[197] R. P. Brent. An algorithm with guaranteed convergence for finding a zero of a function. *The Computer Journal*, 14(4):422–425, April 1971.

[198] T. Maric, J. Höpken, and K. Mooney. The OpenFOAM technology primer. 2014.

[199] M. Baum, T. Poinsot, and D. Thévenin. Accurate boundary conditions for multicomponent reactive flows. *Journal of Computational Physics*, 116(2):247–261, February 1995.

Appendix

A H_2-CO-Air Reaction System Related Coefficients and Parameters

Table A.1: Sutherland coefficients for the H_2-CO-air reaction system.

Species	Structural formula	Sutherland coefficient $A_{k,S}$	Sutherland temperature $T_{k,S}$
Nitrogen	N_2	1.552947e-06	131.0066
Hydrogen radical	H	9.194141e-07	250.1646
Hydrogen	H_2	7.191146e-07	90.2689
Oxygen radical	O	2.106963e-06	141.6835
Oxygen	O_2	1.859288e-06	200.5056
Hydroxide radical	OH	2.172291e-06	141.6610
Water	H_2O	2.218064e-06	896.0192
Hydroperoxyl radical	HO_2	1.831227e-06	140.5622
Hydrogen peroxide	H_2O_2	1.946452e-06	231.5127
Formyl radical	HCO	1.339667e-06	330.2381
Carbon monoxide	CO	1.566857e-06	180.8260
Carbon dioxide	CO_2	1.707006e-06	311.0412

Table A.2: Schmidt numbers Sc_k of species k in the H_2-CO-air reaction system according to Li et al. [14] at reference conditions.

k	Sc_k
N_2	0.7427
H_2O	0.7075
H	0.1318
HO_2	0.7718
H_2	0.2021
H_2O_2	0.7772
O	0.4924
HCO	1.0178
O_2	0.7866
CO	0.7698
OH	0.5019
CO_2	1.0161

B Initialization of Vertical Fuel Concentration Gradients

B.1 GraVent-Facility

The generation of the vertical concentration gradients of H_2-CO-air mixtures was investigated numerically and experimentally [186]. A numerical model verified with experiments was developed for the filling process of the explosion channel of the GraVent facility. From the filling simulation results, correlations were derived to describe the vertical fuel distribution based on the *tanh*-function. The function

$$\frac{x_k(y)}{\overline{x_k}} = 1 + \frac{K_k(t_\mathrm{w})}{0.9} \tanh\left(C\,\frac{y_\mathrm{c}}{h}\right) \tag{B.1}$$

denotes a normalized vertical distribution of the molar fractions x. The vertical distribution is normalized with the mean molar fraction over the channel height $\overline{x_k}$. The mole fractions are evaluated as a function of the vertical position of each cell center y_c normalized by the channel height h. With the scaling factor $C \approx 2.9444$, the *tanh*-expression $\tanh\left(C\,\frac{y_\mathrm{c}}{h}\right)$ becomes a self-similar function on the interval of [-0.9;0.9]. Division by 0.9 scales the self-similar *tanh*-function to unity. The correlated parameter $K_k(t_\mathrm{w})$ is a function of the waiting time. It specifies the slope of the concentration profile corresponding to the waiting time. The filling simulations for fuels of equivalence ratios $\phi = 0.5$ and $\phi = 1$ with fuel compositions 25/75, 50/50, 75/25 and 100/0 H_2/CO are used as data base for the empirical correlation of $K_k(t_\mathrm{w})$. The equations are solved for fuel components k, i.e., H_2 and CO, respectively.

The correlation B.2 determines the prefactor $K_{k,\phi}$ of the fuel component k based on a second-order exponential function. The correlation is a function

of the waiting time t_w) between ignition and the end of the filling process:

$$K_{k,\phi}(t_w) = A\,e^{(b\cdot t_w)} + C\,e^{(d\cdot t_w)}. \tag{B.2}$$

The coefficients of the correlation B.2 are summarized for $\phi = 0.5$ and $\phi = 1$ in tables B.1 and B.2. Since Correlation B.2 needs to be evaluated individually for both fuel components, H_2 and CO. Based on the two support values at $\phi = 0.5$ and $\phi = 1$, the prefactor is calculated at the desired equivalence ratio ϕ by linear interpolation:

$$K_k(t_w) = \frac{K_{k,\phi=1.0}(t_w) - K_{k,\phi=0.5}(t_w)}{0.5}\,\phi + K_{k,\phi=0.5}(t_w). \tag{B.3}$$

Table B.1: Coefficients of the exponential correlation for k=H_2.

	H_2/CO	A	b	C	d
$\phi = 0.5$	25/75	0.3692	-0.2192	0.2243	-0.6552
	50/50	0.6317	-0.2193	0.5358	-0.8996
	75/25	0.4753	-0.2182	0.5672	-0.8721
	100/0	0.7286	-1.015	0.3421	-0.2232
$\phi = 1.0$	25/75	0.1285	-0.2375	0.1099	-0.8389
	50/50	0.4397	-0.2226	0.2766	-0.7891
	75/25	0.3528	-0.2216	0.3156	-0.8233
	100/0	0.472	-0.9462	0.316	-0.2248

Table B.2: Coefficients of the exponential correlation for k=CO.

	H_2/CO	A	b	C	d
$\phi = 0.5$	25/75	0.5028	-0.07896	0.3941	-0.6121
	50/50	0.7863	-0.07214	0.637	-0.6161
	75/25	0.6261	-0.07166	0.7106	-0.5966
	100/0	-	-	-	-
$\phi = 1.0$	25/75	0.2259	-0.1109	0.753	-1.724
	50/50	0.6017	-0.07292	0.4041	-0.6156
	75/25	0.4991	-0.07311	0.4199	-0.4199
	100/0	-	-	-	-

B.2 A1-Vessel

The generation of vertical concentration gradients of the fuel-air mixture in the explosion channel of the A1-vessel was analyzed by the operators using the substitute gas mixture H_2-N_2 [34, 81]. N_2 was chosen because it has the same molar mass than CO. In contrast to species diffusion in the GraVent facility, convective transport generates the vertical concentration gradients in the A1-vessel's channel. The fuel mixture is injected directly under the ceiling through evenly spaced nozzles positioned along the entire channel length and width. The high-momentum fuel jet is directed against the ceiling, where it deflects. The momentum of the jet decays in a downward motion towards the channel bottom. A vertical concentration gradient results. The initial momentum of the jet depends on the pressure in the H_2-N_2 reservoir. Different maximum fuel contents $x_{f,max}$ are achieved in the concentration profile by changing the reservoir pressure. The pressure also alters the slope of the fuel concentration profile over the channel height. Height-resolved fuel-air composition profiles were obtained from measurements of the substitution gas composition at varying maximum fuel contents [81]. The measurements did not show a separation of the fuel components H_2 and CO.

2D interpolation tables are created from the height-resolved fuel-air composition profiles. The input variables are the vertical position y and the maximum fuel content $x_{f,max}$. Different tables exist for the fuel compositions 100/0 (Ta-

ble B.3), 75/25 (Table B.4) and 50/50 H_2/CO (Table B.5). Steady fuel concentration profiles are initialized with the 2D interpolation table as a function of the vertical cell position y and the desired maximum fuel content $x_{f,max}$.

Table B.3: Vertical fuel mole fraction x_f used for inhomogeneous mixture initialization in the A1-vessel simulations with 100/0 H_2/CO.

	x_f for corresponding $x_{f,max}$ in the first row					
Height [mm]	15.107	18.882	20.746	22.333	24.214	27.302
600	15.107	18.882	20.746	22.333	24.214	27.302
500	13.148	16.908	19.167	21.138	23.140	25.742
400	9.362	12.870	15.993	18.600	21.157	23.003
300	5.227	9.207	12.700	15.704	18.270	20.218
200	2.508	5.608	9.110	11.925	15.142	17.285
100	0.823	2.553	6.005	8.376	11.617	13.254
0	0.500	0.958	2.038	3.348	5.082	5.740

Table B.4: Vertical fuel mole fraction x_f used for inhomogeneous mixture initialization in the A1-vessel simulations with 75/25 H_2/CO.

	x_f for corresponding $x_{f,max}$ in the first row						
Height [mm]	12.895	15.308	17.088	19.966	22.657	25.620	30.518
600	12.895	15.308	17.088	19.966	22.657	25.620	30.518
500	10.278	12.730	14.563	17.425	20.183	23.294	28.351
400	6.675	8.978	10.898	13.914	16.705	19.972	25.069
300	3.388	5.314	7.263	10.043	12.679	16.047	21.083
200	1.584	2.644	3.754	6.275	8.370	11.614	16.209
100	0.980	1.243	1.481	2.792	3.342	6.212	9.621
0	0.375	0.375	0.375	0.375	0.375	0.375	0.375

Table B.5: Vertical fuel mole fraction x_f used for inhomogeneous mixture initialization in the A1-vessel simulations with 50/50 H_2/CO.

	x_f for corresponding $x_{f,max}$ in the first row							
Height [mm]	13.974	16.492	19.025	22.122	24.359	26.844	29.157	30.908
600	13.974	16.492	19.025	22.122	24.359	26.844	29.157	30.908
500	11.679	14.247	16.752	19.843	22.196	24.603	26.918	28.746
400	8.329	10.802	13.240	16.278	18.751	21.224	23.814	25.620
300	5.150	7.192	9.266	12.159	14.504	17.049	20.217	21.608
200	2.889	4.110	5.033	7.405	9.214	11.914	14.786	16.442
100	1.851	2.059	2.309	3.213	3.824	5.710	8.801	10.024
0	0.814	0.814	0.814	0.814	0.814	0.814	0.814	0.814

C Load-Balanced Geometrical Volume-of-Fluid Method

C.1 Geometrical Volume-of-Fluid Method

Ensuring a dissipation-free propagation of discontinuities by numerical methods is very challenging on coarse meshes. High-order methods of the WENO family (*weighted essentially non-oscillatory*), capable of minimizing numerical dissipation, are computationally expensive. Front-tracking methods are a cost-efficient alternative, and they ensure a conservative propagation of discontinuous fields [190, 191]. Hasslberger compares front-tracking methods for application to CFD-based risk assessment of explosions [4]. The geometrical Volume-of-Fluid (geoVoF) method is relatively cost-efficient and conservative. Contrary to methods like the Level-Set approach, only one thermodynamic state and velocity vector exists within each cell. The resulting state is a mix of the two states on each side of the discontinuity. This approach has the benefit that no computationally expensive jump conditions, which link the state on each side of the discontinuity, need to be solved in the geoVoF method. A geometrical evaluation of the advection fluxes can ensure minimal dissipation during flame propagation in the numerical scheme on large dimensions or coarse meshes, respectively.

The discontinuity typically separates two fluids according to the geoVoF method's multi-phase flow origin. When a flame front is considered as discontinuity, the interface, i.e., the flame front itself, separates the burnt and unburnt state. In the geoVoF method, the flame front is indirectly tracked by the volume of products and reactants in each cell. The volume fraction field α

indicates the fraction of burnt gas volume V_A of the cell volume V_c:n

$$\alpha = \frac{V_\mathrm{A}}{V_\mathrm{c}}. \tag{C.1}$$

Each position in a cell, indicated by the vector $\boldsymbol{x}$ in Equation C.2, can be assigned to either burnt or unburnt gas. Integrating the Heaviside function ϑ over a cell's volume determines the volume covered by the fluid:

$$V_\mathrm{A} = \int_{V_\mathrm{c}} \vartheta(\boldsymbol{x})\, d\boldsymbol{x} \quad \text{with:} \quad \vartheta(\boldsymbol{x}) = \begin{cases} 1 & \text{where burnt gas is present,} \\ 0 & \text{otherwise.} \end{cases} \tag{C.2}$$

Consequently, α becomes unity in fully burnt cells and zero in fresh gas cells. In interface cells, the volume fraction α is between these bounding limits. Because the α field is only specified on a numerical mesh, it is the spatial discretization of the Heaviside function ϑ. In contrast to a boundary phase in multi-phase flows, the flame front is reactive. In a flame-front tracking scheme, the interface advection must include the flame front velocity due to the chemical reaction. Such treatment results in a source term with a gradient approach, similar to the widely used turbulent flame speed (TFC) model of Zimont [6]. For simplicity, the geoVoF method is described without source term in this section. The description of the source term is one of the key scopes of the thesis concerning the explosion propagation of H_2-CO-air mixtures.

The advection equation of the volume fraction field α stems from the material derivative [141]:

$$\frac{\partial \alpha}{\partial t} + u_j \frac{\partial \alpha}{\partial x_j} = 0. \tag{C.3}$$

The material derivative is non-conservative in compressible flows. Because the density is not known on both sides of the discontinuity in the geoVoF method, a divergence correction is added [12]. The Equation C.3 is cast into the conservative from:

$$\frac{\partial \alpha}{\partial t} + \frac{\partial}{\partial x_j}(\alpha u_j) - \alpha \frac{\partial u_j}{\partial x_j} = 0. \tag{C.4}$$

In order to solve the transport equation, the advection term has to be evaluated in each time step. Using algebraic methods to calculate the advected

burnt volume fraction introduces significant dissipation resulting in a smearing of the discontinuity. These drawbacks are overcome by geometrical evaluation of the advected burnt volume fraction. The interface within an interface cell and the advected burnt volume across each cell surface are evaluated by geometrical reconstruction. This approach results in a robust method on coarse meshes. This approach is computationally more expensive but minimizes numerical dissipation effectively. The geoVoF method evaluates the advected volume fraction α in three steps:

- Gradient evaluation to obtain the interface orientation.
- Interface reconstruction according to V_A (reconstruction step).
- Geometrical evaluation of the advection terms (advection step).

As illustrated in the left image of Figure C.1, a continuous interface shall be represented by the volume fraction field α. Depending on the interface reconstruction method chosen in the geoVoF method, the reconstructed interface can be approximately continuous over the entire mesh. Higher-order profiles in the interface reconstruction method achieve a more continuous overall interface. There are two well-established approaches for reconstructing fluid interfaces:

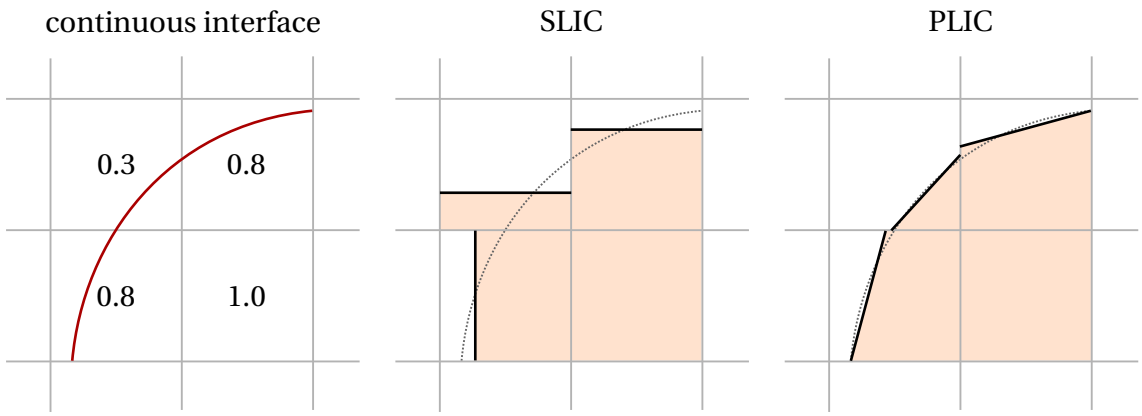

Figure C.1: Continuous interface with mean cell values of α (left) and interface reconstruction with SLIC (middle) and PLIC method (right) [adopted from [12]].

1. Simple Line Interface Calculation (SLIC) [192]:
   This method reconstructs the interface as a line parallel to one of the coordinate axes. It simplifies the determination of the interface orientation. Figure C.1 shows a SLIC reconstruction in the center image. This method results in the worst representation of a continuous reconstructed flame front.

2. Piecewise Linear Interface Calculation (PLIC) [193, 194]:
   A piecewise linear interface orientation within each cell results in a more accurate reconstruction of a continuous overall interface. However, it is also more computationally intensive because the interface orientation must be calculated. Figure C.1 shows a PLIC reconstruction in the right image.

More sophisticated methods, such as Pattern Interface Reconstruction, can further improve the connectivity between reconstructed interfaces of adjacent cells. In the Pattern Interface Reconstruction method, the PLIC reconstructed interface is smoothed in a second step [195]. Any method with at least linear interface reconstruction requires the interface orientation in the three-dimensional space. Generally, the normalized volume fraction gradient

$$\boldsymbol{n} = \frac{\nabla \alpha}{|\nabla \alpha|} \tag{C.5}$$

determines the interface orientation. The gradients are usually evaluated using Gauss' divergence theorem in the finite volume method (FVM) from face values. Typical gradient schemes for arbitrary unstructured meshes [129] are restricted to a limited stencil for interpolating face values, which causes a bad performance on discontinuous fields, eventually resulting in an unstable interface propagation [4, 13]. Higher-order interpolation schemes for face values use an extended stencil but introduce disadvantages in parallelized simulations. They required additional inter-processor communication, decreasing the scheme's computational efficiency.

The recently presented Node-Averaged Gauss (NAG) scheme [141] counteracts the deficiencies by including point neighbors of the face's vertices into the interpolation stencil, in addition to the face neighbors. Thereby effectively

extending the stencil while restricting the evaluation to a single loop over the cell neighbors. The inverse distance weighting method determines the value at each face's vertices ψ_{fi}. Face center values ψ_{fc} required for the gradient scheme are then estimated by an area-weighting approach on each face [141]. By triangulating the face's surface area in the area-weighting approach, the applicability to arbitrary meshes is maintained. Figure C.2 illustrates the NAG scheme. For the sake of brevity, the interested reader is referred to more detailed literature [13, 141, 179].

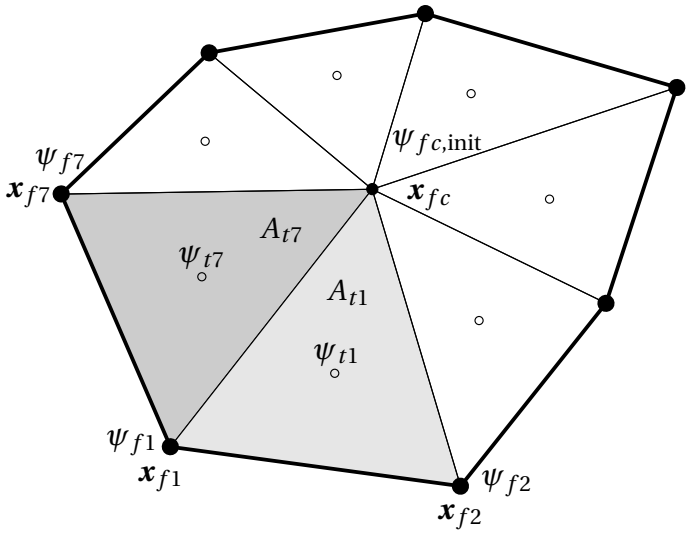

Figure C.2: Stencil for computing α at face center fc of face f in the NAG gradient scheme [adopted from [13]].

C.1.1 Interface Reconstruction

After evaluating the interface orientation within a cell, the interface is positioned in the reconstruction step according to the cell's volume fraction α. The use of the PLIC method is assumed for the following explanation. After evaluating the interface orientation from the gradient scheme, i.e., the NAG scheme mentioned before, the position of an interface in a cell can be expressed in Hesse normal form, which reads

$$\boldsymbol{n} \cdot \boldsymbol{x} + \mathrm{C} = 0. \tag{C.6}$$

The interface plane's normal vector $\boldsymbol{n}$ gives the orientation. The interface plane's offset from the origin of the coordinate system C of the interface plane is determined by geometrical polyhedra reconstruction corresponding to the volume fraction α. Figure C.3 illustrates a cell separated into two fluid volumes by the reconstructed interface. The truncated polyhedron in orange represents the volume of fluid A, which is the burnt gas volume in the context of a flame front application.

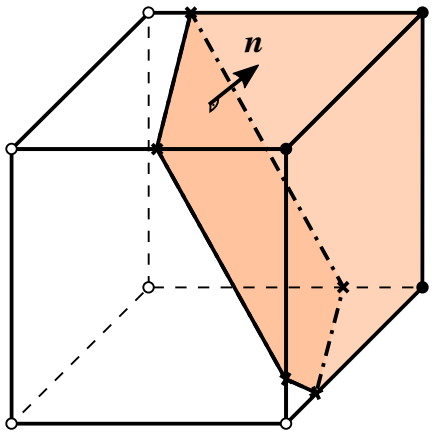

Figure C.3: Truncation of the cell by an interface plane (colored dark orange) with orientation $\boldsymbol{n}$. The truncated volume is colored. Intersection points are marked as × [adopted from [4]].

The volume of the truncated polyhedron V_T is evaluated from a geometrical truncation mechanism in the geoVoF method. The signed distance ϕ between a vertex of the initial cell polyhedron and the interface plane is given by

$$\phi_{j,i} = \boldsymbol{n} \cdot \boldsymbol{x}_{j,i} + \mathrm{C}. \tag{C.7}$$

The evaluation of the signed distance is looped over all vertices (index i) of all faces (index j) in the initial cell. $\boldsymbol{x}_{j,i}$ denotes the position vector of each vertex. Vertices on opposite sides of the interface show different signs. The intersected cell edges are identified by comparing the signs of adjacent points, $\phi_{j,i}$ and $\phi_{j,i+1}$. The position vector $\boldsymbol{x}_{j,\mathrm{new}}$ of the intersection point is determined from:

$$\boldsymbol{x}_{j,\mathrm{new}} = \boldsymbol{x}_{j,i} - \frac{\phi_{j,i}}{\phi_{j,i+1} - \phi_{j,i}} (\boldsymbol{x}_{j,i+1} - \boldsymbol{x}_{j,i}) \tag{C.8}$$

The newly found intersection points are indicated as × in Figure C.3. The truncated volume can be calculated with the cone volume formula:

$$V_{\mathrm{T}} = \frac{1}{3}\sum_{j=1}^{J}(\boldsymbol{n}_{\Gamma j}\cdot\boldsymbol{x}_{j,1})A_{\Gamma j}. \tag{C.9}$$

Equation C.9 is applied to each face Γ_j of the truncated polyhedron. The intersection points and the solid vertices bound each face in Figure C.3. $\boldsymbol{n}_{\Gamma j}$ is the normal vector of face Γ_j. It always points outwards from the truncated polyhedron. The truncated face area $A_{\Gamma j}$ of the truncated face Γ_j is calculated from

$$A_{\Gamma j} = \frac{1}{2}(\boldsymbol{n}_{\Gamma j}\cdot\sum_{i=1}^{I_j}(\boldsymbol{x}_{j,i}\times\boldsymbol{x}_{j,i+1}). \tag{C.10}$$

The face area $A_{\Gamma j}$ in Equation C.9 is substituted with Equation C.10, resulting in the final relation, which reads

$$V_{\mathrm{T}} = \frac{1}{6}\sum_{j=1}^{J}\left[(\boldsymbol{n}_{\Gamma j}\cdot\boldsymbol{x}_{j,1})\boldsymbol{n}_{\Gamma j}\cdot\sum_{i=1}^{I_j}(\boldsymbol{x}_{j,i}\times\boldsymbol{x}_{j,i+1})\right]. \tag{C.11}$$

In order to close the loop over all vertices of any face, the index $i+1$ has to be replaced by 1 for the last vertex. Equation C.11 is valid for arbitrary polyhedrons that are not self-intersecting [196]. Hasslberger and Ketterl [4, 13] provide useful considerations for an OpenFOAM-specific implementation regarding mesh topology and data structure.

The interface reconstruction needs to be conservative with respect to the volume of fluid A (burnt gas). Therefore, the offset C of the interface plane is varied until the condition

$$f(C) = \alpha_{\mathrm{T}}(C) - \alpha = \frac{V_{\mathrm{T}}(C)}{V_{\mathrm{c}}} - \alpha = 0 \tag{C.12}$$

is satisfied. The truncated volume fraction $\alpha_{\mathrm{T}}(C)$ as well as the truncated volume $V_{\mathrm{T}}(C)$ is a non-linear function of the offset C. The root finding problem of Equation C.12 can be solved directly or iteratively. An iterative method gives more flexibility for arbitrary mesh treatment and has less algorithmic complexity but at the cost of higher computational effort than direct methods. Nevertheless, the iterative solution is preferred in most applications, especially in the case of the unstructured mesh topology of OpenFOAM.

The Brent algorithm for iterative solutions is used in the presented CFD solver. Ketterl [13] demonstrated that the Brent algorithm shows good convergence and robustness on arbitrary meshes. The method's convergence is of a higher order while retaining the boundness of the linear bisection method's solution. The Brent method uses three prior solutions to fit an inverse quadratic function [197]. With three consecutive points $(C_{k-2}, f(C_{k-2}))$, $(C_{k-1}, f(C_{k-1}))$ and $(C_k, f(C_k))$ for the iterations $k-2$, $k-1$ and k respectively, the subsequent root estimate is determined with the following set of equations:

$$C = C_k + \frac{P}{Q}, \tag{C.13}$$

$$P = S\left[T(R-T)(C_{k+1}-C_k) - (1-R)(C_k - C_{k-1}))\right], \tag{C.14}$$

$$Q = (T-1)(R-1)(S-1), \tag{C.15}$$

$$R = \frac{f(C_k)}{f(C_{k+1})}, \quad S = \frac{f(C_k)}{f(C_{k-1})}, \quad T = \frac{f(C_{k-1})}{f(C_{k+1})}. \tag{C.16}$$

C_k represents the current offset estimate. Quadratic functions can diverge if the function is not sufficiently smooth, i.e., $Q \to 0$. The algorithm checks for the boundness and eventually returns to a linear bisection step for the current iteration. The offset is initially guessed with the relation

$$C_0 = C_{\min} + (1-\alpha)(C_{\max} - C_{\min}). \tag{C.17}$$

A user-defined tolerance determines the final solution, typically in the order of 10^{-6}.

C.1.2 Interface Advection

After reconstructing the volume fraction within the cell, the next step towards the temporal evolution of the transport Equation C.4 is evaluating the advection term (second term). Usually, the Gauss divergence theorem is applied in FVM approaches to determine the advection term from face values [129]. In the case of the geoVoF method, the face values are estimated by geometrical reconstruction of flux polyhedra instead of standard interpolation schemes. This approach ensures minimum dissipation of the $alpha$ field on coarse

meshes. In the FVM discretization, constant face values approximate the surface integral:

$$\oint_A \alpha u_j m_j dA \approx \sum_f \alpha_f u_{j,f} A_{j,f} = \sum_f \beta F_f = \sum_f F_{f,\mathrm{T}}. \tag{C.18}$$

While α_f denotes the face value of the reconstructed volume fraction field, β resembles α_f if the face values are determined geometrically. The face fluxes $F_f = u_{j,f} A_{j,f}$ can be calculated with standard interpolation schemes or more elaborate methods for compressible discontinuities like a Riemann solver [124, 139]. Finally, $F_{f,\mathrm{T}}$ is the volume flow of fluid A, i.e., advected burnt gas, through face f. Within one time step, the advected volume of fluid A can be calculated ($F_{f,\mathrm{T}} \Delta t = V_{f,\mathrm{T}}$). The total convected volume is geometrically constructed on the face creating a flux polyhedron. The advected volume of fluid A is evaluated by truncating the flux polyhedron with the interface plane. The truncation can be done using the same algorithm applied to the interface reconstruction. Consequently, the volume fraction face value β can be described by the ratio

$$\beta = \frac{F_{f,\mathrm{T}} \Delta t}{F_f \Delta t} = \frac{V_{f,\mathrm{T}}}{V_f} \tag{C.19}$$

of truncated flux polyhedron volume $V_{f,\mathrm{T}}$ and total volume of the flux polyhedron V_f within the time step Δt. Figure C.4 illustrates the truncation of the flux polyhedron by the reconstructed interface concerning the right-hand cell face. The result is the convected volume of fluid A (burnt gas) within the time step.

The flux polyhedron construction can be based on the face-centered velocity u_j or the face-vertex velocities $u_{j,i}$. The face-vertex velocities are obtained from the face-centered values by the inverse distance weighting method. In Figure C.4, face-vertex velocities are used. The position of the unknown vertices $\boldsymbol{x}'_{j,i}$ of the flux polyhedron are constructed by following the face-vertex velocity vectors back in time beginning at the face-vertex position of the cell $\boldsymbol{x}_{j,i}$. The backwards Lagrangian trajectory by the time step size Δt is expressed by

$$\boldsymbol{x}'_{j,i} = \boldsymbol{x}_{j,i} - u_{j,i} \Delta t. \tag{C.20}$$

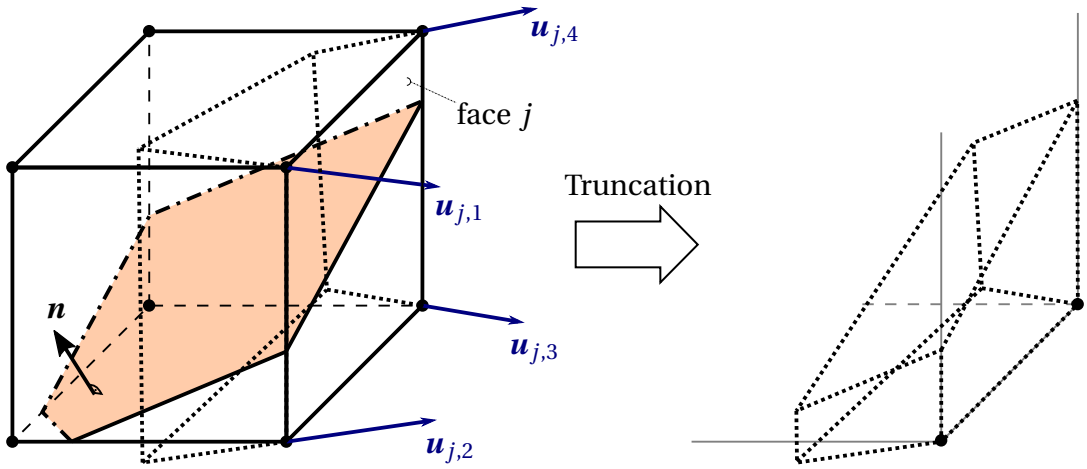

Figure C.4: Truncation of the right-hand face's flux polyhedron (dotted lines) by an interface plane (colored orange) with orientation $\boldsymbol{n}$ [adopted from [13]].

Three-dimensional volume calculation of non-convex or non-planar polyhedrons becomes difficult and can often only be achieved in a general manner by tetrahedral decomposition. The decomposition drastically increases algorithmic complexity and computational cost. The flux polyhedron construction and its volume calculation can be simplified using face-centered velocity instead of face-vertex velocities. When the face-centered velocity is considered, all vertices are traced back in time with the same velocity during the flux polyhedron construction. The simplified approach ensures a planar and convex flux polyhedron with a straightforward volume calculation. Therefore, flux polyhedron construction by face-center velocities is recommended for 3D simulations. Hasslberger commented on several error sources and deficiencies in conserving the convected fluid volumes [4].

The ratio β can initially be approximated from the ratio

$$\beta = \frac{A_{\Gamma,f}}{A_f} \tag{C.21}$$

of the truncated face area $A_{\Gamma,f}$ and the entire face area A_f of the initial cell. The approximation in Equation C.21 becomes more accurate with a smaller time step size, i.e., a lower CFL number in the simulation with an adjustable time step size. The required face areas are available after the interface reconstruc-

tion step. The initial approximation additionally works as a fallback solution if the calculation of the convected volume breaks. Ultimately knowing the convected volume fractions, the transport equation C.4 can be evolved in time. The conservative solution of flow simulations with minimum numerical dissipation, especially on coarse grids, is presented in publications for varying validation cases [4, 13].

C.2 OpenFOAM Specific Implementation of the Load-Balancing Algorithm

The following section explains the OpenFOAM-specific implementation of the load-balancing (LB) algorithm for the geoVoF method. Jofre et al. [179] proposed an LB algorithm for the geoVoF method for a self-developed CFD code. Until now, no implementation of a load-balanced geoVOF method for OpenFOAM-based CFD codes has been presented in the literature. Therefore, implementing the LB algorithm in the present thesis requires some specific adaptations in the algorithm concerning the methodology of the OpenFOAM framework. The LB algorithm is implemented into the CFD framework as the *LB-geoVoF* OpenFOAM class. Class-based encapsulation is a typical approach in object-oriented program languages like C++, which separates the code from the main program section of the solver. It allows easy reuse of the LB-geoVoF class in other solvers and simplifies the migration of the LB-geoVoF class to a different OpenFOAM version.

The NAG scheme is evaluated with equal computational effort on all cells, not only the flame front cells. Hence, imbalances from the NAG scheme only originate from a different number of cells in each processor caused by AMR. A load distribution method is not favorable enough for the NAG scheme. However, the serial code segments of the NAG operation can be optimized by caching the surface area weights of the NAG evaluation. Compared to the CFD solver developed by Hasslberger [4], which computes the surface area weights in every time step, the NAG scheme's gradient evaluation computation time is reduced by roughly 36%. When AMR is applied, the geometrical data needs to

be updated accordingly. As a side note, the capability to store data in encapsulated classes by object-oriented programming languages always allows for reducing computational time because reevaluation of temporary data can be omitted and should thus always be considered during code development.

In contrast to the NAG gradient scheme, the reconstruction and advection steps are only carried out in flame front cells. Hence, the imbalance of computational effort is much higher for the reconstruction and advection step. Consequently, the LB algorithm is designed to distribute the load of the reconstruction and the advection step by sending computation packages from overloaded processors to less loaded processors. Two key aspects to accomplish this task are the design of the inter-processor communication and the provision of the required mesh data for each processor. Both aspects require specific adjustments of the original LB algorithm by Jofre et al. concerning the OpenFOAM methodology. The LB-geoVoF method can be outlined as follows:

- **Inter-processor communication:** In OpenFOAM, the *OpenMPI* library enables communication between processors. OpenFOAM provides an interface class called *PStream* for this purpose. With the interface class, data can be exchanged between the processors via a few communication functions. The communication can be realized according to the *all-to-all* principle (*gatherList*/*scatterList* functions) or the *point-to-point* principle (*IPstream*/*OPstream* functions). The LB algorithm proposed here employs the *all-to-all* principle, in which the data of all processors is available to each processor. The algorithmic code complexity of *point-to-point* communication, in which individual processors communicate directly, is significantly higher. If additional communication between the sending processors becomes necessary to coordinate the data transmission to the individual receiving processors, the computational overhead of *point-to-point* communication becomes even greater. Although considerably more data is transmitted in *all-to-all* communication, the *tree-algorithm* implemented in OpenFOAM ensures high-performance communication. In the *tree-algorithm*, each receiver forwards the data to two or more processors in order to spread (*scatterList* function) or in reverse collect (*gatherList* function) the data with an exponentially increasing

transmission rate down the tree structure.

- **Provision of geometrical mesh data:** OpenFOAM's mesh topology assigns a partial domain of the entire mesh to each processor during the initial decomposition of the global computational mesh. Each processor only has information about its local mesh due to the decomposition. Processor boundary conditions connect the decomposed meshes of the individual processors. The interface reconstruction and advection term evaluation of the geoVoF method require geometrical mesh data of the flame front cells. Therefore, the information must be transmitted in addition to process data. In connection with the chosen *all-to-all* communication strategy, using a global mesh to evaluate geoVoF operations appears practical. The decomposed mesh of each processor is shared with all processors. The mesh data in OpenFOAM is arranged in lists of cells, faces, points and face owners [198]. Cell volume and face area vectors are also arranged in lists. The global mesh data, which all processors will share, is constructed as one coherent nested list. It maintains OpenFOAM's standard structure for mesh data. In the coherent list, each processor's local mesh data is added at the end of the list until the entire global data is present. The storage of the global mesh data has an increased memory demand. From the perspective of ever-increasing RAM (random access memory) capacities, computational efficiency outways this limitation. Since the LB algorithm prohibits a geoVoF evaluation under certain conditions, e.g., a minimal RAM capacity or an extensive calculation mesh, switching off LB-geoVoF and using the non-load-balanced version remains possible. The global mesh approach is opposite to the method proposed by Jofre et al. [179]. They suggested including the geometrical information data in the data exchange for external computation of tasks. However, communication of mesh information proved unpractical for an OpenFOAM-specific implementation, as it drastically increased computation time [10].

The implemented LB algorithm can be described as static. All tasks are considered computationally equally intensive, and additional load from overhead communication of the algorithm is accounted for by a constant param-

eter. Moreover, the initial domain decomposition is not changed. Figure C.5 presents the workflow scheme of the LB algorithm. The workflow is described step by step below:

1. Check for mesh refinement and update global mesh data if necessary to ensure compatibility with AMR. Update geometric cell surface data for the NAG gradient scheme.
2. Apply optimized NAG scheme to calculate the volume fraction gradient $\nabla\alpha$ for all cells.
3. Calculate the optimal workload for all processors from the number of interface cells. Classify each processor in one of three categories - sending, receiving or isolated.
4. Arrange data required for computational operations according to the classification in OpenFOAM *list* structures.
5. Exchange data between all processors for reconstruction and advection step evaluation.
6. Carry out reconstruction and advection step to update the advected volume fraction β on all cell surfaces. The processing sequence of self-owned and foreign calculation operations varies between the processor categories.
7. Communication of the evaluated β data between all processors and subsequent processing of the data by the original owner processor of the tasks.

In order to maintain the advantages of an unstructured mesh topology with AMR, compatibility with AMR must be ensured. The efficient strategy of global mesh data involves extensive data transfer only in the event of mesh refinement or coarsening. Without AMR, mesh-related data transmission is only required once. The time step interval of AMR execution is read from the input file, referred to as *dynamicMeshDict dictionary* in OpenFOAM. Suppose the current time step is a multiple of the AMR execution time step interval.

In that case, the mesh data is exchanged between all processors, and the NAG area weights are recalculated in each processor. The mesh data is initialized as nested lists with fixed allocated memory and can thus be exchanged quickly via the MPI communication function *broadcast*. It should be noted that only the geoVoF operations utilize the global mesh. All other transport equations are solved on the local decomposed mesh of the processor.

The computational load of a processor W_p is evaluated separately for each processor based on the number of flame front cells. The information is then shared among all processors. All subsequent algorithm steps up to the transmission of process data can be carried out in each processor locally. Based on the workload of each processor p, the average or optimal workload can be determined by Equation C.22. The usual processor counting method in OpenFOAM is applied here, starting from 0. The last processor has the number $P-1$. P denotes the physical count of processors:

$$W_{\text{opt}} = W_{\text{avg}} = \frac{\sum_{p=0}^{P-1} W_p}{P}. \tag{C.22}$$

Processors are classified as sending, receiving or isolated processors depending on their workload compared to the optimal workload. Isolated processors already contain the optimal workload. They occur very rarely. The sum of tasks to be sent $L(W_{\text{opt}})$ is determined by Equation C.23 and the sum of tasks to be received $R(W_{\text{opt}})$ is determined by Equation C.24:

$$L(W_{\text{opt}}) = \sum_{p=0}^{P-1} \max(W_p - W_{\text{opt}}, 0), \tag{C.23}$$

$$R(W_{\text{opt}}) = \sum_{p=0}^{P-1} \max(W_{\text{opt}} - W_p, 0). \tag{C.24}$$

As an initial assumption, the number of deficit and excess tasks have to be equal $L(W_{\text{opt}}) = R(W_{\text{opt}})$. However, it is more accurate to assume that local computation of operations is more efficient than computation by a foreign processor. Communication must be taken into account for external computation. In addition, the data packages sent to the receiving processor are nested lists with multiple levels. The handling of which is algorithmically complex.

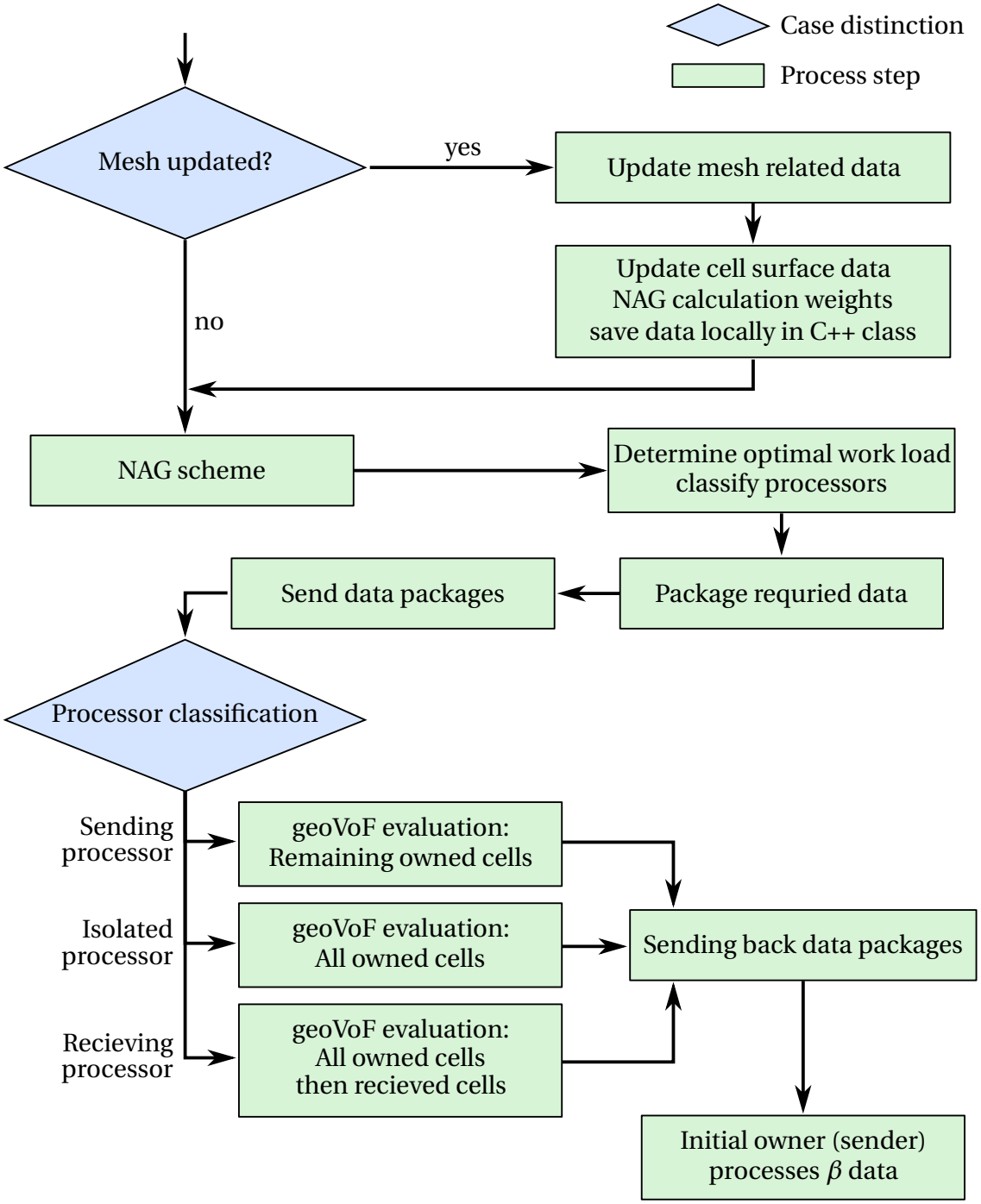

Figure C.5: Work flow of the load balancing algorithm in the LB-geoVoF method.

Jofre et al. [179] propose a factor δ of 10% to account for additional communication cost in terms of computing time for external tasks. The balance of sent and received tasks is accordingly adjusted with $(1+\delta)$:

$$(1+\delta)\cdot L(W_{\text{opt}}) = R(W_{\text{opt}}). \tag{C.25}$$

The equilibrium function

$$B(W_{\text{opt}}) = (1+\delta)\cdot L(W_{\text{opt}}) - R(W_{\text{opt}}) \tag{C.26}$$

must become $B(W_{\text{opt}}) = 0$ for the optimal number of flame front cells N_{opt}. The number N_{opt} can be determined with an iterative root-finding method, such as bisection. The bisection method obtains the solution within a maximum of five iterations. Only integers are allowed for the flame front cell number N_{opt}. Rational numbers for N_{opt} are rounded to integers. If the value is below the mean load W_{avg}, it is always rounded up since the optimal load W_{opt} must be larger than the mean load W_{avg} due to the extra cost of communication.

The sent tasks L and the received tasks R for each processor are gathered in a single list for all processors. A sending processor is assigned to each task in the sent task list. This is repeated for the received tasks. The awareness of each processor of all processors' excess load or load deficiency avoids double allocation for one operation. Due to the *all-to-all* communication concept, no supporting communication is required to assign tasks.

The LB algorithm introduces additional complexity and communication cost, which counteracts the time-saving benefit of load balancing. Synchronization steps are hence reduced to a minimum. When synchronization is required, the *all-to-all* communication allows large data packages to be transmitted efficiently. Therefore, large data packages with a nested list structure are created for data transmission. The required data fields for the geoVoF evaluation are as follows:

- cell index of the sending tasks.
- α values.
- NAG gradient of α.

- velocity vectors on the cell surfaces of the flame front cells.

The nested list data structure is based on the OpenFOAM *List* class. The nested lists usually have three levels. The first level describes the sending processor, the second the receiving processor and the third the cell index of the entry. The third level has the length of the total flame front cells sent. The nested list relates to the OpenFOAM structure of 'List<List<List<*data type*> > >'. For example, the transmitted list of the α field reads alpha1[6][2][4], which refers to the α value of the fifth cell that has been assigned to processor 3 by processor 7. Note that a processor 0 exists. In the case of the velocity vector on the cell surface, an additional layer exists in the nested list to reference the index of the cell's face. Each processor fills the process data lists individually for its processor number in the first level of the nested list as sending processor. The data is then shared between all processors employing *all-to-all* communication, which generates the complete nested list.

If present, the geoVoF calculations are first carried out on the self-owned tasks. In the case of a receiving processor, the externally assigned tasks are evaluated subsequently. The geoVoF operations, reconstruction and advection are executed directly on the nested data structure for received data packets. The geoVoF functions of the C++ class can handle the local and the nested data structure. By directly addressing the elements in the nested lists, the time for unpacking the data structure is saved. Ultimately, the advected burnt volume fractions on the cell surfaces β are determined. The β data field is exchanged to the original sending processor analogously to the process data transmission in a nested list structure. Because only a single data field needs to be transmitted, the communication of β is faster than transmitting the required process data for the external computation of a task.

The introduction of additional communication effort by the load-balancing algorithm counteracts its computation time-saving purpose. Potential scenarios exist in which the original non-load-balanced implementation [10] is more efficient. This scenario can occur when the optimal workload is very low. Reasons for a very low optimal workload can either be a minimal flame front or an excessive processor count. A runtime correction is implemented in the solver, which determines a minimum workload limit based on time measurements

for transmission and processor-internal calculations of each processor. If the optimal workload in the simulation drops below the minimal workload limit, the code automatically switches to the non-load-balanced implementation. Corresponding scenarios for this to happen require an extremely low, optimal workload. This extreme case rarely occurs in combustion-related risk analysis simulations, especially not when AMR is in use.

C.3 Generic Validation of the Load-Balancing Algorithm

The speedup due to the newly implemented LB algorithm and its scaling with increasing processor count is validated on a general configuration. A general simulation case allows ideal comparability to other implementations of the LB geoVoF algorithm. Therefore, a cubic mesh is used. The cubic mesh has an edge length of 8 m and contains 1 million cells. Each dimension comprises 100 cells, which relates to a cell size of 80 mm. Two-staged AMR is applied in the simulation. The refined cell dimensions of 20 mm are similar to the mesh resolution in the large-scale simulations of the A1-vessel presented in Section 4.3 of the thesis. A sphere with a diameter of 0.8 m specifies the ignition kernel. The gas is specified as burnt in the kernel. Combustion remains deflagrative during the entire simulation.

The number of flame front cells and the load imbalance are directly proportional. In an explosion scenario, the flame surface and, thus, the number of flame front cells increase due to geometrical confinement and flame folding during flame acceleration. With the onset of DDT, the number of flame front cells drops abruptly [168]. The fast conversion rate of the detonation front smooths the wrinkled flame, and the remaining fresh gas pockets behind the leading reaction front are quickly consumed. The decreasing number of flame front cells after DDT reduces the imbalance. Consequently, the speedup by the LB-geoVoF algorithm varies over simulation time in an explosion scenario.

The *simple* decomposition method creates uniform decomposed meshes for each processor by manually defining cutting planes. A clearly specified decomposition is essential to assess the speedup trend. Figure C.6 shows the ap-

plication of the *simple* method for decomposing the cubic mesh. The cutting planes are illustrated for different degrees of parallelization. The same number of processors covers the ignition kernel in all three cases. Figure C.6 visualizes the coverage of the ignition kernel by projected circles on the cube surfaces (pink). The more practical *Scotch* method is often used for mesh decomposition, as it decomposes the mesh without manually specifying cutting planes. Although the *Scotch* algorithm distributes the number of cells evenly between processors, the global mesh is not divided geometrically uniform as illustrated in Figure C.6. This leads to unnecessarily high inter-processor boundaries, disadvantaging the LB algorithm's scaling.

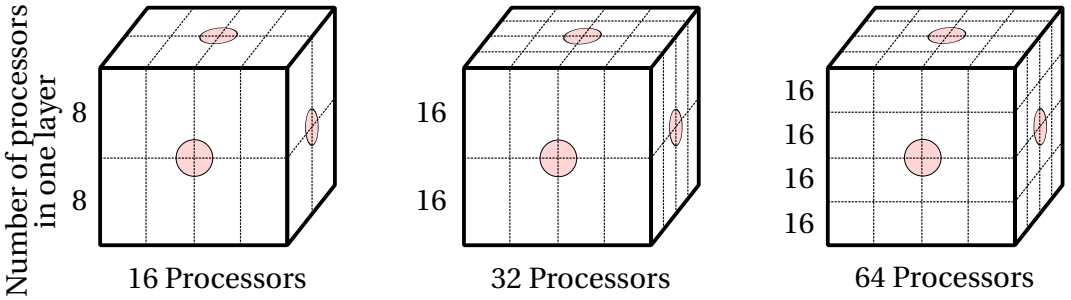

Figure C.6: *Simple* mesh decomposition of general cubic mesh with an additional projection of the ignition kernel on the cube surfaces (pink circles).

The simulation is stopped at an overall volumetric fuel conversion of 25 %, ensuring a deflagrative flame propagation free from wall influences. Figure C.7 shows the accomplished speedup by the LB-geoVoF method for varying processor counts (left graph). The speedup is defined as

$$\text{speedup} = \frac{t_{P,\text{calc}}^{\text{NLB}}}{t_{P,\text{calc}}^{\text{LB}}} \tag{C.27}$$

with P processors. LB indicates the LB-geoVoF algorithm, while NLB denotes the non-load-balanced geoVoF implementation without the external calculation of the reconstruction and the advection step. An increase in speedup with a higher degree of parallelization can be identified clearly. The CFD is developed using the outdated OpenFOAM version 2.1.x. Due to software incompatibilities of the up-to-date operating system of the high-performance clusters (HPC) with the outdated OpenFOAM version, massively parallelized

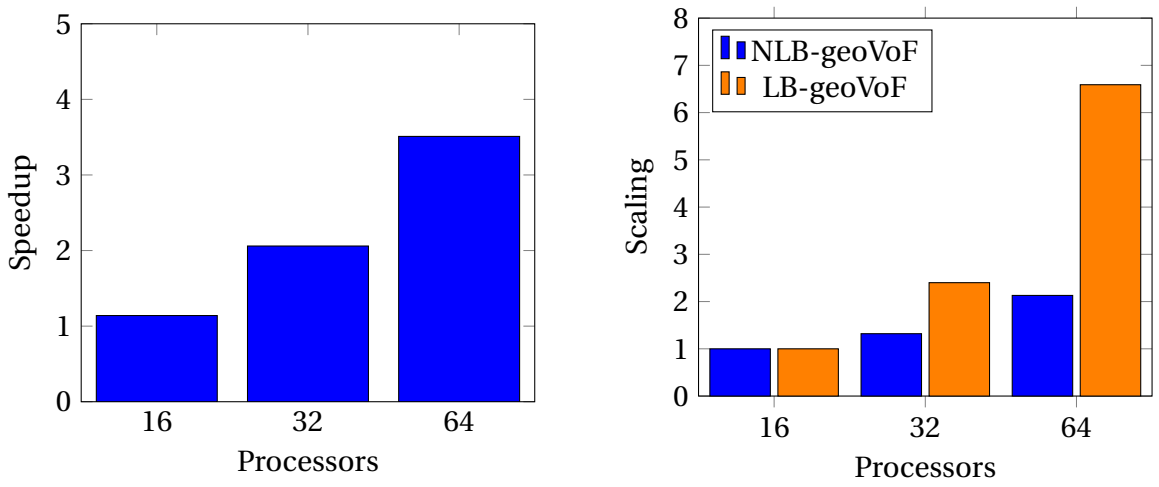

Figure C.7: Computational speedup (left) and scaling (right) of the LB algorithm in a generic deflagration simulation.

simulations could not be conducted. Thus, the maximum processors count in the speedup investigation is limited to 64 processors. Figure C.7 also presents the scaling of the LB and NLB geoVoF method with increasing parallelization (right graph). The scaling of a method is specified as

$$\text{scaling} = \frac{t^{\text{LB}}_{16,\text{calc}}}{t^{\text{LB}}_{P,\text{calc}}} \quad \text{or} \quad \text{scaling} = \frac{t^{\text{NLB}}_{16,\text{calc}}}{t^{\text{NLB}}_{P,\text{calc}}}, \tag{C.28}$$

which is the ratio of the computation time with 16 and P processors. The LB-geoVoF method scales significantly better than the previous implementation on the cube mesh, underlining the limited effectiveness of simple massive parallelization. The values in the plot are summarized in Table C.1.

According to Figure C.6, the ignition kernel is covered by the same number of

Table C.1: Computational speedup and scaling values of the LB algorithm with increasing parallelization.

Processors	Speedup	Scaling geoVoF	Scaling LB-geoVoF
16	1.14	1.00	1.00
32	2.06	1.32	2.40
64	3.51	2.13	6.59

processors for all three different processor counts. The number of processors covering the flame front, i.e., the workload distribution, determines the scaling of the NLB geoVoF version after mesh decomposition. The more processors cover the flame front, the better the efficiency of the calculation becomes. Increasing the processor count does not affect the workload distribution of the ignition kernel. Instead, additional processor domains are introduced close to the wall. The flame reaches these additional processor domains only at higher overall fuel conversion. Therefore, the processor count increase has a limited benefit on the NLB geoVoF method's scaling.

In contrast, adding under-loaded processors close to the wall reduces the optimal workload among all processors in the LB method. Hence, the LB-geoVoF method's scaling increases exponentially. With the increasing difference in scaling between the LB and the original NLB geoVoF with higher processor counts, higher speedups are obtained at high processor counts.

Under certain conditions, the NLB-geoVoF scaling rises above the LB-geoVoF scaling. This circumstance is not present in the presented general validation case. Fundamentally, the scaling results from the balance between additional communication costs and beneficial time-saving. As the increase of the processor count continuously rises the overhead communication, the scaling will eventually reverse its trend and decline. This turning point is reached at a lower processor count in the LB geoVoF method compared to the NLB version. The underlying relations of scaling and speedup can be summarized as follows:

- The LB method guarantees an even distribution of computational load - independent of the processor count. Benefits from the addition of processors originate only from the smaller optimal workload. Hence, the even workload distribution at any processor count combined with the increased overhead communication costs can result in a decline of the LB-geoVoF method's scaling.
- Load distribution is only partially improved by increasing parallelization using the previous NLB geoVoF implementation. Therefore, efficiency gains remain possible even at high processor counts.

- The speedup starts to decline once the scaling of NLB-geoVoF overtakes the scaling of LB-geoVoF. However, the high initial speed up at low processor numbers must be compensated first by the declining LB-geoVoF's scaling before the NLB version becomes faster. Only at very high processor counts, the NLB-geoVoF method might be faster than the LB-geoVoF.
- The maximum in the scaling curve specifies the optimal number of processors for the method. The LB-geoVoF method should be applied at more minor processor counts according to its optimum scaling. In this perspective, a simulation with an acceptable computation time can run on hardware with fewer processors. This circumstance enables additional simulation runs as hardware resources are freed up. Hence, the newly implemented LB algorithm addresses the need for parameter studies in the risk analysis of explosion scenarios.

D OpenFOAM's waveTransmissive Boundary Condition in the Density-Based CFD Framework

The *waveTransmissive* boundary condition (BC) is an implementation of the 1D Euler characteristic boundary conditions (ECBC) [1, 187]. The method has not the highest accuracy but is favorable in its robustness. While the ECBC are usually described with the primitive variables ρ and u, the OpenFOAM implementation is written in terms of p and u due to the typically pressure-based solver architecture of OpenFOAM solvers. Generally, the two primitive variables are linked by the equation of state. In the density-based solver architecture of the CFD solver presented in the thesis, the BC only updates the pressure on the boundary after the equation of state evaluates the cell-center pressure field. The newly determined pressure on the boundary by the *waveTransmissive* BC is used to recalculate the density boundary field. For this, the equation of state is applied to the boundary values. Afterward, the continuity equation can be solved with the updated density boundary values.

Independent of the primitive variables used in the formulation of the ECBC, the velocity is coupled to the pressure or density according to the propagating characteristics in the hyperbolic system of compressible Euler equations. In order to describe the variable p or u on the boundary face, a far-field pressure p_{inf} and a far-field velocity u_{inf} is introduced in the *waveTransmissive* BC. Figure D.1 illustrates the *waveTransmissive* BC relation between cell-center value and far-field of the primitive variable p. Pressure and velocity changes linearly from the boundary face p_f^t to the far-field state p_{inf} at a distance l_{inf}. The evolution of the boundary face pressure in time p_f^{t+1} is determined on the linear slope by the face-normal velocity $u_\perp$ and the time step size Δt. The evolution of velocity on the boundary surface is treated accordingly. By choosing

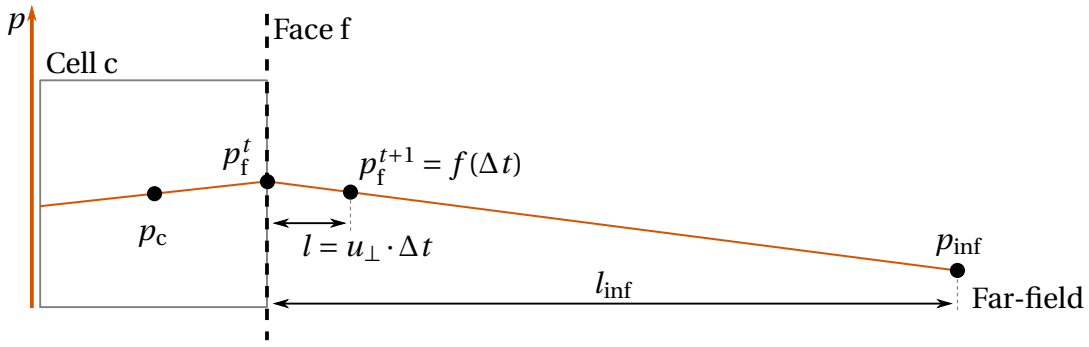

Figure D.1: Schematic of the boundary pressure evaluation of the *waveTransmissive* BC.

an extremely long far-field distance l_inf, the slope at the BC becomes almost negligible $p_f^{t+1} \approx p_f^t$ and no change occurs at the location of the boundary face. Consequently, pressure waves reaching the BC will not be reflected but propagate outward without changes inside the domain. The same applies to outward propagating expansion waves that pass the BC, which would induce an inward flow on the BC. The initial conditions $p_\mathrm{inf} = 1.013\,\mathrm{bar}$ and $u_\mathrm{inf} = 0\,\frac{\mathrm{m}}{\mathrm{s}}$ are chosen as far-field values.

According to the Euler equations, pressure and velocity at the BC must be equal to the cell value to prevent reflection [39]. Intuitively, the *zeroGradient* BC seems capable of predicting an appropriate outflow. However, the characteristics in a hyperbolic system (Euler equations) show that a *zeroGradient* BC would be ill-conditioned. As intended, no gradient would be present for the primitive variables u and p at the boundary. At the same time, no proper definition of the downstream characteristic, which resembles an outward propagating wave, exists with this BC [1, 187]. Unpredictable behavior with numerical instabilities may result even if the upstream characteristic, which refers to a reflected and now inward propagating wave, is zero. In addition, a *zeroGradient* BC can be problematic because no state information in the surrounding would be available for an inflow into the computational domain.

As a change in temperature influences the equation of state, the ECBC have been extended to the Navier-Stokes characteristic boundary conditions (NSCBC) by Poinsot et al. [187] in order to include inviscid effects and the temperature changes due to the compression by the pressure wave. The NSCBC

have been adjusted to account for multi-component reaction fronts [199]. However, the OpenFOAM native *waveTransmissive* BC is considered sufficient for explosion risk assessment simulations, as it prevents any noticeable reflections of strong shock waves origination from fast flames, DDT or stable detonations.

E Supervised Student Thesis and Projects

The author of the present doctoral thesis supervised several student theses. These theses were prepared at the Chair of Thermodynamics of the Technical University of Munich from 2017 to 2021 under the close supervision of the present author. Parts of these supervised theses may be incorporated into the present doctoral thesis. The author would like to express his sincere gratitude to all formerly supervised students for their commitment and support of this research project.

Thoma, Christoph: Evaluierung von H2/CO/Luft-Reaktionsmechanismen zur Vorhersage des Übergangs von Deflagration zu Detontation. Research project, 2017

Schlosser, Lukas: Modellierung der Flammengeschwindigkeit von H2-CO-Luftgemischen in Explosionen. Bachelor's thesis, 2018

Wein, Nicolas: Parameterstudie zur Erzeugung geschichteter H2-CO-Luftgemische in der GraVent-Anlage. Bachelor's thesis, 2018

Pathak, Utkarsh: Efficient simulation of medium to large scale DDT phenomena in H2-CO-air mixtures. Master's thesis, 2020

Coloma Armas, Martin: Beurteilung des Zerstörungspotentials des DDT auf die eingeschließende Geometrie. Research project, 2020

F Previous Publications

Parts of the present doctoral thesis have been published by the author beforehand in journals or at conferences. These printed publications are registered according to the valid doctoral regulations and are listed below. Therefore, they are not necessarily quoted explicitly in the text. Whether they were referenced depended on maintaining comprehensibility and providing all necessary context.

Barfuss, C.; Heilbronn, D.; Sattelmayer, T.: Numerical simulation of deflagration and detonation in homogeneous hydrogen-carbon monoxide-air mixtures. *12th International Symposium on Hazards, Prevention, and Mitigation of Industrial Explosions*, 2018 (ISHPMIE 2018)

Barfuss, C.; Heilbronn, D.; Sattelmayer, T.: Simulation of deflagration-to-detonation transition of lean H2-CO-air mixtures in obstructed channels. *International Conference on Hydrogen Safety*, 2019 (ICHS 2019), pp. 1-12

Heilbronn, D.; Barfuss, C.; Sattelmayer, T.: Deflagration-to-detonation transition in H2-CO-air mixtures in a partially obstructed channel. *International Conference on Hydrogen Safety*, 2019 (ICHS 2019), pp. 1-11

Barfuss, C.; Heilbronn, D.; Sattelmayer, T.: Impact of local flame quenching in the flame acceleration in H2-CO-air mixtures in obstructed channels. *13th International Symposium on Hazards, Prevention, and Mitigation of Industrial Explosions*, 2020 (ISHPMIE 2020)

Heilbronn, D.; Barfuss, C.; Sattelmayer, T.: Influence of geometry on flame acceleration and DDT in H2-CO-air mixtures in a partially obstructed channel. *13th International Symposium on Hazards, Prevention, and Mitigation of Industrial Explosions*, 2020 (ISHPMIE 2020)

Barfuss, C.; Heilbronn, D.; Sattelmayer, T.: Impact of local flame quenching on the flame acceleration in H2-CO-air mixtures in obstructed channels. *Journal of Loss Prevention in the Process Industries* Vol. 71, No. 104491, 2021

Heilbronn, D.; Barfuss, C.; Sattelmayer, T.: Influence of geometry on flame acceleration and DDT in H2-CO-air mixtures in a partially obstructed channel. *Journal of Loss Prevention in the Process Industries* Vol. 71, No. 104493, 2021

Heilbronn, D.; Barfuss, C.; Sattelmayer, T.: Deflagration-to-detonation transition in H2-CO-air mixtures in a partially obstructed channel. *International Journal of Hydrogen Energy* Vol. 46 (Issue 23), pp. 12372-12383, 2021

Barfuss, C.; Heilbronn, D.; Sattelmayer, T.: Verbundvorhaben: Entwicklung von Verbrennungsmodellen und Kriterien für H2-CO-Luft-Schichten bei partiellem Einschluss - Teilvorhaben: Experimentelle Untersuchungen auf Laborskala sowie Entwicklung komplementärer CFD-Verfahren. Technical Report 1501545A, *Bundesministerium für Wirtschaft und Energie (BMWi), Lehrstuhl für Thermodynamik der Technische Universität München*, 2022